

**STUDY AND CHARACTERIZATION OF ELECTRON
CYCLOTRON RESONANCE PLASMA AS AN ION SOURCE**

By

SUNIL KUMAR JAIN

Enrolment No. : PHYS 03 2007 04 015

Raja Ramanna Centre for Advanced Technology

Indore - 452 013, (M.P.), INDIA

*A thesis submitted to the
Board of Studies in Physical Sciences
In partial fulfillment of requirements
For the Degree of
DOCTOR OF PHILOSOPHY*

of

HOMI BHABHA NATIONAL INSTITUTE



OCTOBER, 2013

© Homi Bhabha National Institute, 2013

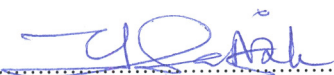
Homi Bhabha National Institute

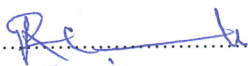
Recommendations of the Viva Voce Board

As member of the Viva Voce Board, we certify that we have read the dissertation prepared by *Mr. Sunil Kumar Jain* entitled "*Study and Characterization of Electron Cyclotron Resonance Plasma as an Ion Source*" and recommend that it may be accepted by fulfilling the dissertation requirement for the degree of *Doctor of Philosophy*.

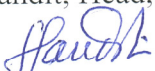
.....

Chairman : Prof. P. D. Gupta, Director, RRCAT Date : April 22, 2014

.....

Guide : Prof. P. A. Naik, Head, LPD, RRCAT Date : April 22, 2014

.....

Tech. Adviser : Shri P. R. Hannurkar, Head, RFSD, RRCAT Date : April 22, 2014

.....
Member : Prof. V. S. Pandit, Head, APD, VECC Date : April 22, 2014

.....

Member : Prof. V. K. Senecha, Head, ISL, RRCAT Date : April 22, 2014

.....

External Examiner : Prof. G. Mohan Rao, IISc, Bangalore Date : April 22, 2014

Final approval and acceptance of this dissertation is contingent upon the candidate's submission of the final copies of the dissertation to HBNI.

We hereby certify that we have read this dissertation prepared under our direction and recommend that it may be accepted as fulfilling the dissertation requirement.

Date : April 22, 2014

Place : Indore

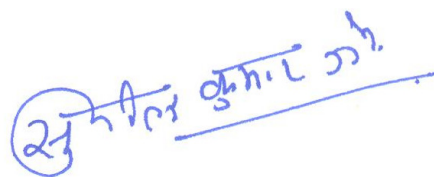
.....

Guide : Prof. Prasad A. Naik

STATEMENT BY THE AUTHOR

This dissertation entitled “*Study and Characterization of Electron Cyclotron Resonance Plasma as an Ion Source*” has been submitted in partial fulfillment of requirements for an advanced degree at Homi Bhabha National Institute (HBNI) and is deposited in the Library to be made available to borrowers under rules of HBNI.

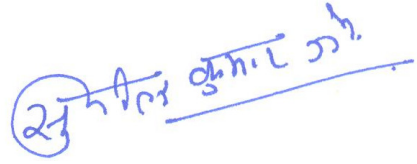
Brief quotations from this dissertation are allowable without special permission, provided that accurate acknowledgement of source is made. Requests for permission for extended quotation from or reproduction of this manuscript in whole or any part may be granted by the Competent Authority of HBNI when in his or her judgment the proposed use of the material is in the interests of scholarship. In all other instances, however, permission must be obtained from the author.



(Sunil Kumar Jain)

DECLARATION

I, Sunil Kumar Jain, hereby, declare that the investigation presented in this thesis has been carried out by me. The work is original and has not been submitted earlier as a whole or in part for a degree / diploma at this or any other Institution / University.



(Sunil Kumar Jain)

Dedicated to my Parents.....

ACKNOWLEDGEMENTS

The work reported in this thesis is a result of help, support, and encouragement provided by a number of colleagues and friends. It is my pleasure to acknowledge them here.

I am particularly indebted to Dr. P. A. Naik for his valuable guidance, constant support and encouragement during the entire course of the Ph. D. work. His way of teaching always encouraged me to think over new ideas and made this entire journey of Ph. D. research and development work a memorable learning experience.

My deep regards and gratitude are due to Shri P. R. Hannurkar (Tech. Adviser) for his ever-helping nature, keen interest, deep involvement, and utmost care throughout my research work. He motivated me to work hard and keep patience under difficult circumstances. He carefully and patiently nurtured this research work to reach the present level. He helped me to solve all kinds of practical problems in the ECR Ion Source development, sharing knowledge and making me comfortable in handling of the required scientific instrumentations. This research and development work would not have been possible without his support and encouragement.

I am extremely thankful to Dr. P. D. Gupta (Chairman, Doctoral Committee) and Director, RRCAT for his keen interest in my research work. His valuable instructions during the yearly reviews inspired me in my work.

I express my sincere thanks to Shri S. C. Joshi, Head, Proton Linac & Superconducting Cavities Division, RRCAT, Indore for constant support, guidance, valuable suggestions and timely feedback about the manuscripts for communicating to journals.

My sincere thanks to Dr. V. S. Pandit, Head, Accelerator Physics Division, Variable Energy Cyclotron Centre, and Dr. V. K. Senecha, Head, Ion Source Laboratory, RRCAT, for their valuable comments, and scientific discussions, which helped in improving the quality of

my work. Their persistent encouragement, perpetual motivation, and valuable technical inputs have immensely benefited me.

I wish to thank whole-heartedly my colleagues Mr. Akhilesh Jain and Mr. Deepak Sharma for their unconditional support and cooperation during the microwave components simulations.

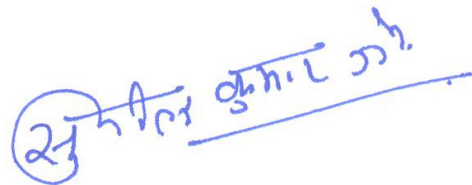
I would like to give special thanks to Dr. Suman Bagchi, Mr. Vipul Arora, Mr. Mohammad Tayyab, Miss Ranjana Rathore, Dr. D. V. Ghodke, Mr. R. M. Vadjikar, and Mr. Rajnish Kumar for providing me their valuable support, guidance and encouragement at different stages of my research work.

I wish to thank all other members of Proton Linac & Superconducting Cavities Division and Radio Frequency Systems Division for their kind support. I would like to thank the staff of Accelerator Workshop who always completed my mechanical jobs in time.

I would like to express my special gratitude to my parents (Shri K. C. Jain / Smt. Nirmala Jain) for keeping my spirits high. I also humbly dedicate this Ph. D. thesis to them.

I am thankful to my wife Anita and sons Akshay and Aditya for their support and sacrifice of family time they have done during this Ph. D. work. I thank to my brothers, sisters, brothers/sisters-in-law and my nephews/nieces (Pradeep, Madhu, Monika, Aproova, Anil, Asha, Ashita, and Anshul) for their constant help, co-operation, and for providing a cheerful atmosphere at home.

Last but not the least, I would like to thank the Almighty, without whose blessings I would not have completed my Ph. D. work.



(Sunil Kumar Jain)

CONTENTS

SYNOPSIS	iii
LIST OF PUBLICATIONS	vii
LIST OF FIGURES	x
LIST OF TABLES	xvii
CHAPTER 1 : Plasma physics aspects of an ECR source	1-26
1.1 Plasma terminology	1
1.2 Motion of electrons in static electric and magnetic fields	8
1.3 Waves in magnetized plasma	12
1.4 Magnetic trap and confinement of plasma	17
1.5 Ionization of hydrogen	21
1.6 Production of charged ions	22
CHAPTER 2 : ECR plasma as ion source : An overview	27-35
2.1 Operating principle of an ECR plasma source	31
2.2 Major components of the RRCAT-ECR plasma source	33
CHAPTER 3 : Plasma chamber and vacuum system	36-39
3.1 Plasma chamber	36
3.2 Vacuum system	37
CHAPTER 4 : Microwave system	40-78
4.1 Magnetron as a source of microwave power	41
4.2 Waveguide components	44
4.3 Characterization of the microwave components	73
CHAPTER 5 : Electromagnet and its power supply	79-90
5.1 Magnetic field design	80
5.2 Fabrication of electromagnet	85
5.3 Magnetic field mapping	86
5.4 High voltage insulator dome	89

CHAPTER 6 : Ion beam extraction system	91-107
6.1 Design considerations : Theoretical background	91
6.2 Software optimization	94
6.3 Three-electrode geometry for Phase-I	96
6.4 Fabrication and testing of the electrode geometry	100
6.5 Three-electrode geometry for Phase-II	101
CHAPTER 7 : Plasma diagnostics with Langmuir probe	108-119
7.1 Langmuir probe : working and characteristics	108
7.2 Langmuir probe construction	112
7.3 Langmuir probe electrical circuit	113
7.4 Interpretations of the probe characteristics	116
CHAPTER 8 : Experimental characterization of the ECR plasma source	120-157
8.1 Plasma characterization as a function of various parameters	122
8.2 Ion beam current measurement	128
8.3 Ion beam characterization using Thomson parabola ion spectrograph	131
8.4 X-ray measurements with silicon P-I-N detector	138
8.5 Application of the ECR source for titanium film deposition	142
8.6 Ion beam characterization with mass analyzing magnet	147
8.7 Supervisory control and monitoring system	156
CHAPTER 9 : Summary	158-161
BIBLIOGRAPHY	162-178

Synopsis

The ion beam sources have become an important tool for numerous scientific investigations in recent times such as heavy ion radio-therapy, radio-biology, radio-oncology, surface science, nuclear transmutation studies, fusion studies, trace analysis, thin film deposition, neutron spallation, ion implantation, sputtering, etching, lithography, plasma processing, x-ray production etc. Charged particle beams of different currents are required for different applications. For example, ion beams of hundreds of amperes current are required for fusion applications, whereas beams of nano-ampere current are adequate for applications like trace analysis, thin film deposition etc. Various types of ion source have been developed. These include : Filament based sources such as Freeman, Duoplasmatron, Penning and Magnetron; and microwave based sources such as electron cyclotron resonance ion sources (ECRIS). Among all these sources, ECRIS offers a number of advantages over other filament based ion sources like no lifetime constraint in absence of filaments, consumes only neutral gases (for plasma production) and has capability of working in a corrosive environment, which gives ECRIS a leading edge over the other sources. The high performance reliability of ECRIS has now made it an integral part of the new age accelerators due to its salient features such as 1) operation in continuous wave or in pulsed mode, 2) high current, 3) low emittance, 4) high brightness, 5) high current stability, 6) multiple charge states ion beams, and 6) high reliability. The only possible drawback of ECRIS is the use of microwave window whose lifetime could be limited because of the electron bombardment and metal deposition on it. The ion sources used for the extraction of charged particles are chosen according to their output beam current, emittance, ion species, intensity, and energy spread.

The ECRIS has been widely accepted by accelerator community world-wide as an injector to high energy proton and heavy ion accelerators because of its capacity to deliver more than 50-100 mA proton beam current at 50-100 keV beam energy, with 80-90 % of proton fraction, and low emittance 0.2π mm mrad (e.g. SILHI, TRIPS, INFN, MIDAS, VIS, ALISES, and SPIRAL2). Keeping this in mind, we have designed and developed an ECRIS capable of generating a CW proton beam with up to 30 mA current at 50 keV beam energy (RRCAT-ECRIS). In recent experiments, it has demonstrated up to 8 mA of stable ion beam current (± 1 %) at 24 kV acceleration (Phase-I).

In an ECRIS, the plasma is produced by the interaction of the microwave radiation, in the presence of appropriate static magnetic field, under the cyclotron resonance condition (i.e. applied microwave frequency equals cyclotron frequency, $\omega_{ce} \cong \omega_{rf}$). The free electrons gyrate in the presence of the applied static magnetic field at the electron cyclotron frequency. The microwave power gets resonantly coupled to the gyrating electrons when the microwave frequency equals the electron cyclotron frequency. The electrons, in turn, transfer their energy to the neutral gas atoms by collisions, thereby ionizing them and creating plasma, leading to the absorption of the microwave radiation. The ECRIS used worldwide to obtain singly and multiply charged ion beams of low to high Z elements. The ECRIS at RRCAT operates at 2.45 GHz microwave frequency. This frequency is chosen because at this frequency the cost of the microwave source is less, the source is compact, and electron energies are suitable for producing singly charged ion beam.

In the context of above discussion the present thesis focuses on the following aspects :

- Plasma physics aspects of an ECR source
- ECR plasma source : An overview
- Plasma chamber as a resonant cavity at 2.45 GHz frequency and as plasma container.
- Design, development and characterization of the microwave transfer line and its sub-components.
- Design, development and magnetic field characterization of electromagnet coils for the confinement of the plasma.
- Design and development of extraction electrode geometry for the extraction of proton / ion beam.
- Development and characterization of Langmuir probe as a diagnostics device.
- Experimental investigations on the plasma parameters (electron density, and electron temperature) using Langmuir probe.
- Extraction of ion beam and its characterization using Thomson parabola.
- Characterization of the x-ray generated using extracted ions.
- Deposition of titanium film using sputtering by the extracted ions, as an application of the ECRIS.

The proposed thesis has nine chapters and is organized as follows : After a brief introduction to the above listed areas of research, **Chapter 1** starts with an overview of the plasma physics aspects of an ECR source. It also covers the basic of electromagnetic wave

propagation under static magnetic field, processes of ionization / recombination, production of charged (singly / multiply) ions etc.

Chapter 2 deals with the operating principle of an ECR source and the major components which are required to build an ECRIS viz. microwave system, plasma chamber and vacuum system, electromagnet coils and their power supplies, beam extraction electrodes, and plasma diagnostics devices.

Chapter 3 deals with the design aspects of the plasma chamber, and the vacuum system. The plasma chamber does two jobs, coupling the microwave power to the plasma and containment of the plasma produced. The dimensions of the plasma chamber as a cylindrical cavity were analytically calculated and cross-checked with electromagnetic software.

Chapter 4 covers various aspects of the microwave system. This includes the design, development of a power supply for energizing the coaxial magnetron source which is used as a source of microwave power at 2.45 GHz frequency and microwave power up to 2 kW continuous wave. This chapter also includes the design, development and characterization of the microwave transfer line which consists of an isolator (which allows the microwave propagation in forward direction while the reflected power is dumped), directional coupler (for power measurement), tunable three-stub tuner (for impedance matching), and microwave vacuum window (for vacuum isolation between the plasma chamber and microwave system), glass-water load (for the characterization of the microwave line and the source), and a microwave launcher (to feed the microwave power to the plasma chamber).

Chapter 5 gives details of the design, development, and characterization of the electromagnet coils used to produce desired magnetic field to confine the plasma, and also to make the electrons gyrate and undergo electron cyclotron resonance with the applied microwave field. The three electromagnets are water-cooled and energized independently with the use of three independent power supplies. With the use of three electromagnet coils, it is possible to operate the source in off-resonance, mirror, and resonance flat magnetic field configurations, for the singly as well multiply charged states. The magnetic field configurations were optimized using Poisson software.

Chapter 6, covers the design simulations and development of the extraction electrode geometry for the extraction of 10 mA proton beam, up to 25 keV beam energy (in Phase-I) and 30 mA proton beam, up to 50 keV beam energy (in Phase-II). The electrode geometry

was designed using IGUN software which uses the Poisson equation in the plasma and the extraction region, using finite difference method.

Chapter 7 deals with the design and fabrication of a Langmuir probe for characterization of the plasma produced with argon / hydrogen / nitrogen gas. The Langmuir probe gives the current-voltage curve, i.e. the variation of the current drawn by the probe with the probe bias voltage. The current-voltage curve was used for evaluating the plasma parameters.

After integration of the source, the experimental procedure used to characterize the ECRIS has been discussed in **Chapter 8**. The source was operated for different operating conditions over a wide range of gas pressure, microwave power, and magnetic field. The source has a wide tuning range for operating the plasma parameters. The radial variation of the electron density also has been measured. The details of the characterization of the extracted ion beam using Thomson parabola, are given. This chapter also includes the measurement of the characteristic x-rays produced using argon / hydrogen / nitrogen ion beams impinging on a copper target. The bremsstrahlung continuum was also seen along with the characteristic lines copper K- α and K- β . As a demonstration of an application of the ECRIS, a titanium film was deposited on a glass substrate, using ECR argon ion beam bombarding a titanium target.

At the end of the thesis, in **Chapter 9**, a summary of the thesis work has been presented. Further scope of improvement in the present system is also discussed in this chapter.

Publications which form a part of this thesis

A. Published : (13)

A.1 Papers in refereed Journals : (6)

- 1) “Acquisition and analysis of Langmuir probe characterization for ECR plasma”
S. K. Jain, A. Jain, D. Sharma, and P. R. Hannurkar,
Ind. J. Phys. **A80**, 1011 (Oct. 2006).
- 2) “Characterization of plasma parameters, first beam results, and status of electron cyclotron resonance source”
S. K. Jain, A. Jain, P. R. Hannurkar, and S. Kotaiah,
Rev. Sci. Instrum. **78**, 053301-1-6 (2007).
- 3) “Design, fabrication and measurement of 90° mass-analyzing magnet”
S. K. Jain, R. Malik, K. Sekar, P. A. Naik, and P. R. Hannurkar,
Ind. J. Pure & Appl. Phys. **48**, 315 (2010).
- 4) “Design, fabrication, and characterization of a solenoid system to generate magnetic field for an ECR proton source”
S. K. Jain, P. A. Naik, and P. R. Hannurkar,
Sadhana : Academy Proceedings in Engineering Sciences **35**, 461 (2010).
- 5) “Characterization of proton beam emission from an electron cyclotron resonance ion source”
S. K. Jain, M. Tayyab, S. Bagchi, J. A. Chakera, and P. A. Naik,
Nucl. Inst. Meth. Phys. Res. **A708**, 51 (2013).
- 6) “Study of microwave power coupling with electron cyclotron resonance plasma using Langmuir probe”
S. K. Jain, V. K. Senecha, P. A. Naik, P. R. Hannurkar, and S. C. Joshi,
Pramana J. Phys. **81**, 157 (2013).

- 7) “Study of microwave components for an electron cyclotron resonance source : Simulations and performance”
S. K. Jain, Deepak Sharma, V. K. Senecha, P. A. Naik, and P. R. Hannurkar,
Accepted in *Sadhana : Academy Proceedings in Engineering Sciences*.

A.2 RRCAT Internal Reports / News Letter : (3)

- 1) “Electron cyclotron resonance based ion beam sputtering techniques to study titanium conductive film deposition on a float glass substrate”
S. K. Jain, R. Dhawan, S. K. Rai, C. Mukherjee, V. K. Senecha, S. C. Joshi, P. A. Naik, and P. R. Hannurkar,
RRCAT Internal Report number : RRCAT/2012-10
- 2) “Modeling and optimization of three-electrode geometry for extraction of proton ion beam with electron cyclotron resonance plasma source”
S. K. Jain, V. K. Senecha, S. C. Joshi, P. A. Naik, and P. R. Hannurkar,
RRCAT Internal Report number : RRCAT/2013-03
- 3) “Hydrogen ion beam extraction from ECR ion source and beam extraction”
S. K. Jain, and V. K. Senecha, RRCAT News Letter, Vol 25, Issue 1, 2012.

A.3 Papers Published in Conferences : (4)

- 1) “Study of extraction electrode geometry for 30 mA, 50 keV ECR proton source using IGUN software”
S. K. Jain, and P. R. Hannurkar,
Indian Particle Accelerator Conference InPAC–2009, Indore, February 10-13, 2009.
- 2) “Development of 90° mass analyzing magnet for charge analysis”
S. K. Jain, R. Malik, K. Sekar, and P. R. Hannurkar,
Indian Particle Accelerator Conference InPAC–2009, Indore, February 10-13, 2009.

- 3) “Electron cyclotron resonance plasma diagnostics to study microwave power coupling with Langmuir probe”

S. K. Jain, V. K. Senecha, D. Mishra, and S. C. Joshi,

Indian Particle Accelerator Conference InPAC–2011, New Delhi, February 15-18, 2011.

- 4) “Development of high current pulsed H⁻ ion source and ECR ion source for the injector Linac at RRCAT”

V. K. Senecha, **S. K. Jain**, D. V. Ghodke, Vikas Jain, V. K. Srivastava, D. Mishra, R. M. Vadjikar, R. Kumar, and S. C. Joshi,

2nd International workshop on accelerator-driven sub-critical systems & thorium utilization, Mumbai, December 11-14, 2011

LIST OF FIGURES

Figure 1.1	: The variations of first ionization cross-section as a function of energy of the ionizing electrons	6
Figure 1.2	: The cyclotron motion of electron in a static magnetic field	9
Figure 1.3	: The $\vec{E} \times \vec{B}$ drift motion of the electron	11
Figure 1.4	: The $\nabla \vec{B}$ drift motion of a positive ion	12
Figure 1.5	: The right hand polarized wave (R-wave) propagating in the magnetized plasma	14
Figure 1.6	: The extraordinary wave propagating in the magnetized plasma	15
Figure 1.7	: The cut-off and resonance of O-, X-, R-, and L-wave (Clemmow-Mullaly-Allis diagram).	17
Figure 1.8	: Plasma trapped between magnetic mirrors created by a pair of solenoid coil	18
Figure 1.9	: Electron trajectory in a homogeneous magnetic field	19
Figure 1.10	: Electron trajectory in an increasing magnetic field	19
Figure 1.11	: The velocity space loss cone in a magnetic mirror	20
Figure 2.1	: A schematic layout of proposed 3 MeV front-end of H^- / H^+ proton linear accelerator at RRCAT, Indore	30
Figure 2.2	: The operating principle of an ECR plasma source	32
Figure 2.3	: A schematic representation of the acceleration-deceleration of electron under right, and left hand polarized wave	32
Figure 2.4	: A schematic block diagram of electron cyclotron resonance ion source (ECRIS)	33
Figure 2.5	: The RRCAT-ECRIS integrated with Thomson parabola ion spectrograph	34
Figure 2.6	: A 3D-view of the RRCAT-ECRIS	34
Figure 2.7	: A photograph of the RRCAT-ECRIS	35
Figure 3.1	: The experimental setup for the measurement of resonance frequency of the plasma chamber	37
Figure 4.1	: A schematic diagram of the microwave system for RRCAT-ECRIS	41
Figure 4.2	: A 3D-view of the microwave system test setup for RRCAT-ECRIS	41
Figure 4.3	: A block diagram of the magnetron power supply	43

Figure 4.4	: The measured waveform and ripple of the magnetron power supply for a) DC output for cathode, and b) AC output for filament	43
Figure 4.5	: A photograph of the magnetron power supply	44
Figure 4.6	: The electromagnetic field pattern a) standard transverse electric TE mode, b) dominant TE ₁₀ mode, and c) <i>microwave studio</i> simulated, inside the WR-284 rectangular waveguide	45
Figure 4.7	: A block diagram of the directional coupler	46
Figure 4.8	: A schematic diagram of the directional coupler	47
Figure 4.9	: A schematic diagram of the orientation of loop plate with respect to direction of propagation axis for the directional coupler	47
Figure 4.10	: A model prepared in <i>microwave studio</i> for the directional coupler	48
Figure 4.11	: The S-parameters optimized with frequency for the directional coupler	49
Figure 4.12	: Variations of coupling factor (S31), and the directivity (S31-S41) with hole diameter for the directional coupler at 2.45 GHz frequency	49
Figure 4.13	: A photograph of the directional coupler	51
Figure 4.14	: The matchable area in the complex reflection coefficient plane	52
Figure 4.15	: A schematic diagram of shunt connected the stub as a three-stub tuner	53
Figure 4.16	: A model prepared in <i>microwave studio</i> for the three-stub tuner	53
Figure 4.17	: A model prepared in <i>microwave studio</i> for the high voltage break	54
Figure 4.18	: The S-parameters optimized with frequency for the high voltage break : Teflon of thickness 7.35 mm	55
Figure 4.19	: A model prepared in <i>microwave studio</i> for the microwave vacuum window	57
Figure 4.20	: Variation of the return loss (S11), the insertion loss (S21) with thickness of quartz plate for the microwave vacuum window at 2.45 GHz frequency	57
Figure 4.21	: The S-parameters optimized with frequency for a microwave vacuum window with quartz thickness of 6 mm	58
Figure 4.22	: A model prepared in <i>microwave studio</i> for a tapered launcher	59
Figure 4.23	: Variation of electric field with the height of waveguide for a tapered launcher	60

Figure 4.24	: The S-parameters optimized with frequency for a tapered launcher	61
Figure 4.25	: The electric field distribution in a tapered launcher	61
Figure 4.26	: A schematic diagram of a four sections ridged waveguide coupled to the plasma chamber	63
Figure 4.27	: Variation of impedance with the length for a standard waveguide and a ridged waveguide	64
Figure 4.28	: An electromagnetic model of a ridged waveguide coupled with a plasma chamber	65
Figure 4.29	: The simulated variations of the return loss (S11), the insertion loss (S21) for a ridge gap I at 2.45 GHz frequency for the ridged waveguide	66
Figure 4.30	: The simulated variations of the return loss (S11), the insertion loss (S21) for a ridge gap II at 2.45 GHz frequency for the ridged waveguide	66
Figure 4.31	: The simulated variations of the return loss (S11), the insertion loss (S21) for a ridge gap III at 2.45 GHz frequency for the ridged waveguide	67
Figure 4.32	: The simulated variations of the return loss (S11), the insertion loss (S21) for a ridge gap IV at 2.45 GHz frequency for the ridged waveguide	67
Figure 4.33	: The optimized variations of the return loss (S11), the insertion loss (S21) for the ridged waveguide with frequency range between 2.2 to 2.7 GHz	68
Figure 4.34	: The variations of the return loss (S11), the insertion loss (S21) with ridge width at 2.45 GHz frequency for the ridged waveguide	69
Figure 4.35	: A vector plot of the distribution of the electric field for a standard waveguide	70
Figure 4.36	: A vector plot of the distribution of the electric field for a ridged waveguide	70
Figure 4.37	: The electric field intensity distribution in the horizontal mid-plane for a standard waveguide and a ridged waveguide of width 12.5 mm	70
Figure 4.38	: The electric field intensity in a horizontal plane of the ridged waveguide coupled with the plasma chamber	71

Figure 4.39	: The electric field intensity in a transverse plane of the ridged waveguide coupled with the plasma chamber	72
Figure 4.40	: A photograph of the glass-water load	73
Figure 4.41	: The test setup for low power characterization of microwave components using network analyzer	74
Figure 4.42	: The measured results for the directional coupler	74
Figure 4.43	: The measured results for the three-stub tuner when stubs are FULL IN	75
Figure 4.44	: The measured results for three-stub tuner when stubs are FULL OUT	76
Figure 4.45	: The measured results for the high voltage break	76
Figure 4.46	: The measured results for the microwave vacuum window	77
Figure 4.47	: An integrated schematic diagram of the microwave components with glass-water load for high power characterization	78
Figure 4.48	: Variation of microwave output power with the cathode current of the magnetron	78
Figure 5.1	: The optimized axial flux along the axis of the source using the <i>Poisson</i> software	82
Figure 5.2	: The optimized mirror magnetic field profile using the <i>Poisson</i> software along the axis of the source	82
Figure 5.3	: The optimized flat magnetic field profile using the <i>Poisson</i> software along the axis of the source	83
Figure 5.4	: The measured mirror magnetic field profile along the axis of the source	88
Figure 5.5	: The measured flat magnetic field profile along the axis of the source	88
Figure 5.6	: Variation of the magnetic field with the solenoid current	89
Figure 5.7	: A schematic diagram of the high voltage insulator dome	90
Figure 6.1	: The meniscus formed at the plasma boundary viz. a) convex, b) planar, and c) concave plasma meniscus with the beam extraction from the plasma	93
Figure 6.2	: A flow chart of the <i>IGUN</i> software	96
Figure 6.3	: The profile of the surface electric fields in the three-electrode extraction geometry	97

Figure 6.4	: The proton beam trajectory for three-electrode extraction geometry for 10 mA proton beam current for 25 keV beam energy	98
Figure 6.5	: A 3D-cross-sectional view of three-electrode extraction geometry	99
Figure 6.6	: Photographs of all three-electrodes	100
Figure 6.7	: A photograph of integrated three-electrode extraction geometry	101
Figure 6.8	: Variation of r.m.s. emittance with opening angle for Pierce geometry	102
Figure 6.9	: The optimized profile of the proton beam trajectory for Pierce geometry	103
Figure 6.10	: The profile of the surface electric fields in the electrodes for Pierce geometry	103
Figure 6.11	: The profile of the r.m.s. emittance beam envelope for Pierce geometry	104
Figure 6.12	: Variation of the r.m.s. emittance with extraction voltage for Pierce geometry	105
Figure 6.13	: Variation of r.m.s. emittance with ion temperature, at different PE aperture for Pierce geometry	106
Figure 6.14	: Variation of r.m.s. emittance with gap between the PE and EE for Pierce geometry	107
Figure 7.1	: A typical current-voltage ($I_{\text{probe}}-V_{\text{probe}}$) curve for a Langmuir probe	109
Figure 7.2	: A typical current-voltage ($I_{\text{probe}}-V_{\text{probe}}$) curve for interpretation of the floating potential obtained from a Langmuir probe	111
Figure 7.3	: A typical current-voltage ($I_{\text{probe}}-V_{\text{probe}}$) curve for interpretation of the plasma potential from a Langmuir probe	112
Figure 7.4	: A typical second derivative of the $I_{\text{probe}}-V_{\text{probe}}$ curve	112
Figure 7.5	: A photograph of indigenously developed Langmuir probe	113
Figure 7.6	: The resistive circuit for measuring the probe voltage (V_{probe}) and the probe current (I_{probe})	114
Figure 7.7	: A basic block diagram for measuring and processing the probe characteristics (V_{probe} and I_{probe})	115
Figure 7.8	: A front panel graphical view of an acquired current-voltage ($I_{\text{probe}}-V_{\text{probe}}$) curve	116
Figure 7.9	: A current-voltage ($I_{\text{probe}}-V_{\text{probe}}$) curve obtained for an ECR plasma discharge	117

Figure 7.10	: A typical $\ln(I_e)$ and V_{probe} curve	119
Figure 7.11	: A typical $\ln(I_{e1})$ and V_{probe} curve	119
Figure 8.1	: A view of plasma discharge through the quartz windows	121
Figure 8.2	: The experimental setup for the characterization of the RRCAT- ECRIS with Langmuir probe	122
Figure 8.3	: Variation of electron density with gas pressure	123
Figure 8.4	: Variation of electron temperature with gas pressure	124
Figure 8.5	: Variation of electron density with microwave power	125
Figure 8.6	: Variation of electron temperature with microwave power	125
Figure 8.7	: Variation of product of electron density and electron temperature with the coupled microwave power	126
Figure 8.8	: Variation of the electron density with radius	127
Figure 8.9	: The radial variation of the electron temperature	128
Figure 8.10	: A schematic diagram of the electrical biasing circuit of the three- electrode extraction geometry with Faraday cup	129
Figure 8.11	: Variation of the measured hydrogen ion beam current with extraction voltage	130
Figure 8.12	: A schematic diagram of a Thomson parabola ion spectrograph	131
Figure 8.13	: Proton beam trajectory recorded by the Thomson parabola ion spectrograph at different extraction voltages	134
Figure 8.14	: Variation of the estimated dispersed particle distribution in the ion beam with increasing extraction voltages	135
Figure 8.15	: Comparison of the proton beam current as measured by the Faraday cup and by the Thomson parabola ion spectrograph	137
Figure 8.16	: Argon ion beam trajectory recorded by the Thomson parabola ion spectrograph for a) short, and b) long exposure time	137
Figure 8.17	: The experimental setup for x-ray detection from RRCAT-ECRIS	140
Figure 8.18	: X-ray emission spectra of copper induced by argon ions at 25 kV extraction voltage	141
Figure 8.19	: X-ray emission spectra of copper induced by hydrogen ions at 25 kV extraction voltage	141
Figure 8.20	: X-ray emission spectra of copper induced by nitrogen ions at 25 kV extraction voltage	142

Figure 8.21	: A schematic diagram of the experimental setup of ECR based ion beam sputtering system with the arrangement for target and the substrate holder	144
Figure 8.22	: The x-ray reflectivity pattern of the titanium conductive metal film along with fitting	145
Figure 8.23	: The atomic force microscopy images of the titanium film	146
Figure 8.24	: The RRCAT-ECRIS integrated with the mass analyzing magnet	148
Figure 8.25	: The magnetic field profile for the mass analyzing magnet : Model-1	150
Figure 8.26	: The magnetic field profile for the mass analyzing magnet : Model-2	150
Figure 8.27	: A cross-sectional view of the magnet yoke for mass analyzing magnet	151
Figure 8.28	: The required magnetic field for hydrogen species H^+ , H_2^+ , and H_3^+ with respect to the beam energy	152
Figure 8.29	: Variation of the magnetic field (calculated and measured) with the current	154
Figure 8.30	: The focussing effect and the beam transmission through the mass analyzing magnet for a proton beam	155
Figure 8.31	: The beam profile in the horizontal and the vertical plane i.e. phase space ellipse	156
Figure 8.32	: The graphical front panel view of RRCAT-ECRIS supervisory control and monitoring system	157

LIST OF TABLES

Table 1.1	: Few cases of ionization	5
Table 1.2	: The Larmour radii (mm) for electrons and ions in ECRIS plasma (B = 875 G)	9
Table 1.3	: The ECR resonance magnetic field (B_{ecr}) values for different frequencies and electron energies	10
Table 1.4	: The cut-off and resonance conditions for the waves propagating inside the plasmas	16
Table 1.5	: The process of ionization possible for hydrogen atom	22
Table 1.6	: The ionization potential for various elements	24
Table 1.7	: The possible processes of ionization of atoms	25
Table 1.8	: The design specifications and present status of the RRCAT-ECRIS	30
Table 4.1	: The technical specifications of the coaxial magnetron	42
Table 4.2	: Return loss, coupling, isolation and directivity calculated when $\theta_1 \neq \theta_2$	50
Table 4.3	: The dimensions and impedances of the four sections of the ridged waveguide	64
Table 5.1	: The optimized design parameters for solenoid coil with iron jacket	81
Table 8.1	: The experimental parameters used for the extraction of ion beam from three-electrode extraction geometry for Phase-I	130
Table 8.2	: The design parameters of the mass analyzing magnet	149
Table 8.3	: The measured magnetic field homogeneity for axial distance ± 30 mm	153
Table 8.4	: The design, calculated effective length and their difference at 3000 G	153

CHAPTER 1

Plasma Physics Aspects of an ECR Source

This chapter gives an overview of the plasma physics aspects of an electron cyclotron resonance (ECR) source. It also covers the basic of electromagnetic wave propagation under static magnetic field, processes of ionization / recombination, production of charged (singly / multiply) ions etc.

An electron cyclotron resonance (ECR) source is based on creation of plasma by means of microwave power in a confined manner, and extraction of the ions from the plasma. Hence it is very important to study the basics of plasma production and its characteristics, and propagation of electromagnetic waves in magnetized plasma.

1.1 Plasma Terminology

Plasma is a quasi-neutral ensemble of ions, electrons, and neutral atoms / molecules, which exhibits a collective behaviour when exposed to external fields. Plasma has a zero net electric charge. It has freely moving charged particles, which make it a very good conductor. The behaviour of the plasma is dominated by the macroscopic electric and magnetic fields. Some of the important terms are presented in the following section, which play an important role in understanding the ion source as well as plasma [1,2,3].

a) Electron density (n_e)

The fractional ionization in a gas in thermal equilibrium is given by the Saha equation (also called *Saha Ionization formula*) as,

$$\frac{n_{i^+}}{n_n} \approx 2.5 \times 10^{15} \left[\frac{T^{3/2}}{n_{i^+}} \right] e^{-\phi_i/kT} \dots\dots\dots(1.1)$$

The degree of ionization of plasma is the ratio of the number of positive ions to the total number of ions and neutrals. It is expressed by,

$$\text{Degree of ionization (\%)} = \frac{n_i^+}{n_i^+ + n_n} \times 100 \% \dots\dots\dots(1.2)$$

where n_i^+ , n_n are the positive ion and neutral densities (cm^{-3}) respectively, T is the plasma temperature (K), k is the Boltzmann's constant, and ϕ_i is the ionization energy of the ion (eV). When percentage of ionization is greater than 10%, the plasma is known as fully ionized.

The density of the free electrons in a plasma is called the *electron density* (n_e) or simply *plasma density*. If Z is the average ionization of the plasma, then the electron density is related to the ion density (n_i^+) as $n_e = Z n_i^+$. For plasma with only singly charged ions, $n_e = n_i^+$.

b) Plasma temperature (T_e , T_i)

Electrons and ions in the plasma follow Maxwellian distribution of velocities, independent of each other, with their own characteristic temperature T_e , and T_i respectively. When there is a thermal equilibrium between electrons and ions, one has $T_e = T_i$. When ions and electrons are not in equilibrium with each other, the electron temperature T_e is generally taken as the plasma temperature. The ion / electron temperature gives the randomness of the velocities of the ions / electrons in the plasma and is related to the width of the Maxwellian distribution.

c) Debye length (λ_d)

When an external electric field is introduced into the plasma, the ions and electrons move out to cancel the field. They form a layer, a sheath, within which the electric field is attenuated almost to zero so that the ions / electrons outside the sheath do not feel the electric field. Thus, the electric field is screened by plasma species and cannot be felt over a distance

greater than a characteristic screening distance known as *Debye length* (λ_d), which depends on plasma parameters as,

$$\lambda_d(\text{cm}) = 743 \sqrt{\frac{T_e}{n_e}} \dots\dots\dots(1.3)$$

where T_e is the electron temperature (eV), and n_e is the electron density (cm^{-3}). The electric field within the plasma can be sensed only within a sphere of radius λ_d .

d) Plasma frequency (ω_{pe})

As mentioned earlier, plasma is quasi-neutral macroscopically. When a plasma is disturbed from the equilibrium condition, the resulting internal space charge fields (due to the Coulomb forces) rearrange themselves collectively so as to maintain original charge neutrality. Ions being massive, can be considered to be stationary. This collective motion of the electrons for maintaining neutrality of the plasma takes place at the natural frequency of the plasma, known as *plasma frequency*. One can understand these oscillations as follows : If the electrons in the plasma are displaced from a uniform background of ions, electric field will be built up in such a direction so as to restore the neutrality of plasma by pulling the electrons back to their original positions. Due to their inertia, the electrons will overshoot and oscillate around their equilibrium positions with a characteristic frequency known as the *plasma frequency*. This plasma frequency (ω_{pe}) is given by,

$$\omega_{pe}(\text{radian/s}) = \sqrt{\frac{e^2 n_e}{m_e \epsilon_0}} \dots\dots\dots(1.4)$$

where e is the electron charge (1.6×10^{-19} C), n_e is the electron density, m_e is the mass of an electron (9.1×10^{-31} kg), and ϵ_0 is the permittivity constant (8.85×10^{-12} F/m). This equation shows that electron plasma frequency depends only on the electron density and is given by,

$$f_{pe}(\text{Hz}) = 8980 \sqrt{n_e} \dots\dots\dots(1.5)$$

where n_e is the electron density (cm^{-3}).

The ions being massive also oscillate at a very low frequency called ion plasma frequency, which is given by,

$$f_{pi}(\text{Hz}) = 210q\sqrt{\frac{n_i}{A}} \dots\dots\dots(1.6)$$

where, n_i is the ion density (cm^{-3}), A is the ion mass (a.m.u), and q is the charge state of the ions.

e) Cut-off frequency (ω_c) / density (n_c)

For propagation of an electromagnetic radiation in plasma, the plasma refractive index is given by $n = [1 - (\omega_{pe}/\omega_{rf})^2]^{1/2}$, where ω_{rf} is the frequency of the electromagnetic radiation. An electromagnetic wave will propagate in plasma only so long as the refractive index is real i.e. $\omega_{pe} < \omega_{rf}$. Beyond this frequency, the plasma becomes opaque. This frequency is known as the *cut-off frequency* and the corresponding density is called *cut-off density* (n_c).

For a microwave frequency of 2.45 GHz, the cut-off density is determined to be $n_c = 7.46 \times 10^{10} \text{ cm}^{-3}$.

f) Plasma potential (ϕ_p)

When plasma particles (contained in the plasma chamber) collide with the wall of the plasma chamber, the electron flux that intercepts is higher than the ion flux because of the much higher mobility of electrons than ions. The velocity of an electron is larger than that of an ion by the ratio of the square root of their masses. Thus, the electron current hitting the wall is much larger than the ion current, making a negative potential sheath due to electrons near the chamber walls. This leads to the plasma being at a positive potential relative to the wall of the plasma chamber. This potential is known as the *plasma potential*.

g) Confinement / Ionization time (τ)

The time scale for which the charged particle remains ionized is known as the *ionization time*. The ionization to a given charge state is possible if ions stay within the discharge for a time interval (*confinement time*) at least equal to the ionization time τ_q^i . This essentially means that the ion confinement time τ must be at least equal to ionization time τ_q^i i.e. τ . For multiple ionization,

$$n\tau = \left[\sqrt{\frac{kT_e}{m_e}} \right]^{-1} \sum [\sigma_{q-1,q}] \dots \dots \dots (1.7)$$

Few cases of ionization are shown in Table 1.1.

$n\tau$ (s-cm ⁻³)	T_e (eV)	Charge State
Any	< 10	No high Z-ions
10 ⁸	< 100	Only low Z-ions
10 ¹⁰	< 5000	Totally stripped light ions
~10 ¹²	< 20,000	Totally stripped heavy ions

Table 1.1 : Few cases of ionization.

In a Penning or Duoplasmatron ion source, the electron density is high (10¹³ to 10¹⁴ cm⁻³), but the confinement time is poor (~ 1 μ s) with electron temperature less than 100 eV. Hence such sources are not suitable to produce high Z-ions.

h) Ionization cross-section (σ)

The ionization cross-section (σ) gives an effective area of interaction between the colliding particles. It is an important quantity in any collision process. The ion current density (J_i) and electron impact ionization cross-section for ion (σ_e^i) are related as,

$$J_i = \sigma_e^i J_e n_n l \dots \dots \dots (1.8)$$

where J_e is the electron current density, n_n is the neutral density, and l is the length of the beam. Ionization cross-section depends on the energy of the electrons and on the charge state

of the ions. The probability of ionization by electron impact varies with the incident electron impact energy. When electron impact energy is less than the ionization potential, there is no ionization. There is a sharp threshold when electron impact energy is equal to the ionization potential. After this, it increases with energy and peaks at about three times the ionization potential. At higher energies, the cross-section falls slowly. In short, the cross-section starts from zero at the ionizing electron energy equal to the ionization potential and has a maximum at around 2 to 3 times the first ionization potential.

In electrical discharges, where some of the atoms may be in various excited states, ionization is possible even if the electron impact energy is less than ionization potential. For example, hydrogen atom having ionization potential 13.6 eV can be ionized at 10.2 eV, 11.84 eV etc. Helium having ionization potential 24.6 eV can be ionized at 19.82 to 22.72 eV. The variations of first ionization cross-section as a function of energy of the ionizing electrons are shown in Fig. 1.1 [4]. This figure represents the first ionization cross-section by electron impact for H, H₂, He, N₂ and O₂ as a function of ionizing energy.

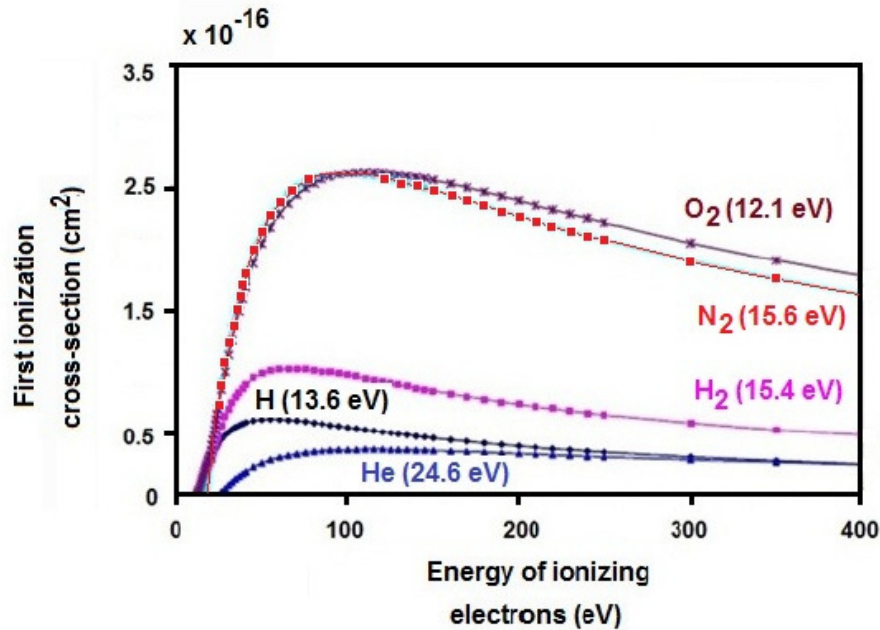


Figure 1.1 : The variations of the first ionization cross-section as a function of the energy of the ionizing electrons.

i) Typical condition of the plasma

Plasma can be practically defined as a quasi-neutral ensemble of charged particles that exhibits collective behaviour when exposed to external electromagnetic fields. It is to be noted that plasma also exhibits collective behaviour via long-range Coulomb interaction. Although plasma is called the *fourth state of matter* after solid-liquid-gas, there is no well-defined phase transition point from the gaseous state to plasma state. A solid can also exhibit plasma behaviour. An ionized gas can be considered as plasma, if the following conditions are fulfilled,

1) The typical length scale (dimensions) L of plasma has to exceed the shielding length λ_d (Debye length) of the plasma. The Debye length determines how far the charge imbalance due to thermal motions in the equilibrium state or the impact of an external electric potential can extend in plasma or in ionized medium. The condition is given as, $L \gg \lambda_d$. If this condition is not valid, the plasma is not necessarily macroscopically neutral.

2) In order to have collective behaviour, the number of particles inside the Debye sphere must be sufficient, $n_e \lambda_d^3 \gg 1$.

3) The plasma collective oscillation frequency ν_{pe} must be greater than the collision frequency of an electron and neutrals ν_{en} , i.e. $\nu_{pe} > \nu_{en}$.

If the above conditions are not satisfied, then there are no collective phenomena possible and the dynamics of the system is dominated by the motion of neutrals. These conditions are better fulfilled as the degree of ionization of the plasma increases.

1.2 Motion of electrons in static electric and magnetic fields

There are various possibilities of having a combination of static electric and magnetic fields. In this sub-section, we will investigate some cases which are relevant to an ECR source.

Case 1 : Electric field $\vec{E} = 0$, and magnetic field $\vec{B} = \text{constant}$

Consider a case when there is no electric field ($\vec{E} = 0$) and the uniform magnetic field ($\vec{B} = \text{constant}$) is directed along the Z-axis. The solution of the equation shows that if the particle velocity has only X and Y components and Z component is zero ($V_z = 0$), then particle start gyrating around Z-axis with an angular velocity known as the *cyclotron frequency* of an electron (ω_{ce}), defined as,

$$\omega_{ce} = \left[\frac{eB}{m_e} \right] \dots\dots\dots(1.9)$$

The radius of this circular path known as radius of gyration (also called as *Larmour radius* for an electron : r_{Le}). It is given by,

$$r_{Le} (\text{mm}) = \left[\frac{m_e V_{\perp}}{eB} \right] = 33.7 \left[\frac{\sqrt{E_e (\text{eV})}}{B(\text{G})} \right] \dots\dots\dots(1.10)$$

where $V_{\perp} = \sqrt{(V_x^2 + V_y^2)}$ is velocity component perpendicular to the Z-axis. If velocity component along Z-axis is non-zero ($V_z \neq 0$), the particle also moves along the Z-axis with constant velocity equal to the Z component of particle velocity (V_z) and it also gyrates about the Z-axis. The cyclotron motion of electron in a static magnetic field is shown in Fig. 1.2. The electron moves in a helical path in a region of constant magnetic field.

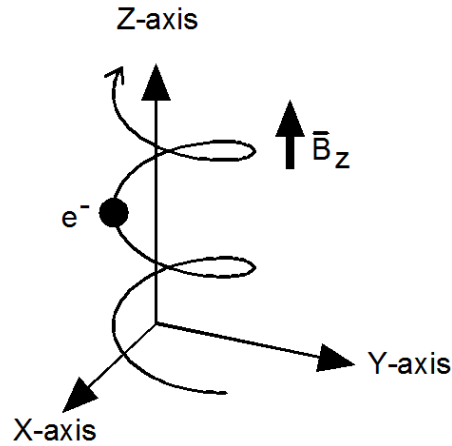


Figure 1.2 : The cyclotron motion of electron in a static magnetic field.

The ions (with opposite charge) also gyrate in the opposite sense in a helix of much smaller radius (being massive). The Larmour radius for ions (r_{Li}) is given by,

$$r_{Li} \text{ (mm)} = \left[\frac{m_i V_{\perp}}{qAB} \right] = 1440 \left[\frac{\sqrt{AE_e} \text{ (eV)}}{ZB(G)} \right] \dots\dots\dots(1.11)$$

The Larmour radii (mm) for electrons and ions in an ECRIS plasma for $B = 875 \text{ G}$ are shown in Table 1.2.

Particles	Particle Energy								
	1 eV	10 eV	20 eV	40 eV	80 eV	100 eV	1 keV	10 keV	100 keV
Electron	0.04	0.12	0.17	0.24	0.34	0.39	1.22	3.85	12.18
1 H⁺	1.65	5.20	7.36	10.41	14.72	16.46	52.04	164.57	520.42
14 N⁺	6.16	19.47	27.54	38.94	55.08	61.58	194.72	615.77	1947.24
40 Ar⁺	10.41	32.91	46.55	65.83	93.10	104.08	329.14	1040.84	3291.43

Table 1.2 : The Larmour radii (mm) for electrons and ions in ECRIS plasma ($B = 875 \text{ G}$).

The cyclotron frequency for electrons is given by,

$$f_{ce}(\text{MHz}) = \left[\frac{\omega_{ce}}{2\pi} \right] = 2.8B \dots\dots\dots(1.12)$$

The cyclotron frequency for ions is given by,

$$f_{ci} \text{ (MHz)} = f_{ci}(\text{MHz}) = \left[\frac{\omega_{ci}}{2\pi} \right] = 1.52 \times 10^3 \left[\frac{qB}{A} \right] \dots\dots\dots(1.13)$$

where q is the charge state of the ion, A is the mass of the ion (a.m.u.), Z is the atomic number, and B is the magnetic field (G). The ECR resonance magnetic field (B_{ecr}) values for different frequencies and electron energies are shown in Table 1.3.

Frequency (GHz)	B_{ecr} (T) 0 keV	B_{ecr} (T) 1 keV	B_{ecr} (T) 10 keV	B_{ecr} (T) 100 keV	B_{ecr} (T) 1 MeV
2.45	0.088	0.088	0.089	0.105	0.259
6.4	0.23	0.23	0.23	0.27	0.68
8.0	0.29	0.29	0.29	0.34	0.84
10.0	0.36	0.36	0.36	0.43	1.06
14.0	0.50	0.50	0.51	0.60	1.48

Table 1.3 : The ECR resonance magnetic field (B_{ecr}) values for different frequencies and electron energies.

Magnetic moment of the gyrating charged particle : When a charged particle is gyrating around Z-axis, it is equivalent to a current loop in the XY-plane. This has a magnetic moment μ , given by,

$$\mu = IA = \left[-\frac{e\omega_{ce}}{2\pi} \right] [\pi r_{Le}^2] = \left[\frac{W}{B} \right] \dots\dots\dots(1.14)$$

where I is the equivalent current, A is the area of loop (πr_{Le}^2).

The kinetic energy (W) of rotation of the charged particle ($\frac{1}{2} m V_{\perp}^2$) in the XY-plane is, given by,

$$W = \left[\frac{1}{2} m(V_x^2 + V_y^2) \right] = \mu \cdot \vec{B} = \mu B \dots\dots\dots(1.15)$$

where V_x is the component of velocity of the charged particle along the X-axis, and V_y is the component of velocity of the charged particle along the Y-axis. This quantity, averaged over a gyro-period, is a constant of motion in the case of a slowly varying magnetic field.

Case 2 : Electric field $\vec{E} = \text{constant}$, and magnetic field $\vec{B} = \text{constant}$

Let the magnetic field \vec{B} be along Z-axis, then, a) the component of the electric field \vec{E} along the magnetic field \vec{B} produces an *acceleration* along the Z-direction, and b) the component of the electric field perpendicular to the magnetic field \vec{B} produces a *drift velocity* \vec{V}_{drift} that is perpendicular to both the magnetic field \vec{B} and the electric field \vec{E} , and is given by,

$$\vec{V}_{\text{drift}} = \left[\frac{\vec{E} \times \vec{B}}{B^2} \right] \dots \dots \dots (1.16)$$

The $\vec{E} \times \vec{B}$ drift motion of the electron is shown in Fig. 1.3.

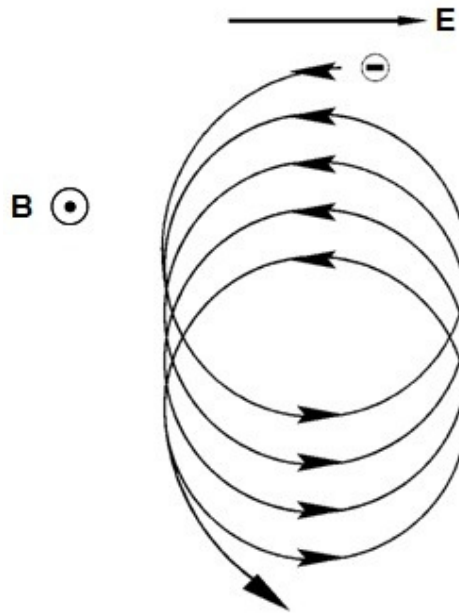


Figure 1.3 : The $\vec{E} \times \vec{B}$ drift motion of the electron.

Case 3 : Electric field $\vec{E} = 0$, and magnetic field B (spatially varying)

In a spatially varying magnetic field, (i.e. magnetic field changes with distance) there is one more drift called *gradient drift*. The velocity gradient \vec{V}_{grad} because of magnetic field gradient $\nabla \vec{B}$ is given by,

$$\vec{V}_{\text{grad}} = \left[\frac{W}{e} \right] \left[\frac{\vec{B} \times \nabla B}{B^3} \right] \dots\dots\dots(1.17)$$

The ∇B drift motion of a positive ion is shown in Fig. 1.4.

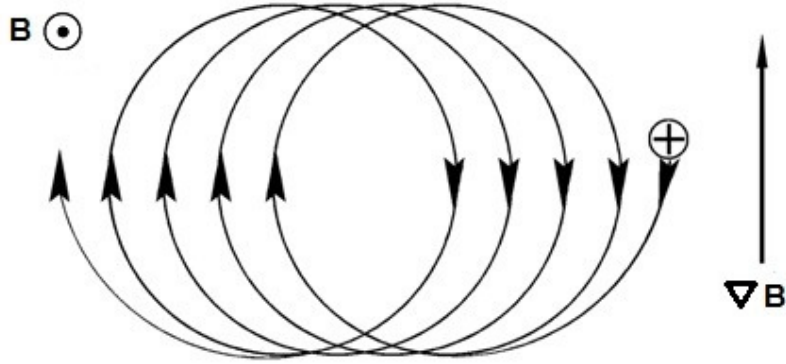


Figure 1.4 : The ∇B drift motion of a positive ion.

1.3 Waves in Magnetized Plasma

Plasma frequency plays a very important role in the behavior of the ECRIS's. As seen earlier, in non-magnetized plasma, electromagnetic waves of frequency higher than the critical frequency can propagate into the plasma, while waves at lower frequencies are reflected from the plasma boundary. The electromagnetic wave propagation in magnetized plasma has been described in this section [2,5,6].

a) High frequency electromagnetic waves in plasma in a magnetic field

In a magnetized plasma, it is reasonable to divide the electromagnetic waves into two cases : 1) waves propagating parallel to the external magnetic field \vec{B}_0 , $\vec{k} \parallel \vec{B}_0$, and 2) waves propagating perpendicular to the external magnetic field \vec{B}_0 , $\vec{k} \perp \vec{B}_0$. Here, $k = 2\pi / \lambda$ is the wave number which describes the direction of the wave propagation, and λ is the free space wavelength. The reflection and the resonance of the electromagnetic wave occur, when $\vec{k} \rightarrow 0$ and $\vec{k} \rightarrow \infty$, respectively.

The propagation of the electromagnetic wave in the plasma can be described by the equation,

$$m_e \left[\frac{d\vec{V}}{dt} \right] = -e [\vec{E} + \vec{V} \times \vec{B}_0] \dots \dots \dots (1.18)$$

and in terms of the Maxwell wave equation as,

$$k^2 \vec{E} - \vec{k} [\vec{k} \cdot \vec{E}] = \left[\frac{\omega_{rf}^2}{c^2} \right] \left[\vec{E} + i \frac{\vec{J}_e}{\epsilon_0 \omega_{rf}} \right] \dots \dots \dots (1.19)$$

where m_e is the mass of an electron, \vec{E} is the electric field, \vec{B}_0 is the external magnetic field, \vec{V} is the velocity of the charged particle, c is the velocity of light, ϵ_0 is the permittivity constant, ω_{rf} is the microwave frequency, $\vec{J}_e = -n_e e \vec{V}$, and n_e is the electron density. The electromagnetic wave is assumed to propagate perfectly perpendicular or parallel to the external magnetic field \vec{B}_0 , which is assumed to be parallel to the Z-axis.

Case 1 : Electromagnetic wave in the direction of external magnetic field

This case corresponds to *Electron cyclotron resonance (ECR)*

In this case, $\vec{k} \parallel \vec{B}_0$ i.e. we are considering the propagation of an electromagnetic wave parallel to the external magnetic field (\vec{B}_0). One can represent a plane polarized electromagnetic wave as a superposition of two circularly polarized waves. When these waves are propagating along the direction of the magnetic field, they see different refractive indices (for the left and right circular polarizations), which are given by,

$$n^2 = \left[\frac{c^2 k^2}{\omega_{rf}^2} \right] = 1 + \left[\frac{\omega_{pe}^2 (\omega_{rf} \mp \omega_{ce})}{\omega_{rf} (\omega_{ce}^2 - \omega_{rf}^2)} \right] = 1 - \left[\frac{\omega_{pe}^2}{\omega_{rf} (\omega_{rf} \pm \omega_{ce})} \right] \dots \dots \dots (1.20)$$

where ω_{pe} is the plasma frequency, ω_{ce} is the cyclotron frequency, and ω_{rf} is the frequency of the electromagnetic wave (in this case an RF wave), n is the index of refraction, and c is the velocity of light. The + sign represents the left hand polarized wave (L-wave), and the - sign

represents the right hand polarized wave (R-wave). The right hand polarized wave (R-wave) propagating in the magnetized plasma is shown in Fig. 1.5.

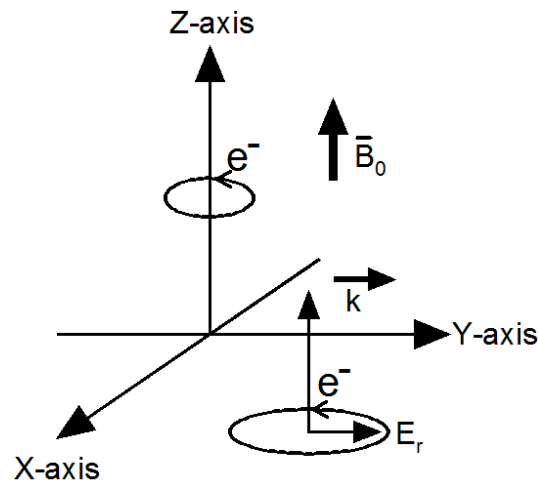


Figure 1.5 : The right hand polarized wave (R-wave) propagating in the magnetized plasma.

For the R-wave has a resonance (refraction index or $\bar{k} \rightarrow \infty$) with the cyclotron motion of the electrons at $\omega_{rf} = \omega_{ce}$. The L wave does not have any resonance. At resonance, the R-wave loses its energy to the plasma electrons, which in turn, further ionize the plasma. This is exactly the way ionization is caused in the ECRIS : the electrons resonantly gyrating around the magnetic field due to the external RF field (neglecting the ions response to the electromagnetic field because of their high inertia) collide with the gas atoms and ionize them to form plasma.

Case 2 : Electromagnetic wave perpendicular to the direction of the external magnetic field

This case corresponds to **Upper hybrid resonance (UHR)**

In this case, $\bar{k} \perp \bar{B}_0$, i.e. we are considering the propagation of the electromagnetic wave to the external magnetic field (\bar{B}_0). These electromagnetic waves can be divided in two classes : “Ordinary” (O-wave) and “eXtraordinary” (X-wave) waves. For the X-wave, the direction of the wave’s magnetic field is chosen to be parallel to the Z-axis (i.e. wave is

polarized in the Y direction) and the direction of the propagation of the electromagnetic wave is chosen to be parallel to the X-axis, i.e. perpendicular to the external magnetic field. For the O-wave, the polarization is along the Z-axis. For this wave, the electron oscillating in the electric field of the electromagnetic wave will oscillate in the direction of the external magnetic field and will not have any Lorentz force ($\mathbf{v} \times \mathbf{B}$) acting on it. So this wave will propagate as if it is propagating in unmagnetized plasma i.e. it will not undergo any resonance. However, for the X-wave, the motion of the electrons oscillating in the electromagnetic field will be in the Y direction, which is perpendicular to the direction of the external field and hence it will undergo cyclotron resonance. Hence only the X-wave has a resonance with the cyclotron motion of the electrons. The extraordinary wave propagating in the magnetized plasma is shown in Fig. 1.6.

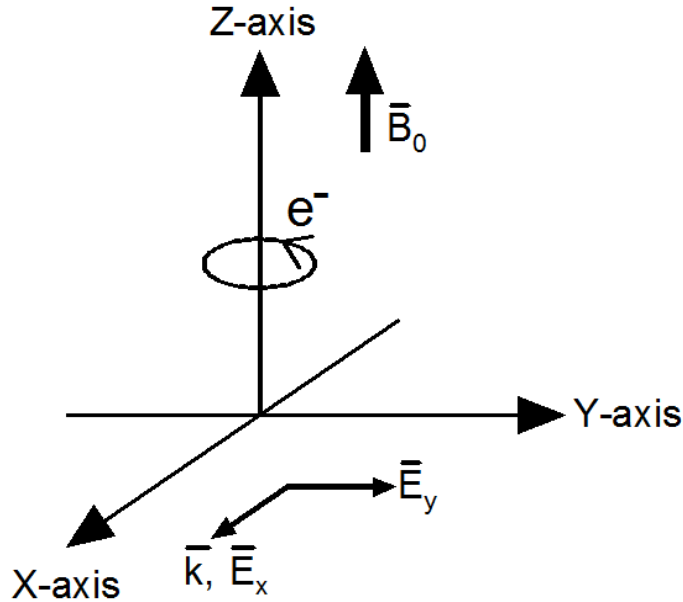


Figure 1.6 : The extraordinary wave propagating in the magnetized plasma.

For the X-wave, the index of refraction n , is given by,

$$n^2 = \left[\frac{c^2 k^2}{\omega_{rf}^2} \right] = 1 - \left[\frac{\omega_{pe}^2 (\omega_{rf}^2 - \omega_{pe}^2)}{\omega_{rf}^2 (\omega_{rf}^2 - \omega_h^2)} \right] \dots\dots\dots(1.21)$$

The “upper-hybrid” frequency ω_h is defined as,

$$\omega_h^2 \approx \omega_{pe}^2 + \omega_{ce}^2 \dots\dots\dots(1.22)$$

The *upper hybrid resonance* (UHR) occurs when the condition $\omega_{rf} = \omega_h$ is fulfilled. It has been assumed that UHR dominates ECR heating when $[\omega_{pe}^2 / \omega_{rf}^2] \geq 0.1$ [7]. This means that the electron density of the plasma n_e has to exceed the value of one tenth of the cut-off density n_c of the plasma. At this point, the strength of the magnetic field has to be higher than ECR resonance in order to have the UHR.

From the above cases, it is clear that, only the X-wave and R-wave have a resonance with the electrons in the magnetized plasma. In the case of R-wave, heating of electrons takes place at the ECR. The X-wave penetrates through the ECR surface without seeing it. In this case, heating takes place at the UHR resonance. Due to the resonance (ECR or UHR) with microwave, electrons get heated up and acquire the energy necessary to produce highly charged ions. In summary, we have four different waves in magnetized plasma called : O-wave, X-wave, R-wave, and L-wave [2]. The cut-off and resonance conditions for the waves propagating inside the plasmas are shown in Table 1.4. The L-wave and the O-wave do not

Vectors Orientation	Refraction Index	Wave Type
$\vec{B}_0 = 0$	$\omega_{rf}^2 = \omega_{pe}^2 + k^2 c^2$	Light wave
$\vec{k} \perp \vec{B}_0, \vec{E} \parallel \vec{B}_0$	$\frac{c^2 k^2}{\omega_{rf}^2} = 1 - \frac{\omega_{pe}^2}{\omega_{rf}^2}$	O-wave
$\vec{k} \perp \vec{B}_0, \vec{E} \perp \vec{B}_0$	$\frac{c^2 k^2}{\omega_{rf}^2} = 1 - \left(\frac{\omega_{pe}^2}{\omega_{rf}^2} \right) \left[\frac{(\omega_{rf}^2 - \omega_{pe}^2)}{(\omega_{rf}^2 - \omega_h^2)} \right]$	X-wave
$\vec{k} \parallel \vec{B}_0$	$\frac{c^2 k^2}{\omega_{rf}^2} = 1 - \frac{\omega_{pe}^2}{\omega_{rf}(\omega_{rf} - \omega_{ce})}$	R-wave
$\vec{k} \parallel \vec{B}_0$	$\frac{c^2 k^2}{\omega_{rf}^2} = 1 - \frac{\omega_{pe}^2}{\omega_{rf}(\omega_{rf} + \omega_{ce})}$	L-wave

Table 1.4 : The cut-off and resonance conditions for the waves propagating inside the plasmas.

show any resonance. Instead, they suffer a cut-off that can be determined from the respective equations, when the index of refraction becomes zero. The cut-off and resonance for the four waves is shown in Fig. 1.7, which is well known as the “Clemmov-Mullaly-Allis diagram”.

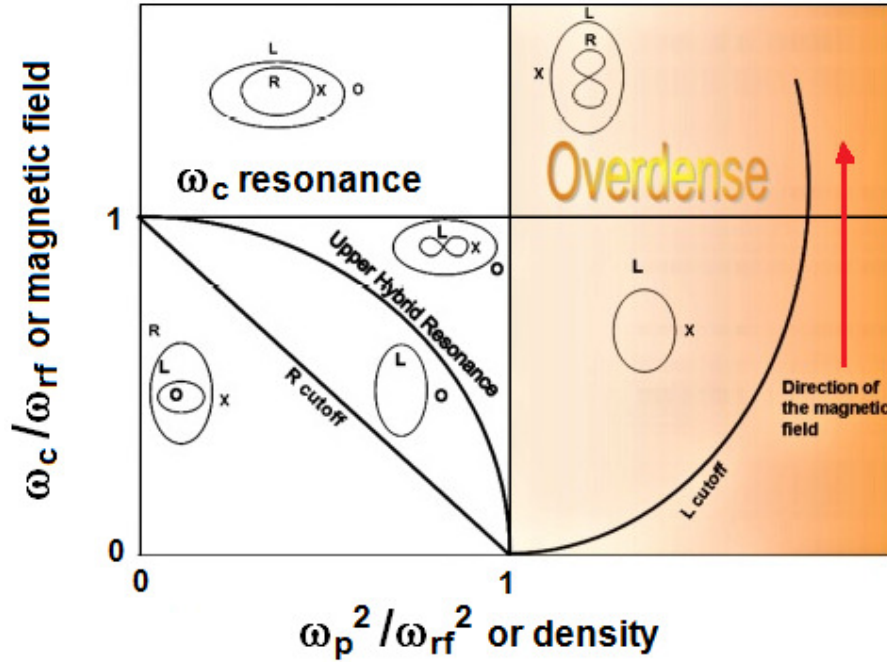


Figure 1.7 : The cut-off and resonance of O-, X-, R-, and L-wave (Clemmov-Mullaly-Allis diagram).

1.4 Magnetic trap and confinement of plasma

The charge state of the ion increases with increasing the ion confinement time. We have seen earlier that an electron travelling perpendicular to a magnetic field will gyrate around the lines of force of the magnetic field. However, those travelling along the magnetic field are unaffected by the magnetic field. So if one uses a magnetic field to confine the plasma, it will leak along the magnetic field. To prevent this leakage, one has to use magnetic mirrors on both sides. The concept of *magnetic mirror* can be understood as follows.

The component of velocity parallel to the magnetic field (V_{\parallel}) of a charged particle will vary when it moves into regions of different magnetic field strengths of the magnetic field according to invariance of the kinetic energy E_k ,

$$\left[\frac{mV_{\parallel}^2}{2} \right] = E_k - \mu B \dots\dots\dots(1.23)$$

where E_k is the kinetic energy of the charged particle and magnetic moment μ is,

$$\mu = \frac{1}{2} \left[\frac{mV_{\perp}^2}{B} \right] \dots\dots\dots(1.24)$$

where V_{\perp} is the component of velocity perpendicular to the magnetic field. Since magnetic moment μ is constant, the parallel velocity of the particle V_{\parallel} decreases with increasing magnetic field B . If magnetic field B is sufficiently high, the parallel velocity component of the particle becomes zero ($V_{\parallel} = 0$) and the particle is reflected back toward the decreasing magnetic field (i.e. weak magnetic field region). Thus, the high magnetic field region acts as a mirror. If one has two such mirrors on either side of the plasma (called *magnetic bottle*), the plasma particles (ions / electrons) will remain trapped inside the magnetic bottle (between the two magnetic mirrors).

The trapping of the charged particle takes place when the magnetic moment of the charged particle become greater than the ratio of kinetic energy of the particle to the maximum magnetic field, i.e. $\mu > [E_k / B_{\max}]$. Plasma trapped between magnetic mirrors created by a pair of solenoid coils is shown in Fig. 1.8. This figure shows that the charged particles are trapped between the two magnetic field minima. This confinement supports the production of the highly charged state ion beams.

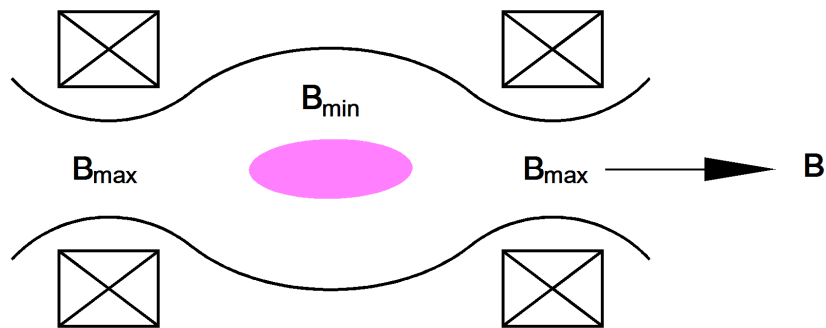


Figure 1.8 : Plasma trapped between magnetic mirrors created by a pair of solenoid coil.

We now go into some more details of the magnetic mirror to understand the concept of *loss cone*. The electron trajectories in a homogeneous and in an increasing magnetic field are shown in Fig. 1.9 and Fig. 1.10 respectively. These figures demonstrate the charged particle motion under the influence of homogeneous and increasing magnetic field configurations.

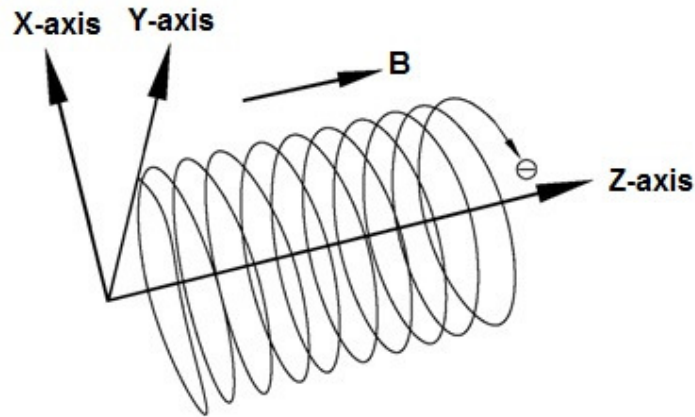


Figure 1.9 : Electron trajectory in a homogeneous magnetic field.

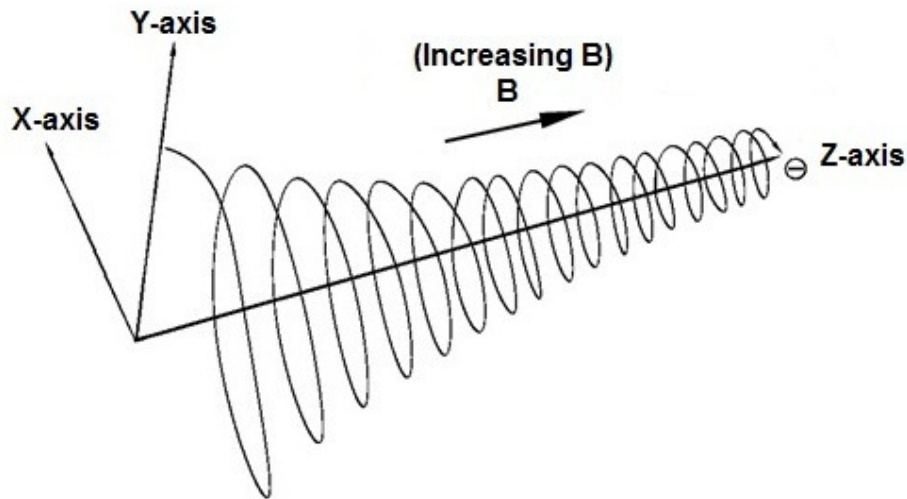


Figure 1.10 : Electron trajectory in an increasing magnetic field.

The loss cone defines the fraction of the charged particles, which are able to escape through the magnetic bottle at a given magnetic field. If V_0 is the initial velocity of the

particle and components of its velocity are denoted by $V_{\perp} = V_{\perp 0}$ and $V_{\parallel} = V_{\parallel 0}$, then invariance of the magnetic moment μ yields,

$$\frac{1}{2} \left[\frac{mV_{\perp 0}^2}{B_{\min}} \right] = \frac{1}{2} \left[\frac{mV_{\perp}^2}{B'} \right] \dots\dots\dots(1.25)$$

where B' is the magnetic field at the turning point. Using conservation of energy one gets,

$$\frac{B_{\min}}{B'} = \frac{V_{\perp 0}^2}{V_{\perp}^2} = \frac{V_{\perp 0}^2}{V_0^2} = \sin^2 \theta \dots\dots\dots(1.26)$$

Replacing B' by B_{\max} in equation (1.26) the minimum angle θ_{\min} of a confined particle can be found. The velocity space loss cone in a magnetic mirror is shown in Fig. 1.11. The magnetic loss cone is independent of the charge and mass of the particles. In ECRIS, the axial confinement is obtained using solenoids and the radial confinement using multi-pole magnets. In any practical case, the particles change their direction of velocity due to collisions with each other and can escape from the plasma. When the temperature of the ions and electrons are equal, i.e. $T_i \approx T_e$, the higher collision frequency of the electrons leads to a higher loss rate of electrons from the plasma. As a consequence, a positive electric charge will build up in the plasma that regulates the loss of low energy electrons.

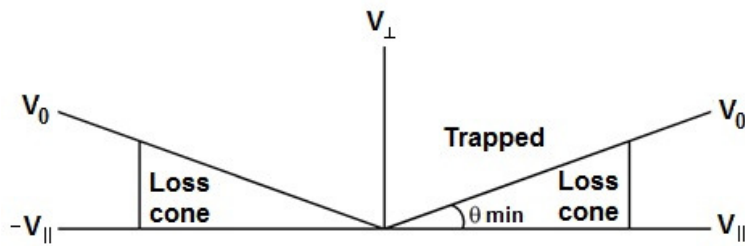


Figure 1.11 : The velocity space loss cone in a magnetic mirror.

In ECRIS, the heated electrons have orders of magnitude higher temperature than the ions, i.e. $T_e \gg T_i$ [8,9]. As a consequence, the electrons have a much smaller probability to collide with the other species. The relatively higher rate of ion loss creates the negative plasma voltage, which regulates the loss of ions. This electrostatic potential well confines the

positively charged ions inside the ECR plasma. The height of the potential well can be increased by increasing the temperature of the electrons or the mirror ratio. Considerable improvement of the ion intensities has been achieved using a strong magnetic field resulting in a high magnetic mirror ratio. Presently, all new ECRIS's are constructed with a high magnetic mirror ratio.

1.5 Ionization of Hydrogen

A singly charged positive ion can be formed if one electron, preferably from the outermost orbit of an atom (which needs minimum energy) is removed to the continuum. This process is known as single electron impact ionization process. The electron energy that has to be imparted to an atom in ground state must exceed the binding energy of the electron, which is called the *first ionization potential*. In order to doubly ionize, second electron has to be removed and the necessary energy should exceed the second ionization potential. As the degree of ionization increases, ionization potential also increases due to increasing attractive force of the nucleus. It is easier to produce singly charged ions, as the first ionization potential is smallest, while to produce highly stripped charged ions, it is much more difficult as the inner shell electrons are more tightly bound and therefore one needs higher electron energy of the order of several keV to tens of keV.

If n_n is the neutral density, and J_e is the electron current density then the rate of production of positive ions by electron impact (dn_i^+ / dt) is given by,

$$\frac{dn_i^+}{dt} = \sigma_e^i n_n J_e \dots\dots\dots(1.27)$$

where n_i^+ is the positive ion density, σ_e^i is the electron impact ionization cross-section for ion (energy dependent).

If l is the length of the beam then ion current density (J_i) at l is,

$$J_i = \frac{dn_i^+}{dt} l = \sigma_e^i n_n J_e l \dots\dots\dots(1.28)$$

If A is the area of the beam, and if all the ions produced in the effective volume (V) are able to leave it, the ion current (total) I_i from this volume is, given by,

$$I_i = A J_i = \frac{dn_i^+}{dt} A l = \sigma_e^i n_n J_e l A = \sigma_e^i n_n J_e V \dots\dots\dots(1.29)$$

The processes of ionization possible for hydrogen atom are shown in Table 1.5.

Process of Hydrogen Ionization								E _i (eV)	σ × 10 ⁻¹⁶ cm ²	Reaction
H ₂	+	e ⁻	→	H ₂ ⁺	+	2e ⁻		15.6	0.98	Direct Ionization
H ₂ ⁺	+	H ₂	→	H ₃ ⁺	+	H		~ 0		Dissociative Attachment
H ₂	+	e ⁻	→	2H	+	e ⁻		9.2	0.90	Dissociative Excitation
H	+	e ⁻	→	H ⁺	+	2e ⁻		13.6	0.70	Ionization
H ₂	+	e ⁻	→	H ₂ ⁺	+	2e ⁻		15.6	0.98	Direct Ionization
H ₂ ⁺	+	e ⁻	→	H ⁺	+	H	+ e ⁻	12.1	4.30	Dissociative Excitation
H ₂ ⁺	+	e ⁻	→	2H ⁺	+	2e ⁻		17.0		Dissociative Ionization

Table 1.5 : The process of ionization possible for hydrogen atom.

1.6 Production of Charged Ions

Ionization of atoms or molecules due to inelastic collision with atoms depends on the kinetic energy of the colliding particles. The energy required to ionization of neutral atom (E_i) is,

$$E_i(\text{atom}) > eV_i \dots\dots\dots(1.30)$$

where e is the electron charge, and V_i is the ionization potential of the atom. The ECRIS, in some applications, is used for the production of singly charged ion beams [10,11,12]. The ECRIS is also widely used for the production of multiply charged ion beams [13,14,15,16].

The atom present in the plasma undergoes step-by-step collisions with the electrons. The build-up of their charge state q is related to the plasma parameters as [17],

$$q \propto n_e \tau_q^i E_e \dots\dots\dots(1.31)$$

where n_e is the electron density, τ_q^i is the confinement time for a given charge state q in the plasma, and E_e is the energy of electron. The rate of the change of the ion density (dn_q/dt) in the ECR plasma at the charge state q is given by [17],

$$dn_q/dt = \underbrace{n_e \langle \sigma_{q-1,q} V_e \rangle n_{q-1} + n_n \langle \sigma_{q+1,q} V_i \rangle n_{q+1}}_{\text{creation}} - \underbrace{n_n \langle \sigma_{q,q-1} V_i \rangle n_q - n_e \langle \sigma_{q,q+1} V_e \rangle n_q}_{\text{destruction}} - \underbrace{n_q / \tau_q^i}_{\text{losses (ion extraction, wall...)}}$$

where

- n_n = Number density of neutrals
- n_q = Ion density in the q^{th} charge state
- n_{q+1} = Ion density in the $(q+1)^{\text{th}}$ charge state
- n_{q-1} = Ion density in the $(q-1)^{\text{th}}$ charge state
- $\sigma_{q-1,q}$ = Ionization cross-section from $(q-1)$ to q^{th} ionization state by electron impact
- $\sigma_{q,q-1}$ = Charge exchange cross-section between highly charged ions and neutrals
- $\sigma_{0,q+1}$ = Charge exchange cross-section by collision with neutrals
- $\sigma_{q,q+1}$ = Ionization cross-section from q to $(q+1)$ charge state by electron impact
- $\sigma_{q+1,q}$ = Charge exchange cross-section from $(q+1)$ to q^{th} by electron impact
- $\sigma_{0,q}$ = Charge exchange cross-section by collision with neutrals
- V_e, V_i = Velocities of electrons and q -ion respectively
- τ_q^i = Confinement time for a given charge state q^{th}

In the above equation, on the right hand side, the first two terms (in green bracket) are production rates of n_q ions from the charge state $(q-1)$ to the charge state q by the electron bombardment / impact and from the charge state $(q+1)$ to the charge state q by the charge exchange reaction. The next two terms (in red bracket) correspond to losses caused by the charge exchange reaction from the charge state q to the charge state $(q-1)$ and by the ionization from the charge state q to the charge state $(q+1)$. The last term gives the loss of ions at the charge state q to the ion diffusion to the wall due to finite confinement time. The ionization cross-section depends very strongly on the energy of the bombarding electrons E_e and on the charge state q^{th} to the target atom. The total ionization cross-section from $(q-1)$ to

q^{th} ionization state by electron impact can be calculated using the Lotz's formula and it is given by [18],

$$\sigma_{q-1,q} = \sum a_i q_i \left[\frac{\ln \frac{E_e}{P_i}}{E_e P_i} \right] \left\{ 1 - b_i \exp\left[-c_i \left(\frac{E_e}{P_i} - 1\right)\right] \right\} \dots \dots \dots (1.32)$$

where E_e is the electron impact energy, P_i is the binding energy of electrons in the sub-shell, q_i is the number of the electrons in the sub-shell and a_i , b_i and c_i are the constants. The total ionization cross-section ($\sigma_{q-1,q}$) of reaction depends strongly on the energy of the electron and binding energy of the electron, it is given by, $A_{q-1,q} + e^- \rightarrow A_q + 2 e^-$.

The ionization potential for various elements is shown in Table 1.6.

Element	Ionization Potential (eV)							
	I e ⁻	II e ⁻	III e ⁻	IV e ⁻	V e ⁻	VI e ⁻	VII e ⁻	VIII e ⁻
${}_1\text{H}^1$	13.6							
${}_2\text{He}^4$	24.5	54.5						
${}_3\text{Li}^7$	5.40	75.6	122.5					
${}_{10}\text{Ne}^{20}$	21.6	41.1	63.5	97.0	126.3	157.9		
${}_6\text{C}^{12}$	11.2	24.4	47.9	77.3	113.8	138.0		
${}_7\text{N}^{14}$	14.5	29.6	47.4	77.5	97.8	552.0		
${}_8\text{O}^{16}$	13.6	35.2	55.0	77.4	113.8	138.0		
${}_{18}\text{Ar}^{40}$	15.8	27.6	40.9	59.8	75.0	91.3	124.0	143.4
${}_{11}\text{Na}^{23}$	5.10	47.3	71.6	98.9	138.6	172.3		
${}_{36}\text{Kr}^{84}$	14.0	24.6	36.9	43.5	63.0	94.0		
${}_{54}\text{Xe}^{131}$	12.1	21.2	31.3	42.0	53.0	58.0	135.0	

Table 1.6 : The ionization potential for various elements.

The charge exchange cross-section is independent or only weakly dependent on the energy of the ions [19,20]. The charge exchange cross-section ($\sigma_{q,q-1}$) between highly charged ions and neutrals is dependent on the charge state of the ions, which is given by [21],

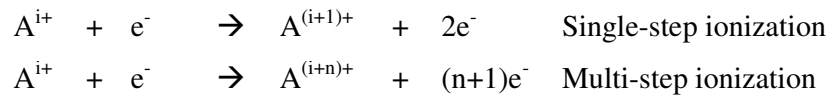
$$\sigma_{q, q-1} = \pi a_0^2 q Z^{1/3} \left[\frac{I_0}{I} \right]^{3/2} \dots\dots\dots(1.33)$$

where a_0 is the Bohr radius, I_0 is the Bohr energy (13.6 eV), I and Z are the ionization potential and atomic number of the target atom, respectively. The charge exchange cross-section is considerably larger than the ionization cross-section of highly charged ions. The possible processes of ionization of atoms are shown in Table 1.7.

Equations	Energy	Type of Process
$e^- + A \rightarrow A^{1+} + 2e^-$	$(eE_c > eV_i^{-1})$	First ionization
$e^- + A^+ \rightarrow A^{2+} + 2e^-$	$(eE_c > eV_i^{-2-1})$	Second ionization
$e^- + A^{(z-1)+} \rightarrow A^{z+} + 2e^-$	-----	Higher ionization
$h\nu + A \rightarrow A^+ + e^-$	$(h\nu > eV_i)$	Photo-ionization
$A^* + B^* \rightarrow A^+ + B + e^-$	Energy exchange	Ionization
$A + B \rightarrow A + B^+ + e^-$	$(E_B^i < E_A^{excite})$	Impact ionization
$A^+ + B \rightarrow B^+ + A$	Charge exchange	Ionization

Table 1.7 : *The possible processes of ionization of atoms.*

The electron bombardment ionization can result in the removal of more than one electron from an atom or ion provided the bombarding electrons have sufficient energy. There are two routes by which this can occur. In single-step ionization, the incident electron must have energy of at least the sum of all ionization potentials of the removed electrons i.e. state q to state $(q+n)$ whereas in multi-step ionization it required only the energy of each electron removed i.e. state n to state $(n+1)$. Following two processes can give rise to multi-step ionization,



The maximum charge state that can be attained is thus limited by the maximum incident electron energy. Hence multi-step ionization is indeed the only feasible route to high charge state ions. This process takes time, which depends on the electron density and the

ionization cross-section, and must be shorter than the ion lifetime in the plasma. The dependence of the ionization cross-section on electron energy means that the higher energies required to produce higher charge states is not useful for the production of low charged ions. However, in the ionization process there is nothing to prevent the removal of more than one electron provided that the incident electron energy is greater than the ionization potential for that charge state. However, in practice, the ionization cross-section for a certain charge state maximum for electrons incident with energy about three times the minimum ionization energy, and then decreases slowly with increasing energy of the bombarding electrons. The probability of producing multi-charged ions by single electron impact falls off rapidly with increased charge state. The only efficient way of achieving high charge states is by successive ionization, which is a time consuming process. Charge state distribution in hot plasma is mainly determined by the ionization cross-section (i.e. the energy of the electrons), the electron current density, and the exposure time of the ions to the plasma electrons. In general, the ionization time required to produce a given charge state, τ_q^i is given by [17],

$$\tau_q^i n_e \propto e \sum_{i=1}^q \frac{1}{\sigma_{i-1,i}} \dots\dots\dots(1.34)$$

where \propto is the proportional constant, e is the electron charge, n_e is the electron density, and $\sigma_{i-1,i}$ is the ionization cross-section from $(i-1)$ to i^{th} ionization state by electron impact. The loss processes working against efficient ion production are : electron capture from neutral background molecules, direct capture of plasma electrons, and losses to the walls.

CHAPTER 2

ECR Plasma as Ion Source : An Overview

This chapter deals with the operating principle of an ECR source and the major components which are required to build an ECRIS viz. microwave system, plasma chamber and vacuum system, electromagnet coils, and their power supplies, beam extraction electrodes, and plasma diagnostics device.

The ion beam sources have become an important tool for numerous scientific investigations in recent times such as heavy ion radiotherapy [22,23,24,25], radiobiology [26], radio oncology [27], surface science [28,29], nuclear transmutation studies [30], fusion studies [31], microprobe trace analysis [32], isotope separation [33], mass spectrometry [34], atomic physics and molecular physics [35,36,37], space propulsion [38], neutron spallation [39], obtaining metal ion beam [40], lithography [41], plasma based applications [42,43,44,45,46], micro-electro-mechanical systems [47], x-ray production [48,49,50,51,52] etc. Charged particles beams of different currents are required for different applications. The various types of ion sources have been developed based on the requirements. For example, ion beams of hundreds of amperes current are required for fusion applications, whereas beams of nano-amperes current are required for applications like microprobe trace analysis and thin film deposition. They include a) Filament based sources such as Freeman, Duoplasmatron, Penning and Magnetron, b) Microwave based sources such as electron cyclotron resonance ion sources (ECRIS) [6,53,54].

Among all these sources, ECRIS offers a number of advantages over other filament based ion sources. Firstly, the absence of filaments relieves ECRIS from the lifetime constraints of other filament based ion sources. Secondly, ECRIS consumes only neutral gases (for plasma production). Thirdly, the capability of working in a corrosive environment

gives ECRIS a leading edge over the other sources. The high performance reliability of ECRIS has now made it an integral part of the new age accelerators due to its salient features such as 1) operation in continuous wave or in pulsed mode, 2) high current, 3) low emittance, 4) high brightness, 5) high current stability, 6) multiple charge states ion beams, and 6) high reliability. The only drawback is that, one has to use a microwave window with the waveguide, and the lifetime of this window could be limited because of the electron bombardment and metal deposition on it. Now a days, it is common practice to use 90° waveguide bend to avoid electron bombardment and metal deposition on the window, so that the limited lifetime problem is overcome.

The ion sources used for the acceleration of charged particles are chosen according to their output beams, emittance, ion species, intensity and energy spread. With the continuous development of ECRIS, it has been observed that it is easy to operate at high voltage platform to obtain the high beam current of all kinds, low energy spread, low phase space area i.e. low emittance, long lifetime, uninterrupted operation, low maintenance, stable, suitable for covering wide mass range, and capability to produce high intensity beam than any conventional ion sources. The source is widely accepted by accelerator community worldwide as an injector to high energy proton and heavy ion accelerators. The well known ECRIS sources are CRL, SILHI, TRIPS, INFN, MIDAS, VIS, ALISES, and SPIRAL2. They can deliver more than 50-100 mA proton beam current at 50-100 keV beam energy with 80-90% of proton fraction and low emittance 0.2π mm mrad, being used as an injector to high energy proton and heavy ion accelerators [11,55,56,57,58,59,60,61,62,63,64,65,66]. The failure was only due to some high voltage spark after a long operation.

In India at Bhabha Atomic Research Centre (BARC) (50 keV, 50 mA) [67], Variable Energy Cyclotron Centre (VECC) (50 keV, 50 mA) [68], and Inter University Accelerator Centre (IUAC) (Superconducting PKDELIS) [69,70]. ECRIS has been commissioned for the

low energy high intensity proton accelerator (LEHIPA), Cyclotron injector, and superconducting linear accelerator (SC-LINAC) respectively for accelerator applications. RRCAT, Indore is planning to take up in a near future a project on research and development of high intensity proton accelerator for pulsed spallation neutron source. Spallation neutron source is a tool for condensed matter physics and material science research. A schematic layout of proposed 3 MeV front-end of H^- / H^+ proton linear accelerator at RRCAT, Indore is shown in Fig. 2.1. In this, one of the challenging tasks is to develop a highly reliable, stable, and compact, high current H^- ion source which will act as an injector, followed with low energy beam transport line (LEBT) to characterize and analyze the extracted beam parameters and a pre-chopper for matching the pulsed ion source beam parameters with the input port of radio frequency quadrupole (RFQ), for bunching and acceleration up to 3 MeV, as a front-end linear accelerator followed by a beam dump for the characterization of the ion beam viz. emittance, energy, energy spectra, bunch width and halo. In this direction, RRCAT has initiated development of a pulsed filament / radio frequency based multi-cusp H^- ion source (50 keV, 30 mA, repetition rate 25 Hz and pulse duration 0.5 ms) as a pre-injector. The electron cyclotron resonance ion source (RRCAT-ECRIS), (50 keV, 30 mA, H^+ continuous wave / pulsed mode) has been developed indigenously to use it as an alternative to the H^- ion source [71,72] as an injector. Keeping this in mind, we have designed and developed an ECRIS capable of generating proton beam with 30 mA current at 50 keV beam energy (RRCAT-ECRIS) at 2.45 GHz microwave frequency. The design specifications and present status of the RRCAT-ECRIS are given in Table 1.8.

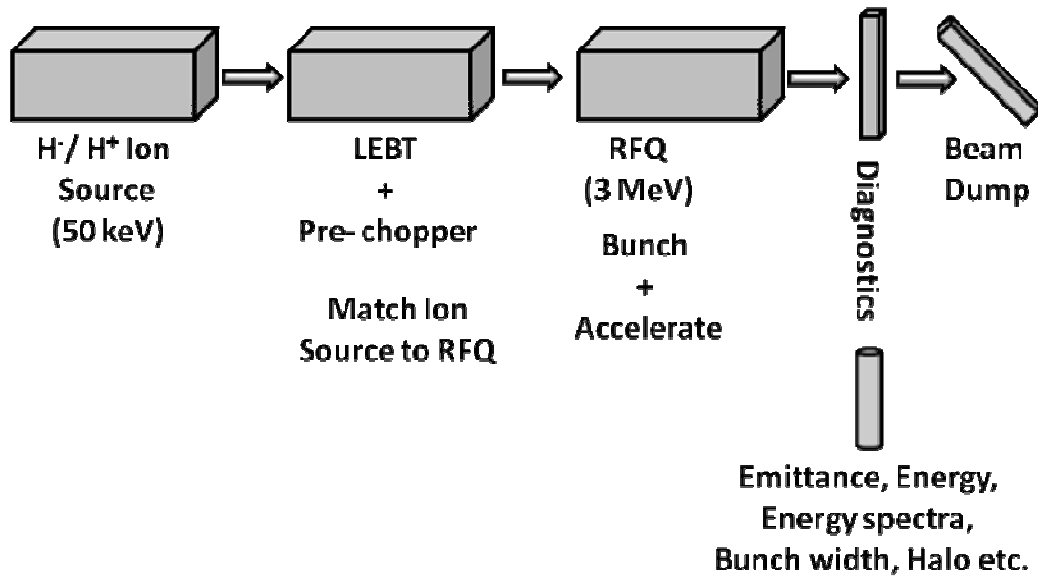


Figure 2.1 : A schematic layout of proposed 3 MeV front-end of H / H⁺ proton linear accelerator at RRCAT, Indore.

System Parameters	Phase-I		Phase-II
	Design Parameters	Present Status	Design Parameters
Beam energy	25 keV	24 keV	50 keV
Beam current	10 mA	8 mA	30 mA
Particles	H ⁺ , H ₂ ⁺ , H ₃ ⁺	H ⁺	H ⁺
Frequency	2.45 GHz	2.45 GHz	2.45 GHz
Microwave power	600 W (CW)	600 W (CW)	0 – 2 kW (CW)
Microwave feed	Waveguide	Waveguide	Ridged waveguide
Base pressure	~ 10 ⁻⁶ mbar	~ 10 ⁻⁶ mbar	~ 10 ⁻⁶ mbar
Axial magnetic field	875 – 1000 G	875 G	875 – 1000 G
Duty factor	100 % DC	100 % DC	100 % DC
Operating pressure	~ 10 ⁻⁴ mbar	~ 10 ⁻⁴ mbar	10 ⁻⁴ – 10 ⁻³ mbar
Gas	Hydrogen	Hydrogen	Hydrogen

Table 1.8 : The design specifications and present status of the RRCAT-ECRIS.

2.1 Operating Principle of an ECR Plasma Source

The operating principle of an ECR plasma source is shown in Fig. 2.2. In ECR plasma source, plasma is produced by matching the cyclotron frequency of an electron (ω_{ce}) in a external static magnetic field, with the microwave frequency (ω_{rf}), i.e. ECR condition ($\omega_{ce} \cong \omega_{rf}$) [6,53,54]. In the case of 2.45 GHz, the required field strength to satisfy the ECR condition is 875 G. The cyclotron frequency of an electron (ω_{ce}), is given by,

$$\omega_{ce} = \left[\frac{eB}{m_e} \right] \dots\dots\dots(2.1)$$

where e is the electron charge, B is the magnetic field, and m_e is the mass of an electron.

A small amount of free electrons is always present in the plasma chamber at room temperature. In a magnetic field of 875 G the cyclotron frequency of the electrons is 2.45 GHz. If a matched frequency of microwave at 2.45 GHz is fed into the plasma chamber, the electrons on the magnetic surface of 875 G will resonate with the microwave frequencies. Therefore, the electrons in the resonance zone will stochastically gain energy from the electric field of the microwave radiation. The gas of interest is fed into the plasma chamber. It gets ionized by the energetic electrons. The amount of free electrons increases instantly and a plasma confined by the external magnetic fields is created. The ECR plasma source can be considered to be composed of three entities : a microwave field, a magnetic field, and low-pressure ionized gas. The neutral gas like hydrogen is fed to the plasma chamber where singly charged ions are produced. The proton beam is extracted by applying the high voltage on the extraction electrodes. A high vacuum is required to minimize the charge exchange reaction between the ions and the neutral atoms. The beam is extracted towards a Faraday cup to measure its current.

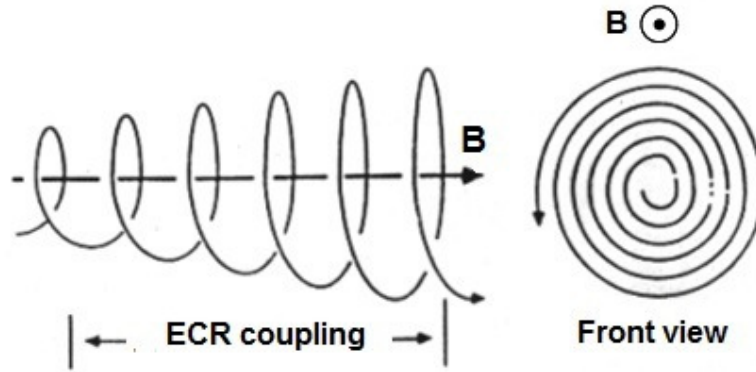


Figure 2.2 : The operating principle of an ECR plasma source.

As mentioned in the previous chapter, a linearly polarized electromagnetic wave is composed of an R-wave, and an L-wave (i.e. waves with right and left circular polarizations). An electron is accelerated along its orbit throughout the entire period of the R-wave field, while there is no energy gain from the L-wave field. A schematic representation of the acceleration-deceleration of electron under right and left hand polarized wave is shown in Fig. 2.3.

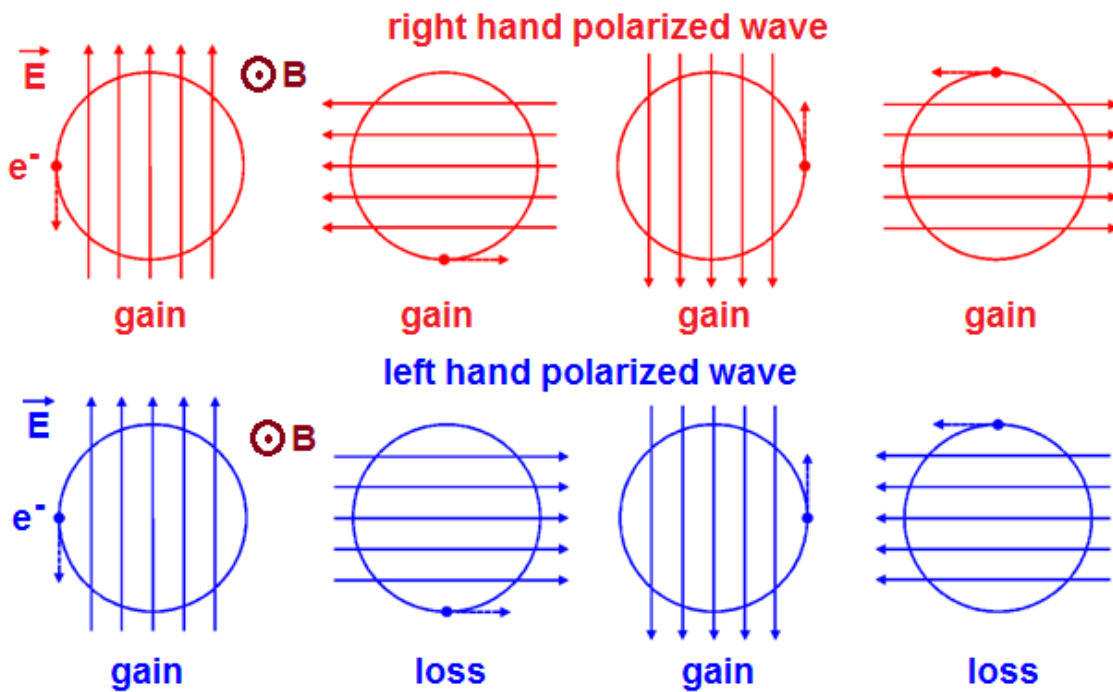


Figure 2.3 : A schematic representation of the acceleration-deceleration of electron under right and left hand polarized wave.

2.2 Major Components of the RRCAT-ECR Plasma Source

The major components of the RRCAT-ECR plasma source are,

- I. Plasma chamber and vacuum system,
- II. Microwave system (i.e. microwave generator and its transfer line),
- III. Electromagnet and its power supply,
- IV. Plasma diagnostic device,
- V. Ion beam extraction electrodes, and
- VI. Beam diagnostics devices

A schematic block diagram of electron cyclotron resonance ion source (ECRIS) is shown in Fig. 2.4.

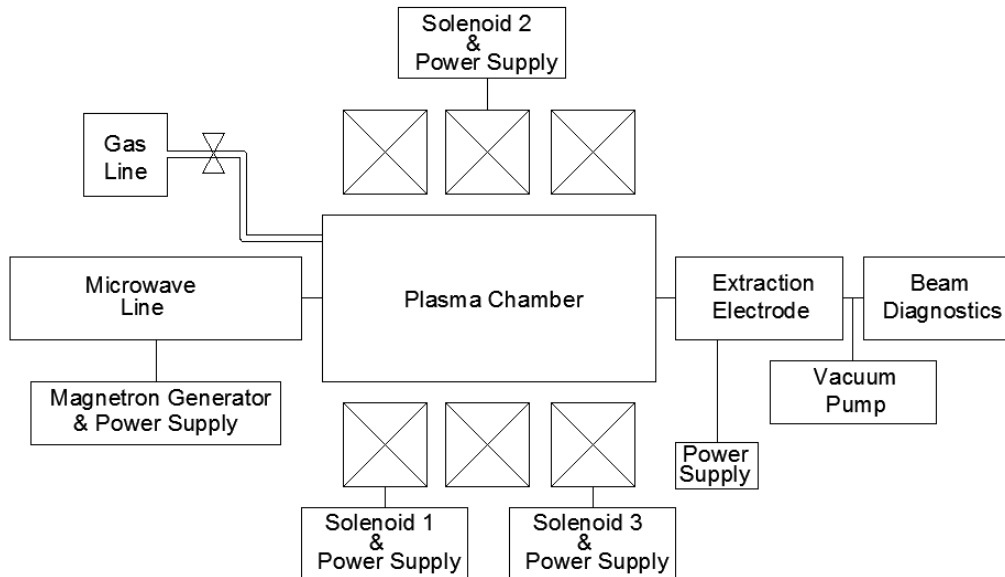


Figure 2.4 : A schematic block diagram of electron cyclotron resonance ion source (ECRIS).

The RRCAT-ECRIS integrated with Thomson parabola ion spectrograph is shown in Fig. 2.5. A 3D-view of the RRCAT-ECRIS is shown in Fig. 2.6. A photograph of the RRCAT-ECRIS is shown in Fig. 2.7. The design details of the major components of the RRCAT-ECRIS are presented in the following chapters.

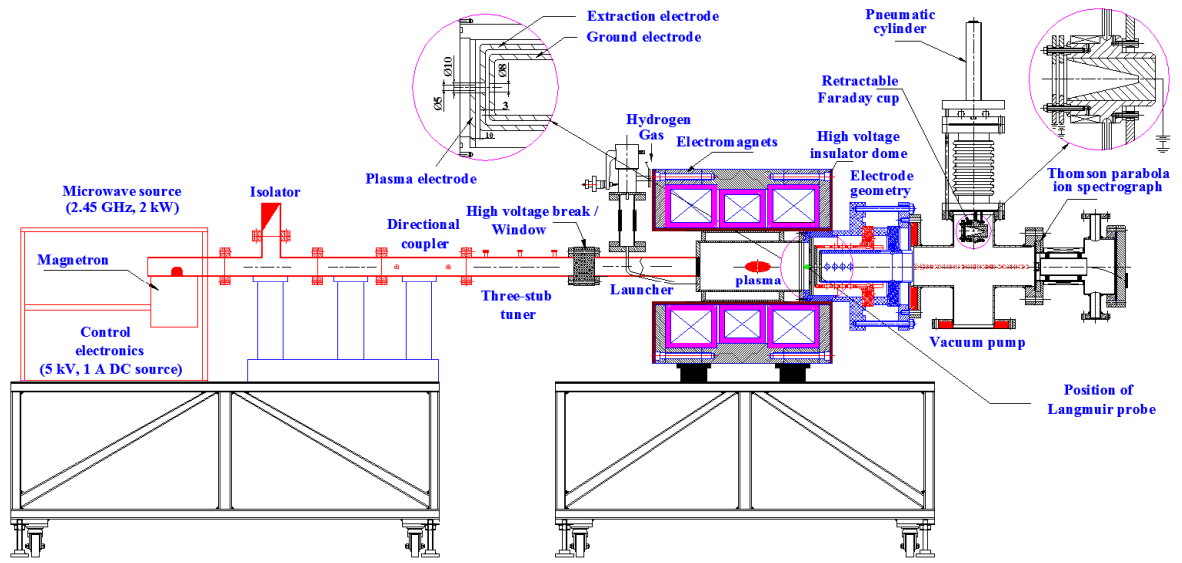


Figure 2.5 : The RRCAT-ECRIS integrated with Thomson parabola ion spectrograph.

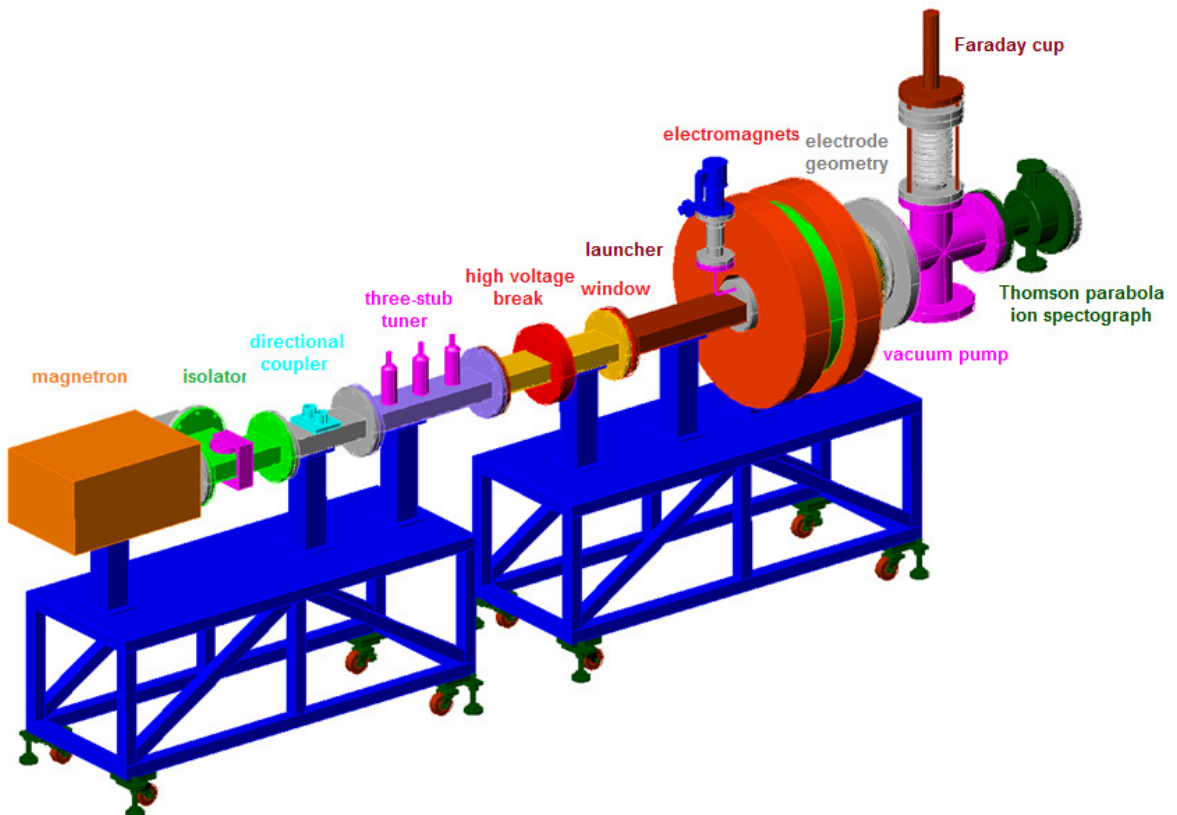


Figure 2.6 : A 3D-view of the RRCAT-ECRIS.

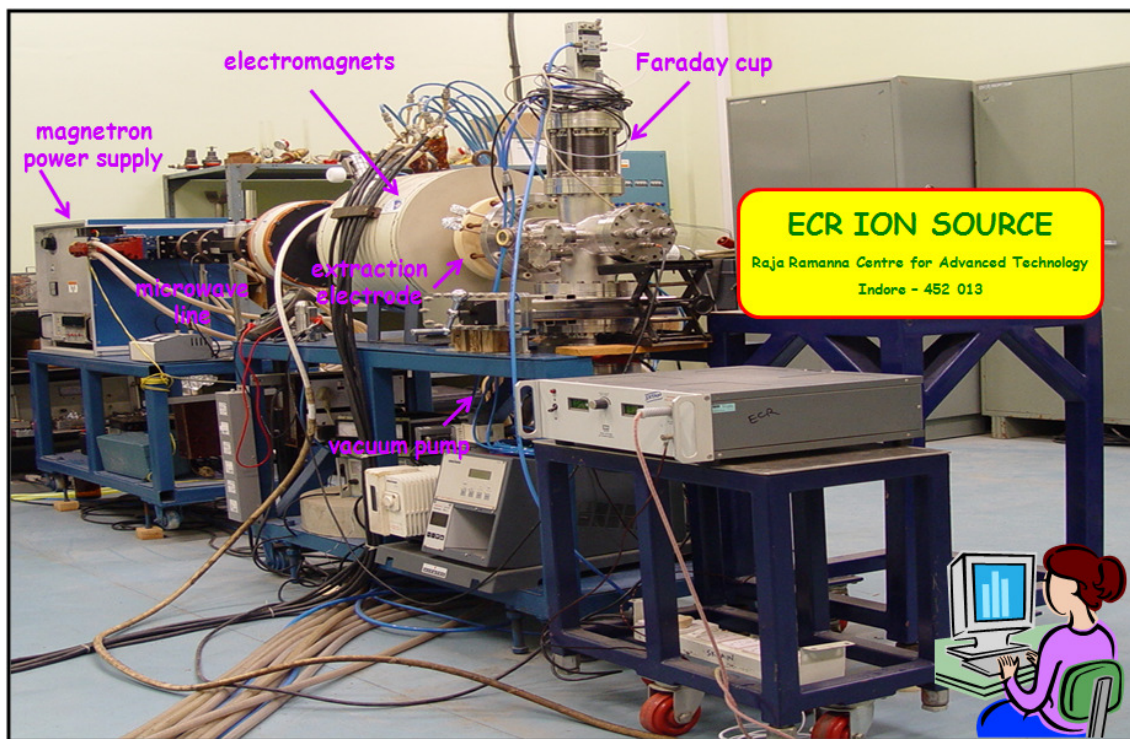


Figure 2.7 : A photograph of the RRCAT-ECRIS.

CHAPTER 3

Plasma Chamber and Vacuum System

This chapter deals with the design aspects of the plasma chamber and its vacuum system. The plasma chamber does two jobs : 1) microwave heating of plasma and 2) containment of the plasma produced using solenoid coils for producing the magnetic field configurations. The dimensions of the plasma chamber as a cylindrical cavity were analytically calculated cross-checked with electromagnetic software.

3.1 Plasma Chamber

The dimensions of the plasma chamber were chosen such that it resonates at 2.45 GHz frequency to absorb efficiently the input microwave power. The dimensions of the plasma chamber as a cylindrical cavity were analytically calculated from standard relation and also with electromagnetic software. In order to support the dominant mode TE_{11} or TM_{01} , the diameter of the plasma chamber has to be 72 or 94 mm, respectively, for the operating frequency 2.45 GHz [73,74,75]. The dimensions of the plasma chamber are 95.5 mm diameter (nominal bore 3½” pipe, outer diameter 101.6 mm, and wall thickness 3.05 mm) and 200 mm length. The overall diameter including water-cooling jacket is 150 mm and is used to accommodate the electromagnet (solenoid coils + iron yoke) and extraction geometry. The plasma chamber was fabricated using seamless non-magnetic stainless steel S.S.304L. The plasma chamber was provided with water-cooling and this helps to avoid the excess heating of wall of the plasma chamber due to absorption of microwaves and bombarding of charged ions on the walls of the plasma chamber. The experimental setup for the measurement of resonance frequency of the plasma chamber is shown in Fig. 3.1.

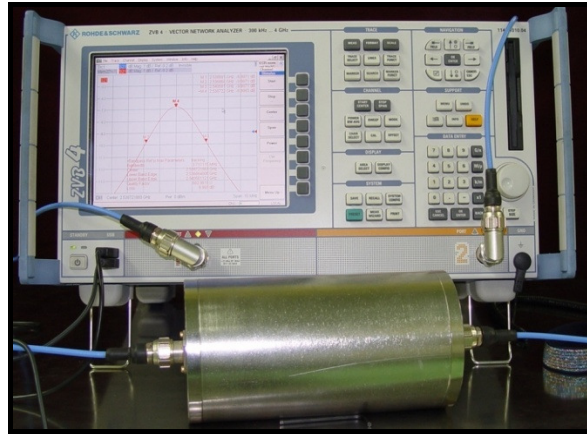


Figure 3.1 : The experimental setup for the measurement of resonance frequency of the plasma chamber.

3.2 Vacuum System

The vacuum system, and its sub-components are required to maintain the basic vacuum in the plasma chamber for plasma production as well as in extraction chamber for ion extraction, and for reducing the charge exchange collisions between the ions and neutrals. The objective of the vacuum system was to evacuate the plasma chamber, beam extraction line, and its components, to avoid loss of particles due to recombination, and to avoid internal electrical breakdown due to high voltage. The ultimate vacuum requirement is less than 1×10^{-6} mbar.

The vacuum system was designed based on the standard calculations was available in refs. [76,77,78]. The vacuum system was designed and fabricated as a "cross-type", consisting of standard knife-edge conflat flange CF203, CF152, and CF70 (six) diagnostics ports. The vacuum chamber and its sub-components were fabricated using seamless non-magnetic stainless steel S.S.304L. The clean vacuum was maintained by using good quality vacuum materials and fabrication techniques. The clean materials have low out-gassing, and low vapour pressure. These ports are used for connection of vacuum pump (bottom), plasma chamber (side), and other devices as required like Faraday cup, plasma diagnostic probe (other side), and pressure gauge (Model : TPR 261, Make : M/s Pfeiffer Vacuum GmbH,

Germany). The high voltage feed through, and quartz window as a view port were connected to CF70 ports. All the vacuum components were helium leak tested using helium mass leak spectrometer (Model : ASM 142, Make : M/s Alcatel Vacuum Technology, France), and the leak rate was found to be less than 5×10^{-10} mbar l/s. A turbo molecular pump, with capacity of 400 l/s (Model : ATP 400, Make : M/s Alcatel Vacuum Technology, France) was selected by considering gas throughput ($\approx 1.5 \times 10^{-3}$ mbar l/s) to maintain a pressure of the order of 10^{-4} - 10^{-3} mbar in the plasma chamber, 10^{-6} - 10^{-5} mbar in the extraction chamber, and to have a hydrocarbon free clean vacuum. The complete ion source was installed on a non-magnetic support bench with wheel carriages for ease of installation and maintenance. A gas inlet system consisting of a high purity gas cylinder, a pressure regulator, precision standard leak valve (Model : UDV 146, Make : M/s Pfeiffer Vacuum GmbH, Germany), and a flow controller (Model : C 100, Make : M/s Sierra, USA) were used.

A standard 3 kW continuous wave water-cooled Faraday cup (Model : Far-3 kW, Make : M/s Penteknik, France) was mounted on the top of the cross-type vacuum system. Faraday cup is a destructive electrically isolated device, used for the measurement of the DC beam current. The incident charged particles were stopped in the Faraday cup, and an electric charge was measured across a resistor connected between the Faraday cup and ground, detected as corresponding electric current. It has an air pressure actuator for up and down movement which helps in on-line current measurement. A five-port diagnostic flange was mounted at the end and right side of the cross-type vacuum system in which the plasma diagnostics probe was fixed at one port and other ports were used as view ports. The experimental gas (argon / hydrogen / nitrogen) was fed through a stainless steel tube of quarter inch size, and was isolated with a 2 meter long polyvinyl chloride (PVC) insulator. This was necessary since the plasma chamber floats at a high potential during the course of the beam extraction experiment. The vacuum requirement was critical due to the high voltage

floating of the plasma chamber. The plasma chamber and the extraction geometry were placed into a special polypropylene tube (dielectric strength > 40 kV/mm and operating maximum temperature 100 °C) to isolate the solenoid coils from the source body. The extraction geometry was connected with the plasma chamber flange. The ground flange of the extraction geometry was connected to the vacuum cross-type chamber, having standard rotatable CF203 flange.

CHAPTER 4

Microwave System

This chapter covers various aspects of the microwave system. This includes the design, development of i) a power supply for energizing the coaxial magnetron source, which is used as a source of up to 2 kW microwave power at 2.45 GHz frequency in continuous wave mode, ii) the design, development and characterization of the microwave transfer line which consists of an isolator (which allows the microwave propagation in forward direction while the reflected power is dumped), iii) a directional coupler for power measurement, iv) a tunable three-stub tuner for impedance matching, v) a microwave vacuum window for vacuum isolation between the plasma chamber and microwave system, vi) a glass-water load for the characterization of the microwave line and the source, and vii) a microwave launcher to feed the microwave power to the plasma chamber.

The microwave system consists of a magnetron as a microwave generator, its power supply, waveguide components (an isolator with dummy load, a directional coupler, a three-stub tuner, a high voltage break, a microwave vacuum window, and a microwave launcher) for transferring microwave power from the microwave source to plasma chamber. This type of microwave systems at 2.45 GHz, 2 kW continuous wave have been widely used in various plasma applications to deliver the microwave power to the plasma chamber [79,80,81]. The microwave system at frequency 2.45 GHz and power up to 2 kW continuous wave have been designed, and developed using rectangular waveguide WR-284. A schematic diagram of the microwave system for RRCAT-ECRIS is shown in Fig. 4.1. A 3D-view of the microwave system test setup for RRCAT-ECRIS is shown in Fig. 4.2.

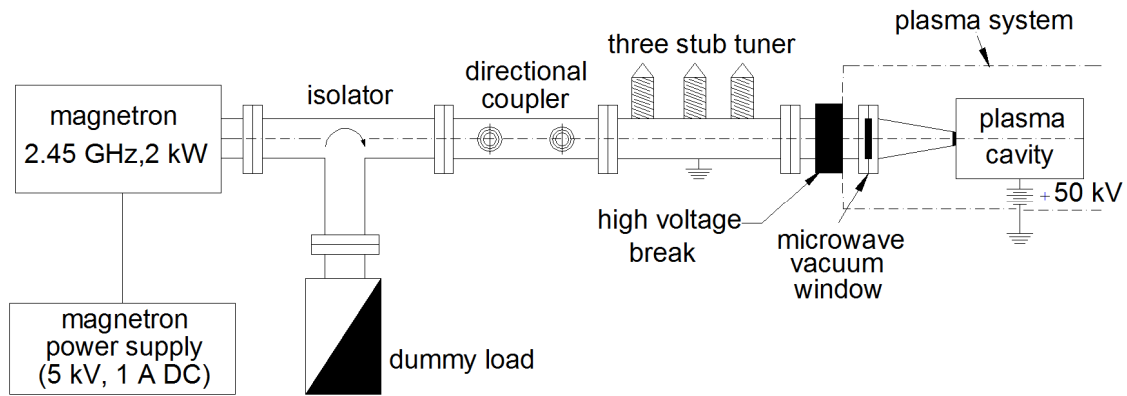


Figure 4.1 : A schematic diagram of the microwave system for RRCAT-ECRIS.

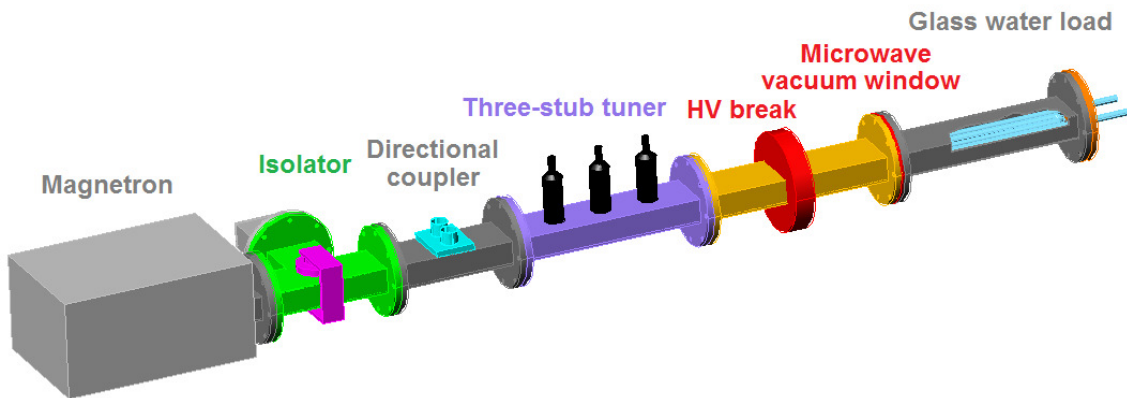


Figure 4.2 : A 3D-view of the microwave system test setup for RRCAT-ECRIS.

4.1 Magnetron as a Source of Microwave Power

As a source of microwave power, we have used standard coaxial magnetron (Model : NL10250L, Make : M/s Richardson Electronics Pvt. Ltd., USA) suitably water-cooled for operating in continuous wave. It is a low cost and efficient device for producing microwave radiation. It is widely used in microwave ovens (frequency : 2.45 GHz) for cooking, and in plasma production for various applications. The technical specifications of the coaxial magnetron are given in Table 4.1.

Description	Parameters
Frequency	2.45 ± 0.025 GHz
Filament voltage	4.6 V AC
Filament current	19 A
Cathode voltage	4 kV DC
Cathode current	725 mA
Output power	2 kW CW

Table 4.1 : *The technical specifications of the coaxial magnetron.*

The magnetron requires a low voltage, high current AC power supply, floated at negative high voltage for the filament (thoriated tungsten coil, directly heated by AC or DC) and a high voltage negative and low current DC power supply. The body of the magnetron is at ground potential. A magnetron can be operated in both continuous wave, and pulsed mode using a suitable pulse-forming network [82,83,84,85,86,87]. To energize this magnetron, a high voltage DC power supply of rating negative (-) 5 kV, 1 A for cathode, and an AC power supply of rating 5 V, 20 A for filament (floating), were developed in-house. A block diagram of the magnetron power supply is shown in Fig. 4.3. The power supply employs a voltage doubler scheme to achieve full voltage 5 kV DC with a 2.5 kV transformer. The power supply was tested independently, and characterized with a DC resistive load up to full rating. The output waveform of the magnetron power supply was measured using a storage oscilloscope, and a high voltage probe. The measured waveform and ripple of the magnetron power supply for a) DC output for cathode, and b) AC output for filament are shown in Fig. 4.4. The measured output voltage was (-) 4.7 kV DC and ripple peak to peak was 0.1 %. The output voltage was stable for the required period of time. A photograph of the magnetron power supply is shown in Fig. 4.5.

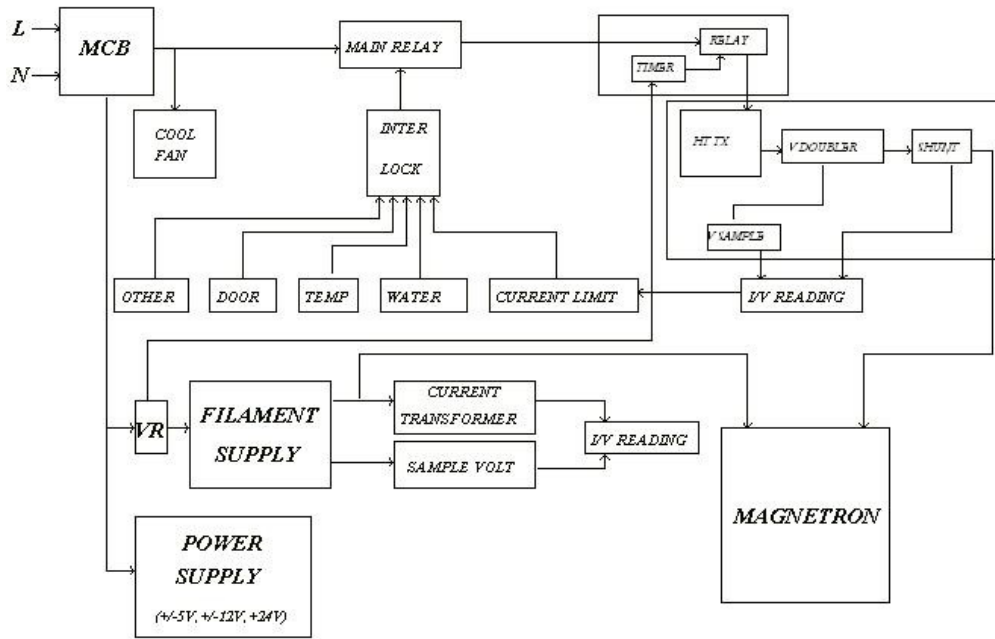


Figure 4.3 : A block diagram of the magnetron power supply.

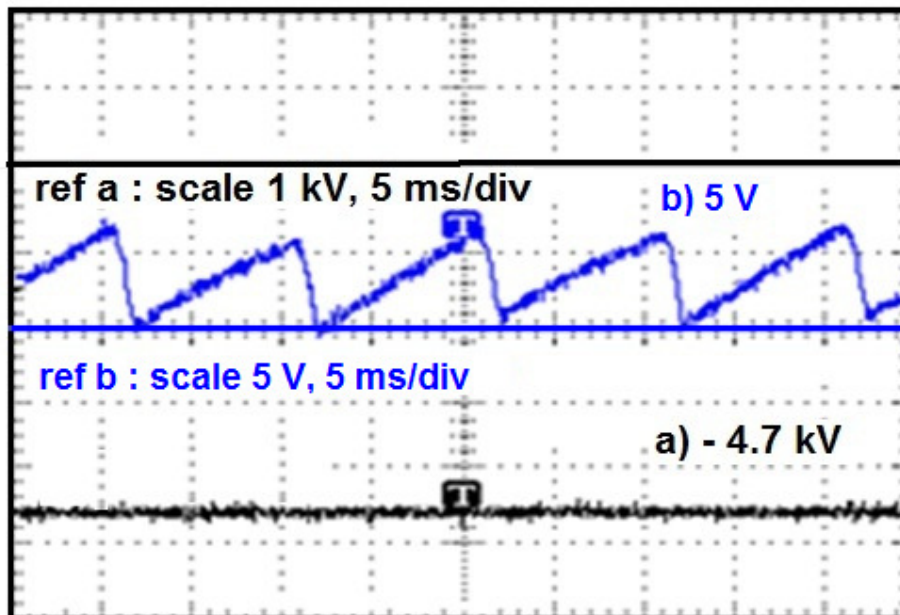


Figure 4.4 : The measured waveform and ripple of the magnetron power supply for a) DC output for cathode, and b) AC output for filament.

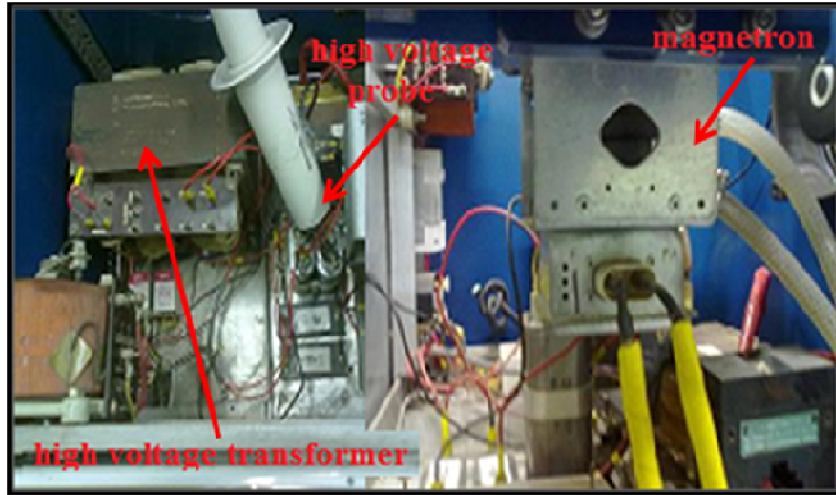


Figure 4.5 : A photograph of the magnetron power supply.

4.2 Waveguide Components

Various devices have been commonly used to transfer the microwave power, viz., coaxial line, and waveguide, depending on power or frequency used. A coaxial line with N-type connector was used where microwave power was slightly less than 200 W. With a specially designed 50 Ω coaxial line, a microwave power of ~ 300 W was coupled to the ECR plasma source and an electron density of $5 \times 10^{10} \text{ cm}^{-3}$ was achieved [88]. Considering the requirement of microwave power of about 2 kW continuous wave for our application, we have chosen a waveguide based microwave system. Although, the designated rectangular waveguide for 2.45 GHz is WR-340, WR-284 was used since its cut-off frequency is 2.078 GHz and it is suitable to operate at average power level of up to 6 kW. The other reason behind using WR-284 was that, this waveguide has also been used in some other on-going projects at RRCAT.

The cross-section of rectangular waveguide WR-284 was 72.14 mm (broader side) \times 34.04 mm (narrow side) with typical wall thickness 2 mm, made up of oxygen free high conductivity copper. Standard plane, and choke type flanges were used for joining of the waveguide components [73]. The choke joint also keeps the electromagnetic field confined in

the waveguide and helps to reduce the transverse microwave leakage. There have been various commercial software's like *CST-MWS* [89], *Ansoft-HFSS* [90], *Mafia* [89] for the electromagnetic analysis / modeling of complex RF and microwave components. We chose the *CST-MWS* software for the electromagnetic analysis of waveguide components to reduce the microwave losses and with an adequate matching of the waves to the plasma chamber operating at frequency 2.45 GHz. It is 3D-electromagnetic simulation software. It has three different simulations techniques based on the finite integration method. Its transient solver technique was found to be suitable for analysis of microwave components. In the simulation, the outer boundaries were chosen as perfect electric conductor. The electromagnetic field pattern a) standard transverse electric TE mode, b) dominant TE_{10} mode, and c) *microwave studio* simulated inside the WR-284 rectangular waveguide are shown in Fig. 4.6. The design and constructional details of the microwave components are presented in the following sections.

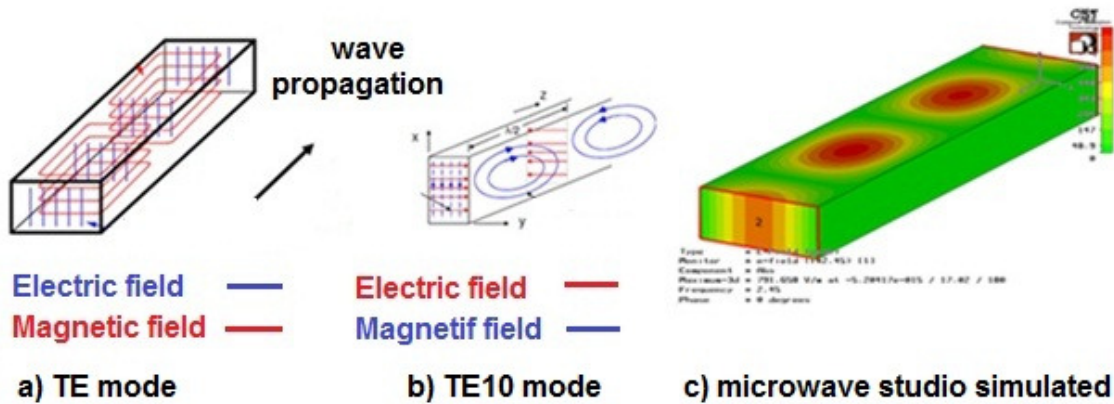


Figure 4.6 : The electromagnetic field pattern a) standard transverse electric TE mode, b) dominant TE_{10} mode, and c) *microwave studio* simulated, inside the WR-284 rectangular waveguide.

1) Isolator with water load : An isolator allows un-attenuated transmission of microwave power in the forward direction whereas power incident from other direction (reflected power) directed towards the load, is completely absorbed. In this way, it is an

important two-port device, which protect the microwave source from any reflected power damage due to mismatch of the waveguide impedance to the plasma impedance. It is a standard device (Model : 2722-163-02004, Make : M/s Richardson Electronics Pvt. Ltd., USA). The operating power of the isolator is 3 kW continuous wave, and it is water-cooled. It provides the isolation of 20 dB to the magnetron.

2) Directional coupler : The directional coupler [73,91,92] is a device which is commonly used for the measurement of the forward, and reflected power simultaneously. It is a four-port network (input port, transmitted port, coupled port and isolated port), and a known fraction of the microwave power flowing in a particular direction is sampled and used for evaluating the forward and reflected power and knowing its coupling factor. A block diagram of the directional coupler is shown in Fig. 4.7.

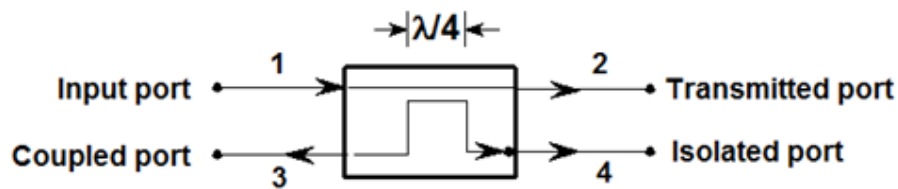


Figure 4.7 : A block diagram of the directional coupler.

The working principle of a directional coupler is simple to understand. When a wave travels from port 1 to port 2, a fixed fraction of its power appears at port 3 (i.e. waves are in phase), and there is no power appears at port 4 (i.e. wave is 180° out of phase). Conversely, if the wave is travelling from port 2 to port 1, a fraction of this power appears at port 4, and there is no power appears at port 3. When the transmission takes place from port 1 (input port) to port 2 (transmitted port), the port 3 is called coupled port, and the port 4 is called isolated port. We have designed, and developed a directional coupler for 45 dB as its coupling factor using the *microwave studio* software. A schematic diagram of this directional coupler is shown in Fig. 4.8. It has waveguide as a main line, two coupling holes for power

coupling, a loop plate, a loop holder, and a power sampling connector (N-Type). The plane of the loop is kept parallel to the axis of the main line to which the loop is coupled. The length of the waveguide is 200 mm. Based on the schematic diagram of the directional coupler, the model has been created in *microwave studio* for simulations, for its scattering parameters. The directional couplers were designed to sample the power propagating in one direction. A schematic diagram of the orientation of loop plate with respect to direction of the propagation axis for the directional coupler is shown in Fig. 4.9. A model prepared in *microwave studio* for the directional coupler is shown in Fig. 4.10.

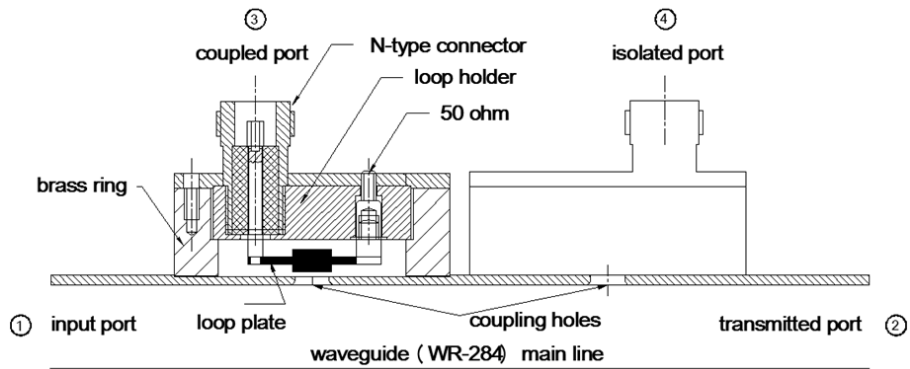


Figure 4.8 : A schematic diagram of the directional coupler.

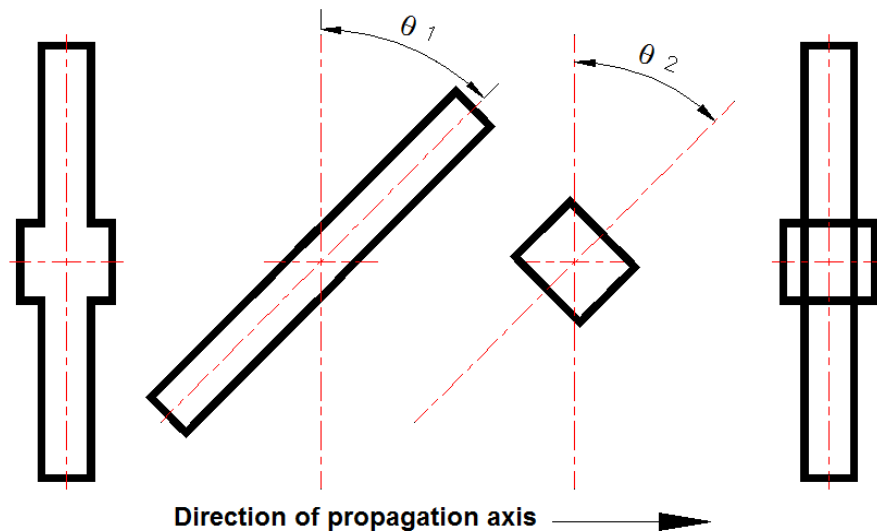


Figure 4.9 : A schematic diagram of the orientation of loop plate with respect to the direction of the propagation axis for the directional coupler.

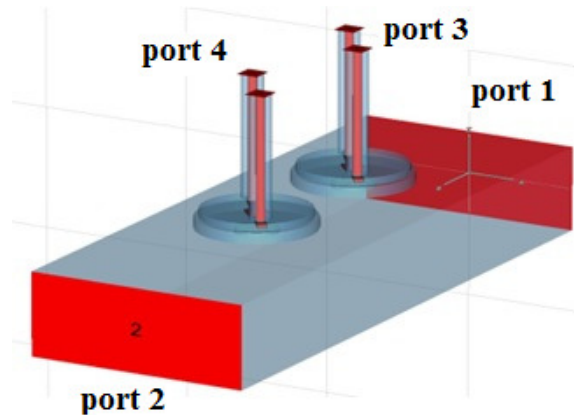


Figure 4.10 : A model prepared in microwave studio for the directional coupler.

For *microwave studio* simulations, the materials for all the parts were chosen to be vacuum, except the inner conductor of the ports, loops, and supporting holder. These were simulated as perfect electric conductors. The distance between the holes for microwave coupling was kept one-fourth of the waveguide wavelength from the centre of the waveguide, to keep the frequency sensitivity to a minimum. A number of iterations were carried out by changing the loop, and the mid plate dimensions like, the thickness (T : 0.5 to 2 mm) of the loop plate, the width of the loop plate (W : 3 to 5 mm), the length of the mid plate (X : 5 mm), the width of the mid plate (Y : 6 to 10 mm), the height of the loop (H : 0.5 to 2 mm) from the main waveguide, and the theta rotations (clockwise) for the loop plate (θ_1) as well as the mid plate (θ_2). The coupling hole diameter (ϕ) was also varied. The S-parameters optimized with frequency for the directional coupler are shown in Fig. 4.11. The S-parameters were optimized at 2.45 GHz frequency. From the figure, one can see that it has a very low insertion loss (S_{21}) of 0 dB, and the return loss (S_{11}) is about 100 dB, the coupling factor (S_{31}) is 45 dB, isolation (S_{41}) is 70 dB and the directivity ($S_{31}-S_{41}$) is 25 dB. The coupling factor and the directivity together decide the performance of the directional coupler. Variation of the coupling factor (S_{31}), and the directivity ($S_{31}-S_{41}$) with the hole diameter for the directional coupler at 2.45 GHz frequency is shown in Fig. 4.12. It was observed in

simulation that the coupling factor, and the isolation depends on the coupling hole diameter (ϕ). The directionality of the coupling of the power remains unchanged, since the coupling and the isolation increases in symmetrical manner as expected, with increasing the hole diameter.

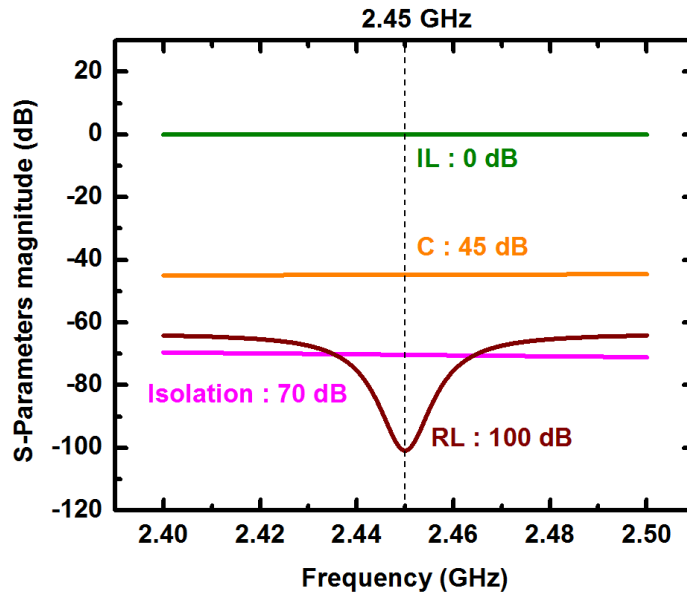


Figure 4.11 : The S-parameters optimized with frequency for the directional coupler.

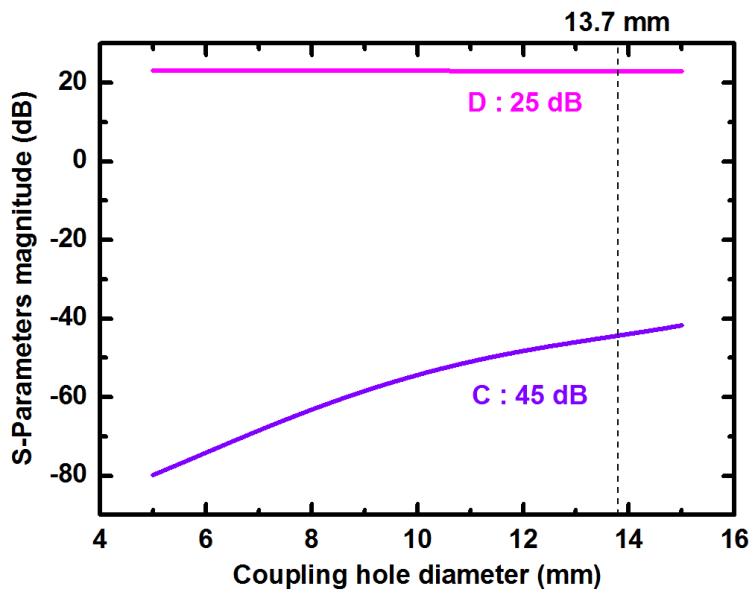


Figure 4.12 : Variation of the coupling factor (S_{31}), and the directivity ($S_{31} - S_{41}$) with the hole diameter for the directional coupler at 2.45 GHz frequency.

It was observed that when the height of the loop (H) of the main waveguide, and the thickness of the loop plate (T) were increased, the coupling (45 dB) was not much affected. The directivity was 30 dB for T = 0.5, W = 1 mm, X = 5 mm, Y = 6 mm, $\theta_1 = 54^\circ$, $\theta_2 = 45^\circ$. The loop was placed close to the waveguide (H = 1 mm) and the effect of the orientation of the loop plate, and the mid plate was studied, keeping T = 1 mm, W = 3 mm, X = 5 mm, Y = 6 mm, and $\phi = 13.7$ mm. The results were as follows :

Case 1 : When θ_1 and θ_2 are equal ($\theta_1 = \theta_2$), there is no directivity except at 90° and 270° . In the case of 90° , the coupling and directivity were 43 and 20 dB respectively. In the 270° case, the results remained the same except that the coupling port and the isolated port interchange.

Case 2 : When $\theta_1 = 90^\circ$ and θ_2 was changed from 0 to 90° , the coupling factor and the directivity were 43 and 20 dB respectively.

Case 3 : When θ_1 was changed from 0 to 90° and $\theta_2 = 90^\circ$, the coupling remained almost same (-) 43 dB, but the directivity changed from 25 to 33 dB.

Case 4 : When θ_1 and θ_2 are not equal ($\theta_1 \neq \theta_2$), some of the results for return loss, coupling, isolation and directivity calculated when $\theta_1 \neq \theta_2$ are given in Table 4.2.

θ_1 ($^\circ$)	θ_2 ($^\circ$)	Return Loss (dB)	Coupling (dB)	Isolation (dB)	Directivity (dB)
54	45	100.00	45.00	70.00	25.00
63	54	100.80	44.11	77.81	33.70
72	18	91.78	43.46	82.65	39.19
63	18	106.30	44.38	78.46	34.08
81	27	95.90	43.65	66.49	22.84
81	45	103.20	43.59	69.86	26.27
81	36	99.07	43.59	69.26	25.67

Table 4.2 : Return loss, Coupling, Isolation, and Directivity calculated when $\theta_1 \neq \theta_2$.

Due to the 4-fold symmetry, the loop plate and the mid plate could be rotated from 0° to 90° . The coupling factor was not much affected with any orientation other than longitudinal, while the directivity was good when the loop plate and the mid plate were oriented at different angles. It was insensitive to the coupling hole diameter. The coupling becomes minimum when the loop is in the transverse direction. For the fabrication of the directional coupler (waveguide length 200 mm), brass rings of $\phi 35$ mm and height 30 mm were fixed over both the coupling holes. Care was taken at the time of brazing that coupling holes remain in the centre of the brass rings. The power sensing loops were fabricated using oxygen free high conductivity copper plate. The loops for sensing the radio frequency signal were mounted on a brass holder. A 50Ω , 10 W chip resistance (for termination) and N-type connector (for sampling the power) were fixed on ends of the loop. The brass holder is an independent device with respect to the main waveguide, and could be freely rotated up to 360° for changing the orientation of the loop for coupling and directivity adjustment. The mechanical dimensions of the coupling loop play an important role in coupling and directivity performance because the electric and magnetic fields get actually coupled through it. All the sharp edges were removed to avoid electrical arcing due to the microwave power. A photograph of the directional coupler is shown in Fig. 4.13.

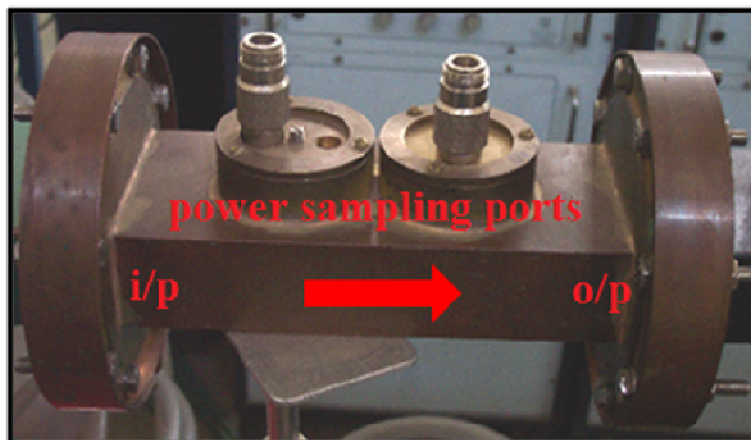


Figure 4.13 : A photograph of the directional coupler.

3) Three-stub tuner : Three-stub tuner [73,74] is a device which is widely used for matching of the impedance. It has three capacitive stubs, which are in parallel, and provides the variable shunt susceptance for matching the impedance. Combination of two neighbouring stubs (1 + 2 or 2 + 3) is used at a time for matching. Each pair covers about half of the complete matchable area in the Smith chart. The matchable area in the complex reflection coefficient plane is shown in Fig. 4.14. The regions A and B are prone to electrical breakdown.

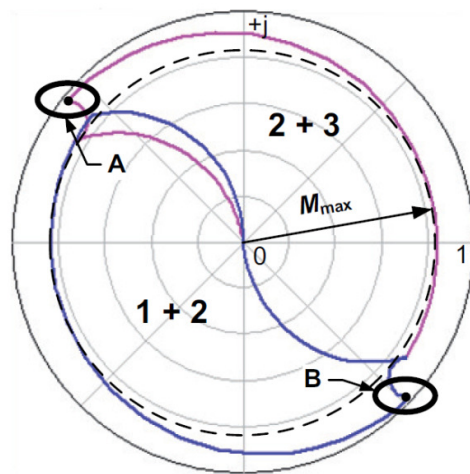


Figure 4.14 : The matchable area in the complex reflection coefficient plane.

The impedance of the plasma is inhomogeneous in nature because of the magnetic field gradients and recombination near the walls of the plasma chamber. It is dynamical in nature, and depends on the gas pressure, magnetic field, microwave power, operating conditions etc. Hence, it is required to match the impedance of the microwave transmission line to the impedance of the plasma, in order to minimize the microwave reflections. This is necessary to prevent the magnetron as well as the microwave vacuum window from damage. We have designed and developed a three-stub tuner as a variable impedance matching device. It matches the modulus and the phase of the incoming wave, in order to match the plasma impedance by adjusting the depth of the stubs (small sections of transmission lines which are

connected as shunt or series to the main line for impedance matching). A schematic diagram of the shunt connected the stub as a three-stub tuner is shown in Fig. 4.15.

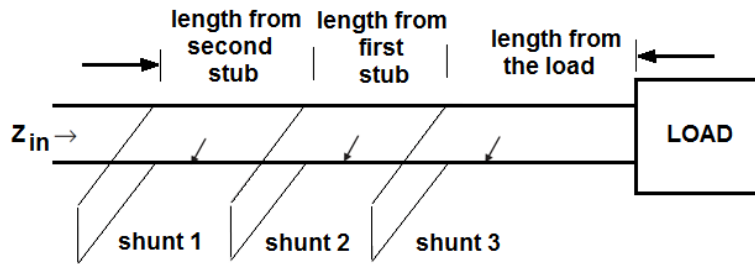


Figure 4.15 : A schematic diagram of the shunt connected the stub as a three-stub tuner.

For understanding the behaviour of the three-stub tuner, it was simulated in *microwave studio*. Vacuum was chosen as the medium for the waveguide, and perfect electric conductor for the shunt stubs. Three-stubs are mounted on the broad wall of the waveguide at equal intervals (three-eighth of the guide wavelength) to keep the frequency sensitivity to minimum. They are manually guided in or out. The length of the waveguide for three-stub tuner was 300 mm. The effect of shunt stubs was checked with *microwave studio* for its tuning range by varying the depth of penetration of the shunt stubs. It was observed that shunt capacitive susceptance changes for a wide range which helps to minimize the reflected power, and matches the impedance of the plasma as a load. A model prepared in *microwave studio* for the three-stub tuner is shown in Fig. 4.16.

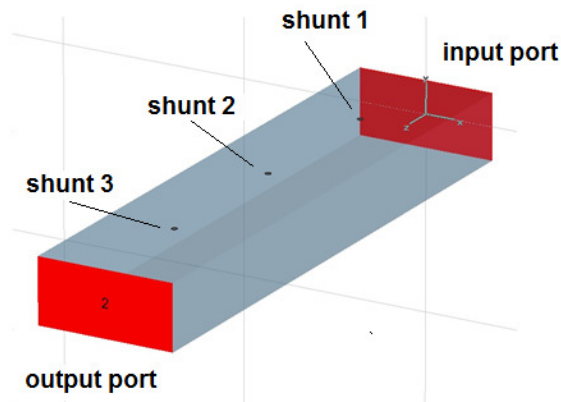


Figure 4.16 : A model prepared in *microwave studio* for the three-stub tuner.

4) High voltage break : A high voltage break [55] is a crucial component which is commonly used for the high voltage isolation between the microwave system and the plasma chamber. The plasma chamber remains floating at a high voltage for extracting the ion beam of required energy. It is essential to keep the microwave side at ground potential during the operation of the source for tuning the reflected power. We have designed and developed a high voltage break to withstand a voltage of 75 kV DC. A high voltage break should have good mechanical rigidity, low microwave loss, and low microwave radiation leakage to the environment. It was simulated using *microwave studio* from microwave point of view (low microwave loss), with the proper thickness to model the insulator to withstand 75 kV DC voltage. A model prepared in *microwave studio* for the high voltage break is shown in Fig. 4.17.

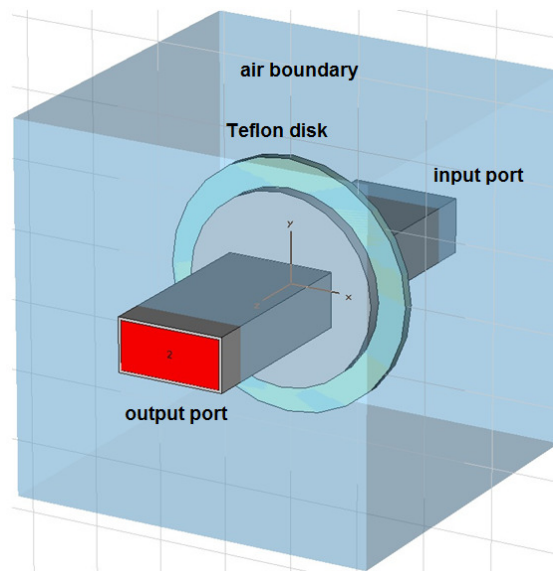


Figure 4.17 : A model prepared in *microwave studio* for the high voltage break.

It has two waveguides of length 150 mm on both sides. Vacuum was chosen as inside material, and perfect electric conductor for the thickness of the waveguide. An insulator was sandwiched in between for finding its scattering parameters. The complete assembly was enclosed in a rectangular box with material as air to see the real effects under actual

environment. Teflon, high-density polyethylene, and polypropylene, which are commercially available, are normally used to get low loss for microwave, good mechanical strength and high voltage isolation. We have used Teflon as the high voltage isolation material. Using *microwave studio*, a numbers of iteration were carried out to get the proper thickness of Teflon to achieve the minimum return loss and insertion loss. The S-parameters optimized with frequency for the high voltage break : Teflon of thickness 7.35 mm are shown in Fig. 4.18. It is noted from the figure, that the return loss is 40 dB and the insertion loss is 0.08 dB for 7.35 mm Teflon thickness at 2.45 GHz frequency. The observed S-parameters show that the device is perfectly matched with input impedance with low microwave loss. The device was backed at 120 °C for two hours, for the settlement of high voltage epoxy under vacuum environment. The high voltage insulation was tested using high voltage Megger (Model : 220123-47, Make : M/s Megger, Biddle, England). It works satisfactorily up to 75 kV DC isolation without any leakage current.

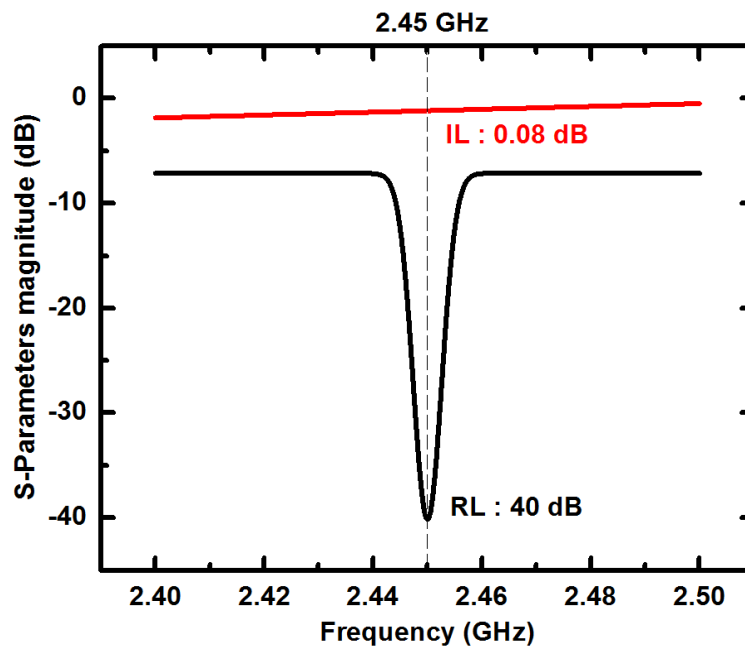


Figure 4.18 : The S-parameters optimized with frequency for the high voltage break : Teflon of thickness 7.35 mm.

5) Microwave vacuum window : Microwave vacuum window [10,11,12,93,94,95] is a device which is widely used for the isolation of microwave system from the plasma chamber which is under vacuum. A microwave vacuum window commonly uses a single / double / triple layer of mica, quartz, Teflon, alumina, aluminium nitride, boron nitride or combinations of these. The properties of these materials are such that they allow microwave propagation with low loss, and have good mechanical strength (except quartz). The thickness of the window material should be chosen in such a way that it can sustain the force of back-streaming of high energetic electrons, and stop the plasma flow back to the microwave source (i.e. magnetron). Sometimes, it may get punctured due to the excessive heating, leading to the failure of the ion source. The use of multilayered window increases the cost as well as complexity of fabrication. We have designed and built a single layer window at 2.45 GHz frequency. For constructing the geometry in *microwave studio* for simulation, the length of the waveguide was chosen to be 100 mm. Very thin capacitive obstacles were used for impedance matching on the both sides of the flange. Quartz was chosen as the window material, since it is cheap and easily available. A model prepared in *microwave studio* for the microwave vacuum window is shown in Fig. 4.19.

For simulation purpose, vacuum was chosen to represent all the components. In the simulations, the thickness of the window material was varied from 0.1 to 10 mm. To check the validity of the design and model, it was first run with zero thickness to make sure that same results are obtained as achieved with only standard flanges (return loss S11, insertion loss S21). Variation of the return loss (S11), the insertion loss (S21) with the thickness of quartz plate for the microwave vacuum window at 2.45 GHz frequency is shown in Fig. 4.20. The S-parameters optimized with frequency for a microwave vacuum window with quartz thickness of 6 mm are shown in Fig. 4.21. The simulations show that for the 6 mm thickness of quartz plate, the return loss is 75 dB and the insertion loss is 2.5 μ dB, which is close to

zero. A rectangular quartz plate was fixed using conductive glue. The window was helium leak tested using a helium leak detector and the leak rate was found to be less than 10^{-10} mbar l/s. The outer periphery was covered with grounded copper strip to avoid any transverse leakage of the microwave power.

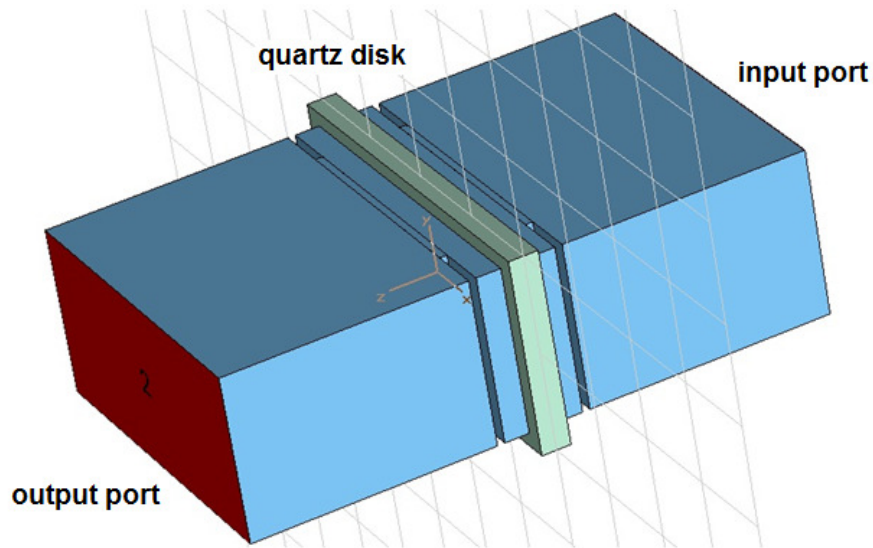


Figure 4.19 : A model prepared in microwave studio for the microwave vacuum window.

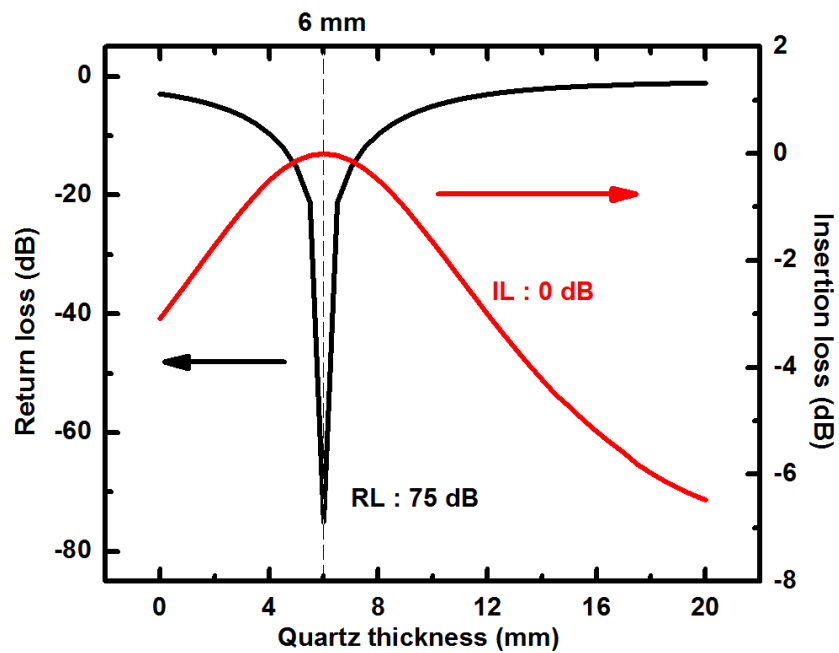


Figure 4.20 : Variation of the return loss (S_{11}), the insertion loss (S_{21}) with the thickness of quartz plate for the microwave vacuum window at 2.45 GHz frequency.

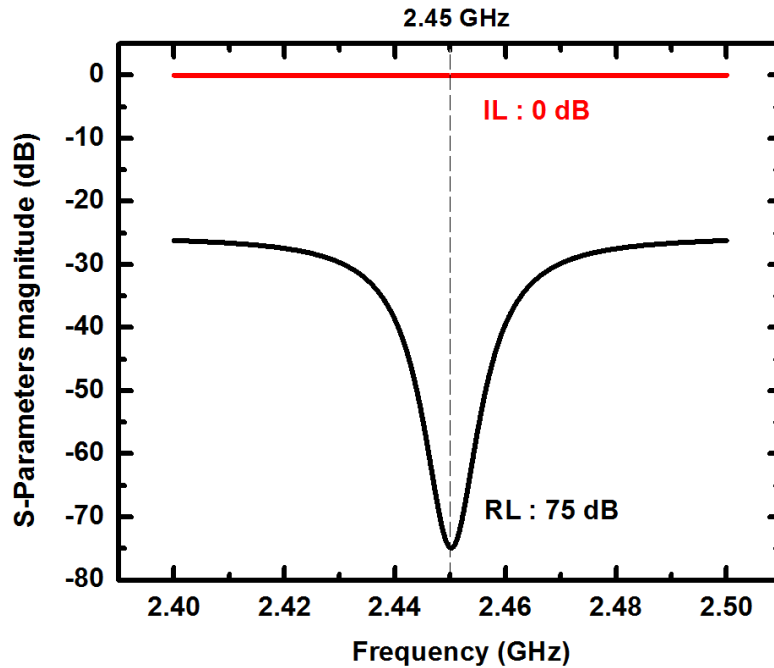


Figure 4.21 : The S-parameters optimized with frequency for a microwave vacuum window with quartz thickness of 6 mm.

6) Microwave launcher : Microwave launcher is a device which is used to couple the microwave power to the plasma chamber. There are various devices used as a microwave launcher viz. coaxial line [96], open ended waveguide [97], horn, slotted and helical antenna [12,80,98], ridged and tapered waveguide [64,99,100,101,102]. The performance of a plasma source (viz. electron density, electron temperature produced) and hence the ion current can be improved significantly by proper selection and design of the microwave launcher. Here, we have studied using *microwave studio* a tapered waveguide as well as a ridged waveguide. The latter is widely used now days as a microwave launcher because of its ease of fabrication, low cost, and wide bandwidth. Both launchers have a special property that they gradually matches the impedance of the microwave transmission to the impedance of the plasma, which leads to a low reflection and a higher order mode coupling. Other devices were ignored because of space limitations. The details of the two launchers are described in the following sections.

a) **Tapered launcher** : We have designed and developed a tapered launcher to feed the microwave power to the plasma chamber. It gradually matches the plasma impedance and increases the intensity of the electric field at the mouth of the waveguide. The intensity of the electric field is a function of narrow dimensions of the waveguide. This was simulated using the *microwave studio*. A model prepared in *microwave studio* for a tapered launcher is shown in Fig. 4.22.

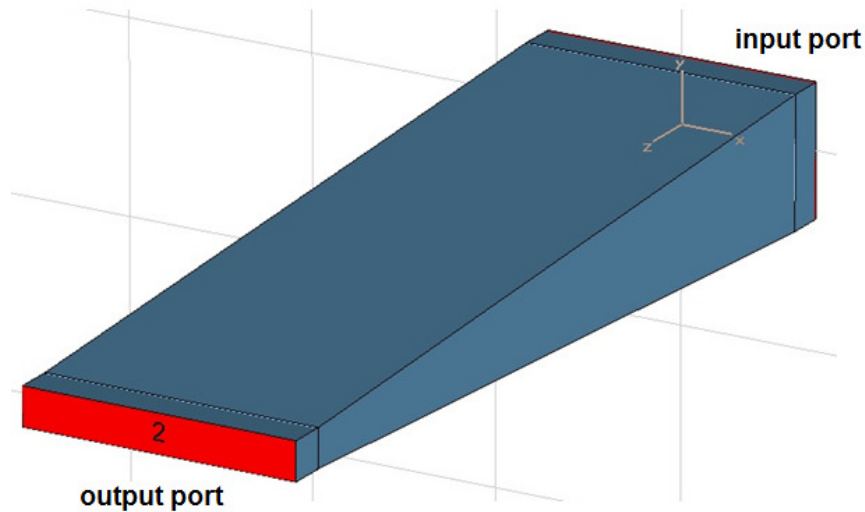


Figure 4.22 : A model prepared in *microwave studio* for a tapered launcher.

For simulations of the tapered launcher in *microwave studio*, two bricks of length 50 mm of dimensions 72.14 mm \times 34.04 mm (matching with waveguide dimension) and 72.14 mm \times 10 mm (achieved with *microwave studio* simulation), with a wall thickness 2 mm, at a distance of one guide waveguide length. Thus by changing the narrow dimensions of the waveguide, the intensity of the electric field was simulated using the *microwave studio* software. It has been observed that the intensity of the electric field becomes almost doubled when the narrow dimension reaches 10 mm. Variation of electric field with the height of waveguide for a tapered launcher is shown in Fig. 4.23.

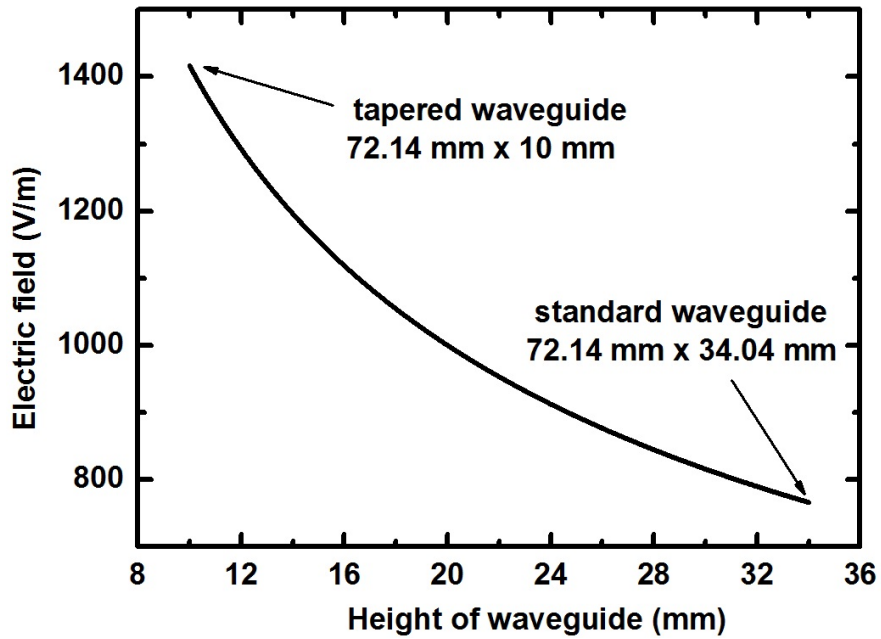


Figure 4.23 : Variation of electric field with the height of the waveguide for a tapered launcher.

This electric field enhances the electron density, since the power is directly proportional to the square of the intensity of the electric field. In *microwave studio* simulation, vacuum was chosen as the inner material and a perfect electric conductor for the wall thickness. The S-parameters optimized with frequency for a tapered launcher are shown in Fig. 4.24. It is noted from the figure, that the return loss is 23 dB and the insertion loss is close to 0.02 dB at 2.45 GHz frequency. The performance of microwave power coupling into the plasma was found to be very good, and most of the incoming power was coupled to the plasma chamber with very low reflected power. The electric field distribution in a tapered launcher is shown in Fig. 4.25.

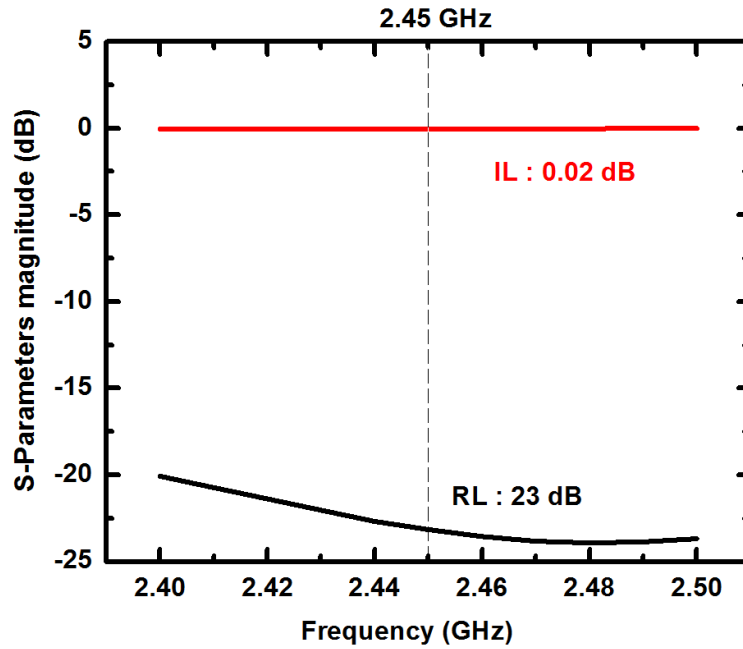


Figure 4.24 : The S-parameters optimized with frequency for a tapered launcher.

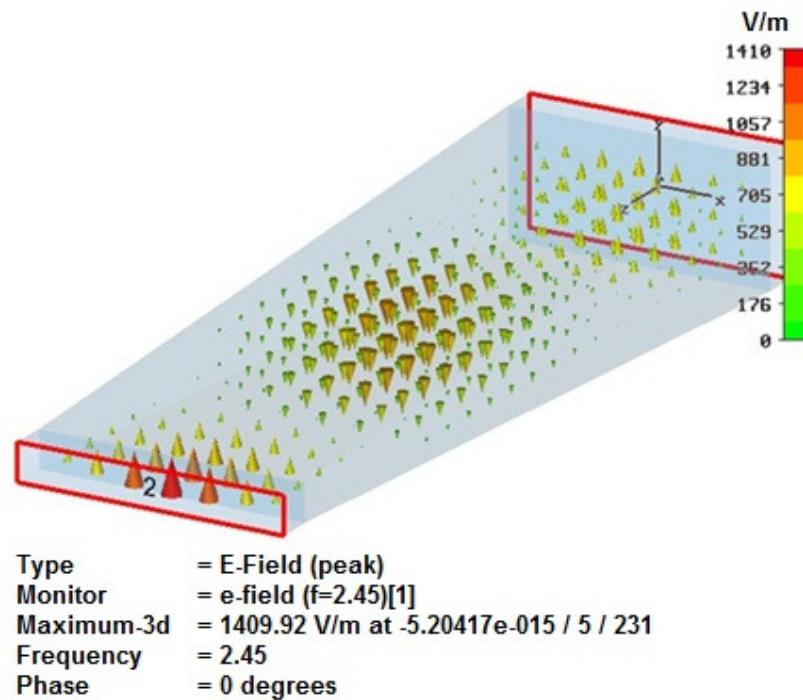


Figure 4.25 : The electric field distribution in a tapered launcher.

b) Ridged Waveguide : A ridged waveguides with three / four sections has been widely used as a microwave launcher in different laboratories like Chalk River Laboratory, Trips, Silhi, MIDAS, VIS, ALISES, and Spiral2. Like a tapered waveguide, a ridged

waveguide also matches the impedance (progressively reducing with ridged gap) from the source waveguide impedance to the plasma impedance which is of the order of 150-100 Ω [103]. A ridged waveguide concentrates the electric field near the source axis, while in a standard waveguide it is distributed in the sinusoidal form along the larger dimensions. It has a wide bandwidth [104,105]. This reduces the necessity of high power level of the microwave for the extraction of higher ion beam current and also reduces the requirement of water-cooling required for the plasma chamber, thereby enabling operation of the source in continuous mode for several hours. The magnitude of the electric field intensity depends on the number of ridged sections.

Analytical approach : There are various devices like coaxial line [96], open ended waveguide [97], E-plane horn antenna, E-plane horn antenna with helical and slotted antenna [12,79,98] etc. have been used to feed the microwave power to the plasma chamber for plasma heating by means of ECR. The use of above devices is limited due to space restrictions, as they make the ECR source bulky in size. With the demand of compact ECR source, advancement of research in science and technology, it has been observed that with the use of ridged waveguide, the performance of the plasma production (electron density and temperature) has improved leading to higher ion beam current extraction. Another advantage of using ridged waveguide is that, it can be operated at a lower frequency and has lower impedance and a wider mode separation between the cut-off numbers of its dominant mode and the first higher mode than a standard waveguide. Due to these advantages, ridge waveguides have been extensively used in microwave active and passive components, and ECR based high intensity, low emittance proton source development at 2.45 GHz frequency. A schematic diagram of a four sections ridged waveguide coupled to the plasma chamber is shown in Fig. 4.26.

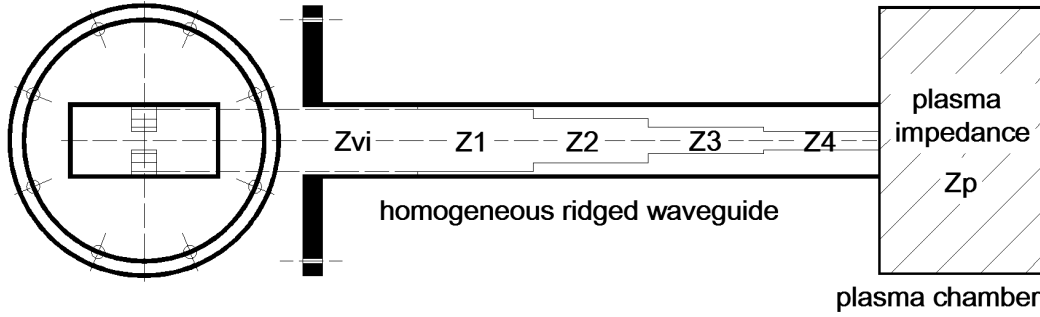


Figure 4.26 : A schematic diagram of a four sections ridged waveguide coupled to the plasma chamber.

Here, Z_{vi} , Z_1 , Z_2 , Z_3 , Z_4 , and Z_p are the impedances of the four sections ridged waveguide, where Z_{vi} is the voltage-current impedance of a standard waveguide, and Z_p is the plasma impedance. The voltage-current impedance of a standard rectangular waveguide is given by,

$$Z_{vi} = \left[\frac{\pi\eta}{2} \right] \left[\frac{2b}{a} \right] \left[1 - \left(\frac{\lambda_0}{\lambda_c} \right)^2 \right]^{-1/2} \dots\dots\dots(4.1)$$

where η is the free space impedance (377 Ω), $2b$ is the height of the waveguide, a is the width of the waveguide, λ_0 is the free space wavelength, and λ_c is the cut-off wavelength, is about $Z_{vi} = 527 \Omega$ for standard waveguide WR-284 (width : 72.14 mm, height : 34.04 mm) operating in a dominant mode TE_{10} at operating frequency of 2.45 GHz. The dimensions of the ridged waveguide have been evaluated using standard characteristics impedance chart for the binomial matching transformers [75], to match the voltage-current impedance of a standard waveguide to plasma impedance, and each sections of the waveguides was one quarter wavelength ($\lambda_g/4$) long at operating frequency, where λ_g is the guide wavelength. The impedances of the ridged section are evaluated by the relation,

$$\frac{Z_{n+1}}{Z_n} = \exp \left[2^{-N} C_n^N \ln \frac{Z_L}{Z_0} \right] \dots\dots\dots(4.2)$$

where n is the number of ridged section, N is the total number of the ridged section, C_n^N is the binomial coefficients i.e. $N! / (N-n)! n!$. Variation of impedance with the length for a standard and a ridged waveguide is shown in Fig. 4.27.

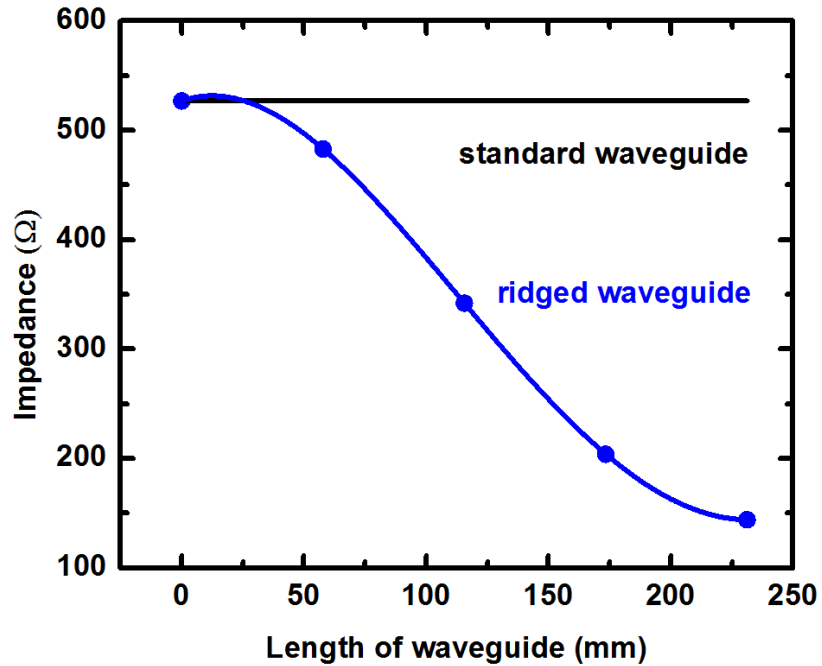


Figure 4.27 : Variation of impedance with the length for a standard waveguide and a ridged waveguide. (The solid blue curve is for visual aid only and dot indicates the calculated impedance in that section, ref. Table 4.3)

The figure shows that the impedance of a ridged waveguide decreases exponentially with increasing the number of ridged sections and progressively approaches to plasma impedance at the fourth section of the ridged waveguide. On the other hand, the voltage-current impedance of a standard waveguide remains constant. The dimensions and impedances of the four sections of the ridged waveguide are shown in Table 4.3.

Number of Ridge Sections (N)	Impedance of the Ridge Section (Z_n) (Ω)	Gap of the Ridge Section ($2b_2$) (mm)
1	483	32
2	341	22
3	203	13
4	144	9

Table 4.3 : The dimensions and impedances of the four sections of the ridged waveguide.

Electromagnetic analysis of a ridged waveguide : The dimensions obtained with the analytical approach, as shown in Table 4.3, are used for generating a model structure of a ridged waveguide. An electromagnetic model of a ridged waveguide coupled with a plasma chamber is shown in Fig. 4.28.

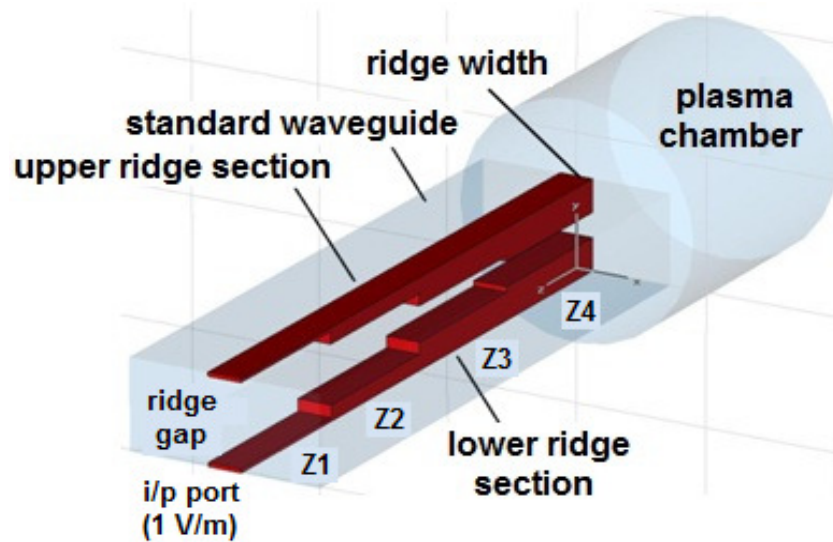


Figure 4.28 : An electromagnetic model of a ridged waveguide coupled with a plasma chamber.

It has a standard waveguide part, an upper and a lower ridge section and a plasma chamber. For modelling purpose, the material for standard waveguide and ridged sections were chosen as vacuum and perfect electrical conductor respectively. The transient solver module of the *microwave studio* was used for modelling the waveguide. The transient signal was fed from a standard waveguide, as input port 1, and ridged waveguide as output port 2. The structure was discretized at 10 lines per wavelength mesh density. The complete geometry had 28510 mesh cells. The dimension of the ridge gap I to IV was varied in the steps of 1 mm and corresponding scattering parameters were recorded at 2.45 GHz frequency. The simulation results in terms of scattering parameters at 2.45 GHz frequency for ridge gap I, II, III, and IV are presented in Figs. 4.29, 4.30, 4.31, and 4.32.

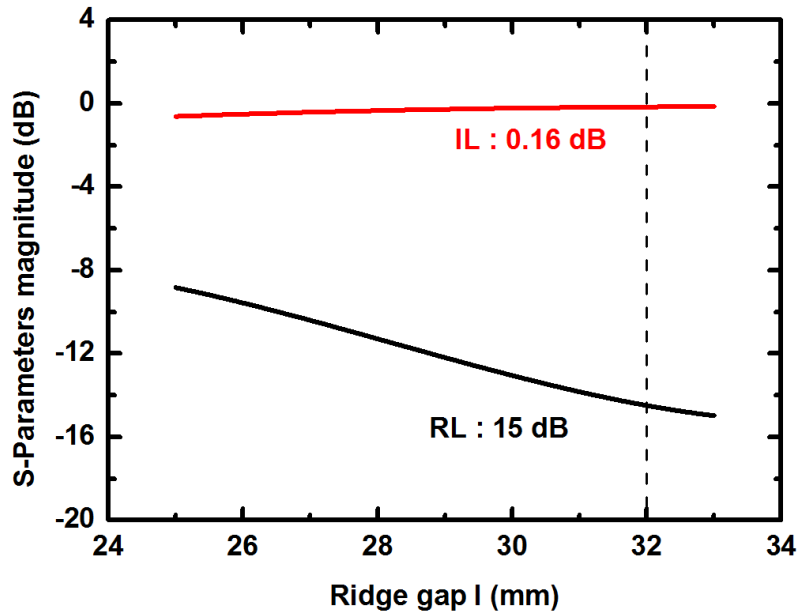


Figure 4.29 : The simulated variations of the return loss (S11), the insertion loss (S21) for a ridge gap I at 2.45 GHz frequency for the ridged waveguide.

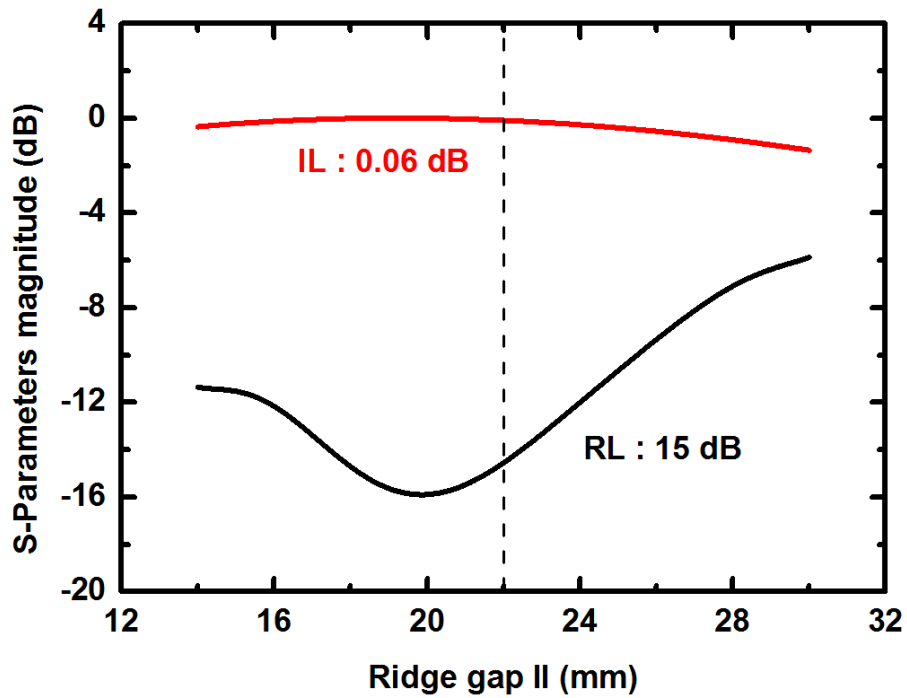


Figure 4.30 : The simulated variations of the return loss (S11), the insertion loss (S21) for a ridge gap II at 2.45 GHz frequency for the ridged waveguide.

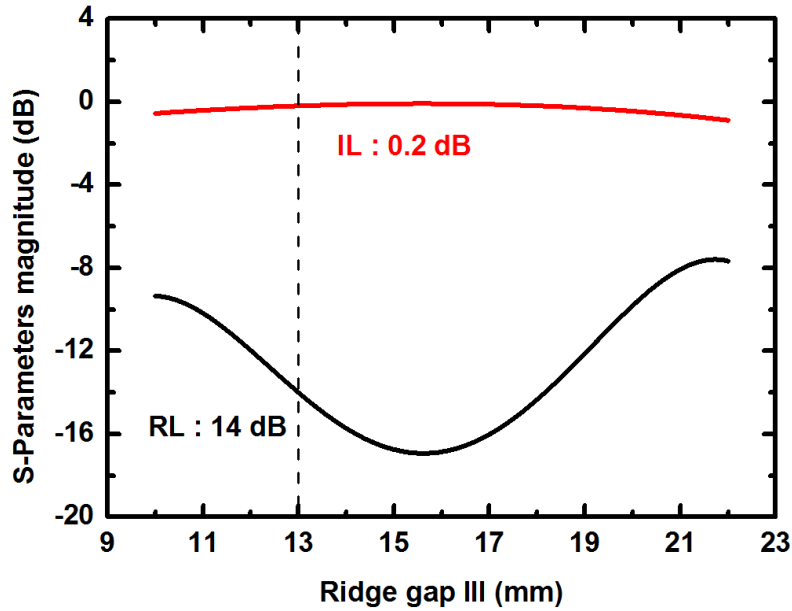


Figure 4.31 : The simulated variations of the return loss (S_{11}), the insertion loss (S_{21}) for a ridge gap III at 2.45 GHz frequency for the ridged waveguide.

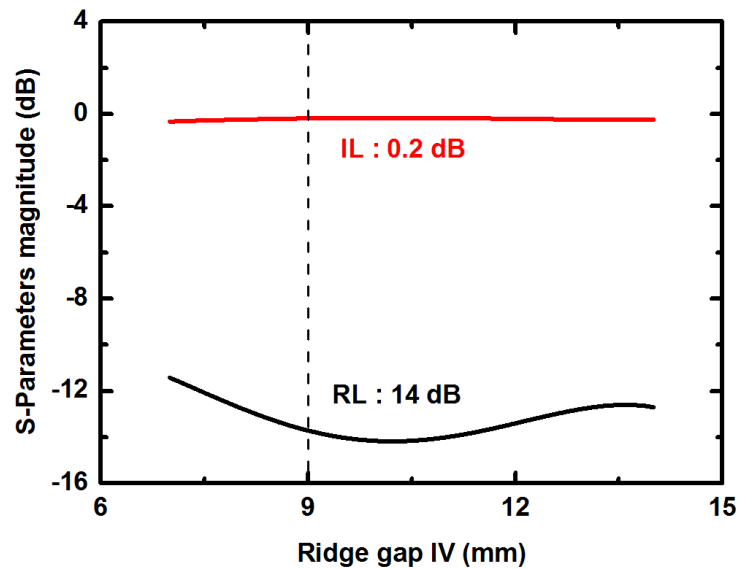


Figure 4.32 : The simulated variations of the return loss (S_{11}), the insertion loss (S_{21}) for a ridge gap IV at 2.45 GHz frequency for the ridged waveguide.

In the above figures, the dashed lines show the actual gap of each ridge. It is observed from these figures that the scattering parameters S_{11} (return loss) is sensitive to the gap of the ridge, whereas the other parameter S_{21} (insertion loss) is not so sensitive. Figure 4.29, shows

that the return loss decreases with increasing gap of ridge gap I. The behaviour seen in Figure 4.30, 4.31, 4.32 is the return loss is 15 dB at an analytical ridged gap values corresponding to the 2.45 GHz frequency and the insertion loss is close to zero. The figure 4.33 show that, optimized ridge gaps (31 mm, 20 mm, 15.5 mm, and 10 mm) are closed to the analytical ridged gap values. The optimized variations of the return loss (S11), the insertion loss (S21) for the ridged waveguide with frequency range between 2.4 to 2.5 GHz is shown in Fig. 4.33.

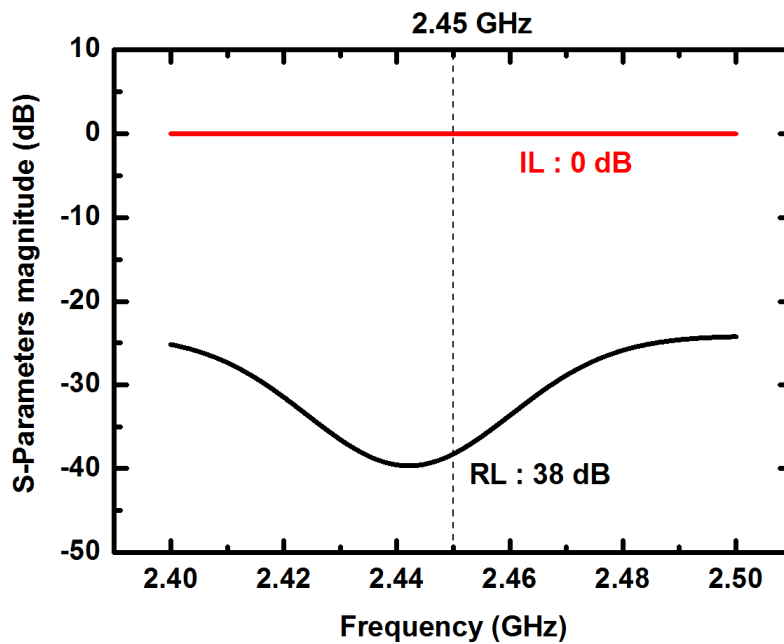


Figure 4.33 : The optimized variations of the return loss (S11), the insertion loss (S21) for the ridged waveguide with frequency range between 2.2 to 2.7 GHz.

The return loss of the integrated geometry of the ridged waveguide is 38 dB (i.e. power transmission ~ 100 %) and corresponding insertion loss is 0 dB at 2.45 GHz frequency. The variations of the return loss (S11), the insertion loss (S21) with ridge width at 2.45 GHz frequency for the ridged waveguide is shown in Fig. 4.34. It shows that the return loss is first decreasing with increasing width of ridge sections from 10 to 11 mm, due to establishing the uniform electric field distribution between the ridge gap. Beyond this, it

increases and reaches a saturation level, may be due to distortions of the electric field intensity between the ridged gap. The insertion loss does not change much; it remains close to zero with increasing the ridged width.

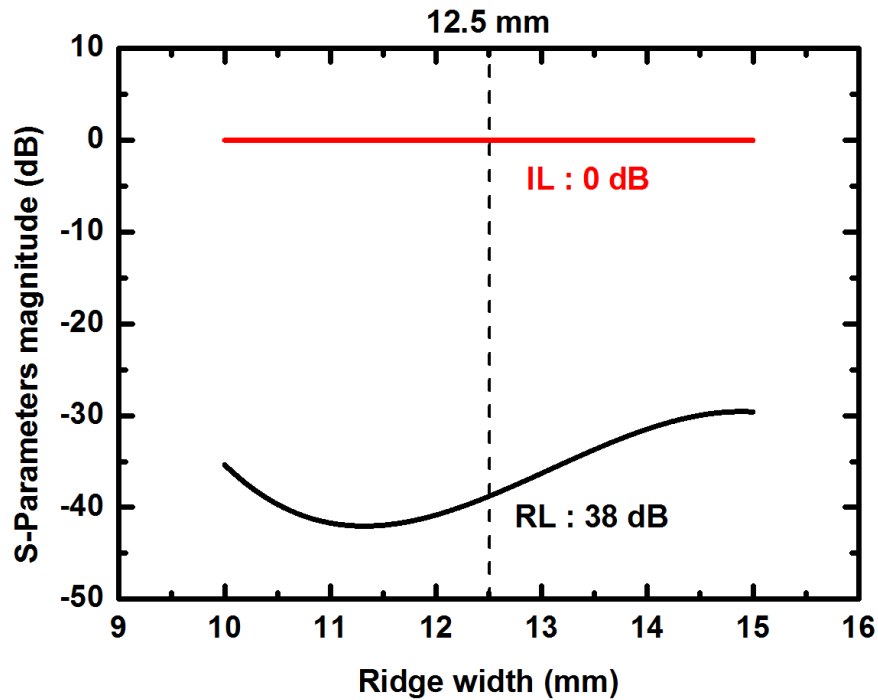


Figure 4.34 : The variations of the return loss (S_{11}), the insertion loss (S_{21}) with ridge width at 2.45 GHz frequency for the ridged waveguide. Dashed lines show the actual width of ridge.

A vector plot of the distribution of the electric field for a standard waveguide is shown in Fig. 4.35. The maximum electric field amplitude along Z-axis is about 757 V/m at port 1. A vector plot of the distribution of the electric field for a ridged waveguide is shown in Fig. 4.36. The maximum electric field amplitude along Z-axis is about 1574 V/m, which is about two times that of the standard waveguide as evaluated with analytical approach and the distribution of electric field intensity is also uniform in the ridge gap.

The electric field intensity distribution in the horizontal mid-plane for a standard waveguide and a ridged waveguide of width 12.5 mm is shown in Fig. 4.37. The electric field

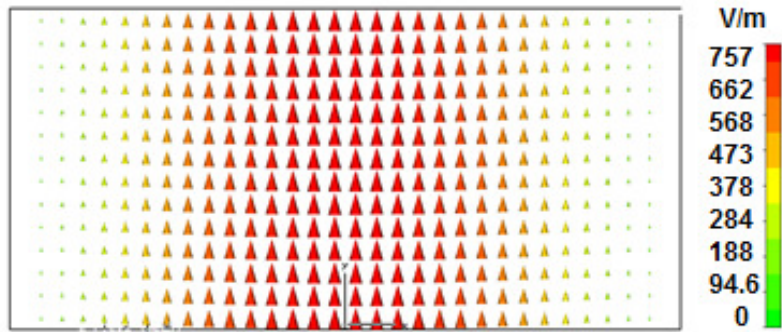


Figure 4.35 : A vector plot of the distribution of the electric field for a standard waveguide.

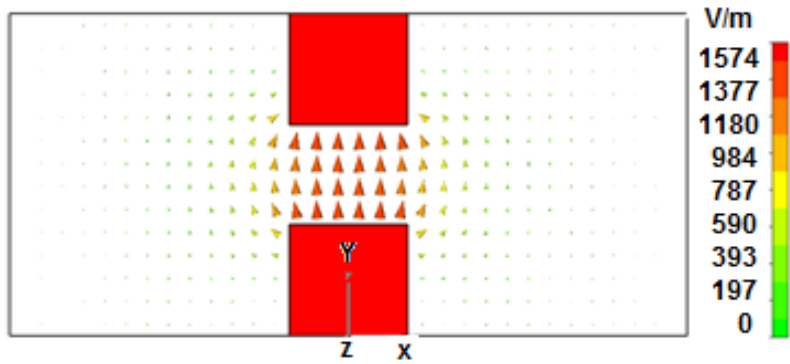


Figure 4.36 : A vector plot of the distribution of the electric field for a ridged waveguide.

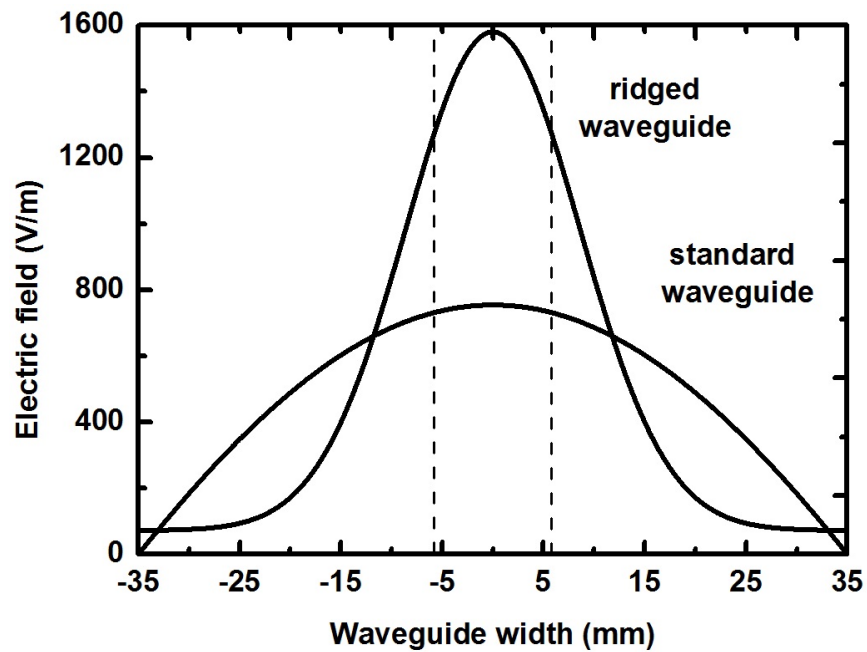


Figure 4.37 : The electric field intensity distribution in the horizontal mid-plane for a standard waveguide and a ridged waveguide of width 12.5 mm.

intensity for a standard waveguide varies in the form of an arc of sinusoidal pattern along the width of waveguide, while that for a ridged waveguide has a Gaussian distribution, with maximum electric field intensity localized within the ridged gap.

Microwave coupling study : For obtaining the best microwave coupling [106,107,108] between the optimized ridged waveguide and the plasma chamber, the optimized ridged waveguide was coupled to the plasma chamber, to check the good match between the ridged waveguide and the plasma and to produce the electric field intensity maximum at the centre of the plasma chamber. The electric field intensity in a horizontal plane of the ridged waveguide coupled with the plasma chamber is shown in Fig. 4.38. The electric field intensity in a transverse plane of the ridged waveguide coupled with the plasma chamber is shown in Figure 4.39. It shows that the absolute electric field intensity in the horizontal plane and in the transverse plane is about 2750 V/m at 2.45 GHz, at the centre of the plasma chamber. It also shows that the electric field intensity is maximum at the centre of

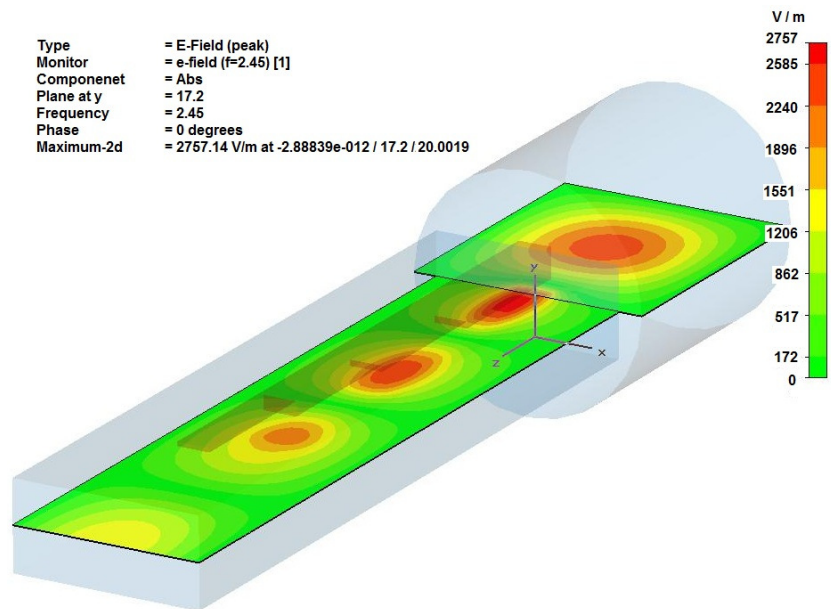


Figure 4.38 : The electric field intensity in the horizontal plane of the ridged waveguide coupled with the plasma chamber.

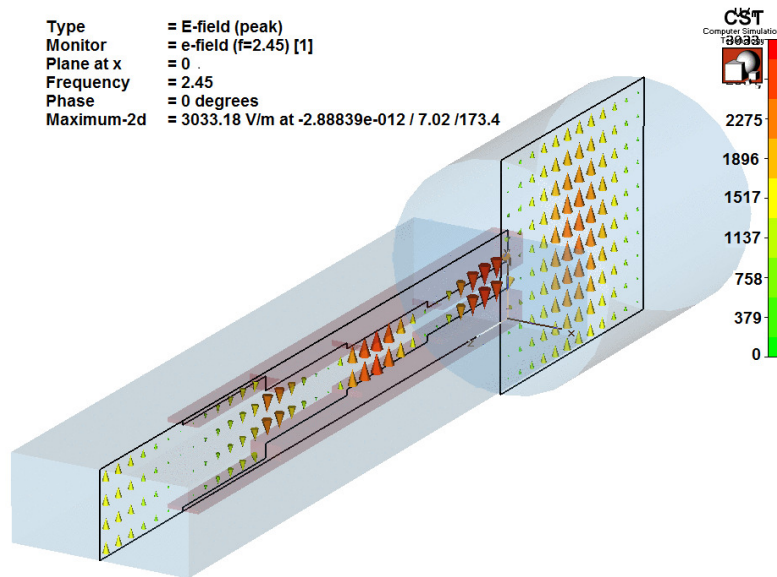


Figure 4.39 : The electric field intensity in a transverse plane of the ridged waveguide coupled with the plasma chamber.

the plasma chamber, suitable to produce high density plasma and further supports the extraction of higher ion beam current. Thus, it is observed that the microwave energy is well coupled to the plasma chamber using a ridged waveguide.

7) Glass-water load : There are various materials like graphite, cement with graphite, wood, quartz, water etc. which are used as a microwave load depending on the level of microwave power to be dissipated [109,110]. We have used water as an absorbing material, since it is a good absorber of the microwave power. One can absorb a good amount of microwave power easily with continuous flow of water. The heat dissipated is removed by continuous flow of water. We have designed and fabricated a pyrex glass-water load for absorbing the 3 kW microwave power at 2.45 GHz frequency, for the characterization of the microwave components at high power. This glass-water load was connected at the end of the microwave-integrated line for initial high power characterization of the microwave components. The glass-water load was fabricated using Pyrex glass having tube diameter of 12 mm and length equal to one guide wavelength. The Pyrex glass-water load has kovar

fittings at both ends of the tube. The glass-water load was calibrated using standard network analyzer at the operating frequency. A photograph of the glass-water load is shown in Fig. 4.40.



Figure 4.40 : A photograph of the glass-water load.

4.3 Characterization of the Microwave Components

The low power characterization [111,112] of the microwave components was carried out using a network analyzer (Model : E5071 ENA series with electronic-cal kit, N4431-60004, Make : M/s Agilent Technologies Pvt. Ltd., USA) for validating the design procedure. Scattering parameters of the microwave components were measured using network analyzer. The test setup for low power characterization of the microwave components using network analyzer is shown in Fig. 4.41.

The full term characterization (two port scattering parameters viz. S11, S21, S12 and S22) was carried out with frequency 2.4 to 2.5 GHz (marker at centre frequency 2.45 GHz, bandwidth 100 MHz), with various standards of network analyzers. The measurement inaccuracy in characterization was 10 m dB. The measurement accuracy in the results could be maintained by routine characterization of the microwave components. The measured results for the directional coupler are shown in Fig. 4.42.

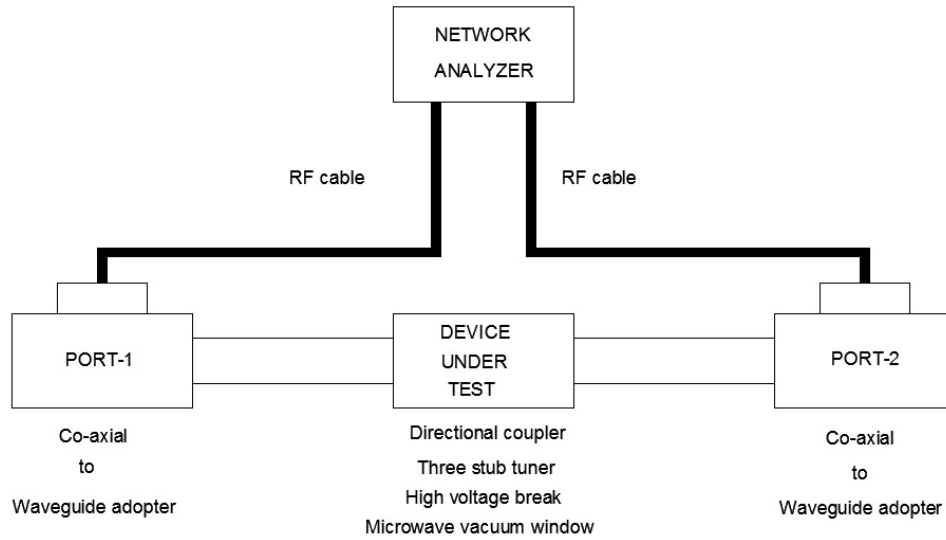


Figure 4.41 : The test setup for low power characterization of microwave components using network analyzer.

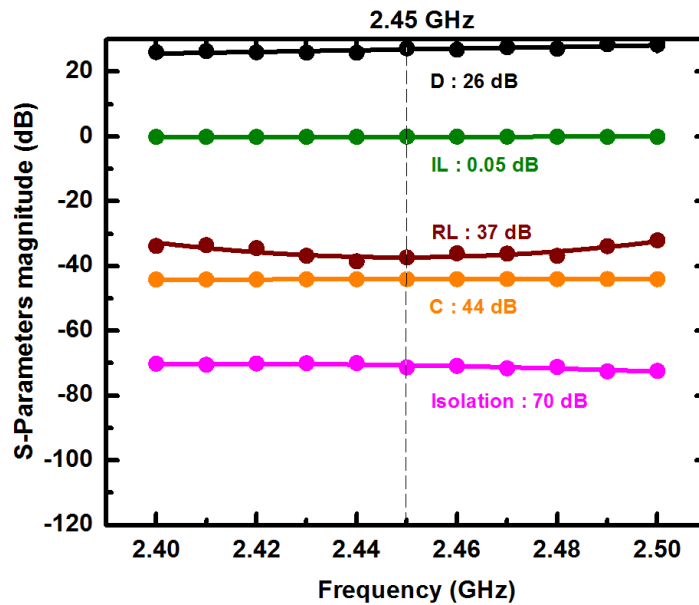


Figure 4.42 : The measured results for the directional coupler. The solid curve is for visual aid only.

The mechanical error of fabrication etc. could not be taken into account in the *microwave studio* simulation. Hence, some differences in simulations and actual results were expected. The results are summarized as : the insertion loss for the device is close to 0.05 dB,

the return loss is 37 dB (measured) and 100 dB {Fig. 4.11, software, assumes ideal conditions}, the coupling factor 44.5 ± 0.5 dB, the directivity is 25.5 ± 0.5 dB at 2.45 GHz frequency, except the return loss, the measured results are close to optimized results. This validates the design procedure of the directional coupler. For the low power measurements of the three-stub tuner, two cases were studied i.e. all stubs were FULL IN and FULL OUT to see the impedance variations on Smith chart. The measured results for the three-stub tuner when stubs are FULL IN are shown in Fig. 4.43. One can see from the figure that, when all stubs are FULL IN, the insertion loss is 32 dB and the return loss is 0.3 dB. In this case, the microwave power was severely reflected which causes more insertion loss. The measured results for the three-stub tuner when stubs are FULL OUT are shown in Fig. 4.44. It is noted from this figure that the measured insertion loss is 0.3 dB and remains unchanged up to 2.46 GHz, whereas the return loss is close to 26 dB up to 2.46 GHz, and beyond this it increases with increasing frequency. The behaviour of the figure is as expected, since the obstacles of the stubs produce standing wave patterns during the propagation of the microwaves which cause the losses of microwave power.

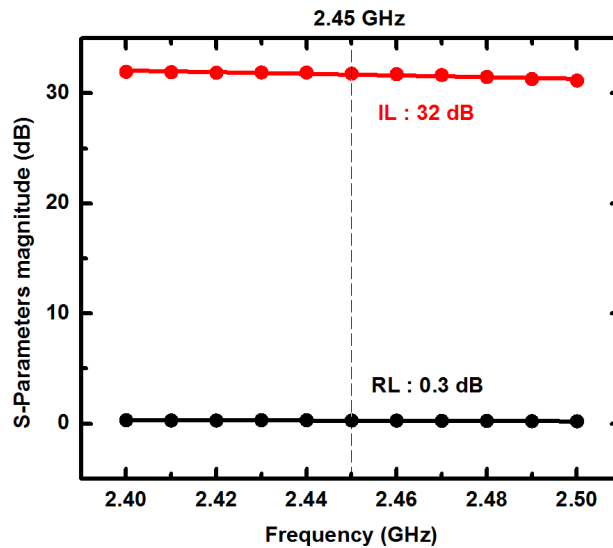


Figure 4.43 : The measured results for three-stub tuner when stubs are FULL IN. The solid curve is for visual aid only.

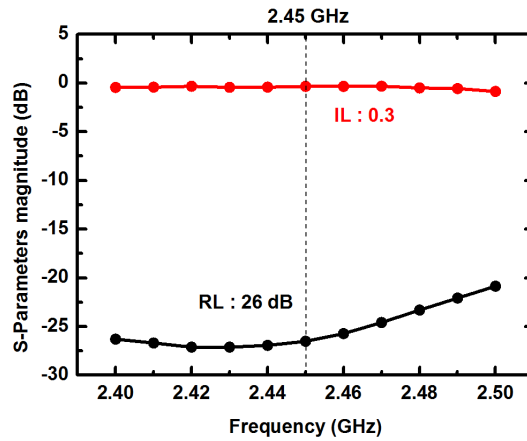


Figure 4.44 : The measured results for the three-stub tuner when stubs are FULL OUT. The solid curve is for visual aid only.

Effectively it covers the wide range of insertion loss 3 to 30 dB (due to obstacles of stubs, simply comprise for impedance matching) and the return loss is 0 to 25 dB. The insertion loss was brought down to less than 1 dB with the multiple combinations of stubs during the operation of the source (matched condition i.e. low reflected power). The measured results for the high voltage break are shown in Fig. 4.45. It is noted from the figure, that the return loss is 25 dB {Fig. 4.18, software, 40 dB} and the insertion loss is 0.1 dB {Fig. 4.18, software, 0.08 dB} at 2.45 GHz frequency.

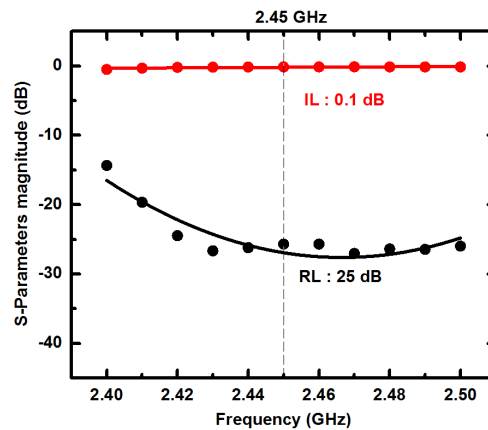


Figure 4.45 : The measured results for the high voltage break. The solid curve is for visual aid only.

The measured results for the microwave vacuum window are shown in Fig. 4.46. It is noted from the figure, that the return loss is 21 dB {Fig. 4.21, software, 75 dB} and the insertion loss is 0.3 dB {Fig. 4.21, software, 0.0 dB} at 2.45 GHz frequency. The discrepancies in the measured and software results may be due to fabrication, misalignment error, test port match, waveguide to coaxial adaptor etc. and software assumes always ideal matched conditions.

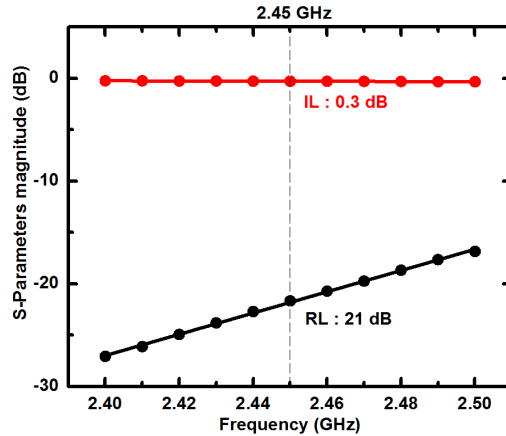


Figure 4.46 : The measured results for the microwave vacuum window. The solid curve is for visual aid only.

Finally, all the microwave components were integrated with the glass-water load at the end, for the high power characterization of the microwave components. This microwave line was energized and tested for 2 kW of microwave power at 2.45 GHz frequency. The performance of the microwave line was quite satisfactory. A radio frequency and microwave survey using radiation survey meter (Model : HI 1501, Make : M/s Richardson Electronics Pvt. Ltd., USA) was carried out. A maximum radiation leakage of 2-3 mW/cm² was observed around the microwave vacuum window and the high voltage break. The radiation level was found to be well within the permissible limit. Further, to avoid any radiation leakage from the dielectric portion, a metallic cover was wrapped externally at the joint. An integrated

schematic diagram of the microwave components with glass-water load for high power characterization is shown in Fig. 4.47.

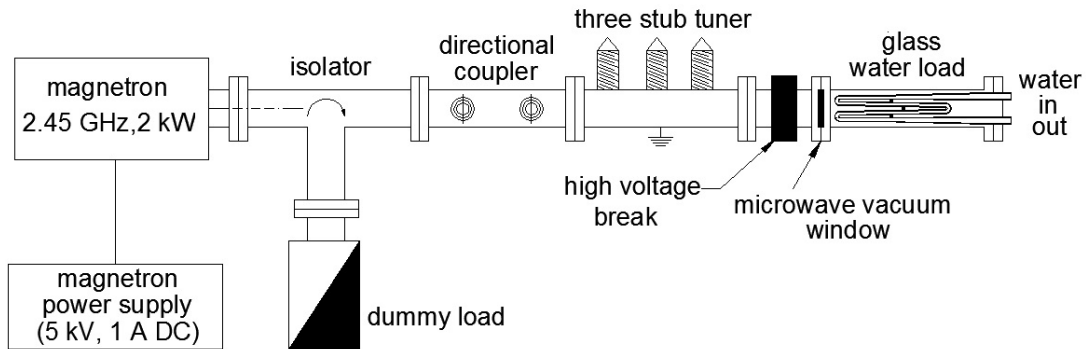


Figure 4.47 : An integrated schematic diagram of the microwave components with glass-water load for high power characterization.

Variation of microwave output power with the cathode current of the magnetron is shown in Fig. 4.48. The figure shows that microwave output power increasing linearly with increase in the cathode current of the magnetron, with a slope of 2.73 W/mA. The reflected power was minimized during the course of experiments with the tuning stubs of the three-stub tuner.

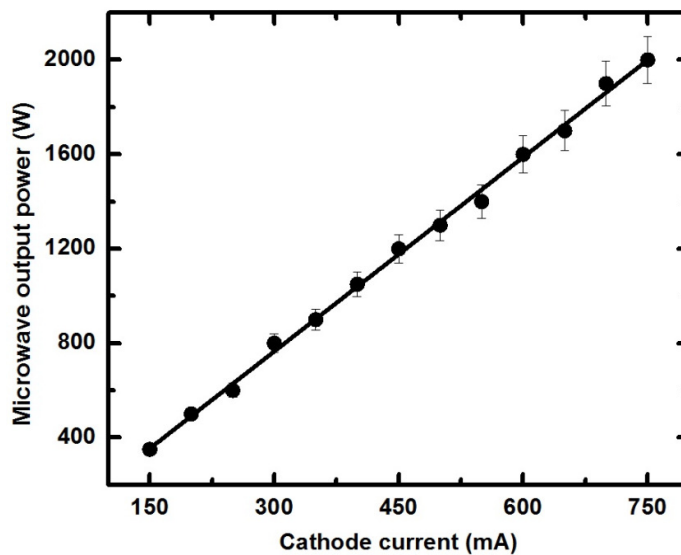


Figure 4.48 : Variation of the microwave output power with the cathode current of the magnetron. The solid curve is for visual aid only.

CHAPTER 5

Electromagnet and its Power Supply

This chapter gives details of the design, development, and characterization of the electromagnets used to produce desired magnetic field to confine the plasma, and also to make the electrons gyrate and undergo electron cyclotron resonance with the applied microwave field. The three electromagnets are water-cooled and energized independently with the use of three independent power supplies. With the use of three electromagnets, it is possible to operate the source in a) off-resonance, b) mirror, and c) resonance flat magnetic field configurations, for the singly as well multiply charged states. The magnetic field configurations were optimized using *Poisson* software.

There are various types of magnetic field configurations which have been used for the generation as well as confinement of the plasma axially as well as radially. The proper selection of the magnetic field configurations is desirable to produce the singly and multiply charged ion beams. The most common magnetic field configurations which are commonly used are : mirror field, flat field, B-minimum field, dipole, multi-pole field [6, 113, 114, 115, 116]. These magnetic field configurations may be achieved by either combination of electromagnets, permanent magnets, and superconducting magnets. In the presence of the magnetic field, as the charged particles are forced to gyrate along the magnetic field lines, their diffusion perpendicular to the magnetic field lines is restricted, thereby confining the plasma radially to produce homogeneous, high-density plasma. Our aim is to produce the singly charged proton beam, so we have used conventional method for producing the magnetic field configuration. The design details, fabrication and field mapping is described in the following sections.

5.1 Magnetic Field Design

The magnetic field required for ECR action is given by [6,53,54],

$$B = 357f_{rf} \left(\text{from } \omega_{ce} = \frac{eB}{m_e} \right) \dots\dots\dots(5.1)$$

where f_{rf} is the microwave frequency (GHz), B is the magnetic field (G), m_e is the mass of an electron (kg), and e is the electron charge (C). The magnetic field corresponding to a microwave frequency of 2.45 GHz is 875 G. Standard software packages like *2D-Poisson* and *Pandira* [117], *3D-Opera* [118], and *Intmag* [119] are commonly used for simulation of magnetic field patterns using solenoid coils, or permanent magnets. Here we have used the “*2D-Poisson*” software package for simulation of the magnetic field pattern using solenoid coils with iron jacket (electromagnet) for shielding the fringing magnetic field and to reduce the power consumption that would otherwise be very high. The use of jacket is to provide a return path for the magnetic field lines and thereby shield the adjacent components. The use of electromagnet has wide flexibility of tuning the plasma to get the best operating conditions. The use of electromagnet (instead of permanent magnets) helps one to investigate the plasma parameters to optimize the beam current.

To start the simulations, the initial parameters of the solenoid coils with iron jacket were fixed as : inner radius 75 mm, outer radius 150 mm, the gap between solenoid coils 20 mm, width to be 70 mm and 80 mm for middle and side solenoid coils respectively. Three solenoid coils were used to get 1) mirror field, 2) flat field, and 3) off-resonance magnetic field configuration [120]. Two side solenoid coils, which were identical, generated the mirror field, and the middle solenoid coil was used to compensate the dip in the magnetic field, to have a flat magnetic field. The use of flat field configuration with high field in the centre has been reported to provide better extraction current in the high intensity ion sources. The combinations of these three solenoid coils can also produce the off-resonance magnetic field. The permeability table for soft iron, low carbon, ‘A’ grade steel has been incorporated in the

Poisson code itself. A numbers of iterations were carried out to get the desired magnetic field configurations. This was accomplished by varying the size of the solenoid coils, thickness of iron jacket, and amp-turns (NI). The optimum values of the amp-turns (NI) for the side and middle solenoid coils were obtained as 12950 and 8250 respectively. Based on these parameters, the total length of the conductor was calculated. A copper conductor having a square cross-section (5 mm × 5 mm) with hole diameter 3 mm for water-cooling was used. The optimized design parameters for solenoid coil with iron jacket are given in Table 5.1. The optimized axial flux along the axis of the source using the *Poisson* software is shown in Fig. 5.1. The optimized mirror magnetic field profile using the *Poisson* software along the axis of the source is shown in Fig. 5.2. The optimized flat magnetic field profile using the *Poisson* software along the axis of the source is shown in Fig. 5.3.

Description	Solenoid coil 1	Solenoid coil 2	Solenoid coil 3
Coil type	Water-cooled solenoid coils		
Coil size	φ300 mm × 80 mm	φ300 mm × 70 mm	φ300 mm × 80 mm
Bore diameter	φ150 mm		
amp-turns (NI)	12950	8250	12950
Conductor size	5 mm × 5 mm × φ3 mm copper		
N, N / L, L	144,12,12	110,10,11	144,12,12
Total conductor length	95 meters	80 meters	95 meters
Power supply	0-32 V, 100 A DC × (Three)		
Coil resistance (measured)	0.15 Ω	0.13 Ω	0.16 Ω

Table 5.1 : The optimized design parameters for the solenoid coil with iron jacket.

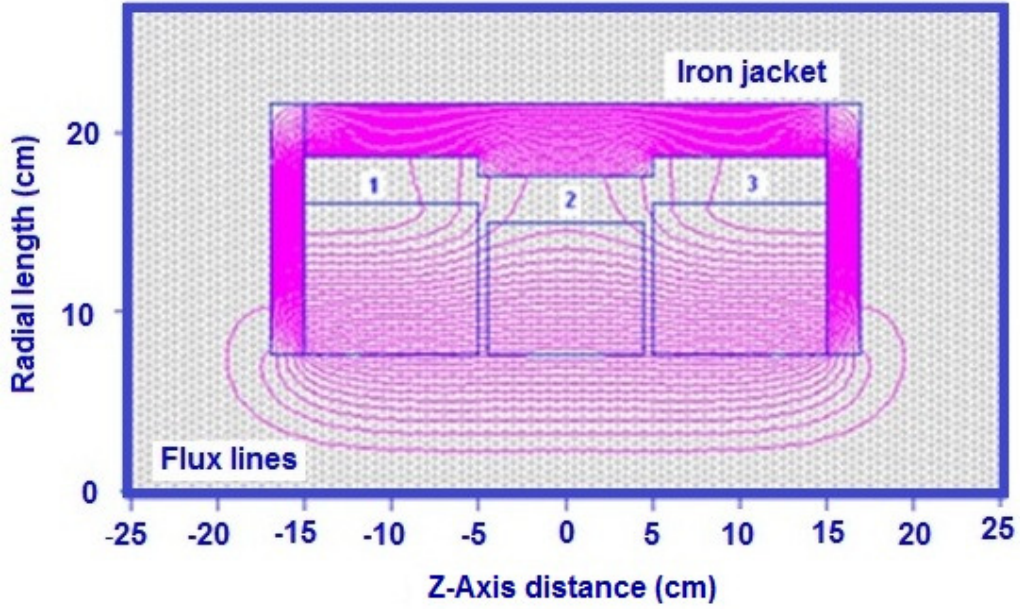


Figure 5.1 : The optimized axial flux along the axis of the source using the Poisson software (1, 2, and 3 marked are the solenoid coils).

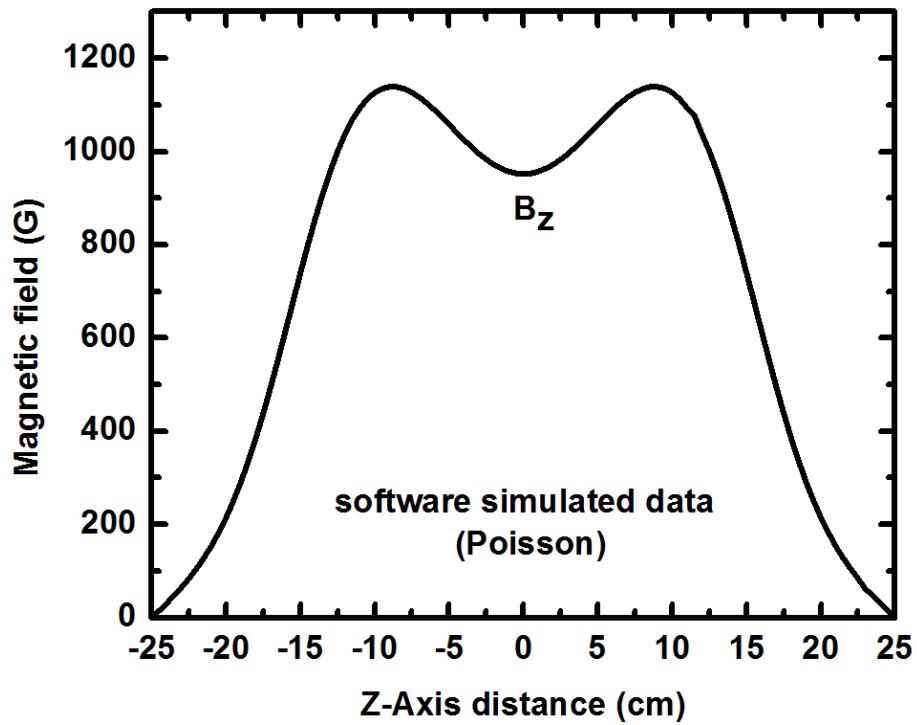


Figure 5.2 : The optimized mirror magnetic field profile using the Poisson software along the axis of the source.

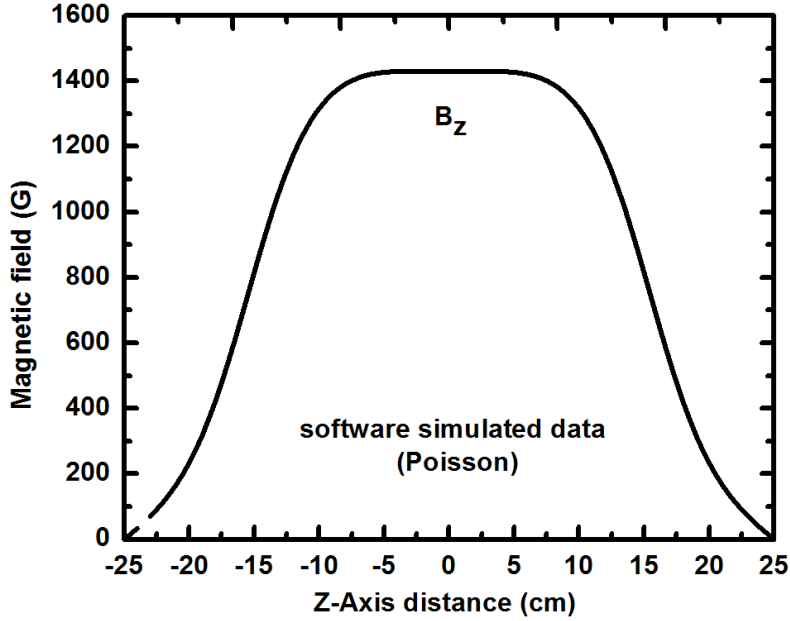


Figure 5.3 : The optimized flat magnetic field profile using the Poisson software along the axis of the source.

The calculation was also done analytically using standard relations for calculating magnetic field. The magnetic field on the axis of loop can be written as [121],

$$H_z(z,0) = \left[\frac{2\pi I}{10} \right] \left[\frac{a^2}{(a^2 + z^2)^{3/2}} \right] \dots\dots\dots(5.2)$$

The central field H_0 , at $z = 0$ is,

$$H_0 = \left[\frac{2\pi I}{10a} \right] \dots\dots\dots(5.3)$$

or,

$$H_z(z,0) = H_0 \left[\frac{a^3}{(a^2 + z^2)^{3/2}} \right] \dots\dots\dots(5.4)$$

where H is the magnetic field (oersteds), I is the loop current (A), "a" is the radius of the loop (cm), and "z" is the on-axis distance from the loop (cm). The current loop can be thought of an element of a larger coil and can form the basis for subsequent integrations,

$$H_0 = \left[\frac{2\pi}{10} \right] I \int_{-b}^b \frac{a^2}{(a^2 + z^2)^{3/2}} dz \dots\dots\dots(5.5)$$

$$= \left[\frac{4\pi}{10} \right] \Gamma \frac{b}{(a^2 + b^2)^{1/2}} \dots\dots\dots(5.6)$$

$$= \left[\frac{4\pi}{10} \right] \Gamma \frac{\beta}{(1 + \beta^2)^{1/2}} \dots\dots\dots(5.7)$$

where $\Gamma = \frac{NI}{2b}$, and $\beta = \frac{b}{a}$ (5.8)

We can further integrate to derive the central field expression for a finite thickness solenoid of uniform density. The elemental current per unit cross-section is,

$$j\lambda = \frac{NI}{2b(a_2 - a_1)} \dots\dots\dots(5.9)$$

which defines the overall current density $j\lambda$, where j is the current density in the conductor, and λ is the space factor. Then,

$$H_0 = \left[\frac{2\pi}{10} \right] j\lambda \int_{-a_1}^{a_2} \int_{-b}^b \frac{a^2}{(a^2 + z^2)^{3/2}} dz dr \dots\dots\dots(5.10)$$

$$H_0 = j\lambda a_1 \frac{4\pi\beta}{10} \ln \frac{\alpha + (\alpha^2 + \beta^2)^{1/2}}{1 + (1 + \beta^2)^{1/2}} \dots\dots\dots(5.11)$$

$$H_0 = j\lambda a_1 \frac{4\pi\beta}{10} \left(\sinh^{-1} \frac{\alpha}{\beta} - \sinh^{-1} \frac{1}{\beta} \right) \dots\dots\dots(5.12)$$

where $\alpha = \frac{a_2}{a_1}$, and $\beta = \frac{b}{a_1}$ (5.13)

$$F(\alpha, \beta) = \frac{4\pi\beta}{10} \left(\sinh^{-1} \frac{\alpha}{\beta} - \sinh^{-1} \frac{1}{\beta} \right) \dots\dots\dots(5.14)$$

$$F(\alpha, \beta) = \frac{4\pi\beta}{10} \ln \frac{\alpha + (\alpha^2 + \beta^2)^{1/2}}{1 + (1 + \beta^2)^{1/2}} \dots\dots\dots(5.15)$$

where $F(\alpha, \beta)$ is entirely geometry dependent factor.

We can write the power in an elemental cross-section and integrate over the coil, if the conductor current density j and the resistivity of the material ρ (ohm \times cm) are considered to be constant over the volume. Then,

$$W = \int dW = j^2 \rho \int dv \dots\dots\dots(5.16)$$

$$= j^2 \rho \lambda a^3 2\pi\beta(\alpha^2 - 1) \dots\dots\dots(5.17)$$

where λ is the space factor and is given by the active cross-section of the winding / total cross-section of the winding.

5.2 Fabrication of Electromagnet

The solenoid coils were fabricated using super enamelled hollow copper conductor (refrigeration type) of square cross-section (5 mm \times 5 mm) with hole diameter 3 mm (for water circulation). The insulation to the conductor layer was provided using ‘H’ class fibre glass insulating tape. The diameter of the bore was 150 mm so that plasma chamber, including water-cooling jacket and high voltage insulator, could be fitted in this. One side flange of the plasma chamber was split type, so that the solenoid coils could be fitted to the plasma chamber. The bore of the solenoid coils was fabricated using high voltage glass epoxy. Each side solenoid coil had 12 turns / layer (N / L), and 12 layers (L), {i.e. 144 turns (N)}, and central solenoid coil had 10 turns / layer (N / L), and 11 layers (L) {i.e. 110 turns (N)}. The total length of the conductor used for the side solenoid coils and the central solenoid coil was 95 m and 80 m respectively. The solenoid coils were impregnated into high voltage, high temperature epoxy for the outer layer insulation. The iron jacket of the solenoid coils was fabricated from 10 mm thick low carbon ‘A’ grade steel. The iron jacket was fabricated in five parts consisting of two side plates and three cylindrical shapes, of

diameter equal to the bore diameter of the solenoid coils. This electromagnet was placed around the plasma chamber to produce the necessary magnetic field.

The solenoid coils were cooled using low conductivity water (conductivity less than 1 $\mu\text{S}/\text{cm}$) having inlet temperature 27 °C. Based on the length of the conductor, the water pressure drop and flow, and the inlet, outlet connections were provided. Total five inlet and five outlet connections were provided. The water flow rate of 3 l/min and pressure of 3.5 kg/cm^2 was maintained. The rise in temperature was restricted to less than 20 °C. The inductance and the resistance of the solenoid coils were measured using precision LCR meter (Model : PM 6306, Make : M/s Fluke). The high voltage insulation to the solenoid coils up to 5 kV DC was tested using high voltage Megger (Model : 220123-47, Make : M/s Megger, U.K.). The solenoids coils were at ground potential and were isolated from the plasma chamber using a polypropylene cylinder. Appropriate measures were taken to ensure electrical isolation between the microwave source, the plasma chamber and the solenoid coils.

5.3 Magnetic Field Mapping

The performance of an electromagnet gets influenced by the design and material limitations, errors in construction, and the stability of the power supply used to energize it. The magnetic field measurements [122] were done using computer controlled three-axis coordinate measuring machine. A Hall probe (Model : MPT-141, Make : Group 3 Technology Ltd., Germany) was attached at the Y-arm with a probe holder. The Hall probe had field ranges 0.3, 0.6, 1.2, 3.0 tesla and corresponding serial / general purpose interface bus (GPIB) resolutions 0.001, 0.01, 0.01, 0.01 G, respectively. The probe size was 15 mm \times 5 mm \times 2 mm, with a sensitive area of 1 mm \times 0.5 mm. The measurement rate was 10

measurements per second. The error associated with the magnetic field measurements was less than 0.5 %. The electromagnets were energized using three independent power supplies of rating 0-32 V and 100 A DC. The stability of the power supplies was 0.1 %.

The quality of the electromagnet was fully characterized before installation in the dynamical environment. The successful operation of an ECR source greatly depends on the quality of the magnetic elements and the uniformity of the magnetic field (better than 5 G). Imperfections in the magnetic field can cause diffusion of the plasma particles to the wall of the plasma chamber. The measured mirror magnetic field profile along the axis of the source is shown in Fig. 5.4. The measured flat magnetic field profile along the axis of the source is shown in Fig. 5.5. The measured values (i.e. experimental measured data shown in Figs. 5.4 and 5.5) and the design values (i.e. simulation results shown in Figs. 5.2 and 5.3) agree within 3 %. The electromagnets were characterized for 50 A to 75 A at steps of 5 A. Variation of magnetic field with the solenoid current is shown in Fig. 5.6. It is observed to be linear with a slope of 21.5 G/A. The mirror ratio (maximum to minimum) field of the electromagnet was 1.1. These electromagnets with the proper combinations of the solenoid coils are capable of producing mirror, flat, and off-resonance magnetic field configurations. The solenoid coil with iron jacket offers a continuous control over the axial magnetic field, giving tuning capability, and allowing the possibility of changes in the source operation. The possibility of a fine tuning of the magnetic field is very important for the stability of an ECR plasma source as any small change in the distribution of the axial magnetic field can result large changes in the source parameters. The amp-turns (NI) were determined to produce the maximum possible magnetic field on the axis.

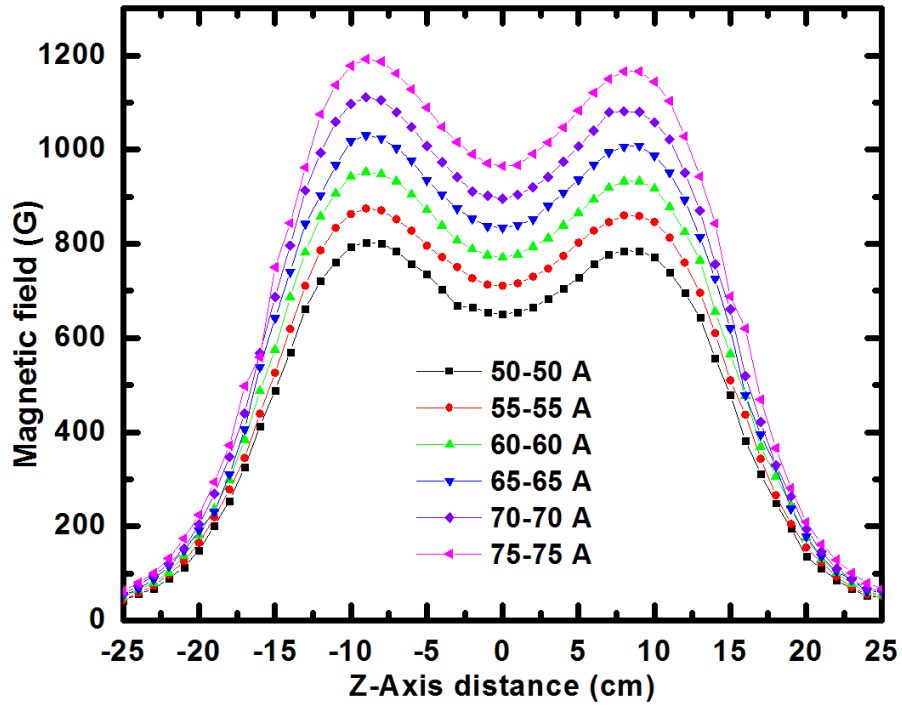


Figure 5.4 : The measured mirror magnetic field profile along the axis of the source.

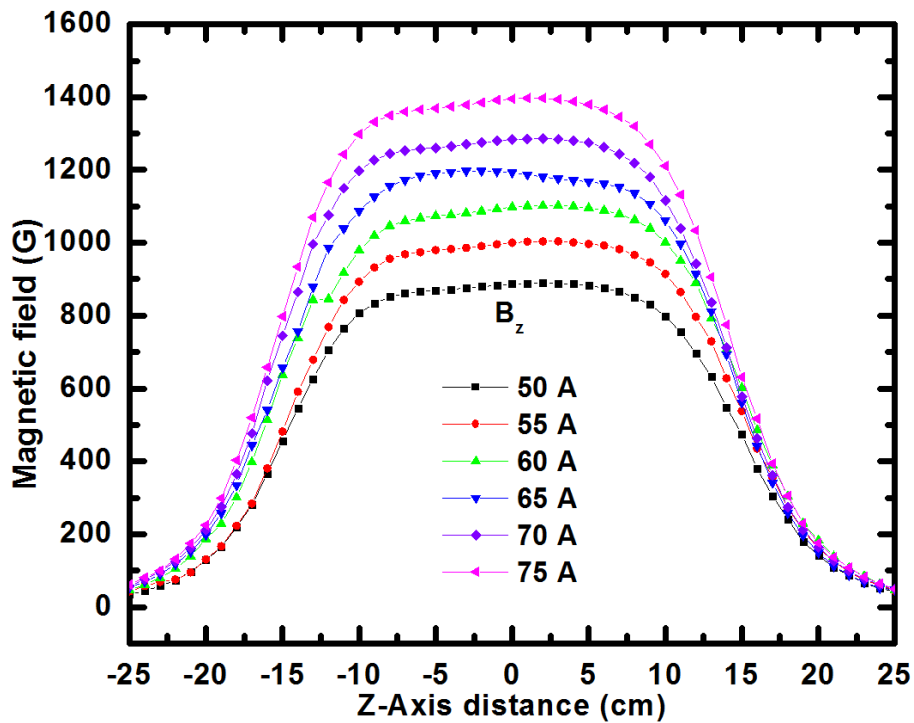


Figure 5.5 : The measured flat magnetic field profile along the axis of the source.

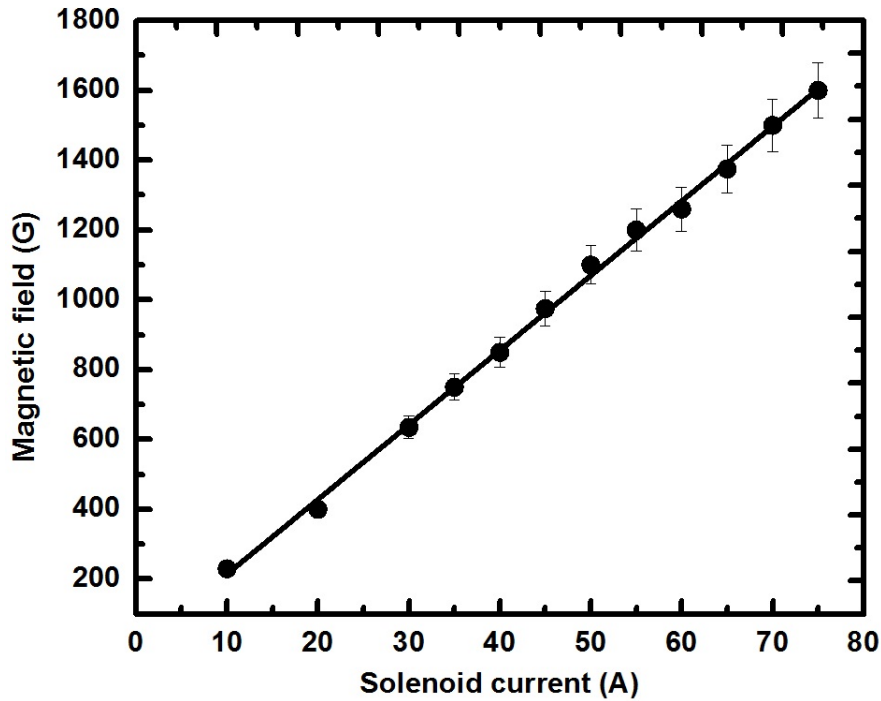
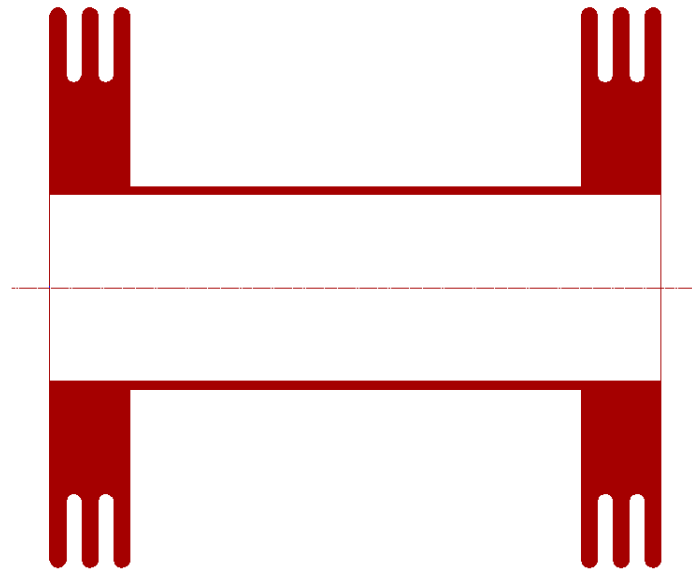


Figure 5.6 : Variation of the magnetic field with the solenoid current. The solid curve is for visual aid only.

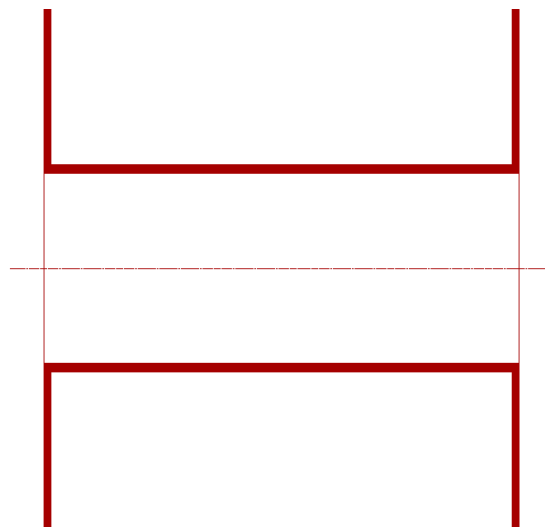
5.4 High Voltage Insulator Dome

The plasma chamber is floated at 50 kV DC high voltage for the extraction of proton beam at 50 kV DC. The electromagnets which surround the plasma chamber are required to be kept at ground potential, for this purpose. We have designed and developed a high voltage insulator dome to withstand 50 kV DC voltage. It was fabricated using high voltage glass epoxy with proper composition (Type-I). It was fabricated in two parts having one side-corrugated flange, which also provides the sides of the electromagnets at ground potential. The overall thickness of the high voltage insulator was 12 mm, which provided an insulation of 50 kV DC voltage. For moulding the high voltage insulator, the plasma chamber (including water-cooling jacket) itself was used as the mould. Hence there was no air gap between the plasma chamber and the high voltage insulator. Due care was taken to remove any sharp edges, which lead to electrical breakdown. All assembly flanges had a common

radius of 6 mm. The high voltage insulator was fitted to over the plasma chamber by sliding. The insulation of high voltage insulator dome was tested using 120 kV Megger. Presently, this was replaced due to its bulky in nature with new insulator with high density polypropylene (Type-II) material. A schematic diagram of the high voltage insulator dome is shown in Fig. 5.7.



Type - I



Type - II

Figure 5.7 : A schematic diagram of the high voltage insulator dome.

CHAPTER 6

Ion Beam Extraction System

This chapter covers the design simulations and development of the extraction electrode geometry for the extraction of 10 mA proton beam current, up to 25 keV beam energy (in Phase-I) and 30 mA proton beam current, up to 50 keV beam energy (in Phase-II). The electrode geometry was designed using *IGUN* software, which solves the Poisson equation in the plasma and the extraction region, using finite difference method.

6.1 Design Considerations : Theoretical Background

The extracted ion beam properties from ECRIS [6,53,54] are dependent on many parameters e.g. electrode geometry, applied extraction voltage, space charge, self-magnetic fields, external magnetic fields, and finally the shape of the plasma meniscus formed at the plasma boundary. The shape of the plasma meniscus is determined by the balance between the plasma current density J_p and the space charge limited current density J_{spc} i.e. $J_p = J_{spc}$. The plasma current density (J_p) is given by [123],

$$J_p = qn_i \sqrt{\frac{kT_e}{M_i}} \dots\dots\dots(6.1)$$

where T_e is the electron temperature (eV), M_i is the mass of the ion (kg), n_i is the ion density (cm^{-3}), k is the Boltzmann's constant, q is the charge state of the ion = $Z_i \times e$ (for hydrogen $Z_i = 1$), and e is the electron charge.

The plasma current density at 5 kV, electron temperature 4 eV, and ion density $5 \times 10^{10} \text{ cm}^{-3}$ is 76 mA/cm². The current density of charged particles that can be extracted from the plasma by the electric field is limited by the plasma density and the space charge of the ion beam, and cannot exceed the Child-Langmuir's law (assuming a planar plasma sheath and an ion beam without space charge compensation) [124,125],

$$J_{\text{spc}} = \left[\frac{4}{9} \right] \epsilon_0 \left[\sqrt{\frac{2q}{M_i}} \right] \left[\frac{V_0^{3/2}}{d^2} \right] \dots\dots\dots(6.2)$$

where d is the extraction gap (cm), V_0 is the applied acceleration voltage for the ion beam (kV), ϵ_0 is the permittivity constant, and M_i is the mass of the ion. The meniscus formed at the plasma surface depends on the plasma density and the applied electric field. The shape of the meniscus may vary from convex to concave as the plasma density decreases. The meniscus formed at the plasma boundary viz. a) convex, b) planar, and c) concave plasma meniscus with the beam extraction from the plasma are shown in Fig. 6.1. The convex meniscus leads the under focussed beam, and hence significant number of ions are lost as they hit the extraction electrodes. This leads to the secondary emission of the electrons and sputtering of the electrodes surface. This may be due to the high plasma density and a low extraction field, i.e. the plasma density is greater than the space charge density. A planar meniscus is the optimum meniscus shape since it well suited and matched condition between the extraction field and the plasma density for the maximum ion beam extraction i.e. the plasma density is equal to the space charge density. It is obtained by proper variation of the applied electric field and the plasma density. A concave meniscus is formed due to a high extraction field and a low plasma density i.e. the plasma density is less than the space charge density. In this condition, the beam is over focussed and then it diverges strongly, which leads to the hitting of the surface of the electrode. The beam is not lost at the extraction area, but the space charge creates the significant problems i.e. beam blow up, further down to the beam line [126]. The *perveance* of the ion beam is defined as,

$$P = \left[\frac{I}{V_0^{3/2}} \right] \left[\sqrt{\frac{M_i}{q}} \right] \dots\dots\dots(6.3)$$

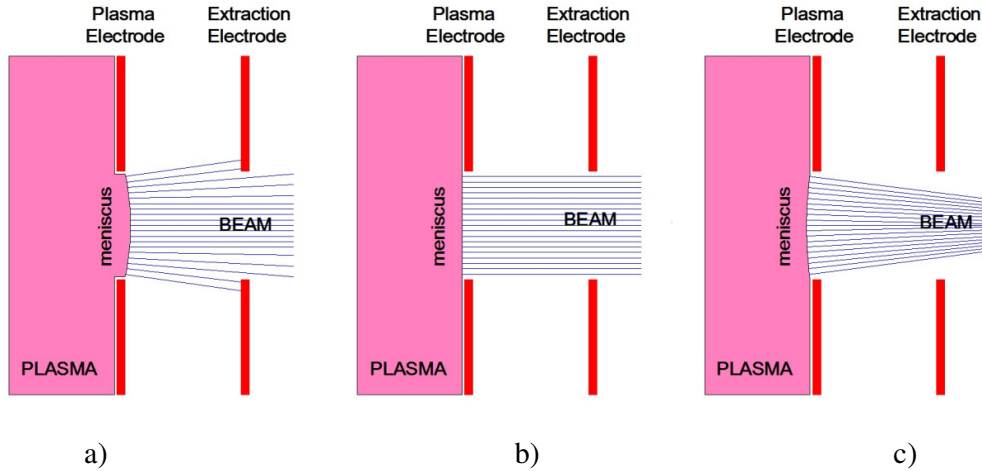


Figure 6.1 : The meniscus formed at the plasma boundary viz. a) Convex, b) Planar, and c) Concave plasma meniscus with the beam extraction from the plasma.

The maximum beam current density to be expected from an extraction system can be calculated from the Child-Langmuir's law, which describes the space charge limited current density. The space charge of the ion beam is automatically compensated by the beam itself via ion impacts on the residual gas molecules etc. These electrons however, have to be kept in the beam path and must not be back-streamed in to the source. The plasma current density depends on the density of the particles and the electron temperature. Therefore to achieve higher current, one must increase the density of particles, which is a function of the microwave power, the magnetic field and the gas pressure in the ECR plasma chamber. As long as the plasma current density is greater than the space charge current density, the extracted current follows the Child-Langmuir's law. The current would increase as the acceleration gap width decreases. Higher extraction voltage is required for higher ion currents. For positively charged ions with charge state q , the energy E_i of the extracted ion beam is given by $E_i = e q V_{\text{plasma}}$, where $V_{\text{plasma}} = V_{\text{extraction}} + \phi_p$. The plasma potential ϕ_p is typically of order 10 V, and can usually be neglected ($\phi_p \ll V_{\text{extraction}}$) in comparison with the extraction voltage which is of the order of several kV. The maximum half-angle

divergence of the beam (assuming the emission to be isotropic in the solid angle 2π and that the ions are accelerated in a homogeneous electric field) is given by,

$$\alpha = \frac{V_0}{V_z} = \sqrt{\frac{2kT_i}{eV_a}} \dots\dots\dots(6.4)$$

where V_0 is the maximum initial velocity of the ions, V_z is the axial velocity of the ions, T_i is the ion temperature, and eV_a is the beam energy. The emittance based on thermal energy assuming Maxwellian distribution is given by [6],

$$\epsilon_{r.m.s.}^{norm} = 0.016r \sqrt{\frac{kT_i}{M_i/q}} \dots\dots\dots(6.5)$$

where $\epsilon_{r.m.s.}^{norm}$ is the normalized $x-x'$ r.m.s. emittance (π mm mrad), r is the plasma electrode aperture radius (mm), kT_i is the ion temperature (eV), M_i is the mass of the ion (a.m.u), and q is the charge state of the ion. The beam emittance can be controlled with the plasma electrode aperture and the ion temperature, but the ion temperature is not easy to control in the plasma. Thus, reducing the aperture of the plasma electrode, low emittance can be achieved. For high quality ion beams, the emittance should be as small as possible, and the brightness as high as possible. The brightness of the beam gives a measure of how much current can be concentrated in a small spot, and it is given by,

$$B_{norm} = \frac{I}{[\epsilon_{r.m.s.}^{norm}]^2} \dots\dots\dots(6.6)$$

6.2 Software Optimization

The design and construction of an ion source extraction system usually starts with simulations of the extraction geometry. There are several ion optical design codes like, *IGUN* (2D) [119], *PBGUN* (2D) [127], *KOBRA* (*Axcel-2D & 3D*) [128], *SIMION* (3D) [129], which have been commonly used for the design of optics for diode, triode, tetrode, and pentode electrode geometries. These codes can be operated on a personal computer in a very

reasonable computation time. Here, we have used the *IGUN* software for the simulation of electrode geometry for the extraction of positive ion beam from plasmas. It provides CAD-like user interface in setting up boundaries, including definition of internal electrodes, dielectric boundaries, slanted Neumann boundaries, and Laplace problems with input for space charge of circular symmetric beams. It is primarily used to calculate the electric fields and the trajectories of charged particles for a given configuration of electrodes, with applied voltages and particle initial conditions. It is a two-dimensional code, suitable for simulating the extraction of positive ions from plasma using ion ray optics, and electrostatic field based on solution of Poisson equation. The code starts with mesh independent input data containing coordinates of the electrodes (either axis-symmetric or rectangular, as entered), boundary conditions, the number of the electrodes, the potential of each electrode, the plasma potential, the current or the electron density or ion current density, the fractions of ion species and or the mass, electron and ion temperature etc. The mesh points are generated once the potential are applied to the fixed electrodes. It automatically determines the ion extraction current during successive cycles, by matching the electric field gradient outside and inside of the plasma. This process is repeated until a self-consistent solution of the Poisson equation for a good quality extracted particle beam is determined. The resulting distribution of the potential along the beam edge is used to match the Laplace's solution in the region external to the beam that will support the charge flow.

The code first checks the input file and then provides interactive coloured graphics plots of equipotential lines, the beam trajectories, the electrode loss tables for different ion species, the emittance diagrams, the emittance growth diagram, the fractional emittance against the current, the beam profiles, the surface fields along the beam axis, the surface fields along the problem boundary, the data files for all the plots, the twiss parameters etc. The ray tracing is simulated by numerical integration and the fields are differentiated and

interpolated from the previous potential map. It also provides extensive supporting functionality in geometry definition, data recording, visualization etc. A flow chart of the *IGUN* software is depicted in Fig. 6.2.

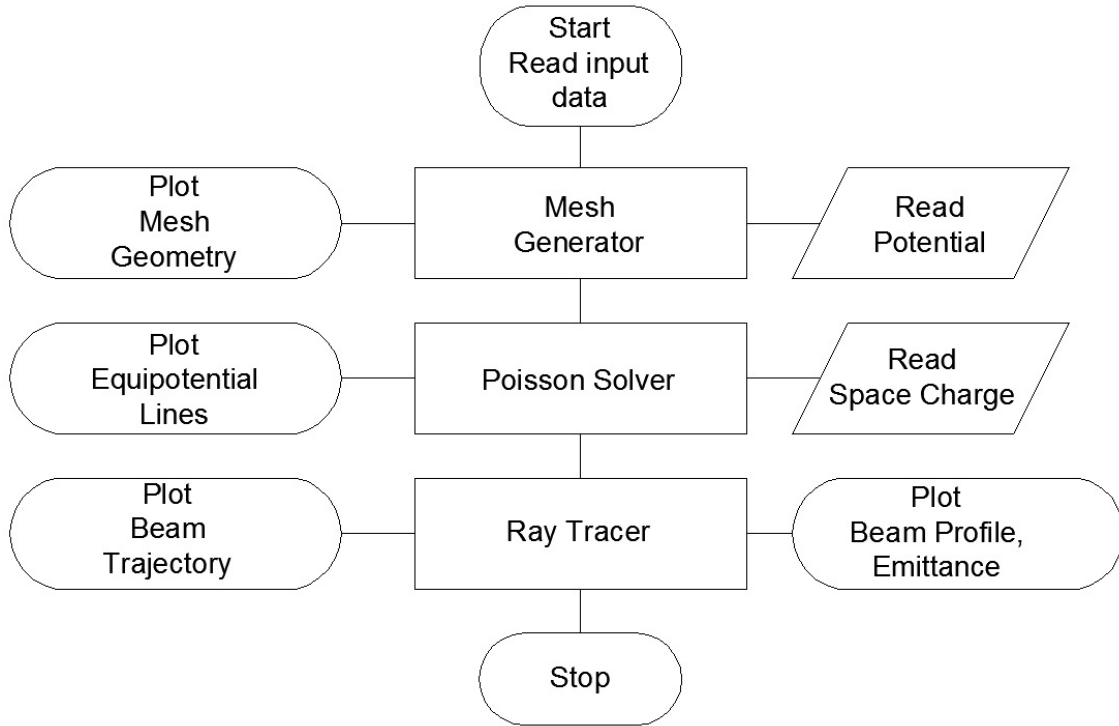


Figure 6.2 : A flow chart of the *IGUN* software.

The details of the simulations results for the three-electrode geometry for Phase-I and Phase-II, using the *IGUN* software, are presented in the next section.

6.3 Three-Electrode Geometry for Phase-I : 10 mA proton current at 25 keV beam energy

The three-electrode geometry is also known as *acceleration-deceleration type extraction geometry* [11,55]. It consists of the plasma electrode (PE), the extraction electrode (EE), and the ground electrode (GE) with respect to the beam axis. The PE terminates the plasma surface at the boundary of the discharge. The downstream side of this PE, EE is used, which provides optimal ion trajectories. The GE is at ground potential which terminates the

electric fields which establish the beam space-charge neutralization. Typical input file for this three-electrode geometry is as follows :

```
&INPUT1    rlim=100,potn=5,pot= - 4000,50000,0,0,0,punit=1E-3,batch=F &END
```

Geometry coordinates (format : potn, y, x)

```
& Input5    maxray=100, rp=4, TE=5, UI=5, TI=0.5, pdens=1E11, mass=1, zp=5,
            ns=14,av=7,avr=1,hold=14,nline=14,zscan=80,dscan=10,nscan=4,maxit=75,
            wrtequ=28000,rfld=16,zfld=13,startl=5,zend=50,ustart=50015 &END
```

```
&BUNDLE    charge=1 &END
```

(Note : input file is not case sensitive).

The electrode geometry was optimized for 10 mA proton beam current at 25 keV beam energy (Phase-I) [71]. The profile of the surface electric fields in the three-electrode extraction geometry is shown in Fig. 6.3.

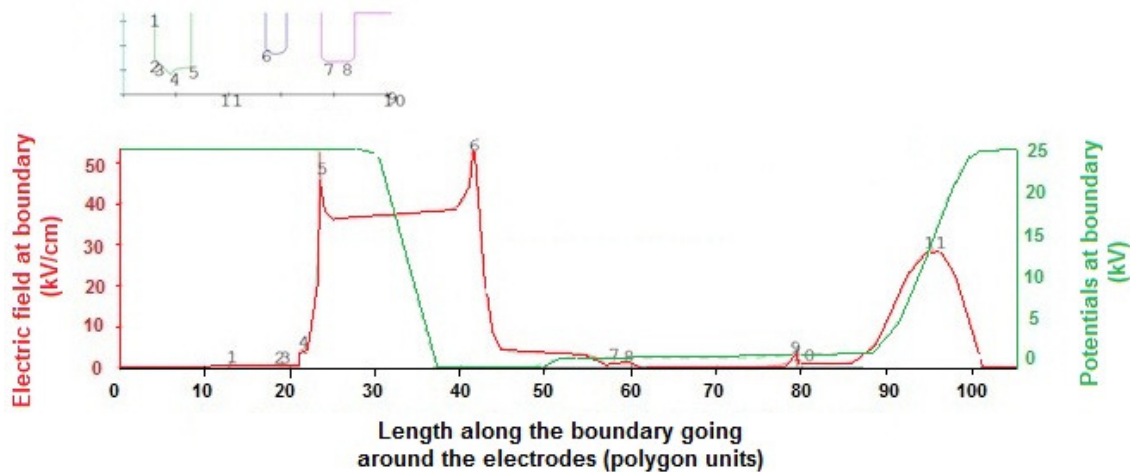


Figure 6.3 : The profile of the surface electric fields in the three-electrode extraction geometry.

Here, the X-axis represents the length along the boundary going around the electrodes, and the numbers of the field maxima around them are shown on the Y-axis. The

peak surface electric field is 5 kV/mm at surface of electrodes. The aligned aperture of three-electrode, acceleration-deceleration (ions are accelerated in the first gap and decelerated in the second gap) type flat extraction geometry was not used further because of the electrical breakdown and its other limitations like high beam divergence, emittance etc. The new geometry also has three-electrodes, but the difference is that some angle (Pierce type) is provided to the PE with respect to beam axis. The opening angle (inside and outside) of the PE with respect to beam axis, and other geometrical parameters were optimized to achieve the desired beam parameters with low emittance and low aberration. The proton beam trajectory for three-electrode extraction geometry for 10 mA proton beam current for 25 keV beam energy is shown in Fig. 6.4. It is showing the position of the PE (green in colour, aperture size 5 mm), the EE (blue in colour, aperture size 8 mm), the GE (red in colour, aperture size 10 mm), and the voltages applied on them. The vertical lines (cyan colour) parallel to the plasma and extraction electrodes indicate the equipotential lines. The proton beam trajectory is shown along the axis (red colour).

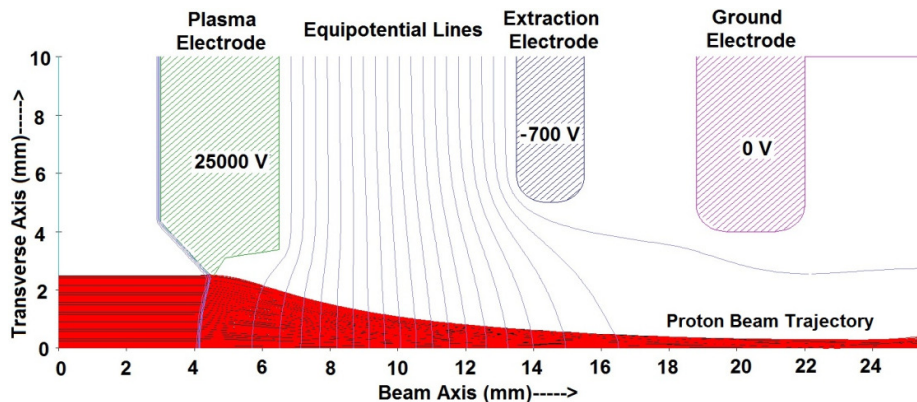


Figure 6.4 : The proton beam trajectory for three-electrode extraction geometry for 10 mA proton beam current for 25 keV beam energy.

The advantage of using a three-electrode geometry are : 1) ease of alignment with respect to the beam axis, 2) better control over the ion beam parameters, including its space charge, by changing the negative voltage on the EE, and 3) easy handling of the high voltages

by avoiding electric breakdowns. Four and five-electrode geometries have also been used to get low emittance and high brightness, but it increases the complexity of alignment and handling of the high voltages. The five-electrode geometry permits on-line optimization of the extracted beam, suitable to operate over a wide range of current by optimizing the beam formation for each working condition. A 3D-cross-sectional view of three-electrode extraction geometry is shown in Fig. 6.5. The electrode profiles and distances were optimized to limit the maximum surface electric fields at relative negative surface

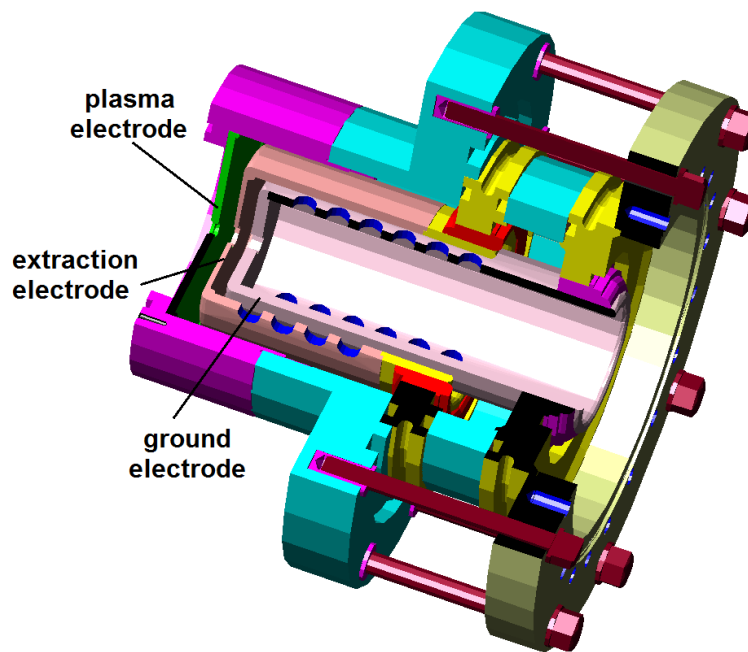


Figure 6.5 : A 3D-cross-sectional view of three-electrode extraction geometry.

points less than 5 kV/mm. For a voltage of 25 kV on the PE, the extraction voltage is -700 V, and the proton beam gets extracted through the electrodes without hitting the electrode geometry. Thus the ion beam envelope fully passed through the extraction system. The optimum proton beam current is calculated to be 10 mA at 25 keV beam energy. The EE was negatively biased with respect to the ground, to stop the back-streaming of secondary electrons which are produced due to residual gas ionization, to trap them near the extraction electrode area, and to neutralize the positive ion beam (space charge compensation), to get a

well-focussed beam. The space charge effects are mainly considered in the gaps between the PE aperture and the EE aperture, where the electric potential changes rapidly.

6.4 Fabrication and Testing of the Electrode Geometry

An acceleration-deceleration type ion beam extraction electrodes geometry was fabricated using oxygen free high conductivity copper. The EE and GE are water-cooled. The parts of the EE and the GE which face the PE were fabricated using circular molybdenum disk, to avoid the sputtering of the material because of direct bombardment of high energetic electrons or ions. The electrodes have been isolated using Macor insulating rings. The EE and GE have radial holes at equal intervals on their body to help in vacuum pumping between the electrodes space and avoid the electrical break down and residual ionization due to poor vacuum. Utmost care has been taken to remove any sharp edges over the surfaces to avoid the electrical breakdown. The electrode geometry was integrated with the RRCAT-ECRIS and assembled in such a way that the beam axis and extraction geometry axis remain coaxial within ± 0.1 mm. The insulation to the electrode geometry was tested using standard Megger. The EE and GE have the provision of axial movement of 20 mm for adjusting the gap between the electrodes for optimization of the ion beam current. However, this movement is possible only after dismantling of the GE. Photographs of all the three-electrodes are shown in Fig. 6.6. A photograph of the integrated three-electrode extraction geometry is shown in Fig. 6.7.

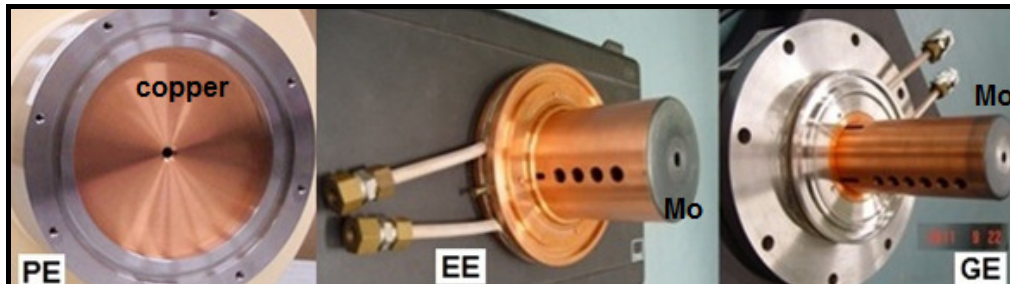


Figure 6.6 : Photographs of all the three-electrodes.

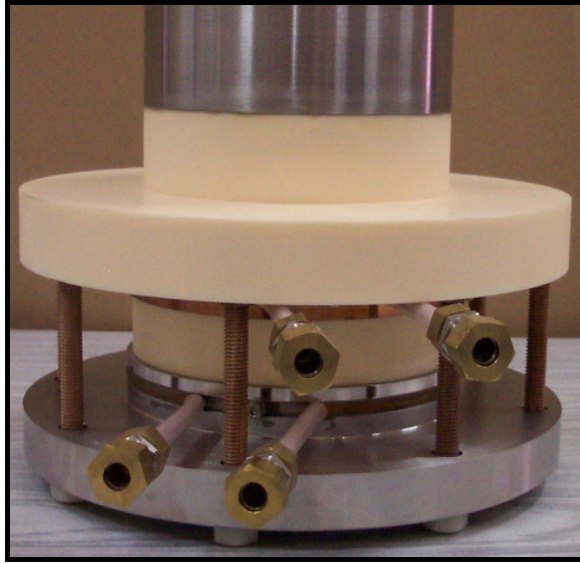


Figure 6.7 : A photograph of integrated three-electrode extraction geometry.

6.5 Three-Electrode Geometry for Phase-II : 30 mA proton current at 50 keV beam energy

For the Phase-II stage operation of the RRCAT-ECRIS for extraction of 30 mA proton beam current at 50 keV, a three-electrode geometry (Pierce type) has been designed and optimized for low emittance. The opening angle of the PE, acceleration voltage, ion temperature, and gap between the electrodes variations have been studied in detail. The opening angle of the PE was varied between 62° and 78° . The lowest possible acceptable r.m.s. emittance of 6.365 mm mrad (equivalent normalized r.m.s. emittance is 0.02π mm mrad), and a divergence is 40 mrad was obtained at an opening angle of the PE 68.7° . Variation of the r.m.s. emittance with opening angle for Pierce geometry is shown in Fig. 6.8. The curve is fitted with a 2nd order polynomial to guide the eyes. With the proper optimization of the opening angle of the PE, firstly, it has been observed that the ion beam envelope is able to pass through the extraction region without loss of current on electrode surface. Secondly, a flat meniscus shape was obtained near plasma emission boundary due to

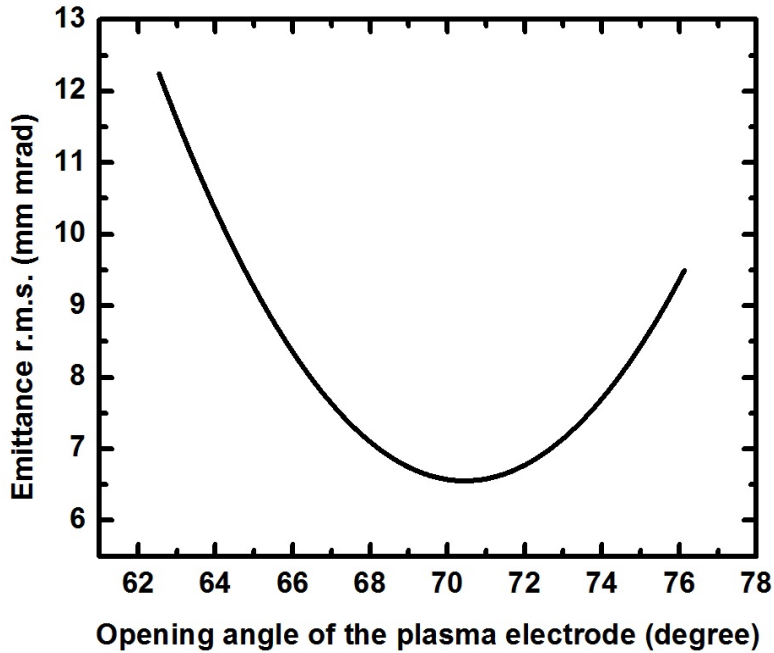


Figure 6.8 : Variation of the r.m.s. emittance with opening angle for Pierce geometry.

proper optimization of opening angle of the PE. It was observed that flat meniscus is suitable to get collimated ion beam with minimum angular divergence and low emittance. It is also suitable to achieve higher beam currents extraction. A concave meniscus formed at the plasma boundary focuses the extracted ions strongly towards the axis of the beam, which subsequently leads to beam blow up due to the space charge effect. Similarly, a convex meniscus formed at the plasma boundary leads to many of the ions trajectories hitting the extraction electrodes. The optimized profile of the proton beam trajectory for Pierce geometry is shown in Fig. 6.9. It is showing the position of the PE (green in colour, aperture size 8 mm), the EE (blue in colour, aperture size 10 mm), the GE (magenta in colour, aperture size 10 mm), and the voltages applied on them. The vertical lines (cyan colour) parallel to the electrodes indicate the equipotential lines. The proton beam trajectory is shown along the axis (red colour). The voltage applied to the PE is 50 kV and -4 kV to the EE. The Pierce geometry was further optimized by providing proper curvature radius to the electrodes. Since there is no high electric field jump, no breakdown condition exists.

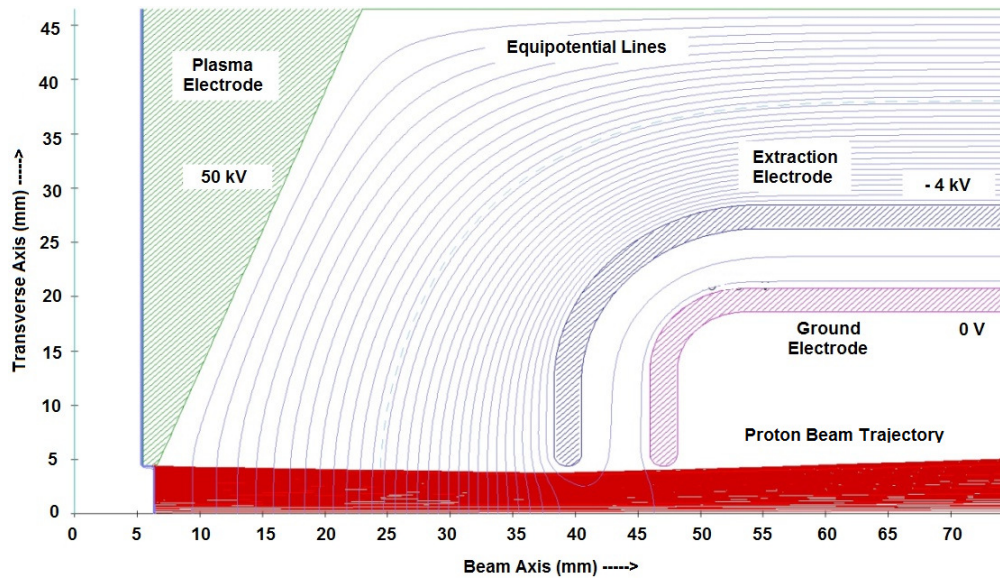


Figure 6.9 : The optimized profile of the proton beam trajectory for Pierce geometry.

The maximum peak electric field on the electrode surface is 5 kV/mm. This made it suitable to operate at higher voltages under clean vacuum conditions. The profile of the surface electric fields in the electrodes for Pierce geometry is shown in Fig. 6.10. The X-axis represents the length along the boundary going around the electrodes (in polygon units), and the numbers of the field maxima around them are shown on the Y-axis (in kV/cm). The green dotted line indicates the variations of the potentials and a red continuous line indicates the variations of electric field at the boundary of the electrodes.

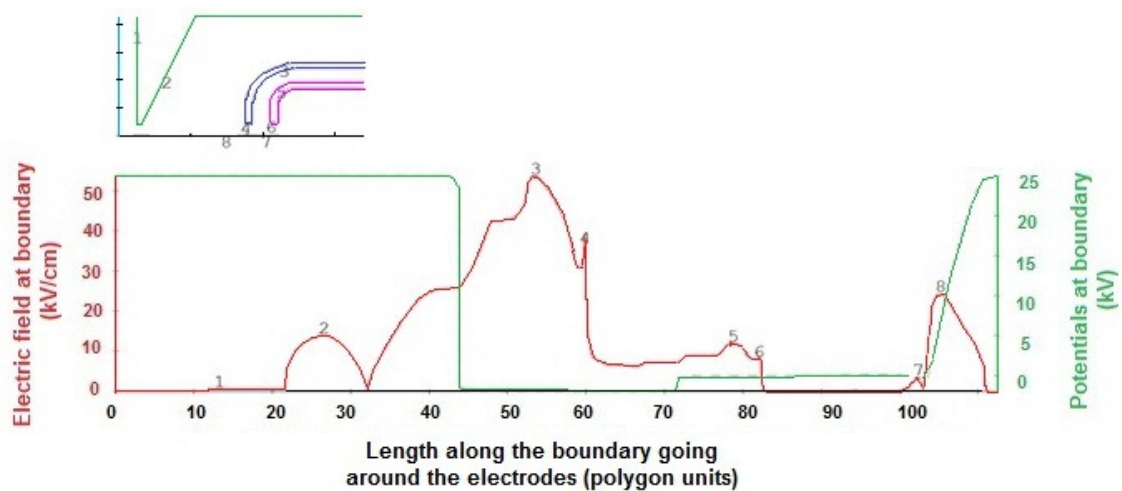


Figure 6.10 : The profile of the surface electric fields in the electrodes for Pierce geometry.

The profile of the r.m.s. emittance beam envelope for Pierce geometry is shown in Fig. 6.11. It shows that, the extracted ion beam emittance profile lies in the first and third quadrant, which indicates the nature of the ion beam to be diverging and it can be focused further with the use of a proper Einzel lens.

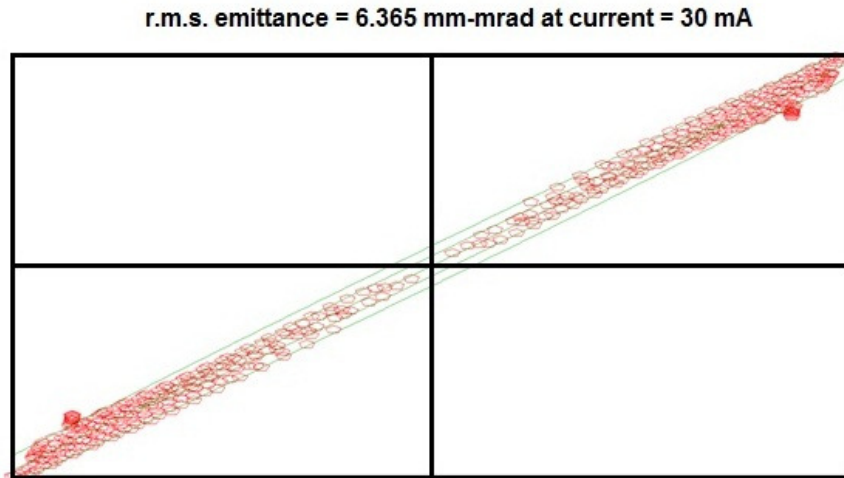


Figure 6.11 : The profile of the r.m.s. emittance beam envelope for Pierce geometry.

a) Extraction voltage variation

In order to examine the effects on r.m.s. emittance, the EE voltage was changed from 2 to 10 kV to accomplish the suitable ion trajectories beam envelope, which do not hit the EE. The EE is biased at negative potential to reduce the emission of secondary electrons from the GE and to maintain the sufficient field gradient in the extraction gap to form the desired plasma meniscus boundary. This also creates a trap for the low energy electrons generated in the extracted beam regions to keep them inside the ion beam for helping in space charge compensation and do not allow them to back stream towards the plasma chamber. Variation of the r.m.s. emittance with extraction voltage for Pierce geometry is shown in Fig. 6.12. The curve is fitted with 2nd order polynomial to guide the eyes. Thus, one can see that the beam profile can be controlled with the variation of the extraction voltage. The care should be taken such that rise in peak electric field does not lead to the vacuum breakdown. It can be noted

from the figure that at 4 kV, the r.m.s. emittance is minimum, this is the optimum condition for the use of this electrode geometry. Beyond this, r.m.s. emittance increases with increasing extraction voltage. This may be attributed to the formation of convex meniscus at the surface of the plasma boundary due to increasing intensity of the electric field with the applied negative extraction voltage.

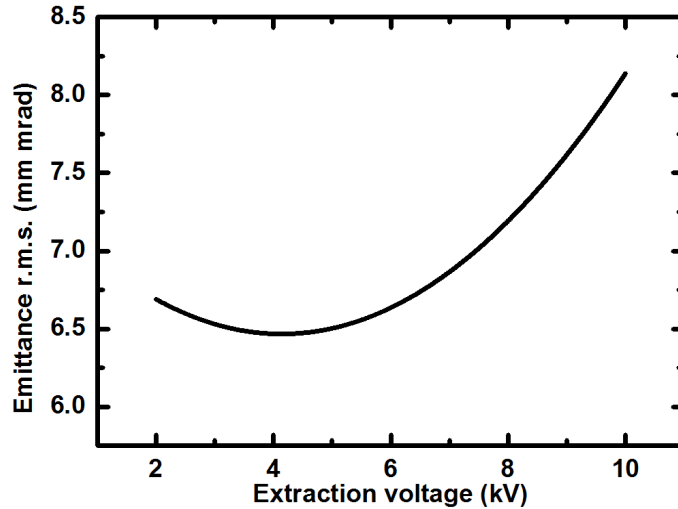


Figure 6.12 : Variation of the r.m.s. emittance with extraction voltage for Pierce geometry.

b) Ion temperature variation

Variation of the r.m.s. emittance with ion temperature, at different PE aperture for Pierce geometry is shown in Fig. 6.13. This graph shows that ion beam current increases with increasing the PE aperture, and r.m.s. emittance with ion temperature. The PE aperture was varied between 5 to 10 mm. It was observed that, in the case of under-dense plasma, the meniscus formed at the plasma boundary has concave shape leading to convergent beam that blows up down the beam line due to space charge, depending on the magnitude of the beam current. Similarly, in the case of over dense plasma, the plasma boundary has convex shape, leading to a divergent beam and many ions hit the extracting electrodes and get lost. In the case of intermediate dense plasma, the meniscus formed at the plasma boundary is planar and is suitable for extraction at desired beam current and energy. In this case, the ions also pass

without hitting to the electrodes. The optimum r.m.s. emittance achieved is 6.365 mm mrad at proton beam current of 30 mA at 50 keV beam energy, with 8 mm extraction aperture of the PE at 0.5 eV ion temperature.

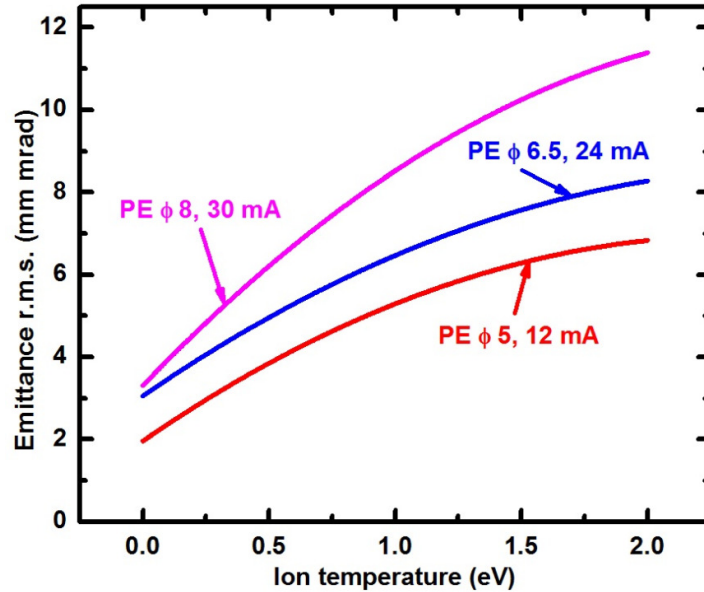


Figure 6.13 : Variation of r.m.s. emittance with ion temperature, at different PE apertures for Pierce geometry.

The variation in r.m.s. emittance is due to integration of the nonlinear radial electric field components and space charge effects along the particle trajectories and leads to particle loss. The opening angle of the PE was optimized to have the low aberration and low emittance. In practical conditions, a low ripple magnetron power supply also helps to reduce the emittance, noise and fluctuations in the beam. Moreover, a good magnetic confinement of the plasma also ensures less fluctuations of the ion temperature leading to better emittance. Thus, ion temperature has major bearing on the extracted beam optics.

c) Gap variation

At low energy and high current, the space charge problem becomes severe and there is always a possibility of beam blow up due to the space charge. This happens due to improper gap. Thus, the gap between the PE and the EE is crucial and needs to be optimized

to have the uniform equipotential lines in the space between them, a proper electric field gradient to overcome the space charge effects, to avoid the electric field breakdown (since sparks starts from fields peaks at negative relative potential), and to generate the proper meniscus at the plasma boundary. To overcome these problems, the EE is kept at sufficiently large distance to have the uniform equipotential lines in between the electrodes, and to have a suitable meniscus to generate a collimated ion beam. The space charge of the beam also gets compensated due to the interaction with residual electrons during the transport of the beam. The optimum gap of ~ 30 mm was obtained, where one gets low emittance and low divergence. The peak electric field on electrode surfaces was found to be 5 kV/mm. Variation of r.m.s. emittance with the gap between PE and the EE for Pierce geometry is shown in Fig. 6.14. It shows that the r.m.s. emittance decreases with increasing in the gap between the electrodes. Thus, it is also important to optimize the gap between the electrodes to achieve the required emittance.

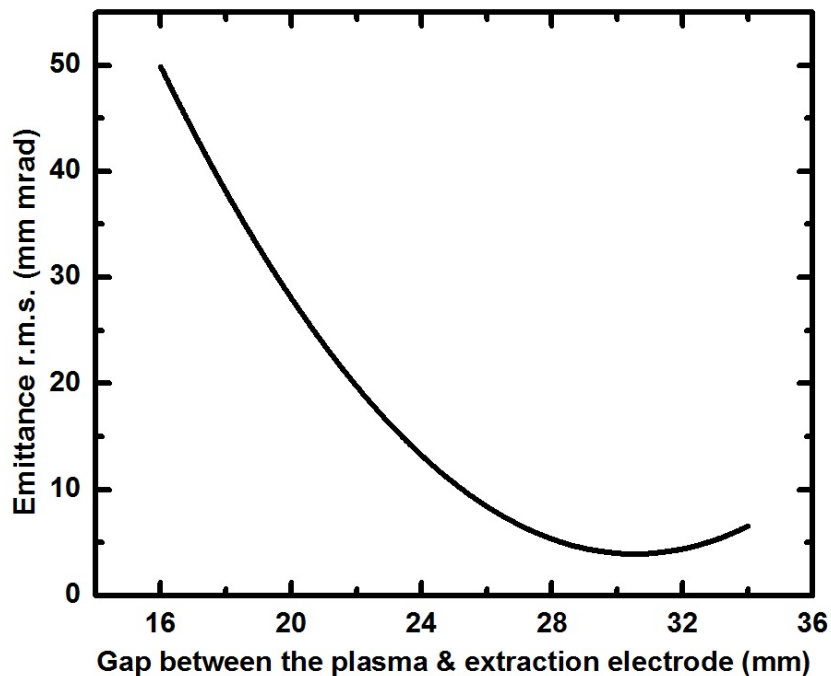


Figure 6.14 : Variation of r.m.s. emittance with gap between the PE and EE for Pierce geometry.

CHAPTER 7

Plasma Diagnostic with Langmuir Probe

This chapter deals with the design and fabrication of a Langmuir probe for the characterization of the plasma produced by argon / hydrogen / nitrogen gases. The Langmuir probe gives the current-voltage characteristic curve, i.e. the variation of the current signal generated by the probe and the probe bias voltage. The current-voltage curve was used for evaluating the plasma parameters.

To characterize the plasma parameters like electron density (n_e), electron temperature (T_e), floating potential (V_f), plasma potential (ϕ_p), and electron energy distribution the Langmuir probe was used [130,131,132,133]. The following assumptions were used,

- i. The effect of collisions on particles reaching to the probe is negligible, i.e. $\lambda_m \gg \lambda_d$.
- ii. The probe is placed in a weak / No magnetic field i.e. Larmour radius \gg probe wire radius, so ions / electrons reaching to the probe, the motion is unaffected by magnetic field.
- iii. Ions / electrons follow Maxwellian distribution function.
- iv. All ions / electrons entering to the sheath are captured by the probe.
- v. The motion of the charged particles from the plasma reaching to the probe surface is collisionless.

7.1 Langmuir Probe : Working and Characteristics

Langmuir probe as a plasma diagnostic device has been widely used to characterize laboratory plasmas and is accepted worldwide for the measurement of plasma parameters like electron density, electron temperature, floating potential, plasma potential, and electron energy distribution. Langmuir probe is a metallic wire inserted into the plasma and

connected to a biasing power supply. The current drawn by the probe at different bias voltages is recorded, and one gets the current-voltage ($I_{\text{probe}}-V_{\text{probe}}$) characteristics curve. This curve is further analyzed (either on-line or off-line) to get the plasma parameters. Langmuir probe technique is widely used because of its simple construction and easy interpretation of the data. The spatial resolution of the probe method is of the order of the magnitude of the Debye length, only issue is that probe perturbs the local surroundings momentarily. A typical current-voltage ($I_{\text{probe}}-V_{\text{probe}}$) curve for a Langmuir probe is shown in Fig. 7.1. It clearly shows the ion saturation region, the transition region, the electron saturation region, and the electron energy distribution region. These regions are used for evaluating the plasma parameters.

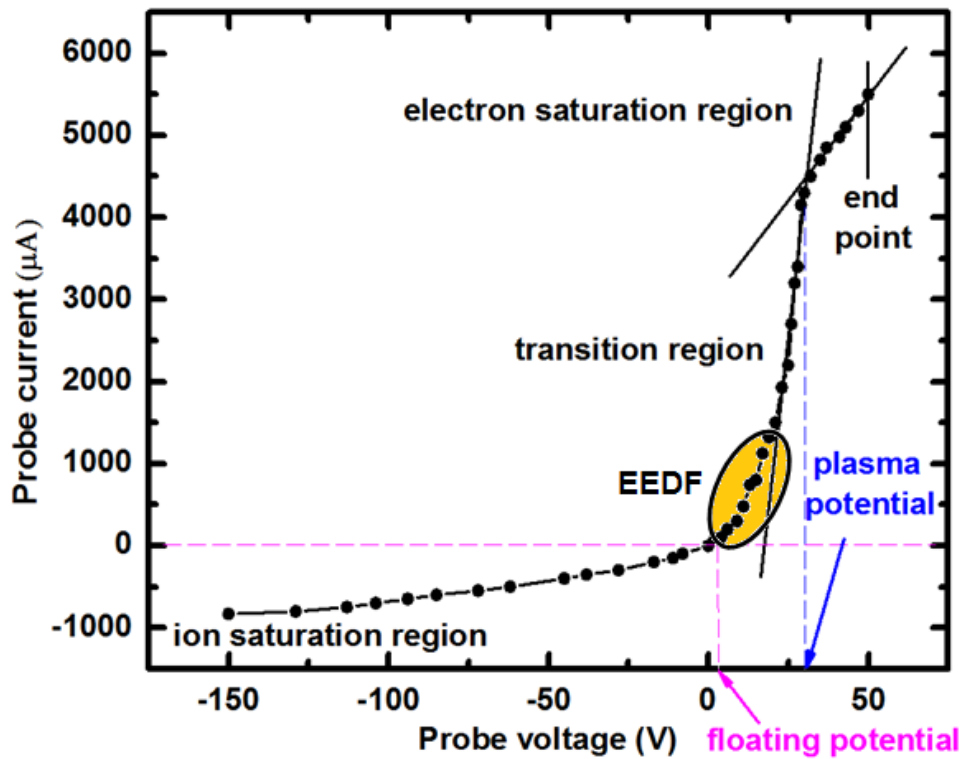


Figure 7.1 : A typical current-voltage ($I_{\text{probe}}-V_{\text{probe}}$) curve for a Langmuir probe.

a) Parts of the $I_{\text{probe}}-V_{\text{probe}}$ Curve

i) Ion saturation region : Biasing the probe increasingly with negative voltage, a point is reached where no electron is able to reach to the probe, only positive ions are collected. This region is called the *ion saturation region* and is used to determine the ion density and ion temperature of the plasma.

ii) Electron transition region : Biasing the probe with negative voltage, the region where the probe starts to attract the electrons which are energetic enough to cross the potential barrier of the applied voltage is called the *electron transition region*. In this region, ions as well as some electrons are attracted towards the probe. The slope of the exponential transition region determines the electron temperature.

iii) Electron saturation region : Biasing the probe with positive voltage, the electrons (and negative ions, if any) are attracted to the probe and electron saturation occurs.

This region is called the electron saturation region and is used to determine the electron

density of the plasma. The expression $I = \left[\frac{1}{2} \right] e A n_e \left[\sqrt{\frac{kT_e}{M_i}} \right]$ is used to calculate the electron

density, where I is the saturation current, e is the electron charge, k is the Boltzmann's constant, T_e is the electron temperature, M_i is the mass of the ion, n_e is the electron density, and A is the area of the probe.

b) Floating Potential

The potential, where no NET current flows through the probe and there is a balance between electron and ion current (sufficient electrons to equate the ion and electron flux), giving zero net current is called the *floating potential*. It is the point on the current-voltage curve where the current drawn by the probe is zero. A typical current-voltage ($I_{\text{probe}}-V_{\text{probe}}$) curve for interpretation of the floating potential obtained from a Langmuir probe is shown in Fig. 7.2.

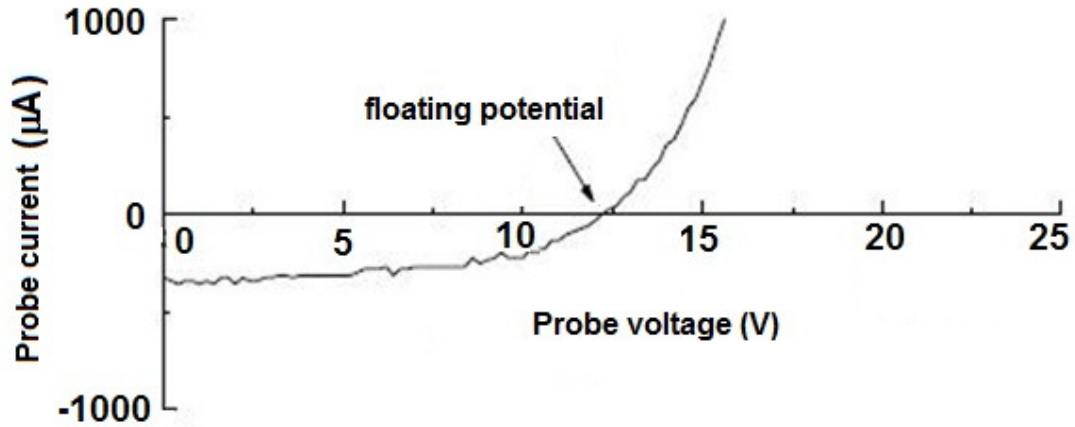


Figure 7.2 : A typical current-voltage ($I_{probe}-V_{probe}$) curve for interpretation of the floating potential obtained from a Langmuir probe.

c) Plasma Potential

When a straight line drawn from electron saturation region, where it intersects with the slope of the exponential part of the current-voltage ($I_{probe}-V_{probe}$) curve, the bias voltage corresponding to the intersection point gives the *plasma potential*. It is the potential acquired by an isolated plasma. A typical current-voltage ($I_{probe}-V_{probe}$) curve for interpretation of the plasma potential from a Langmuir probe is shown in Fig. 7.3.

d) Electron Energy Distribution Function

The electron energy distribution function (EEDF) is proportional to the second derivative of the $I_{probe}-V_{probe}$ curve. It gives a measure of the number density of the electrons as a function of the electron energy [134,135,136]. It is useful to understand the process of formation of the plasma i.e. electron impact ionization and electron excitation. A typical second derivative of the $I_{probe}-V_{probe}$ curve is shown in Fig. 7.4.

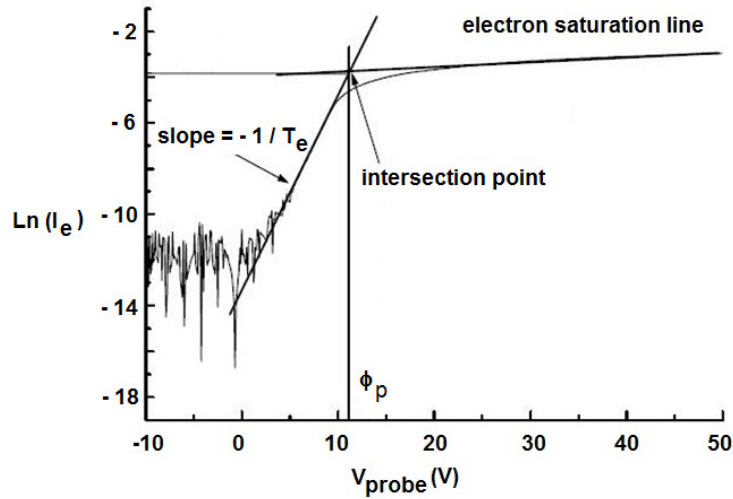


Figure 7.3 : A typical current-voltage ($I_{probe}-V_{probe}$) curve for interpretation of the plasma potential from a Langmuir probe.

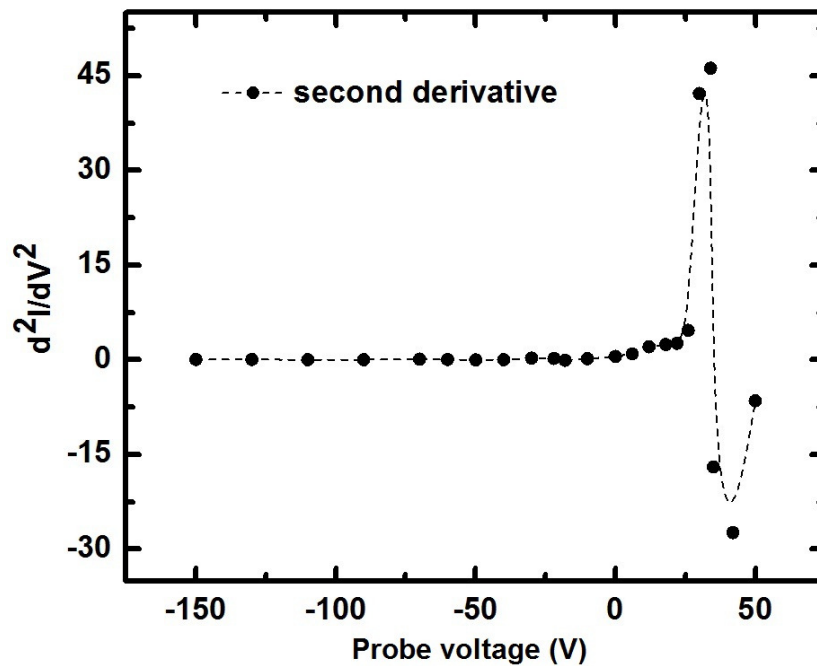


Figure 7.4 : A typical second derivative of the current-voltage ($I_{probe}-V_{probe}$) curve.

7.2 Langmuir Probe Construction

Although the working principle of the Langmuir probe is bit complex, its construction is quite simple. The probe tip is made up of high temperature material like tungsten, molybdenum, platinum, or nickel, which can withstand high temperature. In our case, a

tungsten wire has been used (diameter : 0.3 mm, length : 5 mm) which satisfies the condition of $r_p / \lambda_d \gg 1$, (where r_p is the probe radius, and λ_d is the Debye length), such that the probe is operating in orbital motion limited regime. The tungsten wire is housed in a stainless steel tube of diameter 5 mm supported by an insulating sleeve, connecting to an N-type connector for biasing. Quartz seal was used to enclose the initial part of the stainless steel tube except the probe tip, to avoid direct bombardment of the electrons on the probe assembly, and to minimize the heat flux to the probe in order to avoid damage. The probe was vacuum sealed using a Wilson seal arrangement. It was placed in a magnetic field-free region to avoid any instability at the probe tip due to the magnetic field. The helium leak test of the probe was carried out before using and the leak rate was found to be less than 10^{-9} mbar l/s [137]. A photograph of indigenously developed Langmuir probe is shown in Fig. 7.5.



Figure 7.5 : A photograph of indigenously developed Langmuir probe.

7.3 Langmuir Probe Electrical Circuit

The resistive circuit for measuring the probe voltage (V_{probe}) and the probe current (I_{probe}) is shown in Fig. 7.6. In absence of plasma, the probe is as good as an open circuit, however in presence of the plasma, the probe resistance drops to around a few hundreds of $k\Omega$. This fact was used to decide the values of the resistances used in the circuit. We connect a sensing resistance R_{sense} with the probe to measure I_{probe} . The voltage drop across the R_{sense} was the measure of the I_{probe} , i.e. $V_{\text{sense}} = R_{\text{sense}} \times I_{\text{probe}}$. The current flowing through R_{H2} is negligible as compared to I_{probe} , Thus, the necessary condition is that $R_{\text{probe}} \ll (R_{H2} + R_{L2})$.

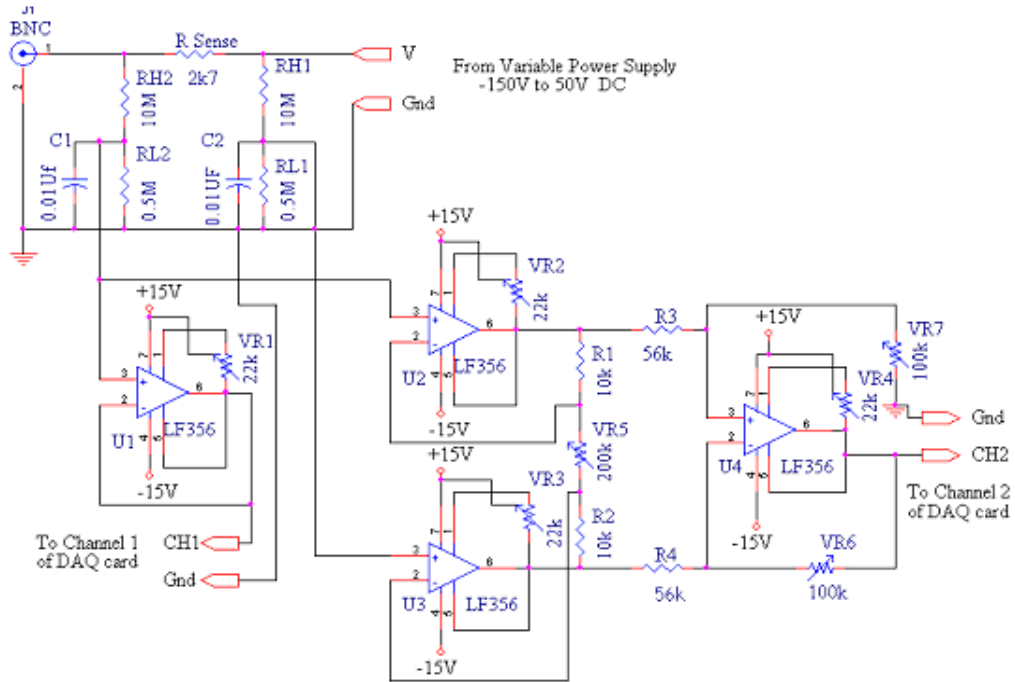


Figure 7.6 : The resistive circuit for measuring the probe voltage and the probe current.

Also the V_{probe} is required to be attenuated before its measurement. This requirement arises due to the fact that hardware for further processing accepts analog input only in the range of ± 10 V DC, whereas the maximum probe voltage that we are applying was about 200 V DC.

Thus, $[R_{L2} / (R_{L2} + R_{H2})] = V_2 / V_{\text{probe}} = 10 / 200$.

We choose,

$$R_{H2} = R_{H1} = R_H = 10 \text{ M}\Omega \quad (1/4 \text{ W}),$$

$$R_{L2} = R_{L1} = R_L = 0.5 \text{ M}\Omega \quad (1/4 \text{ W}).$$

Hence, $V_2 / V_{\text{probe}} = 1 / 21$.

We choose the large sensing resistance wattage values to avoid the damage of the probe.

$$R_{\text{sense}} = 2.7 \text{ k}\Omega \quad (5 \text{ W}).$$

Now,

$$V_2 = [R_{L2} / (R_{L2} + R_{H2})] V_{\text{probe}} = V_{\text{probe}} / 21$$

$$V_1 = [R_{L1} / (R_{L1} + R_{H1})] V_{\text{supply}} = V_{\text{supply}} / 21$$

The voltage developed across R_{sense} is given by,

$$V_{\text{sense}} = V_{\text{probe}} - V_{\text{supply}}$$

$$\Rightarrow 21(V_2 - V_1) = 21 \times \Delta V$$

$$I_{\text{probe}} = V_{\text{sense}} / R_{\text{sense}} = 21 \times \Delta V / R_{\text{sense}}$$

The buffer was basically required to isolate the data acquisition card from the resistive attenuator. It also prevented the input impedance of the analog input of the card from loading the resistive network. The buffer stage basically consists of an instrumentation amplifier and a simple buffer implemented using op-amp IC's LM741 / LF356. The gain $[(1 + 2R_{\text{sense}} / R_{\text{H1}}) (R_{\text{H2}} / R_{\text{L1}})]$ of the instrumentation amplifier can be adjusted so that the maximum I_{probe} corresponds to 10 V DC output. The second buffer having unity gain was non programmable. A basic block diagram for measuring and processing the probe characteristics (V_{probe} and I_{probe}) is shown in Fig. 7.7.

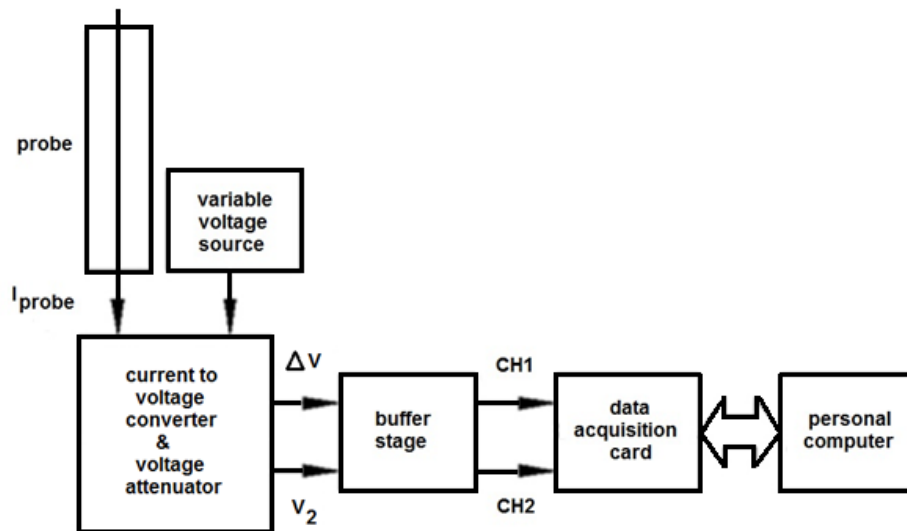


Figure 7.7 : A basic block diagram for measuring and processing the probe characteristics.

The voltage -150 V to +50 V DC applied to the probe was controlled by ± 10 V DC as the input signal to data acquisition card and was varied in steps of 1 V DC. The outer end of the probe is at plasma ground. The probe output was given to a current to voltage converter, which in this case, was a simple resistive network and gave voltage proportional to

the probe current. These signals were given to data acquisition hardware (NI 6024E) through a buffer stage. This stage was used to isolate the data acquisition hardware from the front-end circuitry. The data acquisition hardware is interfaced to a personal computer. The acquired data was processed off-line to characterize the given plasma. An interactive graphics based software package for processing and analyzing Langmuir probe data was developed using LabVIEW. The program can be adapted to any platform using common laboratory instruments. A front panel graphical view of an acquired current-voltage ($I_{\text{probe}}-V_{\text{probe}}$) is shown in Fig. 7.8.

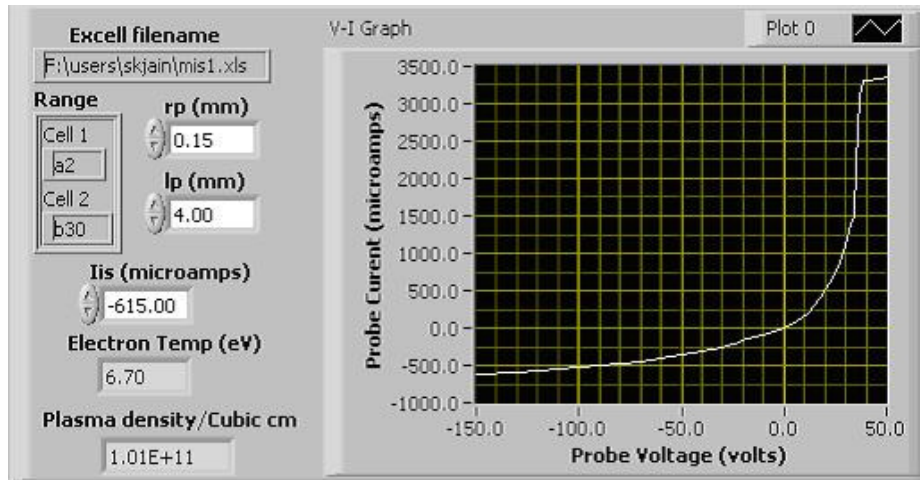


Figure 7.8 : A front panel graphical view of an acquired current-voltage ($I_{\text{probe}}-V_{\text{probe}}$) curve.

7.4 Interpretations of the Probe Characteristics

The recorded data was averaged (adjacent-averaging) to get a smooth current-voltage curve. The data was transferred to Microsoft Excel / Origin / LabVIEW to generate current-voltage curve for calculation of plasma parameters. To calculate the electron density, I_{probe}^2 against V_{probe} , in the electron saturation region (where current is basically electron current) was plotted. From the slope of the graph, electron density was calculated. To obtain the electron temperature, $\ln(I_{\text{probe}})$ and V_{probe} , in the electron transition region (where the current due to electrons varies exponentially) was plotted and from the inverse slope of the linear portion of the curve, electron temperature was obtained.

In our setup, the base pressure was $\sim 10^{-6}$ mbar, operating pressure was $\sim 10^{-4}$ mbar, gases used were argon / hydrogen / nitrogen, and microwave power used was 300 W to 750 W. A current-voltage ($I_{\text{probe}}-V_{\text{probe}}$) curve obtained for an ECR plasma discharge for above conditions is shown in Fig. 7.9.

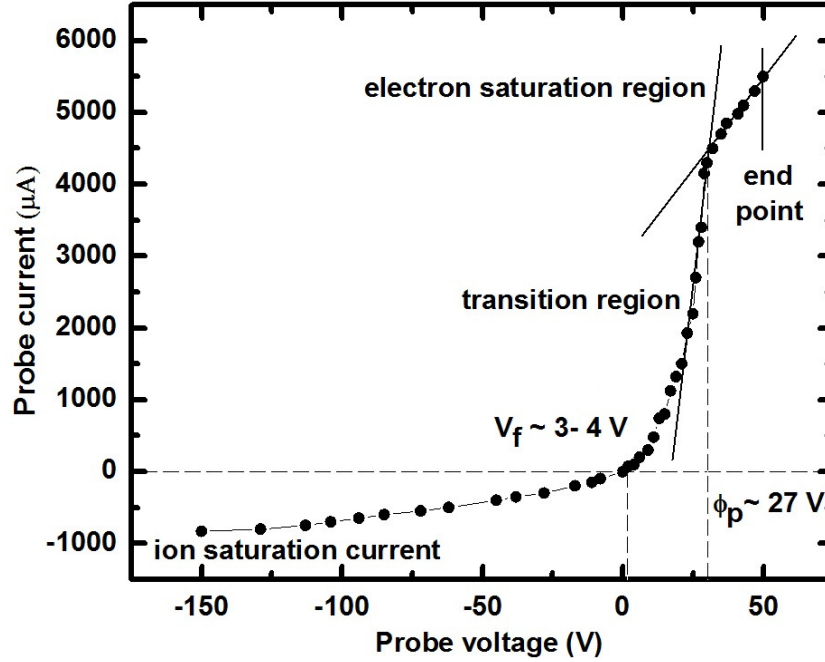


Figure 7.9 : A current-voltage ($I_{\text{probe}}-V_{\text{probe}}$) curve obtained for an ECR plasma discharge.

The procedure followed to derive the plasma parameters (in all type of discharge like DC, RF, ECR, Microwave etc.) was as follows. The electron current I_e is obtained by subtracting the ion saturation current I_{is} from the total probe current I_{probe} for a given probe voltage V_{probe} , where V_{probe} is the probe potential with respect to the ground or plasma chamber. A typical $\ln(I_e)$ and V_{probe} curve is shown in Fig. 7.10. It shows that it has two linear portions. It is an indication that ECR plasma (mirror) have two electron temperatures ($T_{e1}, T_{e2} : T_{e2} > T_{e1}$). To determine these more accurately, the following procedure has been used. Let I_e be the current due to the electrons at a temperature T_e , I_{e1} be the current due to electrons at temperature T_{e1} and I_{e2} be the current due to electrons at temperature T_{e2} . One obtains,

$$I_e = I_{e1} + I_{e2} \dots\dots\dots(7.1)$$

Moreover, $I_{e2} \sim I_0 \exp [e (V_{\text{probe}} - \phi_p) / T_{e2}]$, where e is the electron charge, I_0 is the current due to high electron temperature at $V_{\text{probe}} = \phi_p$.

The above implies,

$$\ln(I_{e2}) = \ln(C_0) + \exp\left[\frac{V_{\text{probe}}}{T_{e2}}\right] \dots\dots\dots(7.2)$$

where $C_0 = I_0 \exp [eV_{\text{probe}} / T_{e2}]$, T_{e2} can be obtained directly from the inverse slope of $\ln (I_e)$ and V_{probe} curve, for $V_{\text{probe}} \ll \phi_p$ (in the region where, $I_e \sim I_{e2}$). The value of C_0 (which contains the two unknown ϕ_p and I_0) can also be determined from the intercept of the above plot on the $V_{\text{probe}} = 0$ axis. Knowing C_0 and T_{e2} , I_{e2} is determined for all the probe voltages V_{probe} , so that using $I_e = I_{e1} + I_{e2}$, the low temperature current I_{e1} can be computed for all the probe voltages also. A typical $\ln (I_{e1})$ and V_{probe} curve is shown in Fig. 7.11. This yields the electron temperature T_{e1} i.e. the temperature due to bulk of electrons. Knowing T_{e1} , one can calculate electron density n_e from the measured value of ion saturation current. Estimation of an order of magnitude of the electron density can be obtained by using the relationship [130, 131,132,133,138,139,140],

$$I_{is} = \left[\frac{1}{2}\right] eA n_e \left[\sqrt{\frac{T_{e1}}{M_i}}\right] \dots\dots\dots(7.3)$$

Hence,

$$n_e = \frac{2I_{is}}{eA\sqrt{T_{e1}/M_i}} \dots\dots\dots(7.4)$$

where A is the area of the probe, M_i is the mass of the ion. This procedure is repeated to calculate the electron temperature T_{e1} , electron temperature T_{e2} , and electron density n_e .

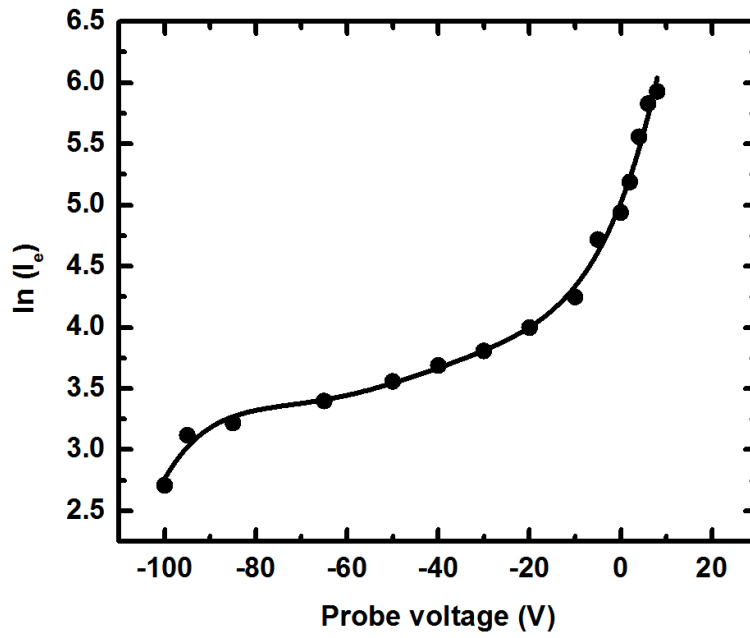


Figure 7.10 : A typical $\ln(I_e)$ and V_{probe} curve.

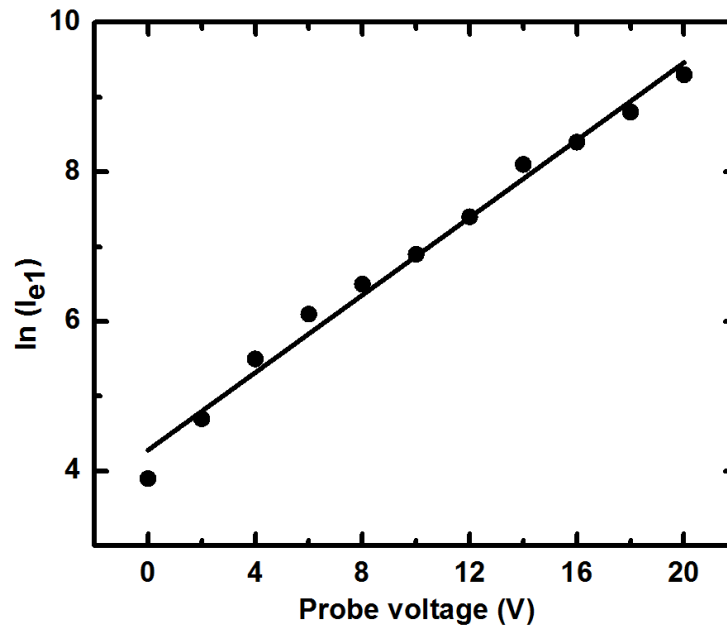


Figure 7.11 : A typical $\ln(I_{e1})$ and V_{probe} curve.

CHAPTER 8

Experimental Characterization of the ECR Plasma Source

This chapter discusses the experimental procedure used to characterize the ECRIS. The source was operated for different operating conditions over a wide range of gas pressure, microwave power, and magnetic field. The source has a wide tuning range for operating the plasma parameters. The radial variation of the electron density has also been measured. The details of the characterization of the extracted ion beam using Thomson parabola, are given. This chapter also includes the measurement of the characteristic x-rays produced using argon / hydrogen / nitrogen ion beams interaction with thick copper target. The bremsstrahlung continuum was also observed along with the characteristic copper K- α and K- β lines. As a demonstration of an application of the ECRIS, an attempt to deposit the titanium film on a glass substrate was made using ECR argon ion beam by sputtering the titanium bulk target.

A base pressure of $\sim 10^{-6}$ mbar was attained in the plasma chamber for the several hours prior to the commencement of the experiment, using a turbo-molecular pump with a two stage rotary pump as a roughing pump. The pressure was measured using standard Penning and Pirani pressure gauges. The experimental gas (high purity argon / hydrogen / nitrogen gas) was then fed through a stainless steel tube (quarter inch size) which was isolated from the high voltage side with a 2 m long PVC tube. The gas flow was regulated with a fine precision needle valve. The system was then maintained at a pressure $\sim 10^{-4}$ mbar for the about 15 minutes. The microwave generator and the microwave system were kept at ground potential. The low conductivity water was circulated through the microwave components, the solenoid coils, the walls of the plasma chamber, EE, and GE using a standard water chiller. The microwave generator was brought into the standby mode and the gas pressure was set to the operating pressure. The currents in the solenoid coils were

adjusted to obtain the required magnetic field. The microwave power was then switched on for initiating the discharge. A stable plasma discharge was obtained with a small variation of the magnetic field and gas pressure. A view of the plasma discharge through the quartz windows is shown in Fig. 8.1.

During the course of experiment, forward and reflected power was monitored using a directional coupler with calibrated analog power meters. The reflected power was minimized using three-stub tuner acting as an impedance matching device. A manual gate valve CF203 (Model : NW150CFF, M/s Varian SPA, Italy) was used for isolating the plasma chamber from turbo-molecular pump. The whole ECRIS setup was assembled on a mild steel stand with castors wheel. Operational safety, particularly with respect to the hydrogen gas used in our facility, and to the microwave power, was a major design consideration. Appropriate safety interlocks were used for safe operation of the system. Hydrogen leak sensor (Model : TIF 8850, Make : M/s Amprobe Europe GmbH, Germany) was used for leak test of hydrogen gas.

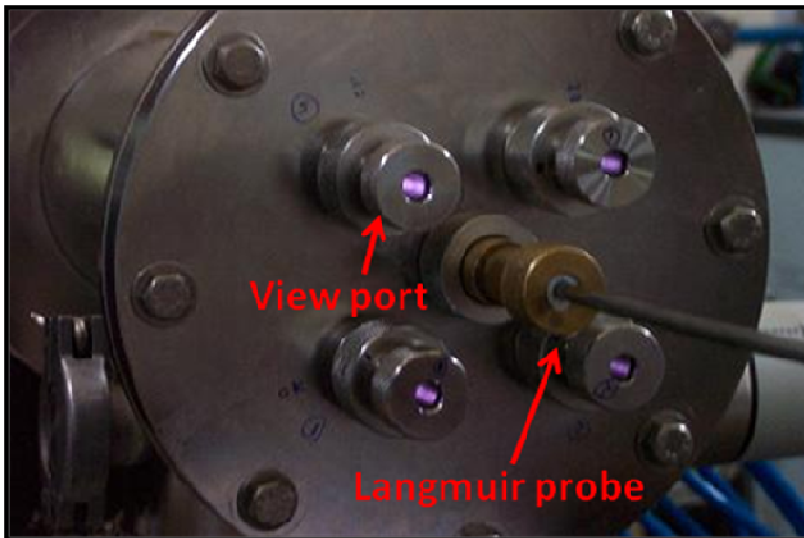


Figure 8.1 : A view of the plasma discharge through the quartz windows.

8.1 Plasma Characterization as a Function of Various Parameters

The ECR plasma was characterized as a function of gas pressure, microwave power etc. and variations in electron (plasma) density / temperature were also studied. For this purpose, the Langmuir probe was axially mounted and placed at the centre of the last coil, just touching the edge of the plasma surface, using a five port flange (as shown in Fig. 8.2). It has four quartz window ports through which plasma discharge could be observed. The experimental setup for the characterization of the RRCAT-ECRIS with Langmuir probe is shown in Fig. 8.2. The probe was biased using a bipolar power supply of ± 200 V DC, 600 mA. The data acquired by the probe as current-voltage form was recorded which was further processed off-line for evaluating the plasma parameters. The electron density of 3 to $6.5 \times 10^{11} \text{ cm}^{-3}$ and electron temperature of 5 to 20 eV was obtained. These values are close to those reported in refs. [141,142,143,144]. The error associated with the Langmuir probe measurement is $\pm 15 \%$. The behaviour of the plasma with gas pressure, with microwave power, and with radial variations is described as below.

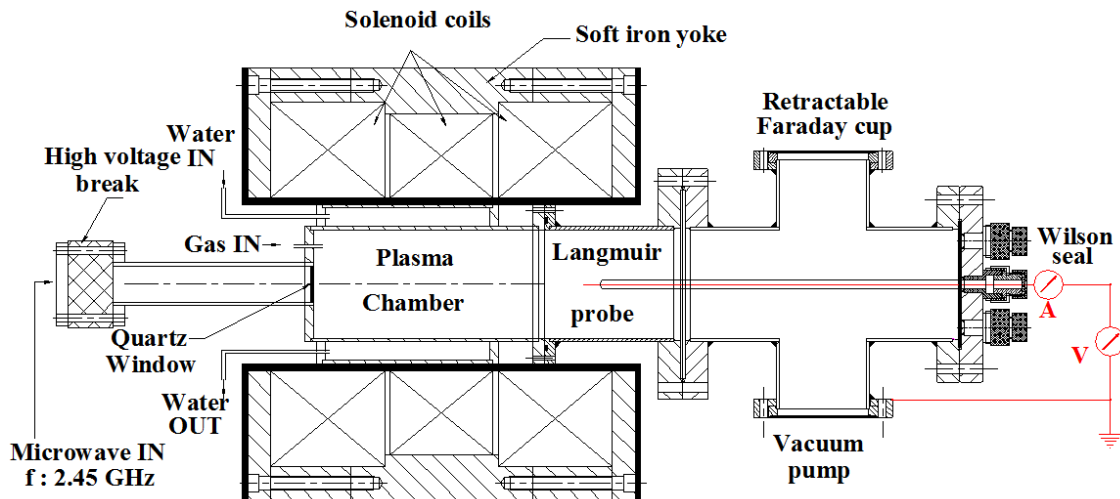


Figure 8.2 : The experimental setup for the characterization of the RRCAT-ECRIS with Langmuir probe.

a) Variation with Gas Pressure

The pressure variations were studied in the range of $\sim 10^{-5}$ mbar to 5×10^{-4} mbar of nitrogen gas, at a microwave power of 300 W. Variation of the electron density with gas pressure is shown in Fig. 8.3. It is observed that the electron density is low ($\sim 4 \times 10^{11} \text{ cm}^{-3}$) at lower pressure ($\leq 10^{-5}$ mbar), due to less number of particles available for ionization and at $\sim 10^{-4}$ mbar it reaches the maximum value of $4.8 \times 10^{11} \text{ cm}^{-3}$. The increase in density is due to the increase in the collisional ionization rate with increasing gas pressure. Then, there is a decrease in electron density with increase of gas pressure $\geq 10^{-4}$ mbar, which is perhaps due to the change in microwave mode structure at the Langmuir probe location resulting in shifting of ECR region.

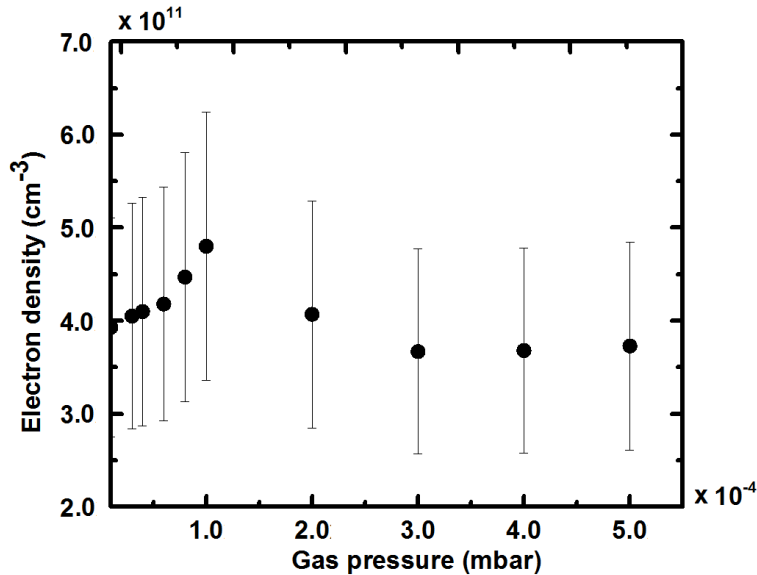


Figure 8.3 : Variation of the electron density with gas pressure.

The variation of the electron temperature with nitrogen gas pressure is shown in Fig. 8.4. It is observed that, the electron temperature decreases from 17 eV to 9 eV with increase in gas pressure from $\leq 10^{-5}$ mbar to 5×10^{-4} mbar. It is a general tendency that electron temperature decreases with increase of neutral gas pressure (i.e. the gas atom density increases), due to the increase in number of collisions with electron and neutral particle

density, as the input microwave energy (which is fixed) is now shared by a larger number of atoms. The loss of plasma is maintained by tuning the magnetic field. Electron temperature is expected to be inversely proportional to the square root of the gas pressure. The observed scaling factor of - 0.43 is in good agreement with the expected scaling of - 0.5.

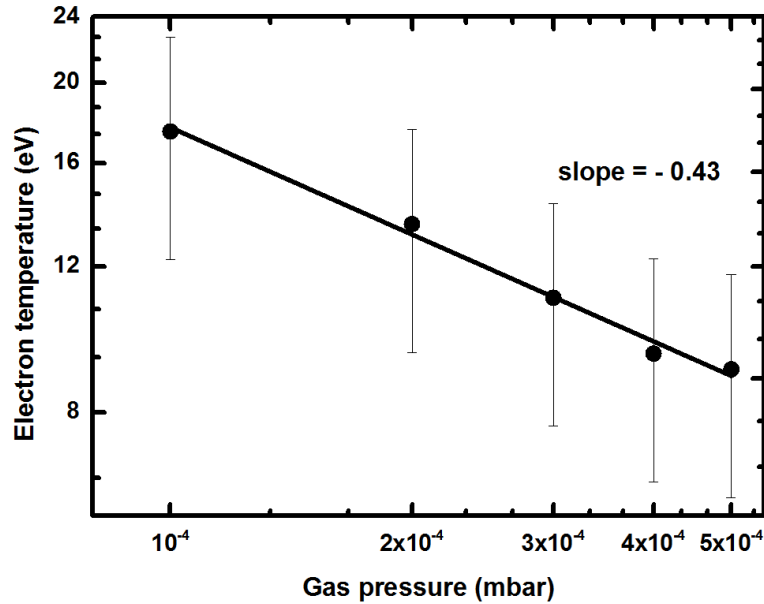


Figure 8.4 : Variation of the electron temperature with gas pressure.

b) Variation with Microwave Power

The variation in plasma parameters with the microwave power was studied in the range of 300 W to 750 W at argon gas pressure of $\sim 10^{-4}$ mbar at ECR resonant condition. The variation of the electron density with the microwave power is shown in Fig. 8.5. The electron density was found to increase ($3 \times 10^{11} \text{ cm}^{-3}$ at 300 W to $6.5 \times 10^{11} \text{ cm}^{-3}$ at 750 W) almost linearly with increase in microwave power absorbed, and reaches beyond the cut-off electron density of $7.5 \times 10^{10} \text{ cm}^{-3}$ (at 2.45 GHz frequency).

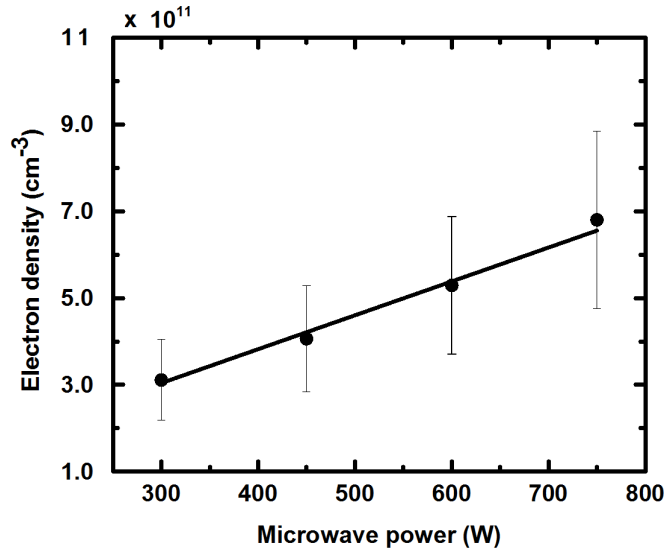


Figure 8.5 : Variation of electron density with microwave power.

The variation of the electron temperature with microwave power is shown in Fig. 8.6. The electron temperature was found to decrease (12.5 eV at 300 W to 6.5 eV at 750 W) increase in the microwave power absorbed. The decrease of electron temperature results in a smaller value of Bohm diffusion coefficient ($D_B = kT_e / 16 B$, where B is the magnetic field), resulting in loss of electrons. This variation shows that that electron density and the electron temperature can be controlled by varying the microwave power.

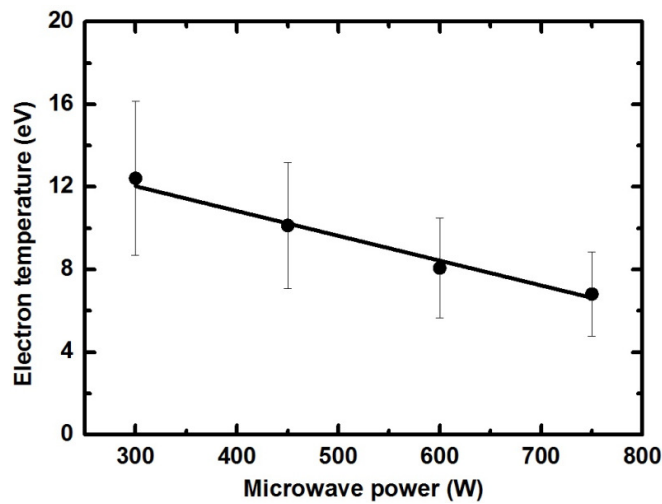


Figure 8.6 : Variation of electron temperature with microwave power.

The observed behaviour of electron density and electron temperature can be further explained phenomenologically as follows. For a given absorbed microwave power, the energy will be shared by the electrons everywhere in a given plasma volume. As the power is increased, the product of the electron density and the electron temperature should increase linearly with power, as it represents the total energy of the plasma electrons. The variation of the product of electron density and electron temperature with the coupled microwave power is shown in Fig. 8.7. This figure shows that the product of electron density and electron temperature is linearly dependent on microwave power. As the microwave power increased, the excursion length of the electrons oscillating in the microwave field increases, thereby increasing the probability of collisions with the plasma ions / neutrals, leading to faster ionization (i.e. higher electron density). As the increase of electron density with microwave power is linear (as seen in Fig. 8.5), energy is shared by a larger number of electrons than the increase in input power (energy), the temperature decreases, (as seen in Fig. 8.6).

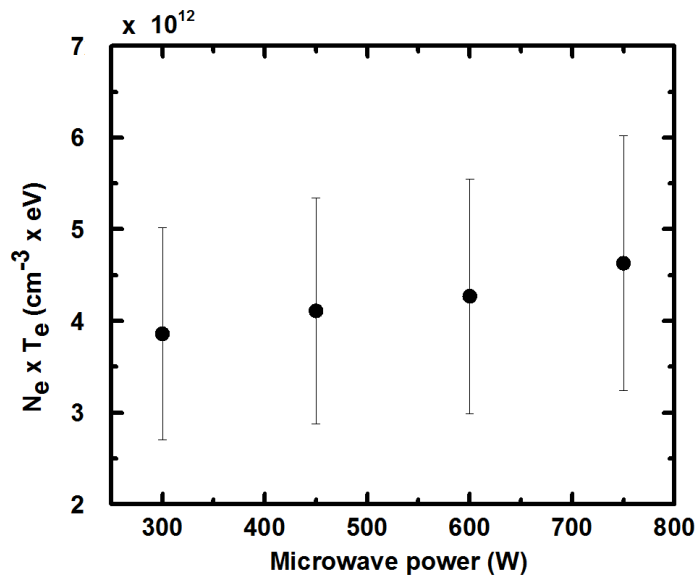


Figure 8.7 : Variation of product of electron density and electron temperature with the coupled microwave power.

c) Radial Variation

The radial variations were studied at $\sim 10^{-4}$ mbar of nitrogen gas pressure and at microwave power 300 W. For the radial variation study, the Langmuir probe was inserted at fixed positions (+ 40 mm, 0, - 40 mm) of the five port flange, as shown in Fig. 8.2. Variation of the electron density with radius is shown in Fig. 8.8. It is observed that, electron density gradually decreases from the centre of the plasma chamber at $r = 0$ mm ($\sim 3.5 \times 10^{11}$ cm $^{-3}$) to the wall of the plasma chamber at $r = - 40$ mm and + 40 mm ($\sim 2.7 \times 10^{11}$ cm $^{-3}$). The radial decrease in electron density is expected as the plasma is expected to leak to the wall or recombine as it approaches the wall of the plasma chamber. This may be also due to non-uniform variations of the microwave power absorption as well magnetic fields distributions.

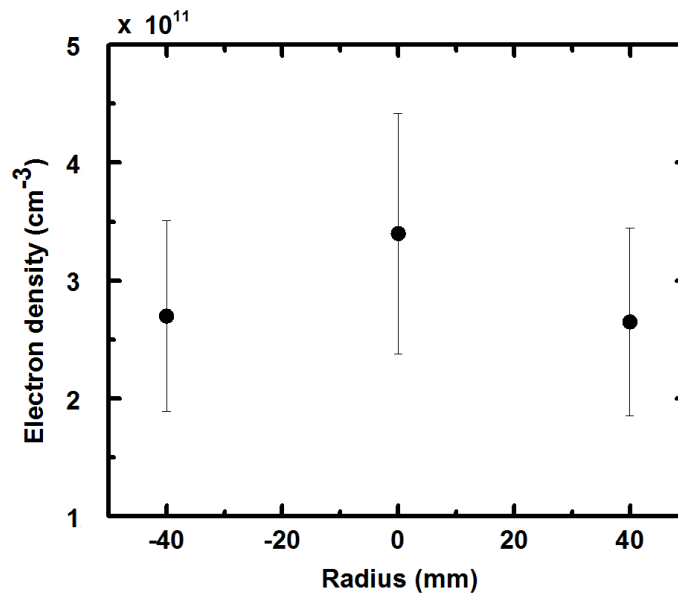


Figure 8.8 : Variation of the electron density with radius.

The radial variation of the electron temperature is shown in Fig. 8.9. It is observed that, the electron temperature decreases from the wall of the plasma chamber to the centre of the plasma chamber and on average it is 7 eV. This is expected since the microwave power is utilized for the ionization of the neutral gas, since the electron density is maximum at the

axis, thereby lowering the temperature. As one goes outwards, since the energy is shared by a lesser number of particles or ionization, the electron temperature increases.

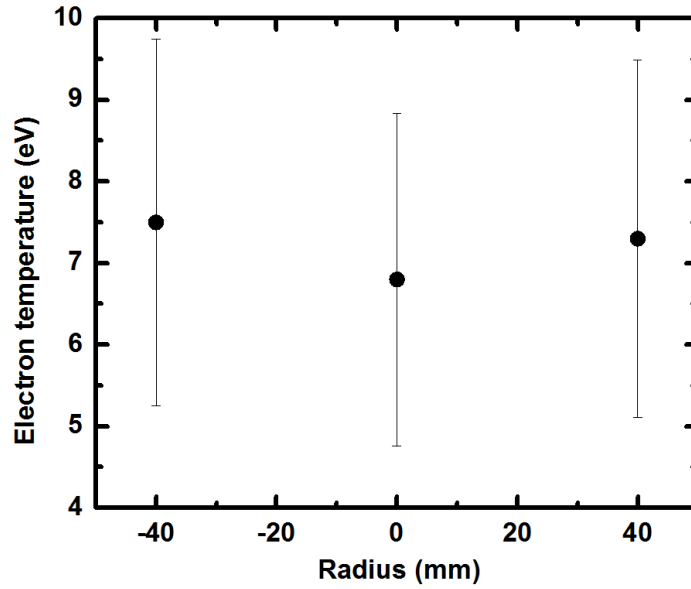


Figure 8.9 : Radial variation of the electron temperature.

8.2 Ion Beam Current Measurement

The three-electrode extraction geometry was integrated with the RRCAT-ECRIS for the extraction of the proton beam [72]. The hydrogen plasma was excited with magnetron power (600 W), hydrogen gas pressure (10^{-4} mbar), and magnetic field (875 G) with slight tuning of these parameters for the extraction of the proton beam. High purity hydrogen gas was continuously fed in the plasma chamber. The reflected power was minimized with the tuning of the three-stub tuner (impedance tuner) and by adjusting the operating parameters. The three-electrode extraction geometry was biased with high voltage DC power supply, PE was connected with 65 kV DC, 40 mA (M/s FUG, Germany), EE was connected with negative 10 kV DC, 60 mA (M/s Spellman, USA), and the last electrode ground electrode was at ground potential. The source was brought in stable operating condition to carry out the extraction of proton beam experimental study. The PE was biased positively up to 24 kV DC (Phase-I) by slowly increasing the voltage and applying the proper negative DC voltage to the

EE. The extracted ion beam was stopped on a Faraday cup, biased to 300 V DC to stop the secondary electron emission. The front plate was also negatively biased to stop the electrons from reaching the Faraday cup used for measuring the hydrogen ion beam current. The maximum of 8 mA hydrogen ion beam current was measured with current stability of $\pm 1\%$ up to 24 keV beam energy. A schematic diagram of the electrical biasing circuit of the three-electrode extraction geometry with Faraday cup is shown in Fig. 8.10.

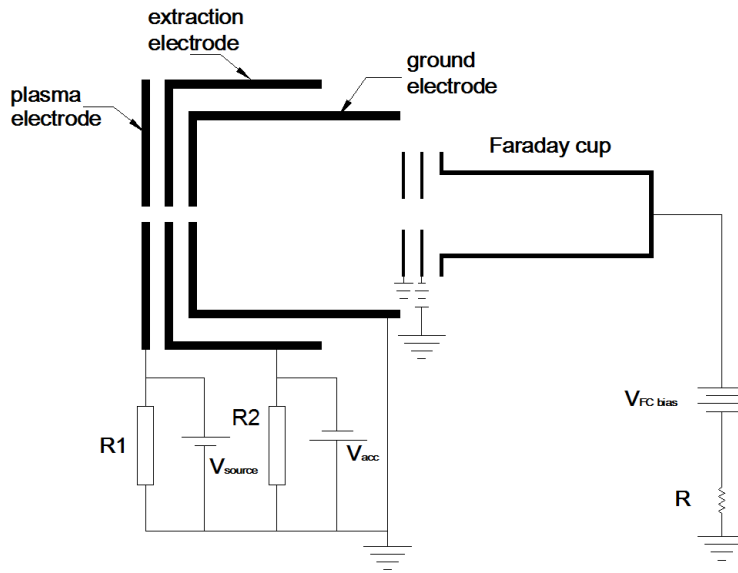


Figure 8.10 : A schematic diagram of the electrical biasing circuit of the three-electrode extraction geometry with Faraday cup.

Variation of the measured hydrogen ion beam current with extraction voltage is shown in Fig. 8.11. The ion beam current increases with increase of applied voltage to the PE which is expected theoretically. The data points are shown as dots and the continuous curve shows the prediction from the Child-Langmuir's law ($I \propto V^{3/2}$). One can see that the experimental values are closely following the ones expected theoretically. The experimental parameters used for the extraction of ion beam from the three-electrode extraction geometry for Phase-I are given in Table 8.1. It is observed that the ion beam current, measured with Faraday cup, has a scaling of 1.6 with the ion beam extraction voltage. With this scaling, it

can be extrapolated to reach 30 mA proton beam current for 50 kV DC extraction voltage. The proton beam intensity can be enhanced with proper coupling of the microwave power and optimizing the operating conditions [72].

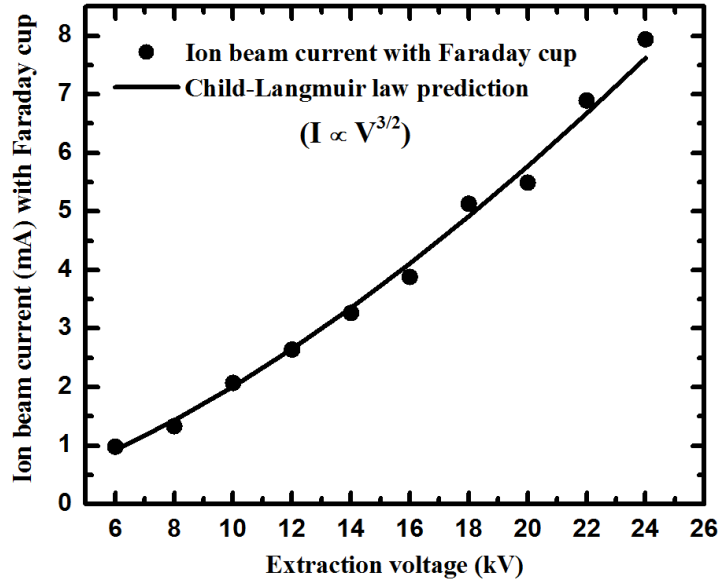


Figure 8.11 : Variation of the measured hydrogen ion beam current with extraction voltage.

Electrode Geometry Parameters	IGUN Simulation Parameters	Present Status
Beam energy	25 keV	24 keV
Beam current	10 mA	8 mA
PE voltage	25 kV DC	24 kV DC
EE voltage	-700 V DC	-200 V to -2 kV DC
PE aperture	5 mm	5 mm
EE aperture	10 mm	10 mm
GE aperture	8 mm	8 mm
Gap between PE and EE	7 mm	7 mm
Gap between EE and GE	3 mm	3 mm

Table 8.1 : The experimental parameters used for the extraction of ion beam from three-electrode extraction geometry for Phase-I.

8.3 Ion Beam Characterization using Thomson Parabola Ion Spectrograph (TPIS)

The ion flux measurement was carried out using two widely used techniques, namely, the field-free ion collector (Faraday cup) which provides a signal proportional to the ion flux incident on it, and a Thomson parabola ion spectrograph (TPIS). The advantage of using a TPIS lies in complete characterization of the ion beam in terms of its flux and charge state. This feature also facilitates the use of TPIS while dealing with gas mixtures or high-Z vapours where different ion species with multiple charged states can be present in the plasma. The basic working principle of a TPIS lies in applying parallel electric and magnetic fields to the charged particle trajectories [145,146]. A schematic diagram of a Thomson parabola ion spectrograph is shown in Fig. 8.12.

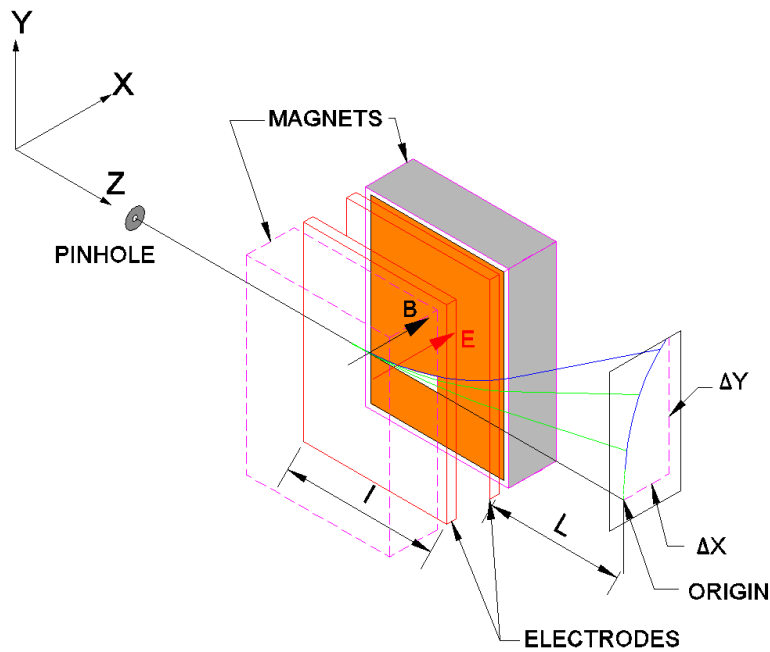


Figure 8.12 : A schematic diagram of a Thomson parabola ion spectrograph.

It is well known that when a charged particles of mass m , energy $\{E = (1/2) m V^2\}$ and charged state q passes through a parallel electric and magnetic field, the deflection due to electric and magnetic field can be written as,

$$x = \left[\frac{qEl}{mV^2} \right] \left[L + \frac{l}{2} \right] \dots\dots\dots(8.1)$$

$$y = \left[\frac{qBl}{mV} \right] \left[L + \frac{l}{2} \right] \dots\dots\dots(8.2)$$

where x and y are the particle deflections due to the electric (E) and the magnetic (B) field respectively, V is the velocity of the particle, L is the charged particle drift length in free space (100 mm), and l is the length of the field region along the direction (Z) of particle propagation (80 mm). The resultant trajectory of the charged particles can therefore be obtained by combining these two equations, which gives the equation of a parabola in the following form,

$$y^2 = \left[\frac{q}{m} \right] \left[\frac{B^2 l}{E} \right] \left[L + \frac{l}{2} \right] x \dots\dots\dots(8.3)$$

As is evident from the above equation, the charged particles will disperse according to their charge to mass (q/m) ratio, following a parabolic trajectory. A two dimensional position sensitive detector (P-42 phosphor screen : $Gd_2O_2S:Tb$, Gadolinium Oxy-Sulphide) placed perpendicular to the direction (Z) of charge particle propagation (i.e. in the XY plane) will therefore record the parabolic tracks corresponding to different charge to mass (q/m) ratios. The energy distribution of a particular charged species can be found by scanning the intensity along the individual tracks.

The resolving power ($\Delta E/E$) of the TPIS can be approximated by calculating the energy range covered by the beam spot on the detector surface divided by its central energy. This can be expressed as,

$$\frac{\Delta E}{E} = 2\Delta s \left[\frac{mV}{qBl(L + \frac{l}{2})} \right] \dots\dots\dots(8.4)$$

where Δs is the ion beam spot size on the detector which, in our case is the pin-hole size used in front of the spectrograph. Please note that contrary to the conventional source size estimation methods where isotropic emission is assumed, here the beam is collimated. The phosphor screen was imaged onto an 8-bit CCD camera to record the particle tracks. The ions entered the electric and magnetic field region through a 0.5 mm diameter, 2.5 mm thick lead collimator. A magnetic field of 400 G and an electric field of 200 V/cm were applied to deflect the ions from their original trajectory. The interaction of energetic electrons with molecular hydrogen can lead to the generation of neutral H, H^+ , H_2^+ and H_3^+ following the processes of i) direct ionization : $e^- + H_2 \rightarrow H_2^+ + 2e^-$, ii) dissociative attachment : $H_2^+ + H_2 \rightarrow H_3^+ + H$, iii) dissociative recombination : $e^- + H_2^+ \rightarrow 2H$, iv) dissociative ionization : $e^- + H_2^+ \rightarrow 2H^+ + 2e^-$, and v) dissociative excitation : $e^- + H_2^+ \rightarrow H^+ + H + e^-$. Apart from this, the proton beam can also be obtained by direct electron - neutral hydrogen atom collision with threshold energy of 13.6 eV. The present setup enables us to visualize all the reaction products on-line except dissociate recombination where the product is neutral H, along with their variation with external parameters such as, gas pressure, magnetic field and microwave power.

Proton beam trajectory recorded by the Thomson parabola ion spectrograph at different extraction voltages is shown in Fig. 8.13. The solid (yellow) lines signify the calculated trajectories for the H^+ , H_2^+ , and H_3^+ species. The proton track is constituted by discrete points formed by the proton beam obtained for different extraction voltages. The pixel intensities along the parabola represent the relative population of proton flux extracted at different extraction voltages and acquired for fixed time interval. The energy scale is

displayed as an aid for visualization. The picture shows that within our detection limit, no other charged species were present in the plasma. An in-house developed algorithm was used to reconstruct theoretically the parabolic trajectory for protons (yellow line) and read the data along the line profile. Since the image in Fig. 8.13 showing the ion spectrum is a composite image obtained for different extraction voltages, the collection time for each recorded image was normalized while estimating the energy distribution from TPIS [72].

To understand the quality of the ion beam, we have also estimated the particle distribution for individual extraction voltages. Fig. 8.14 shows the variation of the estimated dispersed particle distribution in the ion beam with increasing extraction voltages. The insets show the dispersed particle distribution at 9 kV (inset (a)) and accumulation of dispersed particle distribution at 25 kV (inset (b)) extraction voltages. The signature of accumulation of dispersed particle distribution with increasing extraction voltage is evident from the insets. For low extraction voltages, the dispersed particle distribution is found to be more (6-9 %).

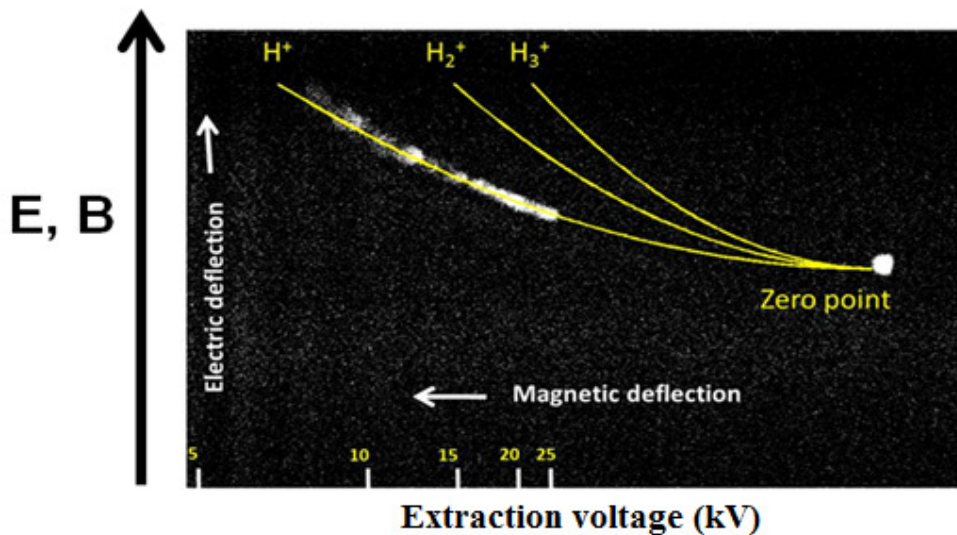


Figure 8.13 : Proton beam trajectory recorded by the Thomson parabola ion spectrograph at different extraction voltages. The solid (yellow) lines signify the theoretically calculated trajectories for the H^+ , H_2^+ and H_3^+ species. The ion energy scale is shown as a visual aid only.

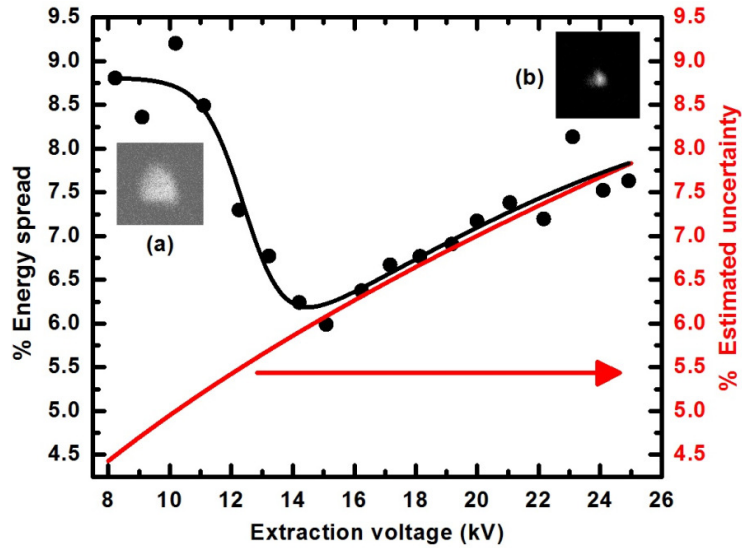


Figure 8.14 : Variation of the estimated dispersed particle distribution in the ion beam with increasing extraction voltages. The solid black curve is for visual aid only. The solid red curve shows the estimated uncertainty in dispersed particle distribution measurement with TPIS. The insets show the dispersed particle distribution at 9 kV (inset (a)) and accumulation of dispersed particle distribution at 25 kV (inset (b)) extraction voltages.

This can be attributed to the formation of plasma meniscus at the PE, as the system is optimized for 25 kV DC extraction voltage. With an increase in the extraction voltage, the dispersed particle distribution goes down but again starts increasing beyond 14 kV DC extraction voltage. To understand this behaviour, we have estimated the error in the TPIS measurement governed by the finite source size (500 μm diameter aperture). The uncertainty in TPIS measurement is known to have a non-linear dependence with ion beam extraction voltage. Also the distance of the plasma volume to the aperture is larger than the distance of the detector plane to the aperture. The variation of the estimated dispersed particle distribution in the ion beam with increasing extraction voltages is shown in Fig. 8.14 (red solid line). Therefore the dispersed particle distribution of the RRCAT-ECRIS, in this case, beyond 14 kV is primarily limited by the energy resolution of TPIS.

Comparison of the proton beam current as measured by the Faraday cup and by the Thomson parabola ion spectrograph is shown in Fig. 8.15. In this figure, the solid curve

shows the space charge limited behaviour expected as per the Child-Langmuir's law. The TPIS measurement clearly demonstrates the presence of pure protons in the beam, as the H_2^+ and H_3^+ population lies below the detection limit of TPIS. The measured ion beam current follows the Child-Langmuir's law ($I \propto V^{3/2}$) showing that the extracted current was limited by the space charge generated between the PE and EE. The main purpose of using TPIS in this study was to identify the impurities present in the plasma. It is well known that apart from the primary gas to be used for plasma generation, unwanted elements such as water molecules, hydrogen molecules are always present in the system in very small quantities. A TPIS is very much capable of revealing these impurity ions. In our system, we have ensured that it can reach a vacuum level of 10^{-9} mbar to prevent significant losses due to charge exchange or even neutralization in interaction with background gases. Moreover, baking was used to remove the unwanted elements. It may be noted that hydrogen is the most difficult element to remove in these cases. However, in the present case, as we are generating hydrogen plasma itself, the above problem is absent. Our measurements clearly reveal that to the best of the detection limit, no traces of any other species from the plasma could be recorded, showing that our ion beam consists of mostly protons [72].

Argon ion beam trajectory recorded by Thomson parabola ion spectrograph for a) short, and b) long exposure time is shown in Fig. 8.16. In this case, the source was operated in the mirror magnetic field configuration. We have observed the Ar^{+8} and Ar^{+3} traces depending on exposure time. The Ar^{+8} traces (closed shell Ne-like stable ion) were recorded for short exposure time, which is why it is preferentially produced. The Ar^{+3} and Ar^{+8} both traces together were seen with the long exposure time. This may be attributed to long confinement time and suitable plasma density with the mirror magnetic field configuration. This validates the RRCAT-ECRIS source design and may be operated in mirror magnetic field configurations also to achieve the high charge states.

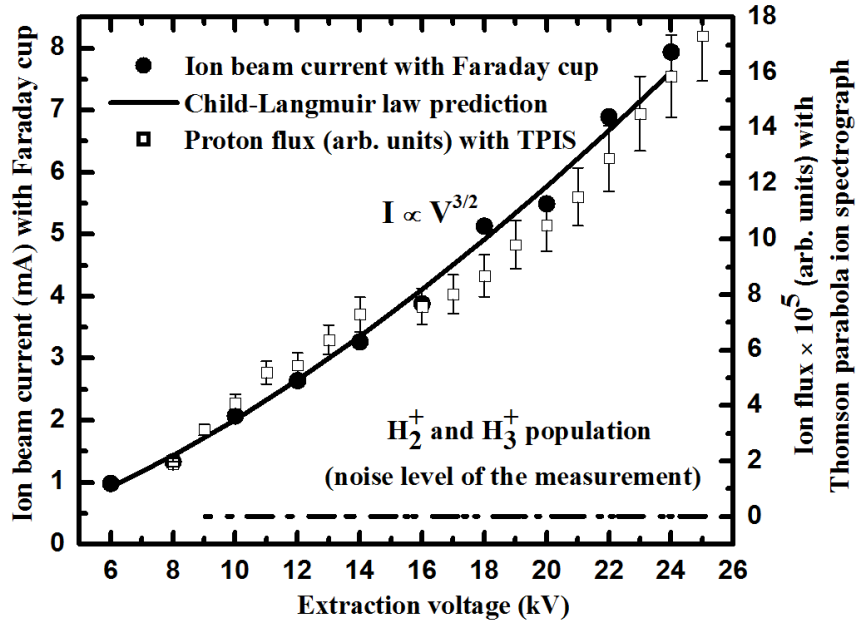
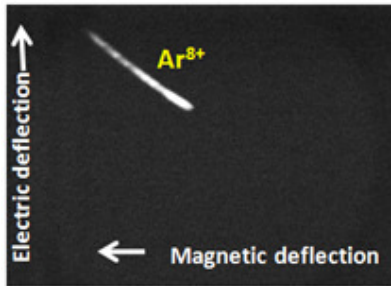
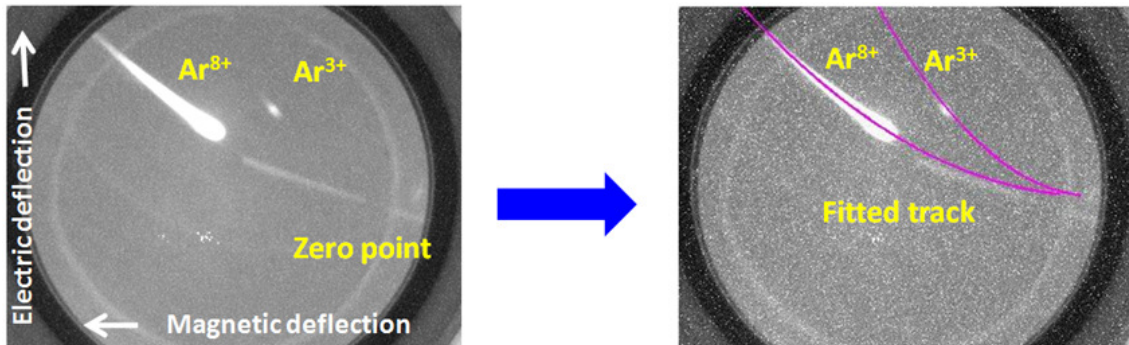


Figure 8.15 : Comparison of the proton beam current as measured by the Faraday cup and by the Thomson parabola ion spectrograph.



a)



b)

Figure 8.16 : Argon ion beam trajectory recorded by the Thomson parabola ion spectrograph for a) short, and b) long exposure time.

8.4 X-ray Measurements with Silicon P-I-N Detector

There is an active research interest in generation of keV x-ray line emitter sources yielding high photon flux with high peak to background ratio for various scientific and technological applications like material structural science [147], medical applications (radiology, mammography, radiobiological, phase contrast imaging applications) [26,148,149], calibration of thermo-luminescent dosimeter [150], trace elemental analysis [151], and non-destructive testing applications [152]. The conventional source like Coolidge tube or rotating anode x-ray generator [153] which uses filament and high voltage power supply are bulky, having a disadvantages like reduction of intensity of x-ray signal with time operation, limited photon flux, high divergence. Although synchrotron radiation x-rays [154] sources are efficient and intensity of x-ray radiation is also several order magnitude higher than conventional sources. However, such sources are capital intensive large central facility and not accessible for routine applications such as elemental analysis or detector calibration etc. The other alternative is the laser produced plasma based x-ray sources. It requires moderate infrastructure and give high peak brightness but has low repetition rate limited by the driving laser system. On the other hand, ECR source generates x-rays that are becoming popular [48, 49, 50, 51, 52]. This is because of its being simple to use, compact, filament less, and easy to control of photon flux. Moreover, there is no reduction of intensity of the x-ray signal with time, it is highly monochromatic, has longer lifetime, and can be operated in pulsed as well as continuous wave mode

The process of generating x-rays is by the collision of ion beam produced by ECR plasma source with a solid target. This is referred to as particle induced x-ray emission (PIXE) [151] where the x-rays are generated when a high current ion beam impinges on a target material (copper, molybdenum, tungsten etc.) and loses its energy to generate continuum bremsstrahlung, and characteristics line radiation. The x-ray continuum emission

extends up to the energy of the ion beam. The energetic ions bombarding the target knock out electrons from inner shells of the atoms thus resulting in an inner shell vacancy. The radiative de-excitation of electrons from outer shells results in characteristic x-ray line radiation. The x-ray photon energy of line radiation easily can be tuned by changing the target material. The photon flux of the x-ray line radiation depends on the energy of the ion beam. A tightly focussed ion beam can generate point x-ray source of nanometre to microns size and qualifies it for applications such as phase contrast imaging. Further, it is nearly monochromatic and has very high peak to background intensity ratio for the x-ray radiation which is desirable for its use in imaging applications.

The extracted ion beam was made incident on the copper disc placed at 150 mm away from the ground electrode. The x-ray spectrum was recorded at different ion accelerating voltage using an energy dispersive silicon detector (Amptek : XR-100CR) (working in a single photon counting mode) coupled to multi channel analyzer (MCA 8000A from M/s Amptek, USA) through a Kapton window (50 μm thick). The detector is sensitive to x-rays with energy from 1.5 keV to \sim 20 keV with efficiency greater than 50% of its peak sensitivity [155]. The energy calibration was performed using an x-ray generator (Amptek cool-X) providing Cu K- α and Ta L- α . The spectral resolution of the detector was determined to be \sim 162 eV at 8 keV, from the full width half maximum of K- α line radiation. The detector distance from the source was optimized to achieve single photon counting and to avoid any pile-up effect on the measured spectrum. Each spectrum was acquired for 5 minutes to accumulate adequate statistics (typically 2000-5000 counts per spectrum) without significant pile-up effect. The experimental setup for x-ray detection from RRCAT-ECRIS is shown in Fig. 8.17.

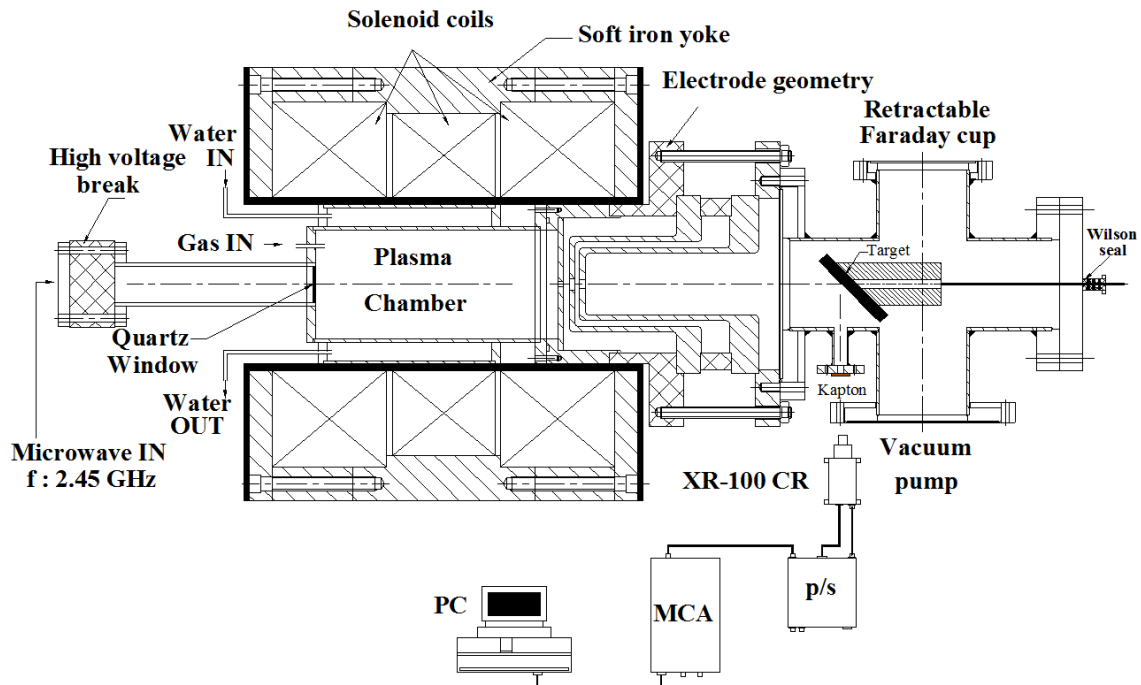


Figure 8.17 : The experimental setup for x-ray detection from RRCAT-ECRIS.

The aim of this experiment was to study the scaling of the x-ray conversion efficiency with ion beam energy. Figures 8.18, 8.19, and 8.20 show the x-ray emission spectra of copper induced argon, hydrogen, and nitrogen ions at 25 kV extraction voltage respectively. It is observed that the x-ray spectrum consists of characteristic line radiation i.e. copper K- α at 8.05 keV and K- β line radiation at 8.9 keV, riding on a very low continuum (bremsstrahlung) background. This results in a very high peak to background ratio of the monochromatic line, which is a highly desirable feature of a source for imaging applications. The intensity ratio of the K- β to K- α lines was measured to be 0.16 ± 0.01 , which is in good agreement with the theoretically expected ratio of 0.17 [156]. The spectral width (FWHM) of the K- α line radiation was ~ 180 eV, close to the resolution of ~ 145 eV offered by the detector system.

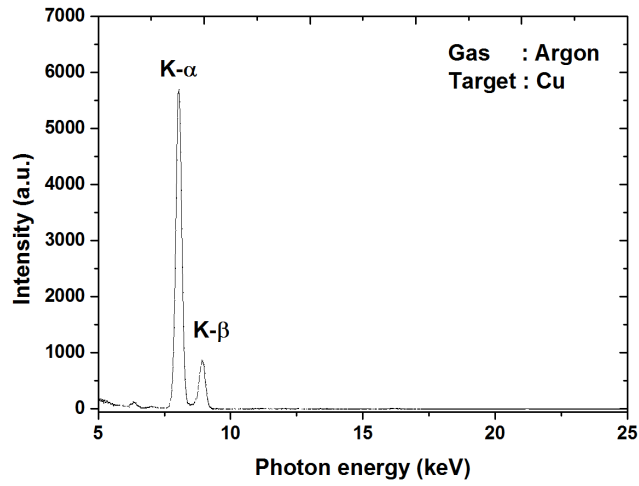


Figure 8.18 : X-ray emission spectra of copper induced by argon ions at 25 kV extraction voltage.

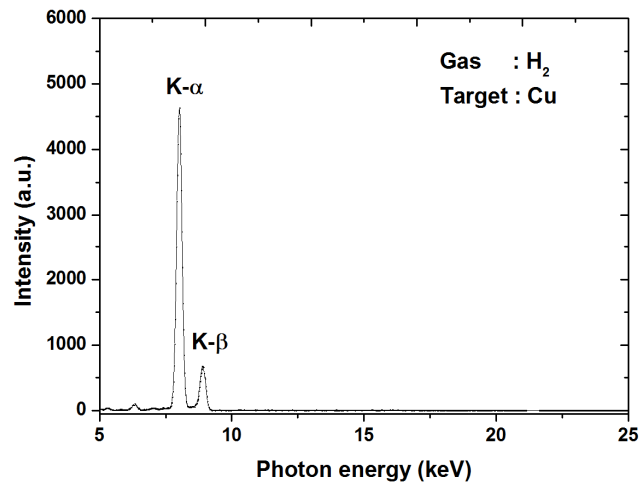


Figure 8.19 : X-ray emission spectra of copper induced by hydrogen ions at 25 kV extraction voltage.

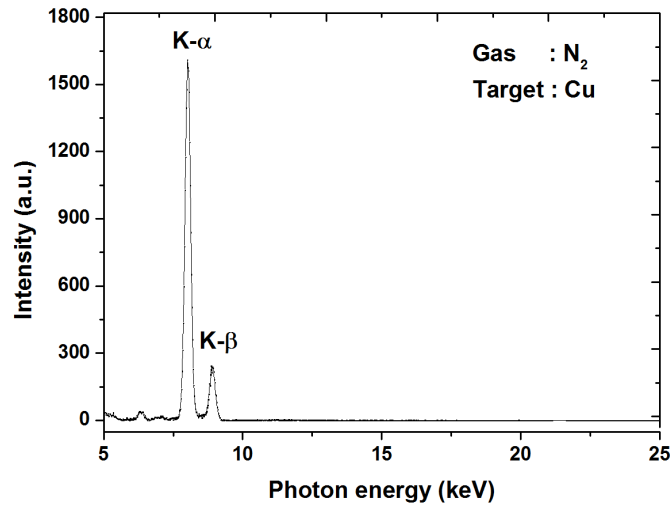


Figure 8.20 : X-ray emission spectra of copper induced by nitrogen ions at 25 kV extraction voltage.

The above observation can be interpreted through the generation of the K-shell x-ray line radiation by creation of K-shell vacancy by the collision of low energy ions (projectile) with the target atoms. For a projectile of atomic number (Z_1) much smaller than the target atomic number (Z_2), the vacancy in K-shell is created by direct Coulomb excitation. On the other hand, for $Z_1 \approx Z_2$, the process is described by the molecular orbital interaction. For the $Z_1 \leq Z_2$ case, that cross section for K-shell vacancy creation by low energy ions (few tens of keV) strongly depends on the energy of the projectile, having an exponent nearly equal to 4 [157].

8.5 Application of the ECR Source for Titanium Film Deposition

An ECR source (with and without Magnetron (rf), with and without DC sputtering) is widely preferred over conventional ion sources for high quality conductive metallic (titanium, nickel, copper, niobium, tantalum, and tungsten) coatings, insulating coatings, dielectric thin film deposition, reactive ion (sputter) etching, molecular beam epitaxy, ion implantation, synthesis of hydrogen-free microcrystalline diamond-like carbon films [158,159,160,161],

and to reduce the metal oxides by hydrogen plasma [162,163]. The role of the ECR plasma in plasma processing has been widely accepted due to several advantages offered like : a) independent control of ion flux and energy, which helps to increase or decrease the rate of plasma processing, b) can be operated over a longer time period without much maintenance, and c) suitable for operation under corrosive environment being filament-less. The other features which make an ECR method superior to use for thin film deposition as compared to other techniques of deposition (like RF magnetron sputtering) are : high plasma density ($\sim 10^{10}$ - 10^{11} cm^{-3}), low ion temperature (0.1-10 eV), low pressure operation (10^{-5} - 10^{-3} mbar), efficient gas utilization, and uniform plasma with a high degree of ionization and decomposition of working gases.

ECR based low pressure chemical vapour deposition, plasma enhanced chemical vapour deposition, ion beam sputtering etc. have numerous applications in scientific research as well as technological development. The films deposited by these techniques (either single or multi-layers with silicon nitride, silicon dioxide, titanium nitride, boron nitride, aluminium nitride, metal multi-layers etc.) have great support to industry. These films are widely used as passivation layers for very large scale integrated circuits (microelectronics), magnetic multi-layers (offers giant magneto resistance or perpendicular magnetic anisotropy) for applications in memory devices, for multi-layer resist lithography, for inter-level dielectrics in multi-level metallization structures, decorative gold coatings and wear / protective coatings for tooling industry, bioengineering, and space technology. The titanium and titanium nitride coatings have become popular (due to their low secondary emission, excellent chemical and thermal stability) among scientific community. They are used to enhance the performance of RF microwave couplers / windows, and RF superconducting cavities to avoid the multi-pacting effects (i.e. reduces the electrical breakdown and excessive heating). They are also widely used in particle accelerators, e.g. RFQ accelerator at Los Alamos, coupler windows at

Fermilab, Tesla couplers at Desy, RF and microwave components of Indus-1 (450 MeV, 100 mA) and Indus-2 (2.5 GeV, 300 mA) synchrotron radiation sources at RRCAT.

A schematic diagram of the experimental setup of ECR based ion beam sputtering system with the arrangement for the target (Ti plate) and the substrate (float glass) holder is shown in Fig. 8.21.

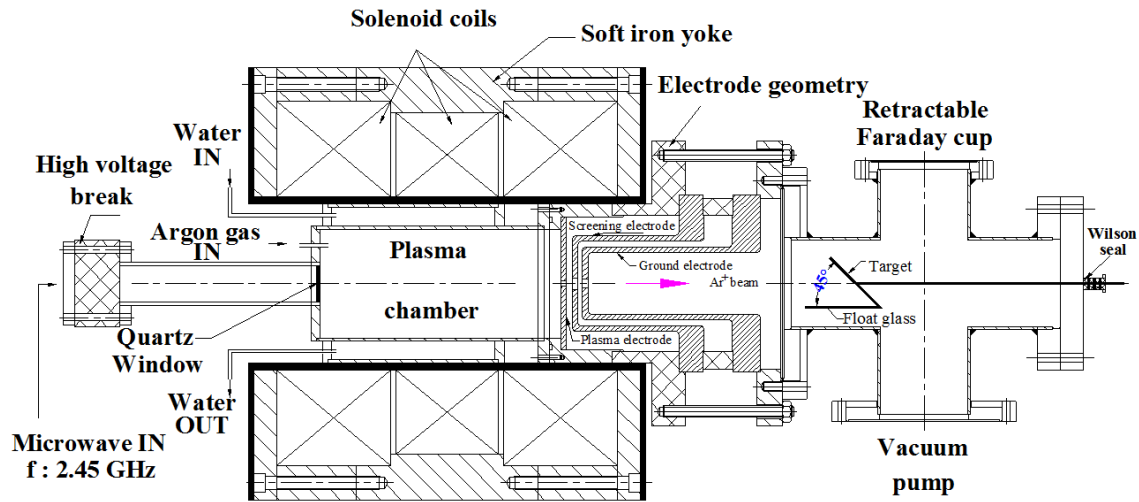


Figure 8.21 : A schematic diagram of the experimental setup of ECR based ion beam sputtering system with the arrangement for the target and the substrate holder.

The sputtering target (titanium, 50 mm × 50 mm × 10 mm thick) was placed 300 mm away from the ground electrode at 45° w.r.to the beam. It was mounted on a vacuum sealed stainless steel tube of 5 mm in diameter, with a Wilson seal arrangement for axial movement. The substrate (float glass, 75 mm × 25 mm, surface roughness ~ 6 Å) was placed parallel to the beam in the processing chamber. The extracted argon ion beam (25 keV, 1 mA) from ECR plasma source strikes the sputtering target surface and the ejected metal flux (sputtered off) get deposited on the substrate. The deposited films were characterized by x-ray reflectivity (XRR) (specular) measurements [164], using a Bruker-D-8 diffractometer with a Cu K-α x-ray source. The x-ray reflectivity pattern (round hollow dots) of the titanium conductive metal film along with fitting (red line) is shown in Fig. 8.22.

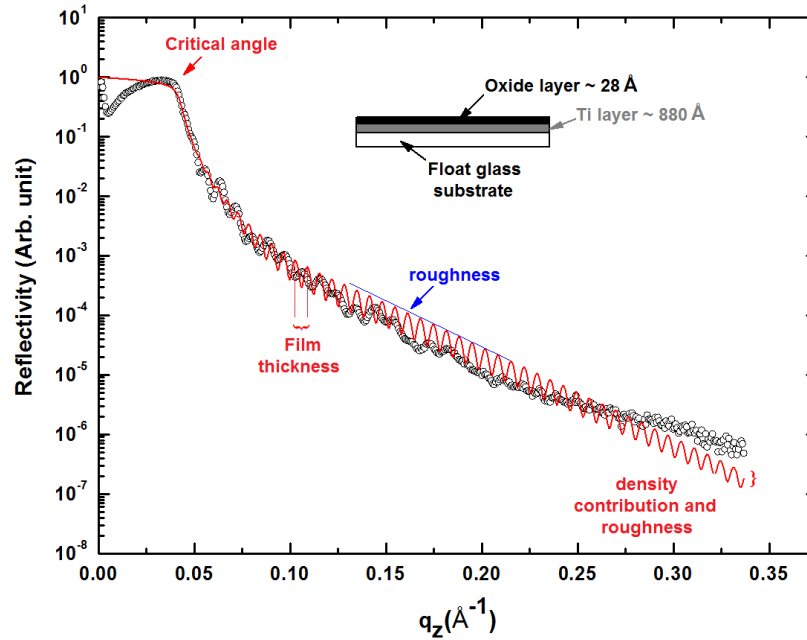
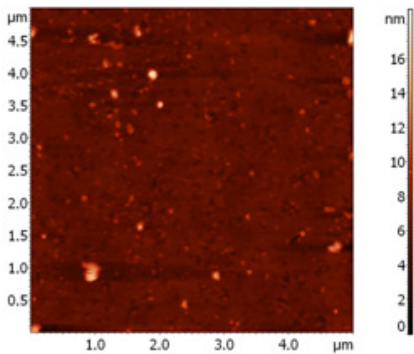


Figure 8.22 : The x-ray reflectivity pattern (round hollow dots) of the titanium conductive metal film along with fitting (red line).

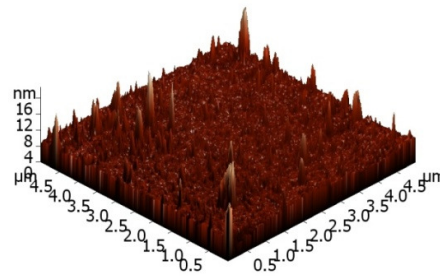
The oscillations corresponding to the total thickness of the film can be clearly seen in the reflectivity pattern. Parratt recursive formalism [165] was used to model the reflectivity parameters and for the analysis of the XRR measurement data. The roughness was also taken into account using Nevot-Croce model [166]. The total thickness of the titanium film was found to be 880 Å, with a surface roughness of 14 Å and density 4.47 gm/cm³ (98 % of bulk), close to standard bulk density 4.54 gm/cm³. A thin oxide layer of thickness 28 Å with surface roughness 5.9 Å and density 3.31 gm/cm³ was used so that the theoretical profile matches the measurement. The additional layer accounts for the oxidation occurring at the surface of the film during exposure to the atmosphere.

Atomic force microscopy (AFM) [167] was done to measure the surface roughness of the titanium thin film deposited. Surface topographies of the two different regions of the samples were imaged using a multimode scanning probe microscope (NT-MDT, SOLVER-PRO, Russia). AFM measurements were carried out in a non-contact mode using silicon cantilever tips having radius of curvature ~ 20 nm and a spring constant 5.5 N/m with a

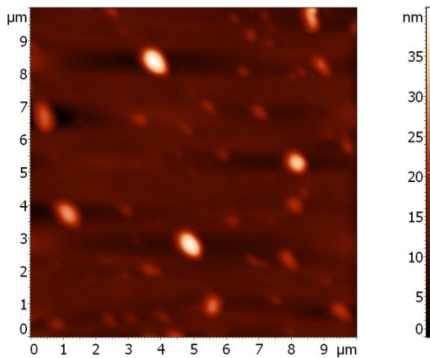
resonant frequency of 190 kHz, under ambient conditions. The top surface was electrically grounded during the measurements. The surface topographic features were estimated using the imaging software *SOLVER-PRO*. Analysis was carried out at various places on the surface of the sample. The atomic force microscopy images of the titanium film are shown in Fig. 8.23. First two images (a, and b) correspond to $5\ \mu\text{m} \times 5\ \mu\text{m}$ scan area. The presence of small particle of size $\sim 0.1\ \mu\text{m}$ is seen. The roughness of this scan area is $\sim 9\ \text{\AA}$. The other two images (c and d) correspond to $10\ \mu\text{m} \times 10\ \mu\text{m}$ scan area in another region, far away from the previous region. This shows few large sizes ($\sim 1\ \mu\text{m}$) and few medium sizes ($\sim 0.4\ \mu\text{m}$) particles. These particles must have formed due to some fluctuation during the deposition process. Roughness of this scan area is $30\ \text{\AA}$. In both the regions, the films are without pores.



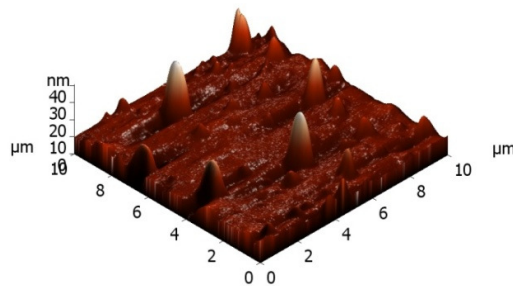
(a) $5\ \mu\text{m} \times 5\ \mu\text{m} \times 2\ \text{D}$, roughness : $9\ \text{\AA}$



(b) $5\ \mu\text{m} \times 5\ \mu\text{m} \times 3\ \text{D}$, roughness : $9\ \text{\AA}$



(c) $10\ \mu\text{m} \times 10\ \mu\text{m} \times 2\ \text{D}$, roughness : $30\ \text{\AA}$



(d) $10\ \mu\text{m} \times 10\ \mu\text{m} \times 3\ \text{D}$, roughness : $30\ \text{\AA}$

Figure 8.23 : The atomic force microscopy images of the titanium film.

In summary, titanium films were successfully deposited on float glass substrate using RRCAT-ECRIS based argon ion beam sputtering. The x-ray reflectivity studies have shown 880 Å thick titanium film deposition on a float glass substrate with 14 Å roughness. The roughness measured with atomic force microscopy was 9 Å. The deposited thin film shows uniformly dense, mirror-like finish, non-porous structure (i.e. insensitive to moisture) and strong adherence to float glass substrate. The deposited film was clean, since pre-bombardment of the target at low energy itself cleans the target surface, and reduces the effect of impurities like oxygen, hydrogen, water etc.

8.6 Ion Beam Characterization with Mass Analyzing Magnet

The mass analyzing magnet [168,169,170,171,172,173] is an important part of the accelerator system and is widely used to analyze the mass and energy of the charged particles. It also provides proper focussing to the charged particles beams. The working principle is quite simple. An ion of mass (M_i) and charge ($q = Z e$) moving in vacuum with a velocity (v), in a direction perpendicular to a magnetic field (B), undergoes circular path with radius (R) which is given by, $R = M_i v / qB$. Thus, all the ions with the same charge and momentum entering the magnetic field from a common point will move in the same path with a radius (R). If all the ions of charge (q) enter the magnetic field with an identical kinetic energy (qV , where V is the accelerating voltage), then the radius will depend on mass, as,

$$qV = \frac{1}{2} M_i v^2, \text{ One gets, } \frac{M_i}{q} = \frac{B^2 R^2}{2V} \dots\dots\dots(8.5)$$

This shows that the radius of curvature for the ions depends only on the ratio of the ions mass to charge, as long as their kinetic energy is the same. Thus a magnetic field can be used to separate a mono-energetic ion beam into its various mass components. The RRCAT-ECRIS integrated with the mass analyzing magnet is shown in Fig. 8.24.

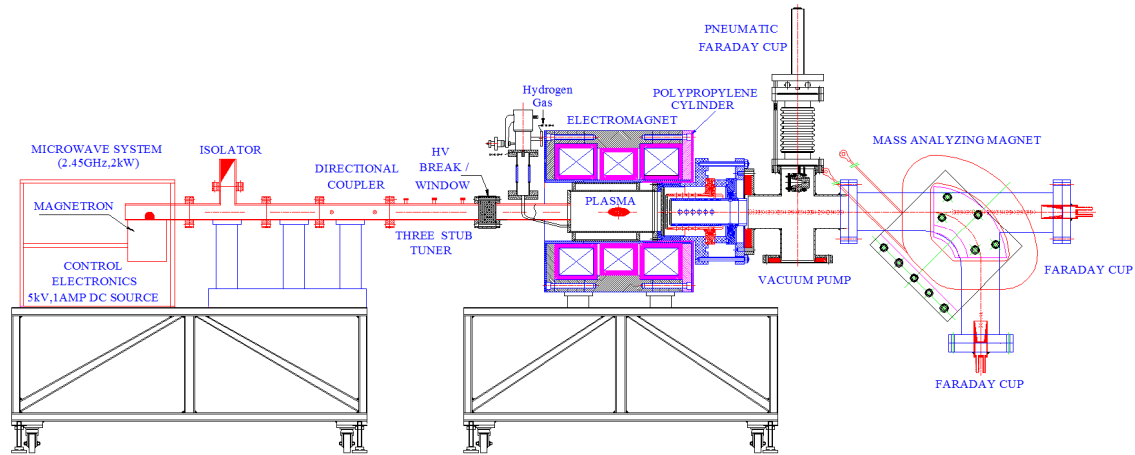


Figure 8.24 : The RRCAT-ECRIS integrated with the mass analyzing magnet.

The extracted ion beam from ECR plasma source is composed of hydrogen species like H^+ , H_2^+ , and H_3^+ . It is very important to know the intensity fraction of the molecular hydrogen ion species presented with the proton beam. We have designed and developed a 90° mass analyzer of suitable magnetic field for this purpose. The intensity fractions H^+ , H_2^+ , and H_3^+ with respect to the analyzing solenoid magnet current could be also studied with respect to the input microwave power and the gas pressure. The microwave power and the gas pressure are the two main parameters, which control the ionization in the plasma. It has been observed that if the microwave power is quite high and the gas pressure is quite low, then the density of molecular hydrogen ions in the plasma is quite low. The salient features of the magnet are : compact size, low weight, mass resolution (1 %), field homogeneity (0.01 %), large acceptance, air-cooled, easily machinable, and easy alignment because of compact size, i.e., $250\text{ mm} \times 250\text{ mm} \times 250\text{ mm}$.

1) Magnetic field design : The design parameters of a mass analyzing magnet are usually simulated using *2D-Poisson* [117] and *3D-Opera codes* [118]. We have used the *2D-Poisson* code for the design of our mass analyzing magnet. We have chosen sector pole with rectangular yoke (C-shaped) type magnet. The C-shaped magnet [174] was chosen because of

the simplicity in design, easy access and fabrication of the vacuum chamber, low machining and fabrication cost, as compared to a sector magnet or circular poles with sector yoke. The design parameters of the mass analyzing magnet are given in Table 8.2.

Magnet Type	Parameters
Bending angle	90°
Good field region	± 30 mm
Bending radius (central orbit)	120 mm
Design field	3000 G
Homogeneity	0.1 %
Pole gap height / width	26 mm / 112 mm

Table 8.2 : *The design parameters of the mass analyzing magnet.*

To get the desired field configuration, a number of iteration has been done in the simulations. Here we compare the analysis of the two models : Model-1 and Model-2. In Model-1, we achieved the good field region as ± 30 mm and the central field at ~ 10 mm off from the centre of the pole toward the back yoke, and changing with the magnet excitement. In Model-2, a cut-out of size 30 mm × 10 mm at the pole near the top yoke was provided to remove the above problem. In this case, we achieved the centre of the magnet and the pole centre at the same point and a good field region of ± 35 mm, and the field symmetric about the centre of the magnet. The magnetic field profiles for the mass analyzing magnet as per Model-1 and Model-2 are shown in Fig. 8.25 and 8.26 respectively.

The amp-turns product (NI) was calculated as $NI = B \text{ (T)} \times \text{pole gap (meter)} / (4\pi \times 10^{-7})$ assuming the permeability of iron to be infinite. The total NI for the required field is 6210. Considering a safety factor for saturation of about 10-15 %, the total NI product chosen for coils was 7200. The calculated mass resolving power ($\Delta M / M$) using standard relation of

the magnet was about 1 %. The focal length (f) of the mass analyzing magnet, $f = - (1/\rho) \sin\theta$, was 120 mm in the present case.

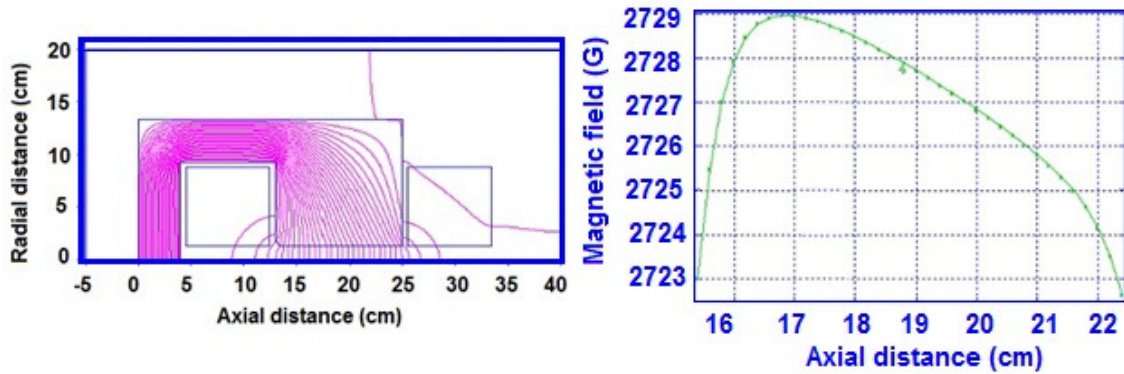


Figure 8.25 : The magnetic field profile for the mass analyzing magnet : Model-1.

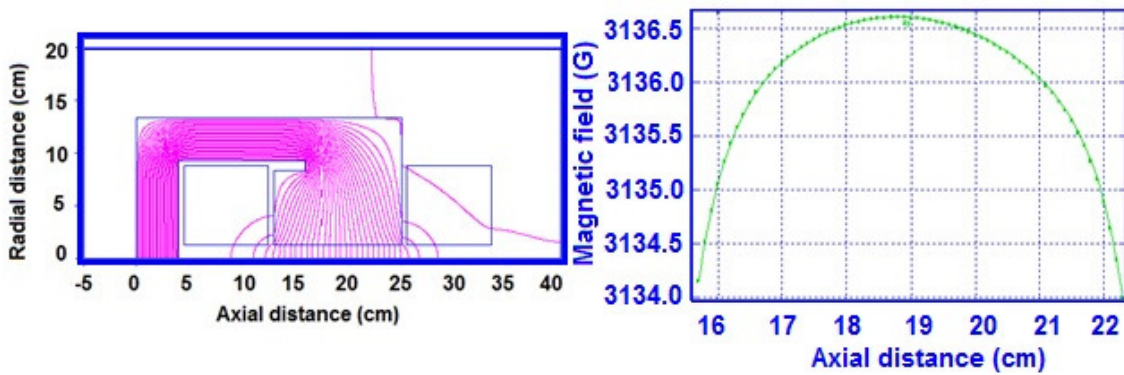


Figure 8.26 : The magnetic field profile for the mass analyzing magnet : Model-2.

This magnet has focussing effect in the horizontal plane only and also acts as drift space in the horizontal plane. It is assumed that the entrance and the exit angles are perfectly same. A small vertical focussing effect can be seen due to fringing field present at the entrance and the exit of the magnet. In general, the image suffers from aberrations due to higher order terms, particularly for marginal beams. We have tried to minimize the geometrical aberrations due to the higher order terms by incorporating multi-pole field components in the magnet itself.

2) **Fabrication of electromagnet :** The magnet yoke for the mass analyzing magnet was fabricated using 35 mm thick low carbon 'A' grade steel. A cross-sectional view of the magnet yoke for the mass analyzing magnet is shown in Fig. 8.27.

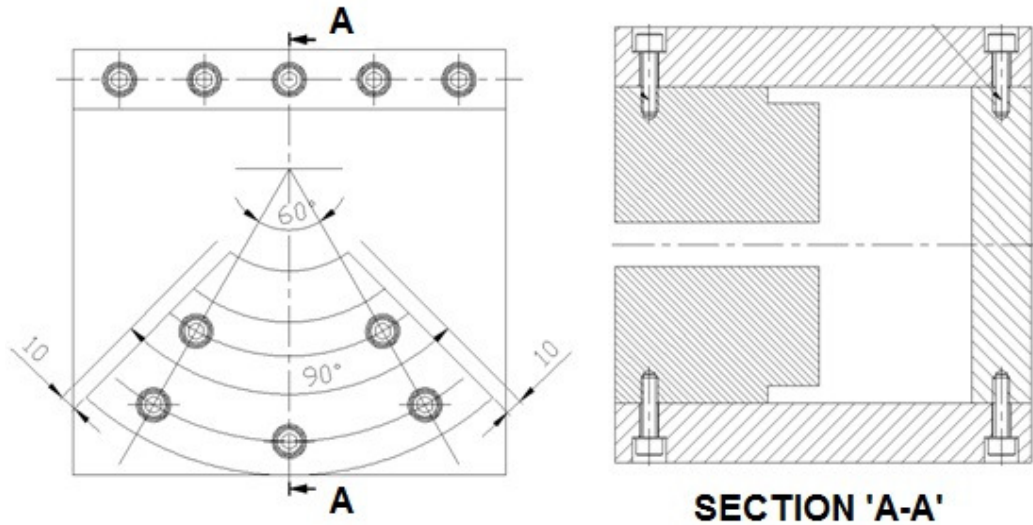


Figure 8.27 : A cross-sectional view of the magnet yoke for the mass analyzing magnet.

The pole pieces of the mass analyzing magnet are of sector type. The pole pieces were individually machined and bolted with the top and bottom yoke plates. The top and bottom of the pole pieces were finished by surface grinding, to maintain the pole gap. The accuracy in the pole gap was ± 0.05 mm. Utmost care was taken at the time of machining to ensure that the entrance and exit angles remain same. Two air-cooled excitation coils were fabricated using standard wire gauge (10 SWG) super enamelled copper conductor. Each excitation coil had 18 turns per layer (N / L) and 20 layers (L), {i.e. N = 360 turns}. The total length of the conductor used for one coil was 250 m and its measured resistance was 0.52Ω . The insulation to the conductor layer was provided using 'H' class fibre glass insulating tape. The excitation coils were connected in series and the operating current was chosen to be 10 A. The excitation coils were energized using constant current power supply of rating 25 V and 15 A DC. The stability of the power supply was 0.1 %. The vacuum chamber for the mass

analyzing magnet had a rectangular cross-section of 120 mm × 25 mm and was fabricated in stainless steel.

The vacuum chamber had three ports having CF152 flanges (either fixed or rotatable). The left side port of the vacuum chamber of the mass analyzing magnet was connected to a vacuum system where a turbo-molecular pump of capacity 400 l/s was mounted for evacuation. On the right side of the straight branch, a Faraday cup was mounted for measurement of the total beam current when the mass analyzing magnet was not energized. A Faraday cup was also mounted on the remaining port of the vacuum chamber of the mass analyzing magnet for measurement of the beam current of desired ion species passing through the magnet. The required magnetic field for the hydrogen species H^+ , H_2^+ , and H_3^+ , with respect to the beam energy, is shown in Fig. 8.28.

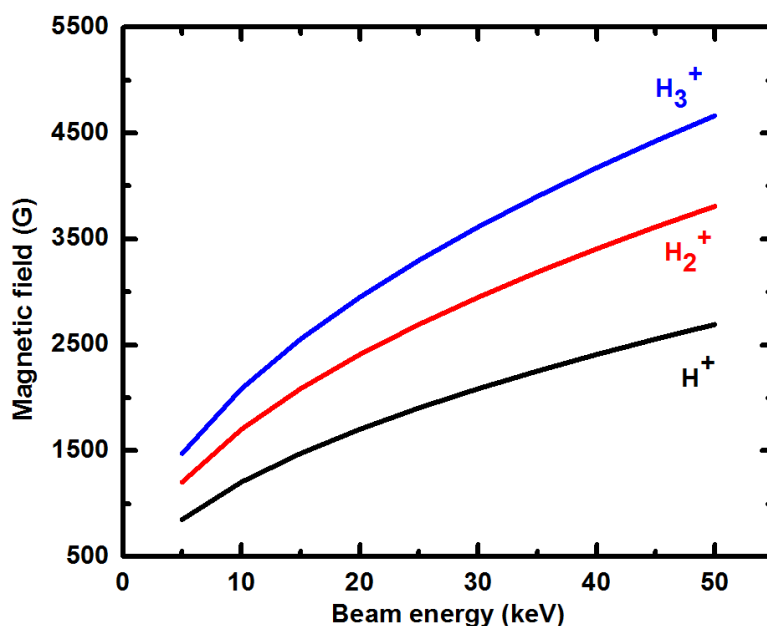


Figure 8.28 : The required magnetic field for hydrogen species H^+ , H_2^+ , and H_3^+ with respect to the beam energy.

3) Magnetic field mapping : The magnetic field measurements were done using a computer controlled three-axis coordinate measuring machine. A Hall probe (Model : MPT-141, Make : M/s Group 3 Technology Ltd., Germany) was attached at the Y-arm with a probe

holder. The Hall probe had field ranges : 0.3, 0.6, 1.2, 3.0 T, and corresponding serial / general purpose interface bus (GPIB) resolutions of 0.001, 0.01, 0.01, 0.01 G, respectively. The probe size was 15 mm × 5 mm × 2 mm, with a sensitive area of size 1 mm × 0.5 mm. The measurement rate was 10 per second. The measured magnetic field homogeneity for axial distance ± 30 mm is given in Table 8.3. A field homogeneity better than 0.1 % was achieved. The design, calculated effective length and their difference at 3000 G is given in Table 8.4.

Field Homogeneity	Field (G)
1.5e-04, 1.1e-04	600
1.9e-04, 3.9e-05	1200
4.1e-05, 2.8e-04	1900
-1.4e-04, 5.5e-04	2500
-3.8e-04, 8.8e-04	3000

Table 8.3 : *The measured magnetic field homogeneity for axial distance ± 30 mm.*

(All data in mm)					
Radius->	85	90	120	150	155
Design	133.52	141.37	188.50	235.62	243.47
Calculated	152.23	160.58	208.82	255.00	262.40
Difference	18.71	19.21	20.32	19.38	18.93

Table 8.4 : *The design, calculated effective length and their difference at 3000 G.*

The effective length was calculated from the measured data using standard relation i.e. $L_{\text{eff}} = [\int B \cdot dl / B_0]$, where B_0 is the field at the centre, and the effect of the fringe field is considered. It is clear that the extra effective length is 20 mm. Variation of the magnetic field (calculated and measured) with the current is shown in Fig. 8.29. The error associated in the field measurement is less than 0.5 %.

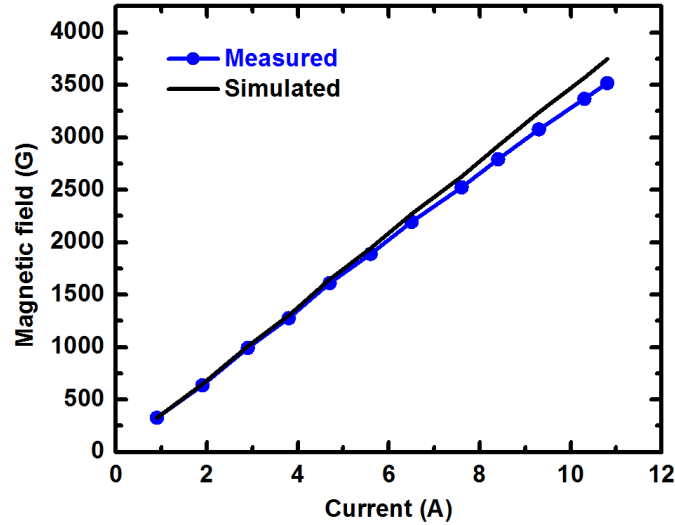


Figure 8.29 : Variation of the magnetic field (calculated and measured) with the current.

4) **Beam transmission through the magnet :** The beam transmission through the mass analyzing magnet has been worked out at 20 keV beam energy for 15 mA proton beam current. The 275 mm distance from the PE was treated as object plane for mass analyzing magnet. The twiss parameters at 275 mm down to the PE were : beta ($\beta_x = \beta_y$) 3.00 m, alpha ($\alpha_x = \alpha_y$) -11.27 rad, and $\gamma_x = \gamma_y$ can be calculated from $\gamma = [(1+\alpha^2) / \beta]$ for 20 keV proton beam energy. The r.m.s. emittance of 0.028 mm-mrad was achieved. This beam was passed through the mass analyzing magnet and the beam transmission was simulated using transport [175].

A drift space before and after the mass analyzing magnet length 300 mm, 50 mm respectively was added in this simulation. The twiss parameters $\beta_x = 0.65$ m, $\beta_y = 28.87$ m, $\alpha_x = -25.72$ rad, and $\alpha_y = -35.04$ rad were achieved. This beam was matched. The focussing effect and the beam transmission through the mass analyzing magnet for a proton beam is shown in Fig. 8.30. This graph shows that there is no focussing effect in the vertical plane. This is because for a mass analyzing magnet, since the radius of curvature becomes infinity, the focussing strength ($K = 1 / \rho^2 = 0$). It had horizontal and vertical beam sizes of 4 mm and

2 mm, respectively. The vertical beam passes directly without any focussing effects but horizontal beam got focussed. The overall envelope of the beam was 4 mm, which was well within the cross-section of the vacuum chamber. The beam profile in the horizontal and the vertical plane i.e. the phase space ellipse is shown in Fig. 8.31.

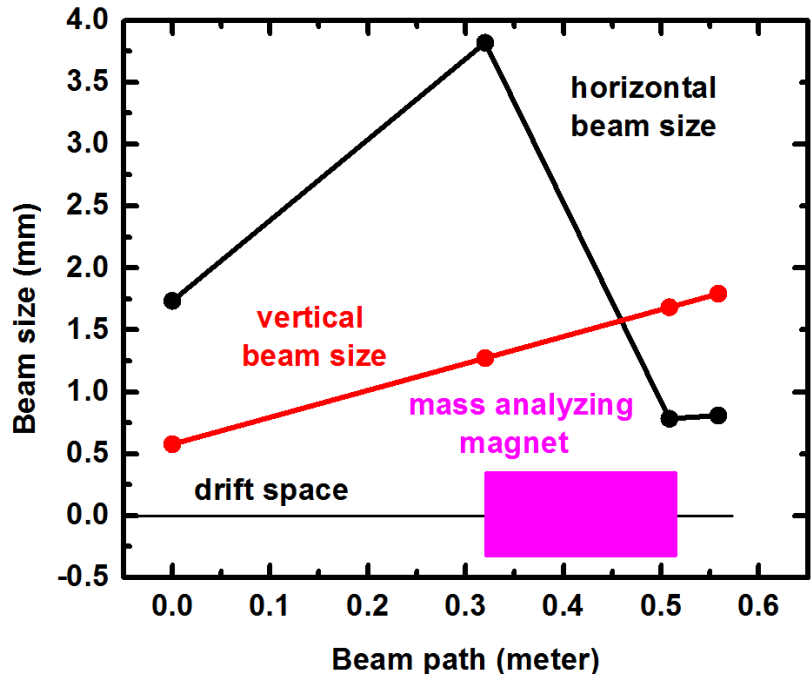


Figure 8.30 : The focussing effect and the beam transmission through the mass analyzing magnet for a proton beam.

Horizontal Plane (Emittance : 0.03 mm mrad)			
Entrance point	Just before bending magnet	Just after bending magnet	Exit point

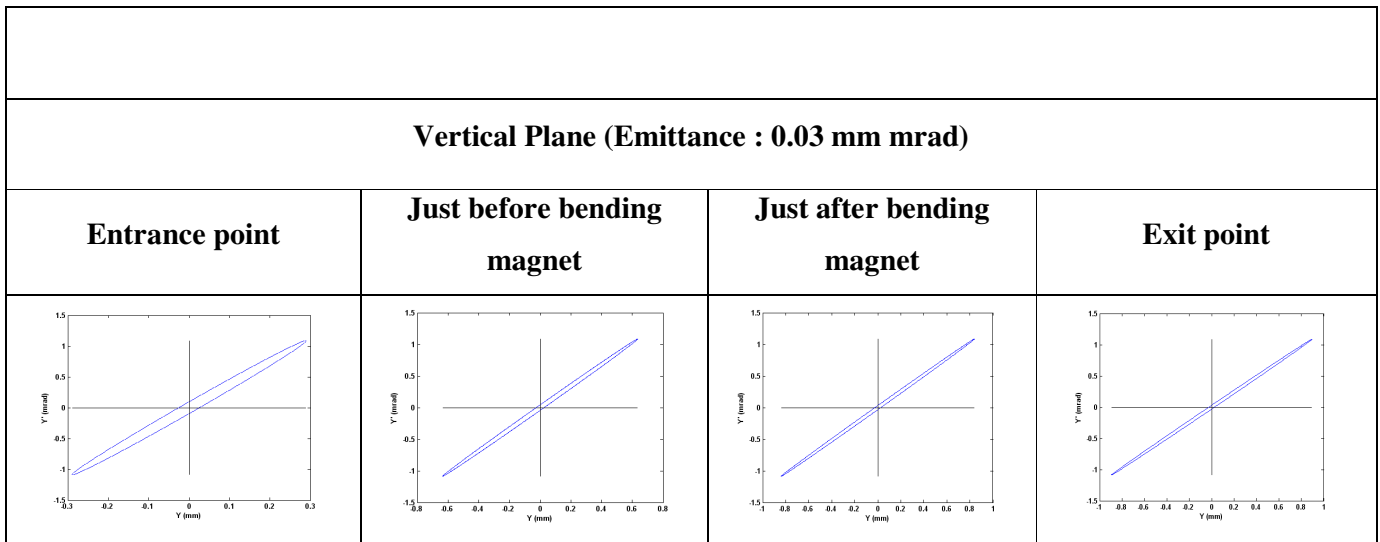


Figure 8.31 : The beam profile in the horizontal and the vertical planes i.e. phase space ellipse.

8.7 Supervisory Control and Monitoring System

For the trouble free, user-friendly, and safe operation of the ECRIS, a graphical supervisory control and monitoring system has been designed and developed using LabVIEW (M/s National Instruments) software. This will be integrated with the ECRIS soon. The graphical front panel view of the RRCAT-ECRIS supervisory control and monitoring system is shown in Fig. 8.32. It has remote as well as local control of this source. The algorithm has been written using LabVIEW which is a compiler for graphical programming language and provides virtual instrumentation for controlling industrial applications. It is a general purpose programming system with extensive libraries of functions for any programming task. It also provides built-in control drivers and connectivity to other systems. The design and development of a graphical interface for controlling the source is consists of,

- i. Data acquisition from serial port to read the values of all the parameters synchronously from the serial port after a specified interval of time.

- ii. Data base management of analog and digital data of the various subsystems to respond to various queries and to generate reports.
- iii. Presenting it in the interface in a user-friendly manner and controlling the systems by sending the commands to the serial port.

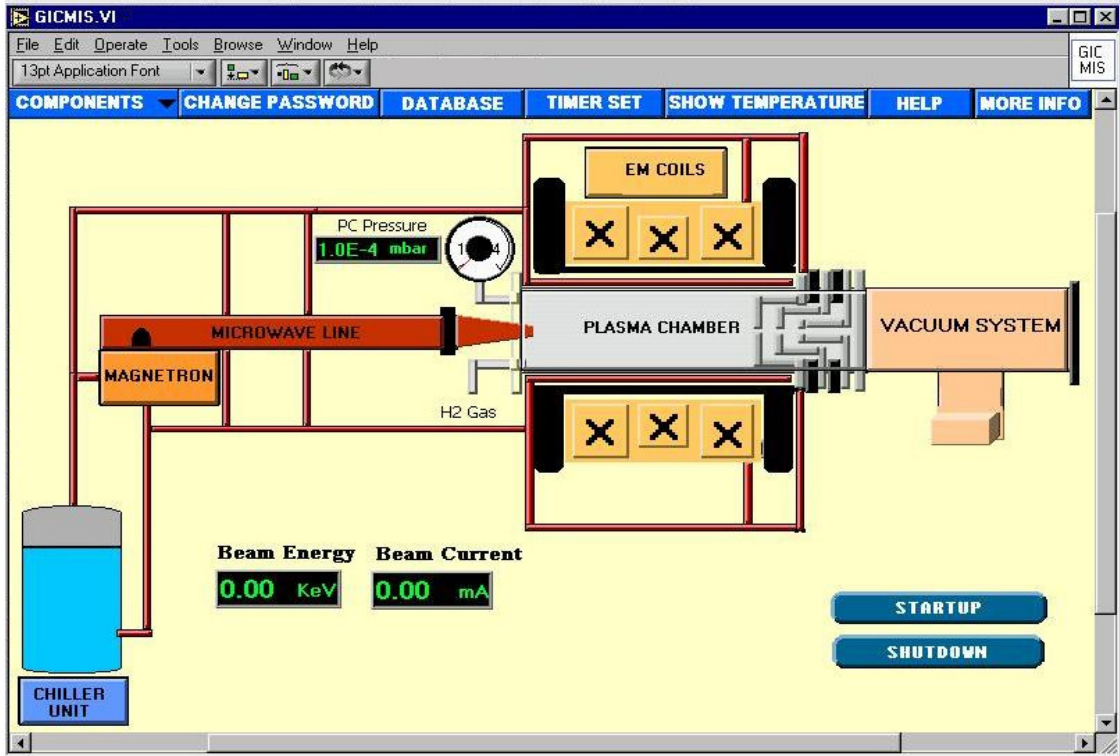


Figure 8.32 : The graphical front panel view of RRCAT-ECRIS supervisory control and monitoring system.

CHAPTER 9

Summary

At the end of the thesis, in **this chapter**, a summary of the thesis work has been presented. Further scope of improvement in the present system is also discussed.

1) Summary :

An electron cyclotron resonance plasma based ion source is an established source for delivering high current, high brightness, stable ion beam, with significantly higher lifetime. In this thesis we have described an electron cyclotron resonance ion source (ECRIS) operating at microwave frequency 2.45 GHz and 2 kW power in continuous wave mode. This source has been designed and developed to produce a proton beam current of 30 mA at 50 keV beam energy. In first phase the source, was operated up to 24 kV acceleration voltage and 8 mA of stable ion beam current has been extracted using acceleration-deceleration type extraction system. The extracted ion beam was characterized using a Thomson parabola ion spectrograph which confirmed the existence of the proton beam without the signature of other ions.

The ECRIS comprises of various sub-systems like plasma chamber and vacuum system, microwave system, electromagnet and its power supplies, plasma diagnostics device, beam extraction electrodes, beam diagnostics devices etc. These sub-systems have been designed using standard software and fabricated in-house. After that they have been individually tested and characterized before their final integration. The microwave system consisted of Magnetron as a source of microwave power (frequency : 2.45 GHz, power 2 kW continuous wave) and waveguide components like isolator with load, directional coupler, three-stub tuner, microwave vacuum window, high voltage break, and microwave launcher. All these components were designed using the *microwave studio* software. The waveguide components were developed using standard rectangular waveguide WR-284 sections. The

low and high power microwave testing was carried out using *vector network analyzer* and glass-water load, respectively. The Magnetron power supply was also developed indigenously and tested for its full load. A microwave radiation level of 2-3 mW/cm² was observed, which is well within the permissible limit.

A water-cooled plasma chamber with waveguide mount port, gas port, and pressure port was fabricated. The vacuum components were qualified with helium leak detector. Three water-cooled solenoid coils were used as electromagnets for the generation and confinement of the plasma. This arrangement can produce various types of magnetic field configurations. Various magnetic field configurations (resonance, off-resonance and mirror) were studied and simulated using the *Poisson* software. The magnetic field mapping was done using a Hall probe. The measured values and the design values are found to have a good agreement within 3 %. The magnetic field configurations are well suited to produce the multiply and singly charged ion beams. Various types of electrode geometries were studied using the *IGUN* software for extraction of the ion beam.

Plasma of argon / hydrogen / nitrogen was produced with the variations of wide range of microwave power (300-750 W), gas pressure (10⁻⁵-10⁻³ mbar). The stable discharge was obtained with the slight tuning of three-stub tuner to keep the reflected power minimum. The basic plasma parameters like electron density, electron temperature, plasma potential, floating potential etc. were studied using a Langmuir probe. Experimentally, electron density of 3 to 6.5 × 10¹¹ cm⁻³ and electron temperature of ~ 5 to 20 eV was obtained with the variation of microwave power (300-750 W) at gas pressure ~ 10⁻⁴ mbar, which is beyond the cut-off electron density of 7.5 × 10¹⁰ cm⁻³. The stability of the plasma has been checked under different operation regime and was found satisfactory. The ECRIS has been operated continuously for more than eight hours in a day without any difficulty.

The x-ray emission produced from a copper target by the impact of low energy ECRIS beam of up to 25 keV energy has been successfully observed for hydrogen, nitrogen, and argon ion beams. The copper K- α and K- β x-ray emission at 8.05 keV and 8.9 keV was observed. The K- α x-ray line intensity exhibited an increase with the increasing energy following the scaling of $I_{K-\alpha} \propto E^\gamma$, where the scaling exponent was 4.0, 4.2 and 4.1 for hydrogen, nitrogen, and argon ion beam respectively. The results are well explained by considering the K-shell ionization cross-section for ion impact. The study is important for characterization of materials, detectors, calibration of thermo-luminescent dosimeter, trace elemental analysis and medical applications.

Using the ECRIS, we have demonstrated deposition of titanium film on float glass substrate using argon ion beam sputtering method. This film was characterized using x-ray reflectivity and atomic force microscopy. The titanium film had a thickness of 880 Å, surface roughness of 14 Å, and density 4.47 gm/cm³. The deposited thin film shows uniform density, mirror-like finish, non-porous structure, and strong adherence to the float glass substrate.

2) **Future Outlook :**

Our future goal is to extract the 30 mA proton beam current up to 50 keV beam energy for injector requirement. To use the present ECRIS, as an ion source for a proton accelerator, it is also required to design and develop a low energy beam transport line to transport the proton beam to the radio frequency quadrupole. The beam transport line has to match properly the emittance ellipse of the beam at the end of the injection line to the acceptance ellipse of the RF quadrupole to avoid the beam loss. Various diagnostic elements like Faraday cup for measuring beam current, a beam buncher for bunching the beam, horizontal and vertical beam profile monitors, and beam emittance measurement device are needed. The ion optics layout should provide reasonable mass separation i.e. rejection of the

molecular hydrogen beam to ensure beam purity to the maximum possible extent and the total length of low energy beam transport should be minimum possible for space restrictions.

The space charge at low energy and high current is a serious problem which has to be considered while using the three-electrode geometry for the extraction of 30 mA proton beam current up to 50 keV beam energy. There is also a scope to design and develop a five-electrode geometry which is widely used for the space charge compensation of ion beams at low energy. With increasing the proton beam current, it has been noticed that there is possibility of back-streaming of the electrons which can damage the microwave window. Use of a 90° waveguide (E-plane bend) with the microwave system that can circumvent the problem of back-streaming of the electrons and prevent damage of the microwave window.

Bibliography

- 1 F. F. Chen, "Introduction to Plasma Physics" (Plenum Press, New York, 1974).
- 2 F. F. Chen, "Introduction to Plasma Physics and Controlled Fusion" (Springer Berlin Heidelberg, New York, 1984).
- 3 J. A. Bittencourt, "Fundamentals of Plasma Physics" (Springer Berlin Heidelberg, New York, 2004).
- 4 Y. K. Kim, and M. E. Rudd, "Binary-encounter dipole model for electron-impact ionization", Phys. Rev. **A50**, 3954-3967 (1994).
- 5 T. H. Stix, "Waves in Plasmas" (Springer Berlin Heidelberg, New York, 1992).
- 6 R. Geller, "Electron Cyclotron Resonance Ion Sources and ECR Plasmas" (Institute of Physics, London, 1996).
- 7 Y. Torii, M. Shimada, I. Watanabe, J. Hipple, C. Hayden, and G. Dionne, "A high-current density and long lifetime ECR source for oxygen implanters" Rev. Sci. Instrum. **61**, 253-255 (1990).
- 8 K. Wisemann, "The ion temperature in a plasma with hot electrons" IEEE Trans. Nucl. Sci. **NS-19**, 156-159 (1972).
- 9 N. Sukudo, "Microwave ion source for ion implantation" Nucl. Instr. Meth. Phys. Res. **B21**, 168-177 (1987).
- 10 M. Shimada, I. Watanabe, and Y. Torii, "Very high current ECR ion source" Nucl. Instr. Meth. Phys. Res. **B39**, 242-245 (1989).
- 11 T. Taylor, and J. S. C. Wills, "A high-current low-emittance dc ECR proton source" Nucl. Instr. Meth. Phys. Res. **A309**, 37-42 (1991).
- 12 R. Baskaran, S. K. Jain, and S. S. Ramamurthi, "ECR ion source using slow wave structures" Rev. Sci. Instrum. **63**, 2525-2528 (1992).

-
- 13 H. Postma, "Multiply charged heavy ions produced by energetic plasmas" *Phys. Letters* **A31**, 196-197 (1970).
 - 14 R. Geller, B. Jacquot, and M. Pontonnier, "Status of the multiply charged heavy-ion source MIMIMAFIOS" *Rev. Sci. Instrum.* **56**, 1505-1510 (1985).
 - 15 C. Lyneis, "Performance of the LBL ECR ion source" *Nucl. Instr. Meth. Phys. Res.* **B10/11**, 775-778 (1985).
 - 16 R. Baskaran, J. M. Heurtier, and C. E. Hill, "Modeling of the electron cyclotron resonance sulphur source" *Rev. Sci. Instrum.* **64**, 191-196 (1993).
 - 17 G. Melin, A. G. Drentje, A. Girard, and D. Hitz, "Ion behavior and gas mixing in electron cyclotron resonance plasmas as sources of highly charged ions" *J. Appl. Phys.* **86**, 4772-4779 (1999).
 - 18 W. Lotz, "Electron impact ionization cross-sections and ionization rate coefficients for atoms and ions from hydrogen to calcium" *Z. Phys.* **216**, 241-247 (1968).
 - 19 A. Muller, and E. Salzborn, "Scaling of cross sections for multiple electron transfer to highly charged ions colliding with atoms and molecules" *Phys. Letters* **A62**, 391-394 (1977).
 - 20 A. Muller, C. Achenbach, and E. Salzborn, "Dependence of the charge transfer between atoms and highly charged ions on the ionization potential of the atoms" *Phys. Letters* **A70**, 410-412 (1979).
 - 21 H. Knudsen, H. K. Haugen, and P. Hvelplund, "Single electron capture cross section for medium and high velocity, highly charged ions colliding with atoms" *Phys. Rev.* **A23**, 597-610 (1981).
 - 22 H. Tsujii, "The present and future of heavy charged particle therapy" *Nihon. Rinsho.* **54**, 268-273 (1996).

-
- 23 Y. Jongen, "Radiotherapy systems using proton and carbon beams" *Bull. Mem. Acad. R. Med. Belg.* **163**, 471-478 (2008).
- 24 A. Kitagawa, T. Fujita, M. Muramatsu, S. Biri, and A. G. Drentje, "Review on heavy ion radiotherapy facilities and related ion sources" *Rev. Sci. Instrum.* **81**, 02B909-1-7 (2010).
- 25 M. Muramatsu, and A. Kitagawa, "A review of ion sources for medical accelerators" *Rev. Sci. Instrum.* **83**, 02B909-1-7 (2012).
- 26 G. Schettino, M. Folkard, B. Vojnovic, A. Michette, and K. M. Prise, "X-ray microbeams for radiobiological studies : Current status and future challenges" *Piers Online* **6**, 207-211 (2010).
- 27 T. Pawlicki, and A. J. Mundt, "Quality in radiation oncology" *Med. Phys.* **34**, 1529-1534 (2007).
- 28 G. D. Alton, "Ion sources for accelerators in materials research" *Nucl. Instr. Meth. Phys. Res.* **B73**, 221-288 (1993).
- 29 I. P. Jain, and G. Agarwal, "Ion beam induced surface and interface engineering" *Surf. Sci. Reports* **66**, 77-172 (2011).
- 30 P. K. Nema, "Application of accelerators for nuclear systems : accelerator driven system" *Energy Procedia* **7**, 597-608 (2011).
- 31 Y. Ohara, "Development of high power ion sources for fusion" *Rev. Sci. Instrum.* **69**, 908-913 (1998).
- 32 S. K. Guharay, J. Orloff, and M. Wada, "Ion beams and their applications in high resolution probe formation" *IEEE Trans. Plasma Sci.* **PS-33**, 1911-1930 (2005).
- 33 D. Yuan, K. Jayamanna, M. Dombisky, D. Lovie, S. Kadantsev, R. Keitel, T. Kuo, M. McDonald, M. Olivo, and P. Schmor, "Design of an electron cyclotron resonance ion

-
- source for the isotope separator and accelerator at TRIUMF” *Rev. Sci. Instrum.* **71**, 643-645 (2000).
- 34 J. B. Friedmann, J. L. Shohet, and A. E. Wendt, “Ion cyclotron resonance mass spectrometry with a microwave plasma source” *IEEE Trans. Plasma Sci.* **PS-19**, 47-51 (1991).
- 35 O. Vogel, “Atomic physics with ECR ion source in Upsala” *Physica Scripta* **42**, 341-342 (1990).
- 36 I. N. Draganic, M. E. Bannister, F. W. Meyer, C. R. Vane, and C. C. Havener, “Production of molecular ion beams using an electron cyclotron resonance ion source” *Nucl. Instr. Meth. Phys. Res.* **A640**, 1-5 (2011).
- 37 R. Racz, S. Biri, Z. Juhasz, B. Sulik, and J. Palinkas, “Molecular and negative ion production by a standard electron cyclotron resonance ion source” *Rev. Sci. Instrum.* **83**, 02A313-1-3 (2012).
- 38 H. Neumann, M. Tartz, F. Scholze, T. Chasse, H. Kersten, and H. Leiter, “Broad beam ion sources for electrostatic space propulsion and surface modification processes : From roots to present applications” *Contrib. Plasma Phys.* **47**, 487-497 (2007).
- 39 A. France, R. Gobin, O. Delferriere, P. A. Leroy, M. Delaunay, and A. Farchi, “High current proton and deuteron ECR source developments at CEA” EPAC-1996, THP010L, 10-14 June 1996, Gran Sitges Hotel, Sitges, Barcelona, (1996).
- 40 H. Koivisto, J. Arje, and M. Nurmi, “Metal ion beams from an ECR ion source using volatile compounds” *Nucl. Instr. Meth. Phys. Res.* **B94**, 291-296 (1994).
- 41 H. Nishimura, T. Ono, M. Oda, and S. Matsuo, “Tantalum film for x-ray lithography mask deposited by electron cyclotron resonance plasma source coupled with divided microwaves” *J. Vac. Sci. Technol.* **B22**, 40-45 (2004).
- 42 B. Chapman, “Glow Discharge Process” (John Wiley & Sons, New York 1980).

-
- 43 K. H. Kretshmer, K. Matl, G. Lorenz, I. Kessler, and B. Dumbacher, "An electron cyclotron resonance plasma source" *Solid State Technol.* **33**, 53-55 (1990).
- 44 Z. Sitar, M. J. Paisley, D. K. Smith, and R. F. Dawis, "Design and performance of an electron cyclotron resonance plasma source for standard molecular beam epitaxy equipment" *Rev. Sci. Instrum.* **61**, 2407-2411 (1990).
- 45 Y. Tani, Y. Aoi, and E. Kamijo, *Appl. Phys. Lett.* "Composition and crystal structure of carbon nitride films prepared by the electron cyclotron resonance plasma sputtering method" **73**, 1652-1654 (1998).
- 46 K. Akiyama, E. Tanaka, and A. Takimoto, "Effects of ions on properties of a-Si:H films prepared by ECR plasma CVD method" *Jpn. J. Appl.* **27**, 2192-2198 (1998).
- 47 Y. Weng, and M. J. Kushner, "Electron energy distribution in electron cyclotron resonance discharges for materials processing" *J. Appl. Phys.* **72**, 33-42 (1992).
- 48 H. R. Garner, T. Ohkawa, A. M. Howald, A. W. Leonard, L. S. Peranich, and J. R. D'Aoust, "An inexpensive x-ray source based on an electron cyclotron" *Rev. Sci. Instrum.* **61**, 724-727 (1990).
- 49 R. Baskaran, "Theoretical analysis of electron cyclotron resonance x-ray sources" *Rev. Sci. Instrum.* **69**, 3510-3514 (1998).
- 50 R. Baskaran, and T.S. Selvakumaran, "Experimental studies on a compact electron cyclotron resonance plasma x-ray source" *Rev. Sci. Instrum.* **70**, 2637-2645 (1999).
- 51 R. Baskaran, and T. S. Selvakumaran, "Analysis of x-ray spectrum obtained in electron cyclotron resonance x-ray source" *Rev. Sci. Instrum.* **77**, 03C103-1-3 (2006).
- 52 J. Noland, J. Y. Benitez, D. Leitner, C. Lyneis, and J. Verboncoeur, "Measurement of radial and axial high energy x-ray spectra in electron cyclotron resonance ion source plasmas" *Rev. Sci. Instrum.* **81**, 02A308-1-3 (2010).

-
- 53 I. G. Brown, "The Physics and Technology of Ion Sources" (John Wiley & Sons, New York, 1989).
- 54 H. Zhang, "Ion Sources", (Springer Berlin Heidelberg, New York, 1999).
- 55 T. Taylor, and J. Mouris, "An advanced high-current low-emittance dc microwave proton source" Nucl. Instr. Meth. Phys. Res. **A336**, 1-5 (1993).
- 56 J. M. Lagniel, P. Y. Beauvais, D. Bogard, G. Bourdelle, G. Charruau, O. Delferrière, D. De Menezes, A. France, R. Ferdinand, Y. Gauthier, R. Gobin, F. Harrault, J. L. Jannin, P. A. Leroy, I. Yao, P. Ausset, B. Pottin, N. Rouvière, L. Celona, and S. Gammino, "Status and new developments of the high intensity electron cyclotron resonance source light ion continuous wave, and pulsed mode" Rev. Sci. Instrum. **71**, 830-835 (2000).
- 57 R. Gobin, P. Y. Beauvais, D. Bogard, G. Charruau, O. Delferrière, D. De Menezes, A. France, R. Ferdinand, Y. Gauthier, F. Harrault, P. Mattei, K. Benmeziane, P. Leherissier, J. Y. Paquet, P. Ausset, S. Bousson, D. Gardes, A. Olivier, L. Celona, and J. Sherman, "Status of the light ion source developments at CEA/Saclay" Rev. Sci. Instrum. **75**, 1414-1416 (2004).
- 58 O. Delferrière, D. De Menezes, R. Gobin, F. Harrault, and O. Tuske, "Electron cyclotron resonance 140 mA D+ beam extraction optimization for IFMIF EVEDA accelerator" Rev. Sci. Instrum. **79**, 02B723-1-3 (2008).
- 59 S. Gammino, G. Ciavola, L. Celona, L. Torrisi, M. Castro, F. Chines, S. Marletta, E. Messina, J. Qin, and Z. Wang, "Off-line efficiency measurements of the microwave discharge source (MIDAS) at the Laboratorio Nazionale del Sud" Rev. Sci. Instrum. **69**, 747-749 (1998).

-
- 60 L. Celona, G. Ciavola, S. Gammino, R. Gobin, and R. Ferdinand, "TRIPS : The high intensity proton source for the TRASCO project" *Rev. Sci. Instrum.* **71**, 771-773 (2000).
- 61 L. Celona, G. Ciavola, S. Gammino, F. Chines, M. Presti, L. Ando, X. H. Guo, R. Gobin, and R. Ferdinand, "Status of the Trasco intense proton source and emittance measurements" *Rev. Sci. Instrum.* **75**, 1423-1426 (2004).
- 62 G. Ciavola, L. Celona, S. Gammino, M. Presti, L. And`o, S. Passarello, X. Zh. Zhang, F. Consoli, F. Chines, C. Percolla, V. Calzona, and M. Winkler, "A version of the Trasco intense proton source optimized for accelerator driven system purposes" *Rev. Sci. Instrum.* **75**, 1453-1456 (2004).
- 63 G. Ciavola, S. Gammino, G. Raia, and J. Sura, "MIDAS, a high efficiency microwave discharge ion source for the EXCYT facility" *Rev. Sci. Instrum.* **65**, 1110-1112 (1994).
- 64 L. Celona, S. Gammino, G. Ciavola, F. Chines, S. Marletta, and E. Messina, "Ionization efficiency measurements with the microwave discharge ion source MIDAS" *Proc. of EPAC-2000*, 26-30 June 2000, Vienna (2000).
- 65 F. Maimone, G. Ciavola, L. Celona, S. Gammino, D. Mascali, N. Gambino, R. Miracoli, F. Chines, S. Passarello, G. Gallo, and E. Zappal`a, "Status of the versatile ion source VIS" *EPAC2008*, MOPC151 (2008).
- 66 R. Miracoli, L. Celona, G. castro, D. Mascali, S. Gammino, D. Lanaia, R. Di Giugno, T. Serafino, and G. Ciavola, "Characterization of the versatile ion source and possible applications as injector for future projects" *Rev. Sci. Instrum.* **83**, 02A305-1-3 (2012).
- 67 P. Roychowdhury, and D. P. Chakravarthy, "High intensity electron cyclotron resonance proton source for low energy high intensity proton accelerator" *Rev. Sci. Instrum.* **80**, 123305-1-8 (2009).

-
- 68 V. S. Pandit, G. Pal, S. K. Thakuar, P. S. Babu, A. Goswami, A. Misra, S. Srivastava, M. Chatterjee, S. Bhattacharya, and R. C. Yadav, "Development of 2.45 GHz high current microwave ion source at VECC" InPAC-2011 (2011).
- 69 D. Kanjilal, G. Rodrigues, P. Kumar, A. Mandal, and A. Roy, "Performance of first high temperature superconducting electron cyclotron resonance ion source" *Rev. Sci. Instrum.* **77**, 03A317-1-3 (2006).
- 70 G. Rodrigues, P. S. Lakshmy, Sarvesh Kumar, A. Mandal, D. Kanjilal, R. Baskaran, and A. Roy, "Studies of emittance of multiply charged ions extracted from high temperature superconducting electron cyclotron resonance ion source, PKDELIS" *Rev. Sci. Instrum.* **81**, 02B713-1-3 (2010).
- 71 S. K. Jain, Akhilesh Jain, P. R. Hannurkar, and S. Kotaiah, "Characterization of plasma parameters, first beam results, and status of electron cyclotron resonance source" *Rev. Sci. Instrum.* **78**, 053301-1-6 (2007).
- 72 S. K. Jain, M. Tayyab, S. Bagchi, J. A. Chakera, and P. A. Naik, "Characterization of proton beam emission from an electron cyclotron resonance ion source" *Nucl. Instr. Meth. Phys. Res.* **A708**, 51-55 (2013).
- 73 A. F. Harvey, "Microwave Engineering" (Academic Press, New York 1963).
- 74 R. E. Collin, "Foundations for Microwave Engineering" (Mc-Graw Hill, New York, 1992).
- 75 D. M. Pozar, "Microwave Engineering" (John Wiley & Sons, New York, 2005).
- 76 A. Guthrie, "Vacuum Technology" (John Wiley & Sons, New York, 1967).
- 77 A. Roth, "Vacuum Technology" (North-Holland Publishing Company, New York, 1990).
- 78 A. Berman, "Vacuum Engineering Calculations, Formulas and Solved Exercises" (Academic Press, New York, 1992).

-
- 79 J. Root, and J. Asmussen, "Experimental performance of a microwave cavity plasma disk ion source" *Rev. Sci. Instrum.* **56**, 1511-1519 (1985).
- 80 R. Baskaran, S. K. Jain, and S. S. Ramamurthi, "E-plane horn excitation of slow wave structures for obtaining high-density electron cyclotron resonance plasmas" *Rev. Sci. Instrum.* **63**, 1939-1944 (1992).
- 81 S. K. Jain, A. Jain, and P. R. Hannurkar, "Indigenous development of a low cost high power 2 kW (CW), 2.45 GHz microwave system" *Ind. J. Pure & Appl. Phys.* **42**, 896-901 (2004).
- 82 S. Chilukuri, and W. L. Lichten, "Building an inexpensive microwave source for electrodeless discharge lamps" *Rev. Sci. Instrum.* **50**, 256-257 (1979).
- 83 L. G. Meiners, and D. B. Alford, "Simple low-cost microwave plasma source" *Rev. Sci. Instrum.* **57**, 164-166 (1986).
- 84 M. A. Brewer, I. G. Brown, M. R. Dickinson, J. E. Galvin, R. A. MacGill, and M. C. Salvadori, "Simple, safe, and economical microwave plasma-assisted chemical vapor deposition facility" *Rev. Sci. Instrum.* **63**, 3389-3393 (1992).
- 85 G. O. White, L. Chen, C. E. Patton, and R. L. Tinkoff, "High-power microwave pulse generator" *Rev. Sci. Instrum.* **63**, 3156-3166 (1992).
- 86 R. C. Rose, and S. W. David, "Performance and test results of a regulated magnetron pulser" LANL report LA-UR-98-3188 (1998).
- 87 T. Zaugg, C. Rose, J. D. Schneider, J. Sherman, and R. Stevens, "Operation of a microwave proton source in pulsed mode" LANL report LA-UR-98-3513 (1998).
- 88 R. Baskaran, S. K. Jain, and S. S. Ramamurthi, "A compact coaxial electron cyclotron resonance plasma source" *Rev. Sci. Instrum.* **67**, 1243-1245 (1996).
- 89 <http://www.cst.com>
- 90 <http://www.ansoft.com>

-
- 91 T. L. Smith, S. Berg, A. Grelick, and G. Waldschmidt, "Bidirectional coupler optimization in WR-284 type waveguide" PAC-2003 (2003).
- 92 H. Downs, P. Matthews, and W. W. Sanborn, "Waveguide directional couplers for high vacuum applications" EPAC-2008 (2008).
- 93 N. Marcuvitz, "Waveguide Handbook" (Mc-Graw-Hill, New York, 1951).
- 94 A. Ganguli, R. Baskaran, P. A. Naidu, and G. V. R. Raju, "High power microwave line with arbitrary impedances matching capability for plasma applications" Rev. Sci. Instrum. **60**, 244-248 (1989).
- 95 R. Baskaran, "Double window configuration as a low cost microwave waveguide window for plasma applications" Rev. Sci. Instrum. **68**, 4424-4426 (1997).
- 96 N. Sakudo, K. Tokigachi, H. Koike, and I. Kanomata, "Microwave ion source" Rev. Sci. Instrum. **48**, 762-766 (1977).
- 97 K. Krestschmer, K. Matl, G. Lorenz, and I. Kessler, Solid State Technology **33**, 53 (1980).
- 98 R. D. Tarey, R. K. Jarwal, A. Ganguli, and M. K. Akhtar, "High-density plasma production using a slotted helical antenna at high microwave power" Plasma Sources Sci. Technol. **6**, 189-200 (1997).
- 99 N. Sakudo, K. Tokiguchi, and T. Seki, "Beam qualities of a microwave ion source" Rev. Sci. Instrum. **61**, 309-311 (1990).
- 100 J. Sherman, A. Arvin, L. Hansborough, D. Hodgkins, E. Meyer, J. D. Schneider, R. R. Stevens, M. Thuot, and T. Zaugg, "Development of a 130-mA, 75-kV high voltage column for high-intensity dc proton injectors" Rev. Sci. Instrum. **69**, 1017-1019 (1998).
- 101 L. Celona, G. Ciavola, and S. Gammino, "Study of microwave coupling in electron cyclotron resonance ion sources and microwave ion sources" Rev. Sci. Instrum. **69**, 1113-1115 (1998).

-
- 102 Z. Yao, X. Tan, H. Du, and B. Luo, and Z. Liu, "A high-current microwave ion source with permanent magnet and its beam emittance measurement" *Rev. Sci. Instrum.* **79**, 073304-1-5 (2008).
- 103 <http://www.lns.infn.it>
- 104 S. B. Cohn, "Properties of ridge waveguide" *IRE Trans. Microwave Theory and Techniques* **35**, 783-788 (1947).
- 105 S. Hopfer, "The design of ridged waveguides" *IRE Trans. Microwave Theory and Techniques* **3**, 20-29 (1955).
- 106 I. S. Hong, B. S. Park, J. H. Jang, H. J. Kwon, Y. S. Cho, and Y. S. Hwang, "Design and construction of a compact microwave proton source for a proton linac" *Rev. Sci. Instrum.* **81**, 02A314-1-3 (2010).
- 107 Y. Mathur, G. Godrigues, R. Ahuja, U. K. Rao, N. Kumar, P. S. Lakshmy, D. Kanjilal, and A. Roy, "Design and development of a low cost 2.45 GHz ECR ion source for material sciences and other applications at IUAC, New Delhi" *InPAC-2011*, 60 (2011).
- 108 M. Bhattacharjee, H. K. Pandey, V. Naik, and A. Chakrabarti, "Design of a 2.45 GHz permanent magnet free ECR ion source for 1+ ion production in RIB facility at VECC" *InPAC-2011*, 104 (2011).
- 109 B. E. Kingdon, "An S-band variable attenuator for high-power working" *Journal of the British Institution of Radio Engineers* **9**, 471-478 (1955).
- 110 R. Baskaran, S. K. Jain, and S. S. Ramamurthi, "A high power low cost S-band waveguide load for accelerator application" *Journal of the Institution of Electronics & Telecommunication Engineers* **38**, 302-304 (1992).
- 111 C. G. Montgomery, "Techniques of Microwave Measurements" (Mc-Graw-Hill, New York, 1947).
- 112 E. L. Ginzton, "Microwave Measurements", (Mc-Graw-Hill, New York 1957).

-
- 113 K. N. Leung, R. D. Collier, L. B. Marshall, T. N. Gallaher, W. H. Ingham, R. E. Kribel, and G. R. Taylor, "Characteristics of a multidipole ion source" *Rev. Sci. Instrum.* **49**, 321-325 (1978).
- 114 K. N. Leung, "Multicusp ion sources" *Rev. Sci. Instrum.* **65**, 1165-1169 (1984).
- 115 G. Ciavola, L. Celona, S. Gammino, M. Presti, L. Ando, S. Passarello, X. Zh. Zhang, F. Consoli, F. Chines, C. Percolla, V. Calzona, and M. Winkler, "A version of the Trasco intense proton source optimized for accelerator driven system purposes" *Rev. Sci. Instrum.* **75**, 1453-1456 (2004).
- 116 O. Delferriere, D. De. Menezes, R. Gobin, F. Harrault, and O. Tuske, "Electron cyclotron resonance 140 mA D+ beam extraction optimization for IFMIF EVEDA accelerator" *Rev. Sci. Instrum.* **79**, 02B723-1-3(2008).
- 117 <http://www.laag1.lanl.gov>
- 118 <https://www.cobham.com>
- 119 <http://www.egun-igun.com>
- 120 S. K. Jain, P. A. Naik, and P. R. Hannurkar, "Design, fabrication, and characterization of a solenoid to generate magnetic field for an ECR proton source" *Sadhana : Academy Proceedings in Engineering Sciences* **35**, 461-468 (2010).
- 121 D. B. Montgomery, "Solenoid Magnet Design" (John Wiley & Sons, New York, 1966).
- 122 A. Septier, C. Germain, "Measurements of Magnetic Fields" (Elsevier, New York, 1967).
- 123 A. T. Forrester, "Large Ion Beams" (John Wiley & Sons, New York, 1988).
- 124 C. D. Child, "Discharge from hot CaO" *Phys. Rev. (Series I)* **32**, 492-511 (1911).
- 125 I. Langmuir, "The effect of space charge and residual gases on thermionic currents in high vacuum" *Phys. Rev.* **2**, 450-486 (1913).

-
- 126 S. A. Self, "Exact solution of the collisionless plasma sheath equation" *Phys. Fluids* **6**, 1762-1768 (1963).
- 127 <http://www.far-tech.com>
- 128 P. Spadtke, Junkernstr. 99, D-65205 Wiesbaden, Germany.
- 129 <http://www.simion.com>
- 130 F. F. Chen, R. H. Huddlestone, and S. L. Leonard, "Plasma Diagnostics Techniques" (Academic Press, New York, 1965).
- 131 J. D. Swift, and M. J. Schwar, "Electrical Probes for Plasma Diagnostics" (Elsevier, New York 1969).
- 132 I. M. Hutchinson, "Principles of Plasma Diagnostics" (Cambridge University Press, New York, 1987).
- 133 N. Hershkowitz, "Plasma Diagnostics" (Academic Press, New York, 1989).
- 134 M. J. Druyvesteyn, *Z. Phys.* **64**, 781-798 (1930).
- 135 O. A. Popov, "Effects of magnetic field and microwave power on electron cyclotron resonance type plasma characteristics" *J. Vac. Sci. Technol.* **A9**, 711-716 (1991).
- 136 V. A. Godyak, R. B. Piejak, and B. M. Alexandrovich, "Probe diagnostics of non-Maxwellian plasmas" *J. Appl. Phys.* **73**, 3657-3663 (1993).
- 137 S. K. Jain, A. Jain, D. Sharma, and P. R. Hannurkar, "Acquisition and analysis of Langmuir probe characterization for ECR plasma" *Ind. J. Phys.* **A80**, 1011-1015 (2006).
- 138 J. E. Heidenreich III, J. R. Paraszczak, M. Moisan, and G. Suave, "Electrostatic probe analysis of microwave plasmas used for polymer etching" *J. Vac. Sci. Technol.* **B5**, 347-354 (1987).

-
- 139 M. Nisha, K. J. Saji, R. S. Ajimsha, N. V. Joshy, and M. K. Jayaraj, "Characterization of radio frequency plasma using Langmuir probe and optical emission spectroscopy" *J. Appl. Phys.* **99**, 033304-1-4 (2006).
- 140 R. Kar, S. B. Singh, N. Tiwari, D. N. Barve, S. A. Barve, N. Chand, and D. S. Patil, "Diagnostics of downstream microwave electron cyclotron resonance plasma" *J. Phys : Conference Series* **208**, 012137-1-7 (2010).
- 141 A. Ganguli, R. Baskaran, and H. D. Pandey, "Feed optimization for slotted line antenna for high density plasma production" *IEEE Trans. Plasma Sci.* **PS-18**, 134-141 (1990).
- 142 P. Roychowdhury, H. Kewlani, L. Mishra, D. S. Patil, and K. C. Mittal, "Langmuir probe diagnostics of plasma in high current electron cyclotron resonance proton ion source" *Rev. Sci. Instrum.* **84**, 073303-1-12 (2013).
- 143 J. E. Allen, "Probe theory-the orbital motion approach" *Physica Scripta* **45**, 497-503 (1992).
- 144 S. K. Jain, V. K. Senecha, P. A. Naik, P. R. Hannurkar, and S. C. Joshi, "Microwave power coupling with electron cyclotron resonance plasma using Langmuir probe" *Pramana J. Phys.* **81**, 157-167 (2013).
- 145 K. Harres, M. Schollmeier, E. Brambrink, P. Audebert, A. Blazevic, K. Flippo, D. C. Gautier, M. Geibel, B. M. Hegelich, F. Nurnberg, J. Schreiber, H. Wahl, and M. Roth, "Development and calibration of a Thomson parabola with microchannel plate for the detection of laser-accelerated MeV ions" *Rev. Sci. Instrum.* **79**, 093306-1-9 (2008).
- 146 J. A. Cobble, K. A. Flippo, D. T. Offermann, F. E. Lopez, J. A. Oertel, D. Mastrosimone, S. A. Letzring, and N. Sinenian, "High-resolution Thomson parabola for ion analysis" *Rev. Sci. Instrum.* **82**, 113504-1-9 (2011).

-
- 147 M. Miyoshi, T. Hamakubo, T. Kodama, M. Tsuchiya, A. Koishikawa, and N. Aoki, “Development of the compact low-energy soft x-ray CT instrument for the soft material structural analysis” *J. Vac. Sci. Technol.* **B26**, 2356-2361 (2008).
- 148 C. Gaudin, M. Lamoureux, and C. Rouille, “X-ray emission from a compact hot plasma : applications to radiology and mammography” *Phys. Med. Biol.* **46**, 835-851 (2001).
- 149 S. A. Zhou, and A. Brahme, “Development of phase contrast X-ray imaging techniques and potential medical applications” *Physica Medica* **24**, 129-148 (2008).
- 150 R. Baskaran, and T. S. Selvakumaran, “Studies on the effective energy of x-rays generated by ECR and their use for the calibration of thermoluminescent dosimeter badges in low energy region” *Rev. Sci. Instrum.* **76**, 046106-1-3 (2005).
- 151 I. M. Govil, “Proton induced x-ray emission-A tool for non-destructive trace element analysis” *Current Science* **80**, 1542-1549 (2001).
- 152 R. Baskaran, and T. S. Selvakumaran, “Use of electron cyclotron resonance x-ray source for non destructive testing application” *Rev. Sci. Instrum.* **77**, 03C101-1-3 (2006).
- 153 W. Longley, and R. Miller, “A simple rotating anode x-ray generator” *Rev. Sci. Instrum.* **46**, 30-32 (1975).
- 154 D. H. Bilderback, P. Elleaume, and E. Weckert, “Review of third and next generation synchrotron light sources” *J. Phys. B : At. Mol. Opt. Phys.* **38**, S773-S797 (2005).
- 155 <http://www.amptek.com>
- 156 <http://www.xdb.lbl.gov>
- 157 H. R. Verma, “Atomic & Nuclear Analytical Methods” (Springer Berlin Heidelberg, New York, 2007).
- 158 F. S. Pool and Y. H. Shing, “Deposition of diamond like films by electron cyclotron resonance microwave plasmas” *J. Appl. Phys.* **68**, 62-65 (1990).

-
- 159 A. Ishii, S. Amadatsu, S. Minomo, M. Taniguchi, M. Sugiyo, Y. Sakaguchi, and T. Kobayashi, "Super-wide electron cyclotron resonance plasma source excited by traveling microwave as an efficient tool for diamond like carbon film deposition" *J. Vac. Sci. Technol.* **A12**, 1241-1243 (1994).
- 160 E. Kamijo, T. Nakamura, and Y. Tani, "AFM observations of DLC films prepared by the ECR sputtering method" *Nucl. Instr. Meth. Phys. Res.* **B121**, 110-115 (1997).
- 161 H. Inaba, S. Fujimaki, K. Furusawa, and S. Todoroki, "ECR-plasma parameters and properties of thin DLC films" *Vacuum* **66**, 487-493 (2002).
- 162 Y. Sakamoto, and Y. Ishibe, "Reduction of metal oxides by electron cyclotron resonance plasma of hydrogen-a model study on discharge cleaning" *Japanese J. Appl. Phys.* **19**, 839-843 (1980).
- 163 S. Y. Shapoval, P. V. Bulkin, A. A. Chumakov, S. A. Khudobin, I. Maximov, and G. M. Mikhaiov, "Compact ECR-source of ions and radicals for semiconductor surface treatment" *Vacuum* **43**, 195-197 (1992).
- 164 E. Chason, and T. M. Mayer, "Thin film and surface characterization by specular x-ray reflectivity" *Critical Reviews in Solid State and Materials Sciences* **22**, 1-67 (1997).
- 165 L. G. Parratt, "Surface studies of solids by total reflection of x-rays" *Phys. Rev.* **95**, 359-369 (1954).
- 166 L. Nevot, and P. Croce, "Caractérisation des surfaces par réflexion rasante de rayons X. Application à l'étude du polissage de quelques verres silicates" *Rev. Phys. Appl.* **15**, 761-779 (1980).
- 167 N. Jalili, and K. Laxminarayana, "A review of atomic force microscopy imaging systems : Application to molecular metrology and biological sciences" *Mechatronics* **14**, 907-945 (2004).

-
- 168 A. A. Sysoev, "The Physics and Engineering of Mass Spectrometry Devices & Electromagnet Setups" (Energoatomizdat, Moscow, 1983).
- 169 D. Henke, H. Tyrroff, R. Grotzschel, and H. Wirth, "Slow, highly charged ions from a 7.25 GHz ECR ion source" Nucl. Instr. Meth. Phys. Res. **B98**, 528-531 (1995).
- 170 D. Henke, and H. Tyrroff, "Ion optical system for transport and deceleration of highly charged ions" Rev. Sci. Instrum. **67**, 1070-1072 (1996).
- 171 L. T. Sun, H. W. Zhao, Z. M. Zhang, H. Wang, B. H. Ma, J. Y. Li, X. Z. Zhang, Y. C. Feng, X. H. Guo, X. X. Li, X. W. Ma, M. T. Song, and W. L. Zhan, "A latest developed all permanent magnet ECRIS for atomic physics research at IMP" Rev. Sci. Instrum. **77**, 03A319-1-3 (2006).
- 172 V. I. Gushenets, A. S. Bugaev, E. M. Oks, T. V. Kulevoy, A. Hershcovitch, and I. G. Brown, "Experimental comparison of time-of-flight mass analysis with magnetic mass analysis" Rev. Sci. Instrum. **79**, 02B701-1-3 (2008).
- 173 S. K. Jain, R. Malik, K. Sekar, P. A. Naik, and P. R. Hannurkar, "Design, fabrication and measurement of 90° mass analyzing magnet" Ind. J. Pure & Appl. Phys. **48**, 315-320 (2010).
- 174 J. J. Livingood, "The Optics of Dipole Magnets" (Academic Press, New York, 1969).
- 175 K. L. Brown, CERN 73-16 (1973), CERN 80-04 (1980), SLAC 95-06 (1995).